

OSMRE National Technology Transfer Team (NTTT)
Applied Science Final Report

U.S. Department of the Interior
Office of Surface Mining Reclamation and Enforcement

Field Investigation and Stability Analysis of Coal Slurry Impoundments
Final Report

OSM cooperative agreement number: S16AC20074

Reporting Period: 10/01/2016 to 02/28/2019

Principal Authors:

Ming Xiao, Principal Investigator
Department of Civil and Environmental Engineering
The Pennsylvania State University
University Park, PA, 16802
Email: mxiao@engr.psu.edu; Phone: (814) 865-8056

Min Liew and Sajjad Salam, Graduate Research Assistants
Department of Civil and Environmental Engineering
The Pennsylvania State University
University Park, PA, 16802

Shimin Liu, Co-Principal Investigator
Department of Energy and Mineral Engineering
The Pennsylvania State University
University Park, PA, 16802

Jamal Rostami, Co-Principal Investigator
Department of Mining Engineering
Colorado School of Mines
Golden, CO 80401

April 22, 2019

DISCLAIMER

This report was prepared as an account of work sponsored by an agency of the United States Government. Neither the United States Government nor any agency thereof, nor any of their employees, makes any warranty, express or implied, or assumes any legal liability or responsibility for the accuracy, completeness, or usefulness of any information, apparatus, product, or process disclosed, or represents that its use would not infringe privately owned rights. Reference herein to any specific commercial product, process, or service by trade name, trademark, manufacturer, or otherwise does not necessarily constitute or imply its endorsement, recommendation, or favoring by the United States Government or any agency thereof. The views and opinions of authors expressed herein do not necessarily state or reflect those of the United States Government or any agency thereof.

ABSTRACT

The main objective of this project was to evaluate coal slurry impoundments stability under field conditions and impacts of dynamic loading in active surface mines. There are over 200 coal waste tailings dams in the US that are classified as having high hazard potential by the Federal Emergency Management Agency's (FEMA) hazard rating system. OSMRE requires comprehensive safety analysis in the design of coal slurry and refuse dams. There was a need for a field study on the geotechnical properties of fine coal refuse as it exists in coal refuse (tailings) dams after placement. This research project was conducted to address the above issues by conducting field investigation of the in-situ geotechnical properties of coal refuse under static and dynamic conditions. The necessity to look at both static and dynamic loading conditions is the possibility of unstable impoundments in the case of an earthquake or blasting as part of production or road construction in the area. This study combines field observations with numerical modeling to evaluate the stability of coal slurry impoundments under different loading conditions using the measured in-situ properties as input parameters. Numerical modeling and verifications/validation allows for the use of this approach in assessment of stability of more complex impoundments under various conditions.

Three tasks were included in this project: (1) site investigation of geotechnical properties to characterize the in situ properties of coal refuse; (2) seismic surveys and analyses of coal slurry impoundments under blasting shock waves to characterize the seismic behavior and dynamic properties, (3) development of numerical models to evaluate the stability of coal slurry impoundments under static and dynamic loadings. The work completed involved extensive on site geotechnical investigations and sampling for laboratory testing as well as direct measurement of material properties pertinent to tailings dam stability under various conditions, including dynamic loading which was simulated by seismic studies of the sites. The results were used in calibration of numerical models that can be subsequently used for assessment of different tailing dam geometry and dynamic loading (in terms of magnitude and frequency). The study coupled the soil mechanics and hydrological behavior of the ground in evaluation of ground stability.

The final report of the project includes: (1) detailed field investigation approach (including drilling, sampling, and laboratory and in-situ testing) and summary of the geotechnical properties of the representative coal slurry samples, with related statistical analysis; (2) detailed seismic survey approach and data analyses for coal refuse impoundments under dynamic loading by onsite blasting; (3) results of numerical modeling and calibration of upstream coal slurry impoundment dams under static and dynamic loadings.

ACKNOWLEDGEMENTS

This project is supported by the Office of Surface Mining Reclamation and Enforcement (OSMRE), U.S. Department of Interior, under the cooperative agreement number S16AC20074. Ronald Miles is the technical program manager of this project. Any opinions, findings, and conclusions or recommendations expressed in this report are those of the authors and do not necessarily reflect the views of OSMRE. Pagnotti Enterprises, Inc provided site access to the coal slurry impoundments and partial financial support; the authors thank James Pagnotti, President of Coal Operations of the Pagnotti Enterprises, Inc and Victor Raczka, Director of Engineering at Pagnotti Enterprises, Inc, for supporting the field testing. The authors thank Vibra-Tech Engineers, Inc. for performing seismic survey and providing partial financial support. Douglas Rudenko of Vibra-Tech Engineers, Inc provided technical support in the field testing and data analysis of the seismic surveys. The Pennsylvania State University provided partial financial support of this project. The authors also thank Drs. Behnoud Kermani and Jintai Wang, former PhD students at Penn State for their help in the seismic survey.

TABLE OF CONTENTS

| | |
|---|------------|
| ABSTRACT..... | III |
| ACKNOWLEDGEMENTS | IV |
| CHAPTER 1. INTRODUCTION | 1 |
| 1.1 Case Histories of Tailings Impoundment Failures..... | 1 |
| 1.2 Construction Methods of Coal Refuse Impoundments | 1 |
| 1.3 Literature Review..... | 3 |
| 1.3.1 Basic Properties of Fine Coal Tailings | 3 |
| 1.3.2 Cyclic Behavior and Liquefaction Resistance of Fine Coal Tailings | 4 |
| 1.3.3 Stability Analysis of Coal Refuse Impoundments | 4 |
| 1.4 Background on Seismic Survey and Seismic Monitoring..... | 5 |
| 1.5 Background on Numerical Modeling of Stability of Coal Slurry Impoundments | 6 |
| 1.6 Project Objectives | 6 |
| 1.7 Report Outline | 7 |
| CHAPTER 2. FIELD INVESTIGATION | 9 |
| 2.1 Site History..... | 9 |
| 2.2 Site Reconnaissance | 11 |
| 2.3 Field Investigation Approach (Sampling and Testing) | 13 |
| 2.4 Sample Retrieval and Sample Storage | 17 |
| 2.5 Field Testing Results..... | 18 |
| CHAPTER 3. LABORATORY TESTING..... | 20 |
| 3.1 Laboratory Testing Methodology..... | 20 |
| 3.2 Index Properties of The Samples | 22 |
| 3.3 Static Triaxial Test Results | 29 |
| 3.4 Resonant Column Test Results | 34 |
| 3.5 Liquefaction Susceptibility and Cyclic Behavior Characterization | 37 |
| CHAPTER 4. SEISMIC SURVEY AND SEISMIC MONITORING..... | 47 |
| 4.1 Methodology of Seismic Survey | 47 |
| 4.2 Methodology of Seismic Monitoring | 51 |
| 4.3 Results, Analyses, and Discussion | 54 |
| 4.3.1 Compressional Wave Velocity from Seismic Refraction Survey..... | 54 |
| 4.3.2 Shear Wave Velocity from Multichannel Analysis of Shear Waves (MASW)..... | 57 |

| | | |
|---|---|------------|
| 4.3.3 | Determination of Poisson’s Ratio, Young’s Modulus, and Small-strain Shear Modulus from Compressional and Shear Wave Velocities..... | 61 |
| 4.3.4 | Peak Particle Velocity and Vibration Attenuation Equation | 66 |
| 4.3.5 | Liquefaction Resistance of Coal Tailings | 68 |
| CHAPTER 5. | NUMERICAL MODEL | 72 |
| 5.1 | Geotechnical Properties and Model Generation..... | 72 |
| 5.2 | Cyclic DSS Tests..... | 73 |
| 5.3 | PM4Silt Plasticity Model Calibration | 74 |
| 5.4 | Dynamic Input Motions | 77 |
| 5.5 | Results and Discussion..... | 78 |
| 5.5.1 | Shear Bands and Strain Contours | 78 |
| 5.5.2 | Pore Pressure Ratio | 79 |
| 5.5.3 | Deformations..... | 96 |
| 5.6 | Conclusions | 100 |
| CHAPTER 6. | CONCLUSIONS AND RECOMMENDATIONS | 102 |
| 6.1 | Conclusions | 102 |
| 6.1.1 | Characterization of Static and Dynamic Geotechnical Properties and Behavior of Fine Coal Tailings | 102 |
| 6.1.2 | Seismic Investigation of Coal Tailings Using Multichannel Analysis of Surface Waves, Seismic Refraction, and Seismic Monitoring | 102 |
| 6.1.3 | Numerical Models..... | 104 |
| 6.2 | Recommendations | 104 |
| REFERENCES..... | | 106 |
| APPENDIX I: GEOPHYSICAL INVESTIGATION REPORT | | 112 |
| APPENDIX II: BLAST DATA FOR SITE 1 | | 217 |
| APPENDIX III: BLAST DATA FOR SITE 2..... | | 235 |

LIST OF FIGURES

| | |
|--|----|
| Figure 1-1. Schematic cross sections of coal refuse impoundment construction methods..... | 3 |
| Figure 2-1. Vicinity map of Jeddo impoundments | 9 |
| Figure 2-2. Plot plan of Jeddo impoundments | 10 |
| Figure 2-3. Topographic map of Site 1 | 10 |
| Figure 2-4. Topographic map of Site 2..... | 11 |
| Figure 2-5. Field sampling and testing sites, Ebervale, PA. Photo taken on 11/22/2016..... | 11 |
| Figure 2-6. Views of Site 1 | 12 |
| Figure 2-7. Photos of Coal slurry that was being discharged in to Site 1..... | 13 |
| Figure 2-8. Layout of field testing and sampling at Site 1. Note: B-1 and BS-3 are at the approximately same location, and the same for B-2 and BS-4..... | 14 |
| Figure 2-9. Layout of field testing and sampling at Site 2. Note: B-1, BS-1, and SPT-1 are at the approximately same location. “B” represents boring, and “BS” represents bulk sample..... | 14 |
| Figure 2-10. Field testing equipment. Photos taken on 06/29/2017. | 16 |
| Figure 2-11. Topography of Site 2..... | 16 |
| Figure 2-12. Field testing and sampling gadgets | 17 |
| Figure 2-13. The retrieved fine coal refuse samples with PVC liners. Photos taken on 06/29/2017. | 17 |
| Figure 2-14. Labeling of the relatively undisturbed fine coal refuse samples..... | 18 |
| Figure 2-15. Photos of the fine coal refuse samples retrieved from the SPT. Photos taken on 06/29/2017. | 19 |
| Figure 3-1. Laboratory testing conducted on the fine coal refuse samples | 21 |
| Figure 3-2. The particle size distributions of the FCR samples..... | 24 |
| Figure 3-3. Variation of the fine content of coal slurry with depths. The bar length represents the corresponding standard deviation at different depths. | 25 |
| Figure 3-4. Consolidation curves for the fine coal refuse samples at different sites and depths.. | 28 |
| Figure 3-5. A linear relationship between the coefficient of consolidation of the fine coal refuse samples and the percentage of fine content | 29 |
| Figure 3-6. Staged CU triaxial test results (S1B2-U) | 30 |
| Figure 3-7. Staged CU triaxial test results (S1B1-D) | 31 |
| Figure 3-8. Staged CD triaxial tests results (S2B1-U and S2B1-D)..... | 32 |
| Figure 3-9. Shear modulus and shear wave velocity of the FCR samples..... | 35 |
| Figure 3-10. Damping ratio of FCR samples and their initial index properties | 36 |
| Figure 3-11. Liquefaction susceptibility assessment criteria proposed by | 38 |

| | |
|---|----|
| Figure 3-12. Relationship of cyclic stress ratio (CSR) with number of cycles (N) to reach 5% DAS..... | 39 |
| Figure 3-13. Cyclic DSS test results at CSR~0.15 | 40 |
| Figure 3-14. Cyclic DSS test results at CSR~0.12 | 41 |
| Figure 3-15. Cyclic DSS test results at CSR~0.1 | 41 |
| Figure 3-16. Cyclic behavior of the FCR based on Idriss and Boulanger (2008) criterion | 43 |
| Figure 3-17. Post-liquefaction shear strength characteristics of FCR | 45 |
| Figure 4-1. Layouts of seismic lines and seismographs for seismic survey and monitoring..... | 48 |
| Figure 4-2. Seismic refraction and MASW testing..... | 49 |
| Figure 4-3. MASW testing on July 6, 2017 | 50 |
| Figure 4-4. Seismic refraction testing on July 31, 2017 | 50 |
| Figure 4-5. Deployment of seismographs and location tracking | 51 |
| Figure 4-6. Measurements of ground velocities induced by artificial blasting..... | 52 |
| Figure 4-7. Plan view of the blast hole locations..... | 53 |
| Figure 4-8. A blast hole for ground motion generation during the seismic monitoring on July 6, 2017..... | 53 |
| Figure 4-9. Photos showing the impacts of artificial blasting | 54 |
| Figure 4-10. Two-dimensional compressional wave velocity profiles determined in the two coal tailings impoundments | 55 |
| Figure 4-11. Shear wave velocity profiles determined for the coal tailings | 60 |
| Figure 4-12. The Poisson's ratio, Young's modulus, and small-strain shear modulus determined for the fine coal tailings along the depths | 65 |
| Figure 4-13. <i>PPV</i> prediction equation for fine coal tailings and its comparisons with other general attenuation equations by ISEE (2011)..... | 67 |
| Figure 4-14. Plots of (a) the calculated <i>CRR</i> and (b) the <i>FS</i> of the coal tailings upon blast loading, and the CSR is based on Equation (4-9) | 70 |
| Figure 4-15. <i>CRR</i> of the coal tailings over a wide range of percentages of <i>FC</i> | 71 |
| Figure 5-1 Upstream construction of tailings dam (model configuration) | 72 |
| Figure 5-2 Cyclic stress ratio versus number of cycles to 5% double amplitude strain | 75 |
| Figure 5-3 Shear stress-strain loops from cyclic DSS and PM4Silt | 76 |
| Figure 5-4 Pore pressure ratio from cyclic DSS and PM4Silt..... | 76 |
| Figure 5-5 Model input motions (a) Earthquake (b) Blast..... | 78 |
| Figure 5-6 Estimated shear strain due to earthquake for strong and weak dikes..... | 78 |
| Figure 5-7 Estimated shear strain due to blast for strong and weak dikes..... | 79 |

| | |
|--|-----|
| Figure 5-8 Pore pressure ratio generated by earthquake in the model with strong dikes | 81 |
| Figure 5-9 Pore pressure ratio generated by earthquake in the model with weak dikes..... | 83 |
| Figure 5-10 Pore pressure ratio generated by blast in the model with strong dikes | 85 |
| Figure 5-11 Pore pressure ratio generated by blast in the model with weak dikes..... | 87 |
| Figure 5-12 Pore pressure ratio generated by earthquake in the model with strong dikes | 90 |
| Figure 5-13 Pore pressure ratio generated by earthquake in the model with weak dikes..... | 92 |
| Figure 5-14 Pore pressure ratio generated by blast in the model with strong dikes | 94 |
| Figure 5-15 Pore pressure ratio generated by blast in the model with weak dikes..... | 96 |
| Figure 5-16 Deformations due to earthquake for both models with strong and weak dikes | 98 |
| Figure 5-17 Deformations due to blast for both models with strong and weak dikes | 100 |

LIST OF TABLES

| | |
|--|----|
| Table 2-1. Details of borings and SPT | 15 |
| Table 2-2. SPT blow counts and N-values..... | 18 |
| Table 3-1 Locations and labels of the samples | 20 |
| Table 3-2. Index properties and hydraulic conductivity of the FCR samples | 22 |
| Table 3-3. Consolidation test results..... | 26 |
| Table 3-4. Staged triaxial test results | 34 |
| Table 4-1. Details of blast holes | 53 |
| Table 4-2. Descriptions of the subsurface profile of the fine coal tailings impoundments | 56 |
| Table 4-3. Seismic site classification of fine coal tailings (International Code Council 2009).... | 61 |
| Table 5-1 Geotechnical properties of the impoundment sections..... | 72 |
| Table 5-2 PM4Silt input parameters | 74 |

CHAPTER 1. INTRODUCTION

Coal tailings are the waste product produced during the coal preparation process and are usually hydraulically deposited in coal tailings dams. Depending on the milling process and particles size distribution, coal refuse can be classified as either coarse coal refuse (CCR) or fine coal refuse (FCR) (Zamiran et al. 2015). Due to the low economic value of coal tailings, tailings dams are typically built with coarse coal tailings using the upstream staging method (D'Appolonia Engineering, Inc. 2009). The upstream staging method refers to the construction of an embankment on top of the settled fine coal tailings when the previously constructed layer has been fully filled with coal tailings. Coal tailings dam failures can be immensely destructive, especially when the tailings dams are constructed using the upstream staging method, because the stability of the dams is greatly affected by the mechanical strength of the settled coal tailings (D'Appolonia Engineering, Inc. 2009).

1.1 Case Histories of Tailings Impoundment Failures

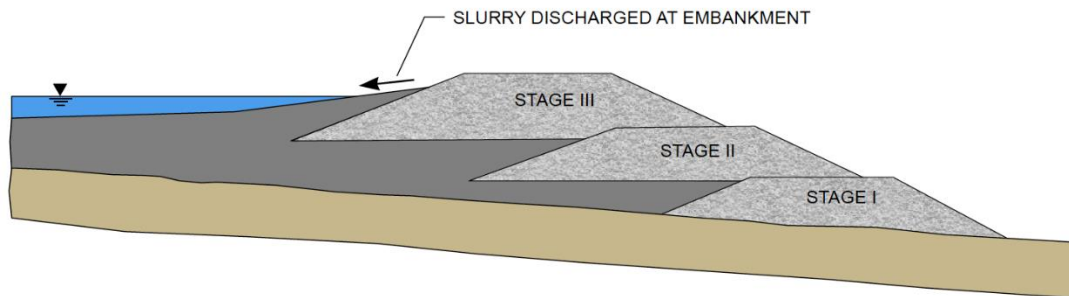
Based on the National Inventory of Dams report there are 1172 tailings dams in the U.S., and they are mostly classified as high hazard facilities (CEER 1985). The tailings dam failures in the recent history include the Buffalo Creek dam failure in 1972, the Big Branch impoundment failure in 2000, the Kingston Fossil Plant's slurry spill in 2008, and the Vale mining failure in Brazil in 2019. Case histories of the tailings dam failures (e.g., Blight and Fourie 2005; Rico et al. 2008; Azam and Li 2010; Puri and Kosteci 2013) and the failure modes of tailings dams (Michael et al. 2010; ICOLD 2001) have been reported. Two most known tailings impoundment failures due to liquefaction are the 1965 El Cobre Dam failure in Chile and the 1978 Mochikoshi impoundment failures in Japan (Dobry and Alvarez 1967; Ishihara 1984). The recent failure of the Kingston Tennessee Valley Authority coal ash impoundment in 2008 was also claimed to be partially due to the liquefaction of the coal ash slurry (Plant and Harriman 2008) that was caused by rapid static loading on the slurry.

FCR is commonly loose, saturated, and under- to normally consolidated in the field (Ishihara et al. 1981; Vick 1990). Therefore, FCR has low strength and stiffness, resulting in stability issues specifically under dynamic loading. Earthquake-induced cyclic loading can cause significant reduction in stiffness and strength of contractive soils such as FCR. Accordingly, one of the predominant causes of failure of FCR impoundments is earthquake, which can result in liquefaction (Martin and Davis 2000; Rico et al. 2008). Although FCR consists of appreciable amount of fines content, it is not considered as liquefaction resistant material. FCR has been found significantly contractive and liquefaction susceptible due to its loose and saturated structure. In addition, high water content and low hydraulic conductivity associated with FCR facilitate the liquefaction potential and generation of excess pore pressure under static and dynamic loading (Zeng et al. 2008).

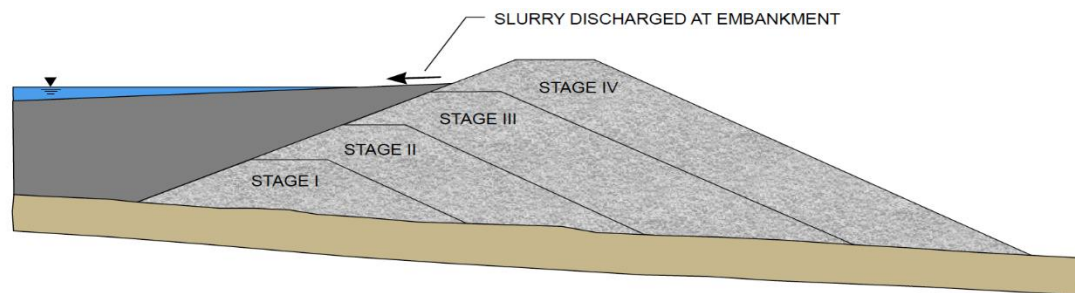
1.2 Construction Methods of Coal Refuse Impoundments

The configuration of coal refuse impoundments generally has four categories: (1) cross-

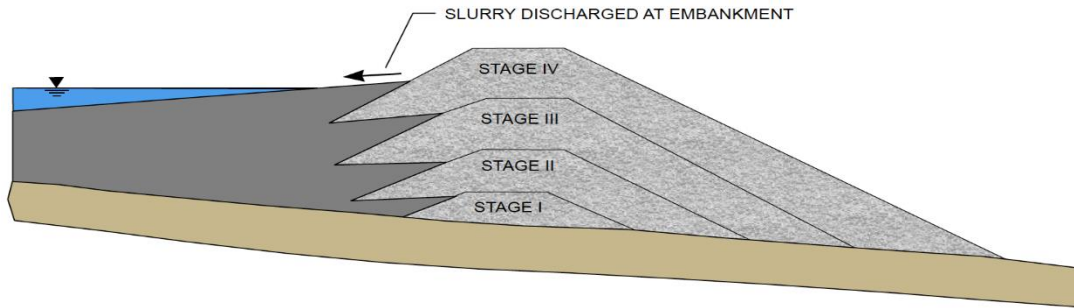
valley impounding embankment, (2) incised impoundment, (3) side-hill impounding embankment, and (4) diked impounding embankment. Planning and design of an impounding embankment generally involve distinct development and construction stages. The direction of construction normally falls into two categories: upstream and downstream. Upstream construction, as shown in Figure 1-1 (a), involves initial construction and placement of coarse refuse in downstream areas to form the impoundment with sequential placement during subsequent stages in upstream locations, typically at higher elevations. Downstream construction, as shown in Figure 1-1 (b), involves initial construction and placement of coarse refuse in upstream areas with placement during subsequent stages in downstream locations. It is common to have both upstream and downstream construction stages as part of a disposal facility design. An intermediate development condition is centerline construction (which is essentially the same as alternating upstream and downstream construction), where refuse stages are constructed both upstream and downstream of the previous stage, with the crest of the two stages generally in alignment but separated by the elevation increment of the stage (Figure 1-1 (c)). Upstream construction, and to a lesser degree centerline construction, with placement of coarse refuse embankments on settled fine coal refuse, introduce stability concerns due to the potentially low strength of the fine coal refuse during initial covering and the potential for seismically-induced strength degradation (D'Appolonia Engineering, Inc. 2009).



(a) Upstream staging method



(b) Downstream staging method



(c) Center staging method

Figure 1-1. Schematic cross sections of coal refuse impoundment construction methods (figures are from D'Appolonia Engineering, Inc. 2009)

1.3 Literature Review

1.3.1 Basic Properties of Fine Coal Tailings

The geotechnical and mineralogical properties of coal tailings are quite different from typical soils. Numerous studies were conducted on coal tailings to determine the index properties, shear strength, permeability, and consolidation properties (e.g., Busch et al. 1975; Leventhal and Ambrosis 1985; and Qiu and Segó 2001). Coal tailings are typically classified as silty sand (SM) and low plasticity silts (ML) with plasticity indices less than 12 (Almes and Butail 1976; McCutcheon 1983; Hegazy et al. 2004; Genes et al. 2000; Cowherd and Corda 1998; Huang et al. 1987; Busch et al. 1977; Zeng and Goble 2008, Zamiran et al. 2015). Based on the findings presented by the previous researchers, the coal tailings samples have moderate to high effective friction angles (23° - 36°) but generally low effective cohesions (0 kPa). However, a relatively high effective cohesion (11 kPa) was reported by Hegazy et al. (2004).

The high scatter in physical and geotechnical properties of FCR has been observed in the past studies (Qiu and Segó 2001; Hegazy et al. 2004). FCR may show varying characteristics depending on its sampling location, as the FCR near the discharge point consists of larger particles, while the FCR becomes finer at farther distance from the discharge point. Evaluating the strength and stiffness properties of FCR by in-situ testing or using undisturbed samples has been highly recommended, as these characteristics are substantially affected by void ratio, degree of saturation, and density (Castro 2003). Slurry deposition method has been developed and found to be a suitable approach to prepare samples resembling the fabric and structure of hydraulically deposited soils such as FCR when undisturbed samples are not available (Kuerbis and Vaid 1988).

The advancement in coal preparation processes to extract and yield higher percentages of clean coal from raw coal has resulted in finer coal tailings and a shift of delta formations towards the upstream side of the embankment, raising concerns relating to upstream construction and pushouts. The fines content can greatly affect the stability and liquefaction potential of the fine coal tailings. As a result, the possibility of having low-strength FCR due to the shifts in the FCR particle size distributions should be carefully evaluated.

1.3.2 Cyclic Behavior and Liquefaction Resistance of Fine Coal Tailings

Among physical and geotechnical properties of FCR, cyclic behavior and liquefaction resistance of FCR has not been sufficiently investigated. To date, liquefaction has been mostly studied for clean sands and low plasticity silts and clays. However, FCR is identified as a “transitional soil”, as it is composed of sand and silt with low plasticity and its behavior may behave between sand and silt. To evaluate the liquefaction potential, there are empirical and experimental approaches. In the empirical methods, the index properties such as Atterberg limits and moisture content are used to determine the liquefaction susceptibility of soil (Seed et al. 2003; Bray and Sancio 2006; and Idriss and Boulanger 2008). However, assessing the liquefaction potential solely based on index properties was questioned by Ajmera et al. (2015), as the composition and mineralogy of the material was found to be an influencing factor. Laboratory testing such as cyclic triaxial test and cyclic direct simple shear (DSS) test and in-situ testing such as standard penetration test (SPT) and cone penetration test (CPT) are common methods in evaluating the liquefaction resistance of soils.

Few studies have been conducted to characterize the FCR specifically under cyclic loading (e.g., Ishihara et al. 1981; Zeng et al. 1998a; Zeng et al. 1998b; Castro 2003; Zeng et al. 2008; James et al. 2011; Salehian 2013; Geremew and Yanful 2013). Although cyclic triaxial test has been adopted in several studies to assess the dynamic properties of FCR (Thacker et al. 1988; Ullrich et al. 1991), cyclic DSS test better simulates the mode of loading during earthquake. Post-liquefaction strength of FCR is also important. The FCR peak strength may deteriorate to a fraction of its previous peak strength or residual strength due to excessive strain experienced during earthquake (Castro 2003). The post-liquefaction strength of soil was observed to be strain dependent (Sivathayalan and Vaid 2004; Wijewickreme et al. 2005). Castro and Troncoso (1989) studied the residual strength and post-liquefaction strength of fine refuse by performing in-situ vane shear tests, indicating considerable drop in strength of fine refuse after liquefaction. Caution should be exercised when the post-liquefaction characteristics of material are evaluated by laboratory testing, as void redistribution and water film effect after liquefaction are not perfectly represented (Kokusho 2003).

1.3.3 Stability Analysis of Coal Refuse Impoundments

Ground shaking is one of the major causes of tailings dam failures. Among the 221 total case records collected by ICOLD (2001), 35 of them (about 16%) are due to strong ground motions. Among these 35 failure cases, about 71% of the dams are active whereas the remaining 29% are inactive (ICOLD 2001), inferring that active dams are more susceptible to failure than inactive dams. For coal tailings dams specifically, 15 of them have failed worldwide due to earthquake loading over the past 40 years (Kalinski and Phillips 2008). Recently, other than earthquake-induced liquefaction, blast-induced liquefaction has received substantial attention. Charlie et al. (2013) listed the cases of explosive-induced liquefaction that had been reported in the literature. Bench blasting, in which numerous explosives are detonated in one series, is the most common method used in the mining industry. In bench blasting, only 20% to 30% of the blast energy is used to fracture rock and the rest of the energy are lost in the forms of flying debris and seismic waves, resulting in ground vibration that could possibly affect the stability of the nearby infrastructures

(Soltys et al. 2017). Coal tailings impoundments, which are built to store the mine debris, are usually constructed in the proximity of the open-pit mines so that the debris can be transported to the impoundments in a rather short distance and time. Hence, safety concern has been raised regarding the liquefaction susceptibility of the loosely deposited coal tailings when subjected to ground vibrations induced by bench blasting.

1.4 Background on Seismic Survey and Seismic Monitoring

In most of the studies, the geotechnical properties of coal tailings were determined from laboratory testing using remolded samples or relatively undisturbed samples. Due to the non-plastic to low plastic behaviors, coal tailings samples can be disturbed during sample handling and transportation in the field. The in situ ground freezing technique, a type of sophisticated sampling method that uses liquid nitrogen to freeze the loose, non-cohesive soils so that the soil samples can retain their in situ structural integrity, is recommended to obtain high quality undisturbed samples. However, this technique is both complicated to conduct and expensive, approximately $\$0.32/\text{cm}^3$ (Hofmann et al. 2000). There is a need to conduct the field testing using non-destructive geophysical techniques to realistically determine the in situ geotechnical properties of coal tailings.

Coal tailings impoundments typical extend in great distances. It can easily reach up to $1.6 \times 10^5 \text{ m}^2$ in the impoundment surface area (D'Appolonia Engineering, Inc. 2009). A seismic survey, which is a non-invasive geophysical test, can be conducted in the tailings impoundments as the seismic lines can be easily spread out over a wide area to provide quick interpretations of the soil profiles (Andrus and Stokoe 2000). The impoundments, especially those with the slurry-like tailings, usually cannot be easily accessed by large drill rigs or cone penetration testing (CPT) trucks to determine the blow counts or cone resistances, respectively. The seismic survey equipment is relatively light and handy to be carried by research personnel into the impoundments, therefore it is suitable for the investigation at tailings impoundments.

The seismic refraction and multichannel analysis of surface waves (MASW) methods (Park et al. 1999) are two types of seismic surveys that can be used to determine compressional wave velocity and shear wave velocity, respectively. The shear wave velocity is a basic mechanical property that can be used to evaluate the liquefaction resistance of the coal tailings (Andrus and Stokoe 2000), whereas compressional wave velocity is used as an indicator of the stiffness of the soils (Kramer 1996). Due to the nondestructive nature of the seismic surveys, the geotechnical properties of in situ coal tailings can be obtained and used for validating properties determined from the laboratory testing (Lin et al. 2004) and future stability assessment of coal tailings dams.

The liquefaction potential of coal tailings can also be evaluated using peak particle velocity. The peak particle velocity (*PPV*) is often used to determine the blast loading imposed on infrastructures and to evaluate the excess pore water pressure ratio (Al-Qasimi 2005; Charlie et al. 2001, 2013). Due to the complexities of the wave characteristics, site factors, and blasting parameters, the prediction equation for peak particle velocity has been developed as a function of the amount of charge per delay (*W*) and the distance (*D*) between the blast location and the infrastructure under investigation using empirical relationships (Kumar et al. 2013). *W* and *D* are usually combined as one parameter known as the scaled distance (*SD*) for easier interpretation. *SD*

is typically calculated as D divided by the square-root or cube-root of W for cylindrical charges and spherical charges, respectively (Kumar et al. 2013).

1.5 Background on Numerical Modeling of Stability of Coal Slurry Impoundments

Various constitutive plasticity models have been developed to assess liquefaction resistance and cyclic behavior of sand and low plasticity silt and clay. For example, UBCSAND, a non-linear effective stress plasticity model, was proposed by Beaty and Byrne (1998) to determine mechanical response of sand under cyclic loading. UBCSAND has been successfully used to simulate dynamic behavior of sand and low plasticity tailings in engineering practices (Seid-karbasi and Byrne 2004; Castillo et al. 2005; James 2009; Ferdosi et al. 2015).

UBCSAND is a non-linear effective stress plasticity model, which was proposed by Beaty and Byrne (1998) to determine mechanical response of sand under cyclic loading. UBCSAND is able to conduct fully coupled analysis including flow calculations. UBCSAND has been successfully used to simulate dynamic behavior of sands and low plasticity tailings in engineering and laboratory practices. Seid-karbasi and Byrne (2004) studied the failure of Mochikochi tailings dams in Japan by UBCSAND model. The results were in well agreement with the observed deformations after the dam's failure. Castillo et al. (2006) investigated the seismic response of a heap leach pad with high phreatic line using UBCSAND model in a fully coupled analysis. Effect of drainage system to reduce the liquefaction and failure potential was also discussed. UBCSAND model was adopted by James (2009) and Ferdosi et al. (2015) to evaluate the reinforcing effect of waste rock inclusion on stability of liquefiable mine tailings impoundments.

PM4Sand and PM4Silt are plasticity models developed by Boulanger and Ziotopoulou (2013, 2018). PM4Sand assesses the undrained cyclic and monotonic mechanical response of sand and non-plasticity silt, while PM4Silt assesses those of non-plasticity to low plasticity silt and clay. Both PM4Sand and PM4Silt plasticity models are based on the framework of the stress-ratio controlled, critical state compatible, bounding-surface plasticity model for sand developed by Dafalias and Manzari (2004). PM4Sand and PM4Silt models have less required input parameters compared to UBCSAND. PM4Sand has been successfully implemented in analysis of different geotechnical applications such as dams, embankments, and foundations (Ziotopoulou and Boulanger 2016; Ziotopoulou and Montgomery 2017). The last version of PM4Sand (Version 3.1) was released in 2017, while the previous limitations were resolved (Boulanger and Ziotopoulou 2017). The PM4Silt (Version 1) was also released in 2018 by Boulanger and Ziotopoulou (2018).

1.6 Project Objectives

The overall objective of this research project is to evaluate the stability of coal tailings impoundments under field impacts using the static and dynamic properties of representative coal tailings samples and in situ coal tailings. Three specific objectives, which are derived from the overall objective, are presented as follows.

Task 1 is to comprehensively characterize the physical and hydraulic properties of FCR using relatively undisturbed and representative samples. Geomechanical behaviors of the undisturbed samples, including shear strength and stiffness properties, were determined. The cyclic behavior and liquefaction resistance of the slurry-deposited FCR samples, which sufficiently resembled the fabric and structure of in-situ FCR, were assessed by cyclic DSS tests. The cyclic behavior of the FCR was further evaluated by empirical approaches and in-situ data. The effect of liquefaction on static shear strength of the FCR samples was also determined by conducting monotonic shear loading at the end of the cyclic DSS tests.

Task 2 is to determine the basic mechanical properties of in situ coal tailings, such as the shear wave velocity, compressional wave velocity, Poisson's ratio, Young's modulus, and small-strain shear modulus, using in situ seismic survey and seismic monitoring; these field tests contribute to the scarce database of in situ coal slurry characteristics. The properties derived from this study are compared with those derived from the standard penetration test (SPT) to show the effectiveness of the seismic investigations in reviewing the in situ properties of coal tailings. A prediction equation for peak particle velocity is also developed specifically for coal tailings. The peak particle velocity obtained in this study is used to evaluate the cyclic stress ratio due to mine blasting. The liquefaction resistance of coal tailings is then evaluated using the simplified procedure presented by Andrus and Stokoe (2000).

Task 3 is to first adopt the geotechnical properties and cyclic resistance of coal slurry. Then, PM4Silt model is calibrated for coal slurry using laboratory results. The seismic stability of coal slurry impoundment constructed by upstream method is investigated using earthquake and blasting input motions. The deformations and excess pore pressure developed during dynamic loading are analyzed. This task aims to compare the numerical results obtained by PM4Silt plasticity model for two loading scenarios (i.e. an earthquake, and a blasting event), while two different set of properties are assumed for the slope (i.e. slope with loose and strong shear properties). The applicability and limitations of PM4Silt plasticity model to assess cyclic behavior of fine coal refuse, along with the seismic performance of an upstream impoundment are evaluated and discussed.

1.7 Report Outline

This report consists of six chapters. Chapter 1, where this report outline is located, elaborates on the case histories of tailings impoundment failures, construction methods of tailings impoundments, the literature review of the static and dynamic geotechnical properties of fine coal tailings, and the research motivation and objectives of this study.

Chapter 2 presents the field investigation of coal tailings. The logistics of field sampling and testing are included in detail.

Chapter 3 presents the laboratory testing that was conducted to characterize the physical and hydraulic properties of coal tailings. The geomechanical behavior of the undisturbed samples, including shear strength and stiffness properties, were determined. The cyclic behavior, liquefaction resistance, and the effect of liquefaction on static shear strength of the fine coal tailings samples were also assessed.

Chapter 4 presents the in situ seismic survey and seismic monitoring that were used to determine the basic mechanical properties of in situ coal tailings. A prediction equation for peak particle velocity was developed specifically for coal tailings. The liquefaction resistance of coal tailings was also evaluated using the simplified procedure based on the field data from seismic survey.

Chapter 5 presents the numerical models of the coal tailings impoundments subjected to earthquake and blast motions. The pore pressure ratio and shear strain contours are presented. The seismic stability and deformations of the impoundment are also evaluated.

Chapter 6 summarizes the significant findings and conclusions of this study. Recommendations for future work are also provided.

CHAPTER 2. FIELD INVESTIGATION

2.1 Site History

The field investigations were conducted on two coal refuse impoundments (Site 1: Jeddo #14 and Site 2: Jeddo #8), which are operated by Pagnotti Enterprises, Inc. The Jeddo Basin was acquired by the Jeddo Coal Company in 1964 and the coal refuse has been deposited in the region since then (jeddocoal.com). Site 1 is an active and relatively new coal refuse impoundment, whereas Site 2 is an inactive impoundment that is older than Site 1. The difference in their periods of placement provided an opportunity to study the changes in the geotechnical properties and flow behaviors of coal refuse over time.

The two impoundments are located in Ebervale, Pennsylvania. The GPS coordinates of Site 1 and Site 2 are (40.983501, -75.945369) and (40.981951, -75.939492), respectively. Figure 2-1 shows the vicinity map of the two impoundments. The two impoundments on a closer view are shown in Figure 2-2. Figure 2-3 and Figure 2-4 are the topographic maps of Site 1 and Site 2, respectively.

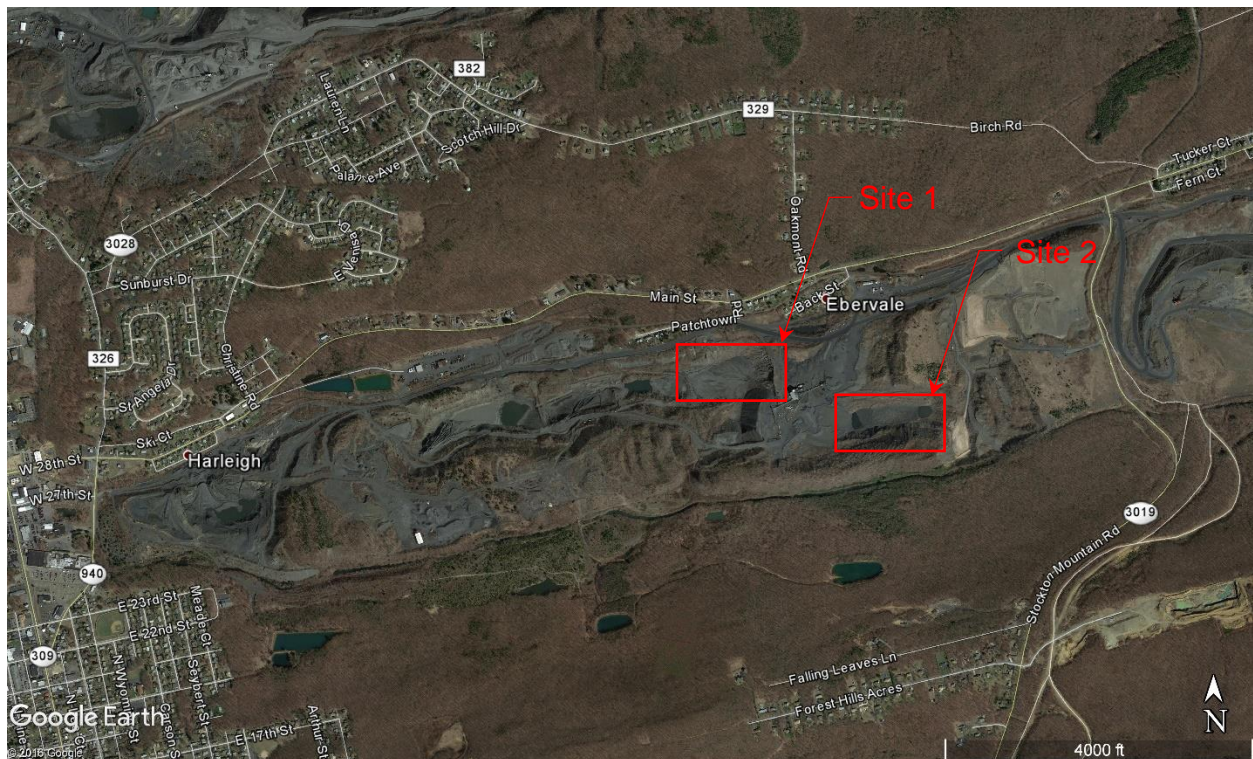


Figure 2-1. Vicinity map of Jeddo impoundments



Figure 2-2. Plot plan of Jeddo impoundments

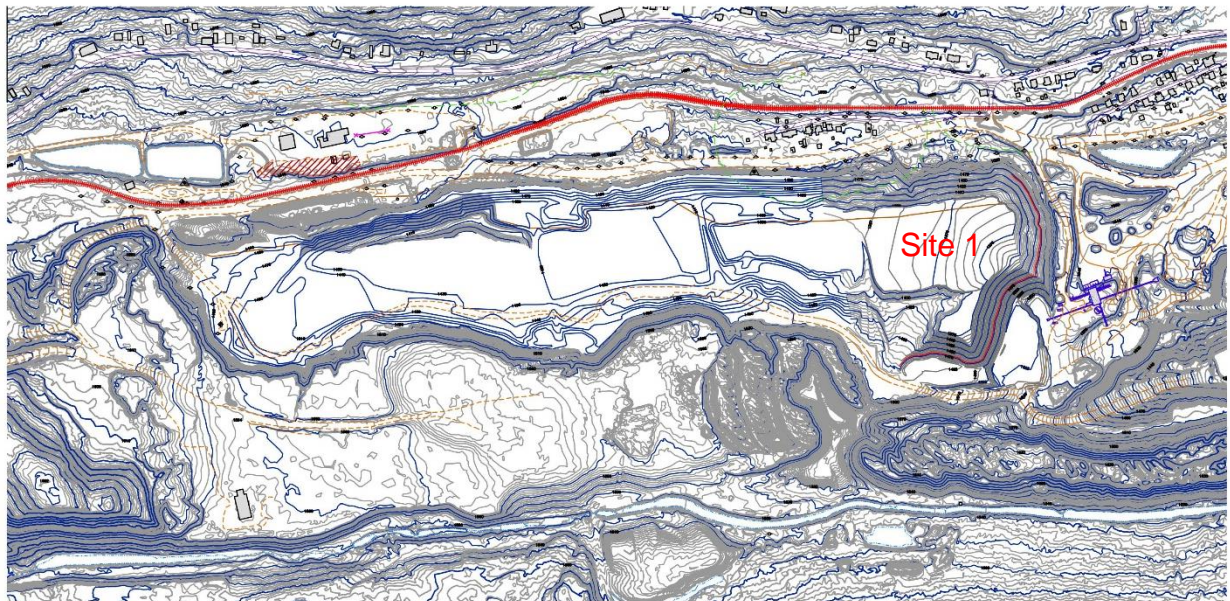


Figure 2-3. Topographic map of Site 1

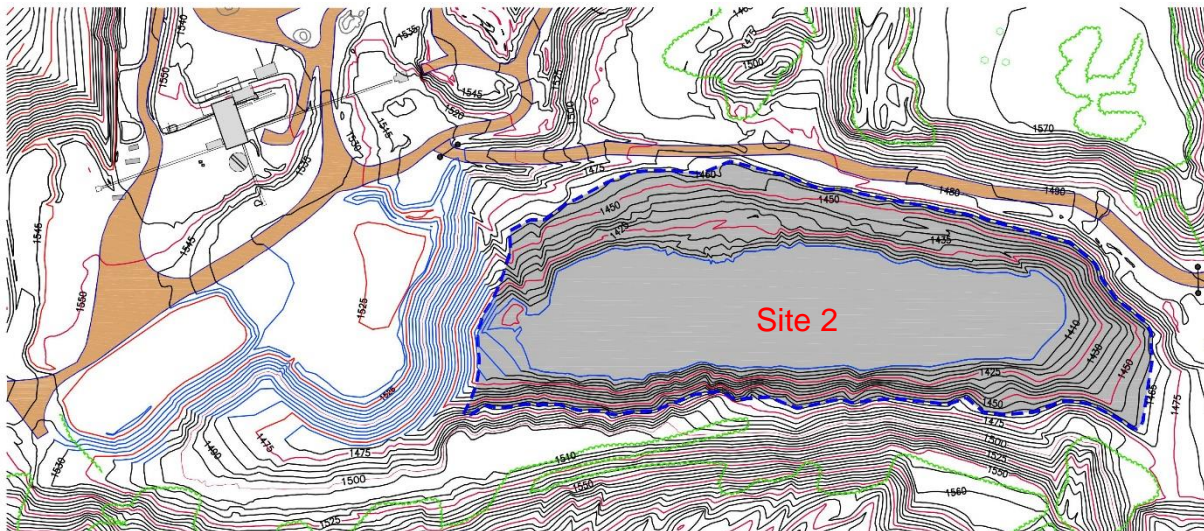


Figure 2-4. Topographic map of Site 2

2.2 Site Reconnaissance

Site reconnaissance had been performed six months before the testing program of this study on November 22, 2016. Figure 2-5 shows the photos of the two testing sites during the winter season where the fine coal refuse was frozen. Due to the difficulty in drilling the frozen coal refuse, the field investigations had been planned accordingly to occur in the summer months when the ground fully thawed and the surface water drained away. Figure 2-6 shows the views of Site 1.



(a) Site 1: Jeddo #14



(b) Site 2: Jeddo #8

Figure 2-5. Field sampling and testing sites, Ebervale, PA. Photo taken on 11/22/2016



(a) The coal refuse became wet after the raining season, July 2017



(b) A pond of standing water in Site 1 after a rainfall, July 2017

Figure 2-6. Views of Site 1

Figure 2-7 shows multiple views of the slurry discharge into the active impoundment (Site 1). Due to the length of the impoundment as shown in Figure 2-7 (a), the coal refuse that was slightly coarser and heavier (i.e. usually in the grain size of sandy soils) was more likely to settle near the point of slurry discharge and would stay relatively stable in its original location throughout the entire deposition period. Figure 2-7 (b) shows the size of the trench as being compared to the human height. A deep trench was also formed by the flowing coal slurry at the upstream side as depicted in Figure 2-7 (c). The trench became shallower as it is farther away from the discharge point.



(a) A panoramic view of the slurry discharge (the discharge direction is from right to left)



(b) A photo showing the size of the trench being compared to the human height



(c) A deep trench created by the flowing coal slurry

Figure 2-7. Photos of Coal slurry that was being discharged in to Site 1

2.3 Field Investigation Approach (Sampling and Testing)

The field sampling and testing were planned by considering the geological cross sections of the two impoundments and the associated hazard potential to be investigated. The borehole layout and depth were designed following the guidelines in the Soil Mechanics Design Manual by the Naval Facilities Engineering Command (NAVFAC 1986). The design optimized the subsurface information that are required for stability analysis and the cost of geotechnical investigation. The field sampling and testing were performed by Hawk Mountain Lab Inc. on June 29, 2017. The locations of boreholes and SPT are shown in Figures 2-8 and 2-9. Table 2-1 presents the details of the borings and SPT.

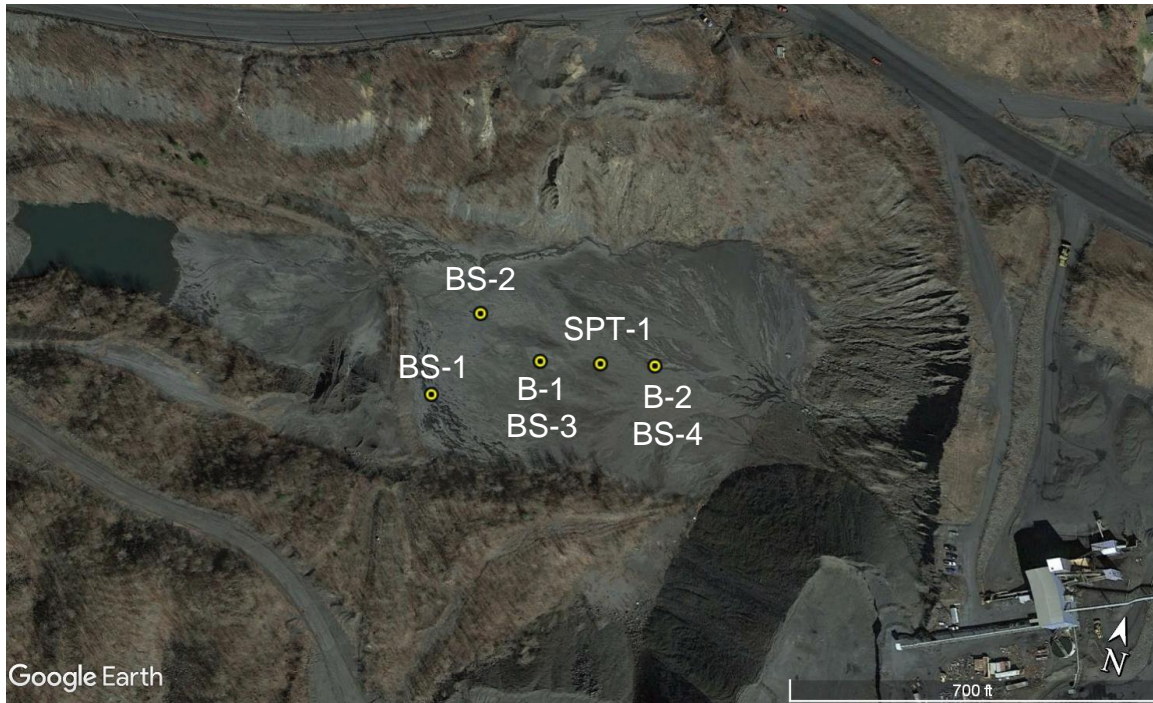


Figure 2-8. Layout of field testing and sampling at Site 1. Note: B-1 and BS-3 are at the approximately same location, and the same for B-2 and BS-4.



Figure 2-9. Layout of field testing and sampling at Site 2. Note: B-1, BS-1, and SPT-1 are at the approximately same location. “B” represents boring, and “BS” represents bulk sample.

Table 2-1. Details of borings and SPT

| Site | Name | Symbol | Depth, z m (ft) | Elevation m (ft) | GPS Coordinates |
|------|-------|--------------------------------|--------------------|---------------------|---------------------------------|
| 1 | B-1 | Boring 1 | 0.0-12.2 (0-40) | 411 (1347) | 40°58'59.41"N, 75°56'48.05"W |
| | B-2 | Boring 2 | 0.0-12.2 (0-40) | 411 (1347) | 40°58'60.00"N, 75°56'45.00"W |
| | BS-1 | Bulk sample 1 | 0.3 (1) | 411 (1347) | 40°58'58.10"N, 75°56'50.66"W |
| | BS-2 | Bulk sample 2 | 0.3 (1) | 411 (1347) | 40°58'60.00"N, 75°56'50.00"W |
| | BS-3 | Bulk sample 3 | 0.3 (1) | 411 (1347) | 40°58'59.41"N, 75°56'48.05"W |
| | BS-4 | Bulk sample 4 | 0.3 (1) | 411 (1347) | 40°58'60.00"N, 75°56'45.00"W |
| | SPT-1 | Standard Penetration Test 1 | 7.6, 12.2 (25, 40) | 411 (1347) | 40°58'59.72"N, 75°56'46.45"W |
| 2 | B-1 | Boring 1 | 0.0-9.1 (0-30) | 422 (1384) | 40°58'55.34"N, 75°56'17.93"W |
| | BS-1 | Bulk sample 1 | 0.3 (1) | 422 (1384) | 40°58'55.34"N, 75°56'17.93"W |
| | BS-2 | Bulk sample 2 | 0.3 (1) | 423 (1389) | 40°58'55.60"N, 75°56'13.63"W |
| | SPT-1 | Standard Penetration Test 1 | 4.6, 7.6 (15, 25) | 422 (1384) | 40°58'55.37"N, 75°56'17.91"W |

Three boreholes were drilled and two Standard Penetration Tests (SPT) were conducted. A Geoprobe model 6620DT track rig with DPT (direct push technology), outfitted with DT 3.25 tooling strings, were utilized to conduct drilling and sampling at locations as shown in Figure 2-10. The drill rig uses percussion technique at percussion rate of 32 Hz to continuously push a split-spoon sampler (model: DT3.25) into the subsoil. This type of light and all-terrain track-mounted rig was chosen and used for the field drilling, sampling, and testing as the two sites are hardly accessible by a typical large truck-mounted drill rig. Although the terrain is relatively flat in the impoundment as shown in Figure 2-11 (a), the road access to the impoundment is steep and narrow as presented in Figure 2-11 (b). Figure 2-11 (b) shows that the Geoprobe model 6620DT track rig was slowly driven up the steep slope.



(a) Geoprobe model 6620DT track rig



(b) DH-100 Automatic Drop Hammer

Figure 2-10. Field testing equipment. Photos taken on 06/29/2017.



(a) A flat terrain was observed in the impoundment



(b) The track rig was moving up a steep slope

Figure 2-11. Topography of Site 2

Probe rods as shown in Figure 2-12 (a) were used to retrieve the fine coal refuse samples. A PVC liner was fitted inside the probe rod during drilling. The sampling provided continuous coal slurry samples along the entire drilling depth. After the retraction of the probe rod, the coal refuse samples were retrieved and cut as shown in Figure 2-12 (b). The coal refuse samples encased with PVC liners were then delivered to the laboratory in the Pennsylvania State University for further sectioning and analysis. The PVC liners were meant to ensure an effective shipment and to reduce sample disturbance. Figure 2-10 (b) shows the SPT that was conducted using the same track-mounted rig with a DH-100 Automatic Drop Hammer. Bulk samples were also collected at

the first foot of coal fine refuse at three of the borehole locations and other randomly selected locations.



(a) Probe rods



(b) sample retrieval and cutting

Figure 2-12. Field testing and sampling gadgets

2.4 Sample Retrieval and Sample Storage

Six bags of bulk samples were collected and sealed properly to prevent moisture loss; each bag weighed approximately 1 kg (2 lbs). Figure 2-13 shows the retrieved fine coal refuse samples. The diameter of each slurry sample that was retrieved from the borings was 47 mm (1.85 inches) and the length was 1.5 m (5 feet). The sample disturbance, which depends on sampler dimensions, sampler driving mechanism, and soil types and consistency, was not assessed. The slurry samples were kept in PVC liners and both ends were capped. The coal refuse samples were also labelled accordingly as shown in Figure 2-14. For each laboratory test, the 15.2 cm (6-inch) long specimen was cut and prepared immediately before use to ensure minimal sample disturbance and moisture loss.



Figure 2-13. The retrieved fine coal refuse samples with PVC liners. Photos taken on 06/29/2017.



Figure 2-14. Labeling of the relatively undisturbed fine coal refuse samples

2.5 Field Testing Results

The N-values for the standard penetration tests were listed in Table 2-2. For the depth above 7.6 m (25 feet), both impoundments have N-value readings of 2 to 3. At the depth of 12.2 m (40 feet) at Site 1, the N-value is 7. Figure 2-15 presents the loose fine coal refuse recovered from the SPT.

Table 2-2. SPT blow counts and N-values

| Site | Depth, m (ft) | SPT Blow Count | <i>N</i> -value | <i>N</i> ₆₀ | (<i>N</i> ₁) ₆₀ |
|------|---------------|----------------|-----------------|------------------------|---|
| 1 | 7.6 (25) | 1 / 1.5 / 1.5 | 3 | 1.86 | 4.0 |
| | 12.2 (40) | 2 / 3 / 4 | 7 | 2.08 | 3.4 |
| 2 | 4.6 (15) | 1 / 1 / 1 | 2 | 3.12 | 4.8 |
| | 7.6 (25) | 0 / 1 / 1 | 2 | 7.66 | 9.0 |

Note: *N* value is the sum of blow counts for the last 30 cm of penetration; *N*₆₀ is *N* value corrected for field procedures; and (*N*₁)₆₀ is *N* value corrected for field procedures and overburden stress.



(a) The slurry-like fine coal refuse flowing out of the SPT split tube sampler



(b) The cross-section of a coal refuse sample

Figure 2-15. Photos of the fine coal refuse samples retrieved from the SPT. Photos taken on 06/29/2017.

CHAPTER 3. LABORATORY TESTING

3.1 Laboratory Testing Methodology

The laboratory testing was planned based on the amount of retrieved samples. Each 1.5-meter long sample was divided into 10 units or specimens. Any samples with lengths lesser than 1.5-meter were divided into the maximum possible units each of 15-centimeter long. Half of the retrieved samples were shared with Jeddo Coal Company. Table 3-1 shows the depths at which the specimens were retrieved for laboratory testing. A unique label shown on the last column of Table 3-1 was assigned to each sample for simplicity. The laboratory tests were conducted as per ASTM standards. Figure 3-1 (a-e) shows the laboratory tests conducted using the fine coal refuse.

Table 3-1 Locations and labels of the samples

| Impoundment | Borehole | Depth (m) | Label |
|-------------|----------|-----------|--------|
| S1 | B1 | 0-1.5 | S1B1-S |
| S1 | B1 | 4.5-6 | S1B1-U |
| S1 | B1 | 10.5-12 | S1B1-D |
| S1 | B2 | 0-1.5 | S1B2-S |
| S1 | B2 | 4.5-6 | S1B2-U |
| S1 | B2 | 10.5-12 | S1B2-D |
| S2 | B1 | 0-1.5 | S2B1-S |
| S2 | B1 | 4.5-6 | S2B1-U |
| S2 | B1 | 7.5-9 | S2B1-D |



(a) Atterberg limits test



(b) Specific gravity test



(c) Triaxial test



(d) Consolidation test



(e) Resonant column test



(f) Fine coal refuse specimen

Figure 3-1. Laboratory testing conducted on the fine coal refuse samples

Representative samples were collected and used for static triaxial test, resonant column test, density measurement, and consolidation test. The static triaxial and resonant column tests were conducted at several confining pressures. The hydraulic conductivity of all the specimens were also measured using flexible-wall permeameter method. The hydraulic conductivity of the samples was measured under 34.5 kPa consolidation stress. Although the 34.5 kPa confining pressure may not accurately represent the consolidation stress of the samples in the field, the resulting hydraulic conductivities are relevant references, which can help compare samples in terms of hydraulic conductivity at the same consolidation stress. The diameter of all the samples used for static triaxial and resonant column tests was 35.5 mm. The retrieved samples were extruded and trimmed axially and longitudinally by a sharp thin-bladed ring and trimming knife, respectively, with great caution to avoid disturbing the samples. The requirement of height to diameter ratio of 2:1 was met for all the samples. The index properties such as grain size distribution and Atterberg limits were determined using the samples after they were used for static triaxial tests. The index properties were verified by duplicate tests. The specific gravity was determined by two approaches: 1) ASTM D854 “Standard Test Method for Specific Gravity of Soil Solids by Pycnometer”, 2) Micromeritics Accupyc II 1340 Gas Displacement Pycnometry System with a chamber volume of 1.0 cm³ at room temperature (about 23.5°C). In the second approach, after filling up the chamber with coal tailings sample, helium gas was released and allowed to displace the sample pores; the absolute density of the specimen was then calculated using the volume that was not displaced by helium; ten measurements were made and the average absolute density was computed. The average values of the specific gravity are reported in this paper, as the measurements varied marginally.

The extruded representative samples could not be used for cyclic DSS tests because the diameter of representative samples was smaller than the diameter of the cyclic DSS mold. Of the sample preparation methods, wet pluviation and slurry deposition methods were effective in mimicking the fabric of the in-situ hydraulically deposited materials such as FCR (Carraro and Prezzi 2007). However, as wet pluviation method is not reliable for silty sands, due to the possibility of particle segregation, slurry deposition method developed by Kuerbis and Vaid (1988)

was adopted to prepare the sample. A series of cyclic DSS tests were conducted on reconstituted S1B2-D samples, with void ratio in the range of 0.6~0.7, until repeatable and consistent results in terms of cyclic resistant ratio were observed. The target void ratio of 0.6-0.7 was chosen as a matter of consistency since it could be repeatedly achieved during sample preparation, even though the target void ratio was slightly lower than the average void ratio of the representative samples (~0.9) obtained in the field. The liquefaction resistance of FCR was obtained at different cyclic stress ratio (CSR). The cyclic DSS device is made by GeoComp and applies cyclic shear loading under the constant volume condition. Therefore, the pore-water pressure is back-calculated from the change in vertical total stress. The soil samples are confined by Teflon rings lined with latex membrane to ensure uniform shearing of the sample. The horizontal stress is unknown throughout testing. The post-liquefaction strength characteristics of FCR were also studied by statically shearing the liquefied samples. The failure plane is typically formed closed to the slope, where there is not enough shear strength against the induced shear stresses. The coal refuse has shown significantly lower shear strength compared to the material used in the dike construction. Therefore, the geomechanical behavior of the fine coal refuse in that region is of great importance. Accordingly, the S1B2-D sample was chosen for the cyclic DSS and post-liquefaction tests is that the corresponding location is close to the potential failure plane, therefore, the geomechanical properties of this sample was more of interest than other locations. The dimensions of the sample in cyclic DSS tests were 63.5 mm in diameter and 12.7 mm in height. The consolidation pressure was 60 kPa, the frequency of cyclic loading was 0.1 Hz, and the liquefaction criterion was set as 5% double amplitude shear strain (DAS). The cyclic loading was stress-controlled, while the static loading was strain-controlled with shear strain rate of 1.4% per hour.

3.2 Index Properties of The Samples

The groundwater depth in field was measured by lowering a measuring tape into the borehole. The depths of groundwater table that were measured at the time of the field sampling was 1.1 m at Site 1 and 4.9 m at Site 2. The fine coal refuse samples that were retrieved from drilling and tested in this study were all below groundwater table. Table 3-2 presents the basic index properties, hydraulic conductivity, and classification of the samples that were used for the static triaxial tests. The moisture content of the samples retrieved from the greater depth (i.e. 10.5 m from impoundment S1 and 7.5 m from impoundment S2) were higher as expected due to the less exposure to evaporation and desiccation. The saturation degree of all the samples except S1B1-D and S2B1-U are noticeably high and above 80%, which can be attributed to the deposition method (i.e. slurry) of FCR in field. The Atterberg limits tests were conducted several times until repetitive and consistent results for each sample were achieved. The reported moisture contents are the average values with standard deviation of 3%.

Table 3-2. Index properties and hydraulic conductivity of the FCR samples

| Sample | Moisture Content (%) | Density (KN/m ³) | e_{mi} | Saturation Degree (%) | LL (%) | PL (%) | PI | G_s | k (cm/s) | USCS Classification |
|--------|----------------------|------------------------------|----------|-----------------------|--------|--------|----|-------|------------|---------------------|
| S1B1-S | 35 | - | - | - | 27 | 21 | 6 | 2.1 | - | CL-ML |
| S1B1-U | 35 | 15.6 | 0.8 | 92 | 33 | 29 | 4 | 2.1 | 3.3e-6 | SM |
| S1B1-D | 49 | 12.9 | 1.4 | 73 | 34 | 30 | 4 | 2.1 | 5.1e-7 | ML |
| S1B2-S | 15 | - | - | - | - | - | 0 | 2.3 | - | SM |

| | | | | | | | | | | |
|--------|----|------|-----|-----|----|----|---|-----|--------|-------|
| S1B2-U | 35 | 14.6 | 0.9 | 82 | 31 | 27 | 4 | 2.1 | 8.8e-7 | ML |
| S1B2-D | 36 | 16.1 | 0.8 | 94 | 27 | 25 | 2 | 2.1 | 1.3e-4 | SM |
| S2B1-S | 10 | - | - | - | - | - | 0 | 2.3 | - | SW-SM |
| S2B1-U | 25 | 15.4 | 0.7 | 75 | 20 | 19 | 1 | 2.2 | 3.6e-7 | SM |
| S2B1-D | 48 | 15.6 | 1.0 | 100 | 35 | 33 | 2 | 2.2 | 1.0e-6 | ML |

Unit weight of the samples was determined using the representative samples before they were mounted on triaxial base plate. The highest variation in unit weight was observed in Borehole 1 in S1 impoundment. The unit weight of S1B1-U and S1B1-D were 15.6 kN/m^3 and 12.9 kN/m^3 , respectively. The unit weight of the samples taken from Borehole 2 in S1 impoundment was 14.6 kN/m^3 and 16.1 kN/m^3 for S1B2-U and S1B2-D, respectively. The sample S1B2-D showed the highest unit weight among the studied samples. The location of S1B2-D is close to the discharge point where the coal slurry is hydraulically deposited. Typically, the larger and heavier grains settle first near the discharge point while the slurry with fines remains on top. The least variation in unit weight was in the samples collected from the S2 impoundment, which was geographically located in the middle of the impoundment. The unit weights of 15.4 kN/m^3 and 15.6 kN/m^3 were measured for S2B1-U and S2B1-D, respectively. Initial void ratio of the FCR samples ranged from 0.7 to 1.4 with an average of 0.9. All the samples can be considered as non-plastic to low plasticity, as the plasticity indices were less than 7. During the Atterberg limits tests for S1B2-S and S2B1-S using a liquid limit device, the fine coal refuse samples slid on the surface of the cup for several trials at successively higher water contents. The numbers of drops required to close the groove were always less than 25. As a result, it was considered that the LL for the samples could not be determined and the samples were reported as non-plastic (i.e. $PI = 0$) without the need to perform the plastic limit tests, according to ASTM D4318-17. The LL and PL values for S1B2-S and S2B1-S were therefore not available and not included in Table 3-2. Excluding S1B2-S and S2B1-S, the moisture content of all the other samples was higher than their liquid limit, which is representative of soils greatly prone to liquefaction (Byrne and Seid-Karbasi 2003). Specific gravity (G_s) shown in Table 2 is the average values, with standard deviation of 0.03. The specific gravity of the FCR samples was lower than typical values reported for fine-grained soils due to high carbon content (Hegazy et al. 2004). The values for specific gravity obtained in this study were in agreement with other studies (e.g., Huang et al. 1987; Ullrich et al. 1991; Cowherd and Corda 1998).

Particle size distribution of the samples used for triaxial tests was determined by conducting sieve analysis and hydrometer analysis, as per ASTM C136 and ASTM D422, respectively. The classification of each sample was determined based on the Unified Soil Classification System (USCS), and the particle size distributions of the samples are presented in Figure 3-2. As shown in Table 3-2, the FCR samples were all classified as either silty sand (SM), low-plasticity silt (ML), clayey silt (CL-ML), or well-graded sand with silt (SW-SM). Silt and sand content of the FCR samples ranged from 12% to 65% and 35% to 88%, respectively. The wide range associated with sand and silt content further emphasizes the scattered physical properties of the FCR in the field. The FCR samples approximately showed similar silt content to limiting silt content (i.e. 25% to 45%) defined by Polito and Martin (2001). Accordingly, the liquefaction resistance of FCR samples may not follow typical behavior observed for most sandy soils.

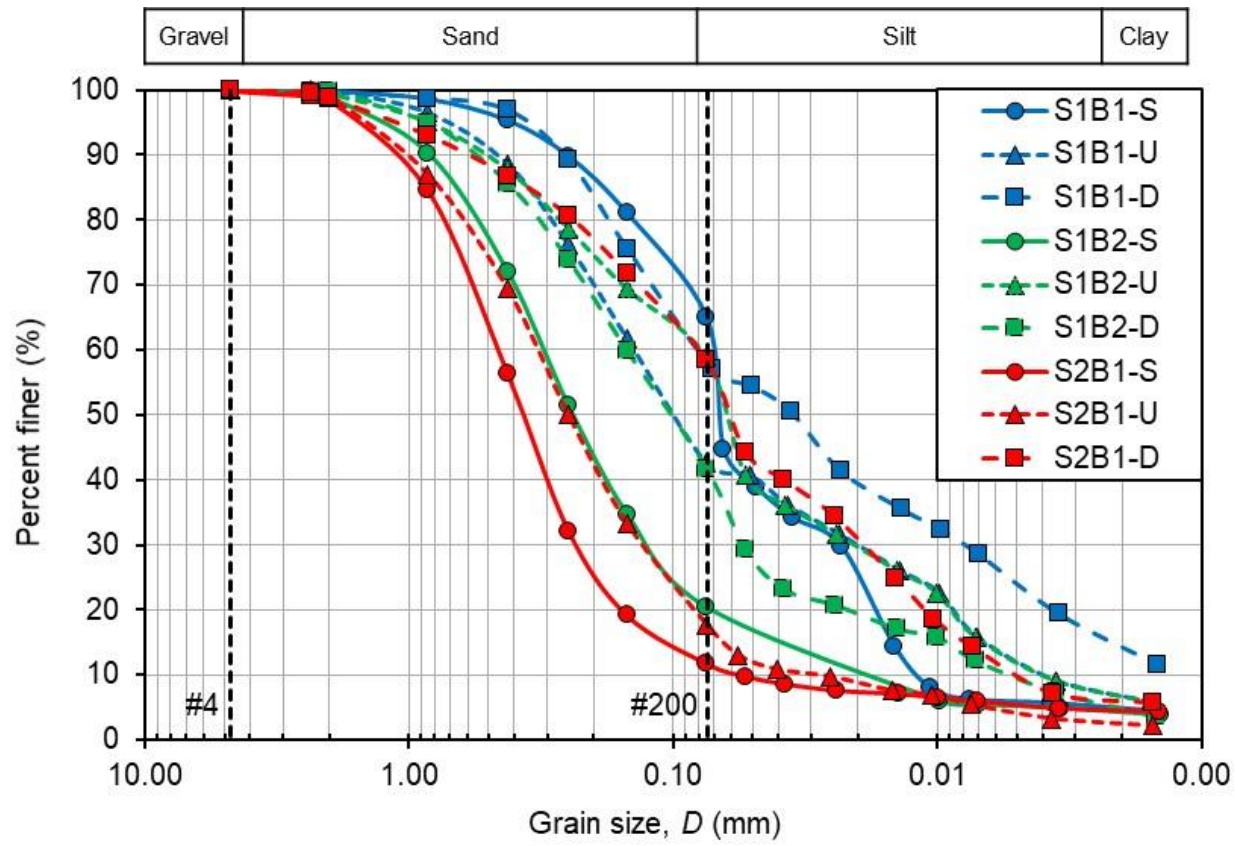


Figure 3-2. The particle size distributions of the FCR samples

Figure 3-3 shows that the variability of the percentage of fines (percent finer than #200 sieve) of coal slurry reduces with depth. High variability of fine content is observed at the upper layer of fine coal refuse. At the upper layer, the gain size distribution of coal refuse depends on the direction of the slurry discharge. At the location closer to the discharge point, the coal refuse with large grain size (i.e. the heavier coal refuse) settles first while the coal refuse with small grain size keeps flowing. Whenever the discharge direction changes, the grain size distribution will change along the impoundment, resulting in a large range of percentages of fine contents at the upper layer. At the deeper layer, the grain size of coal refuse converges to a range of 38% and 60%. The mean value of the percentages of fine contents also increases with depth.

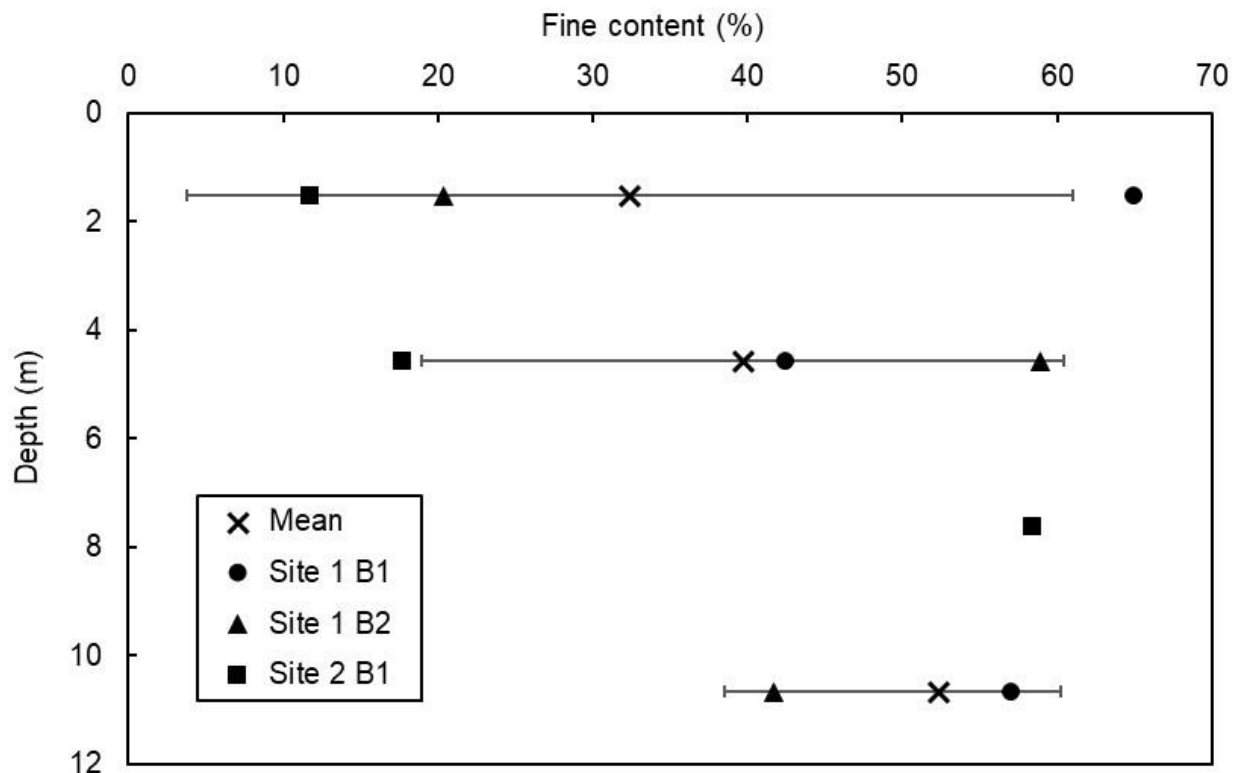


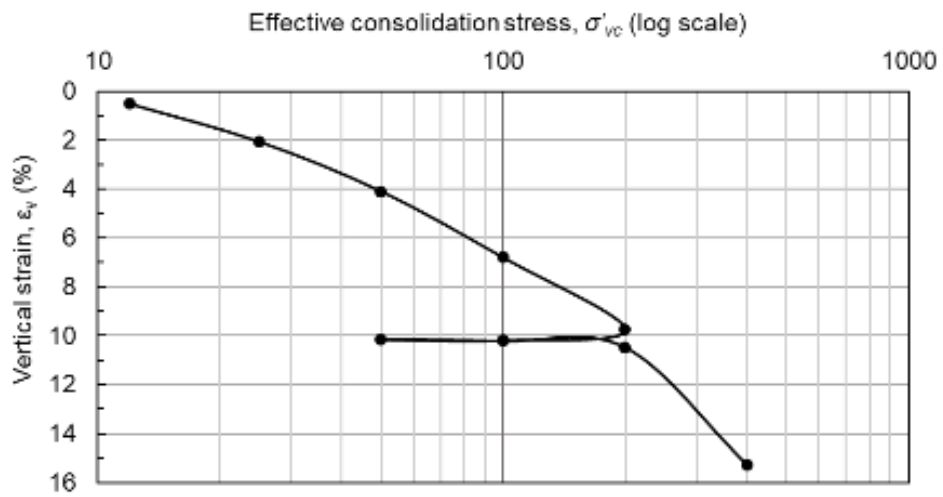
Figure 3-3. Variation of the fine content of coal slurry with depths. The bar length represents the corresponding standard deviation at different depths.

A narrow range of hydraulic conductivity from $1.0\text{e-}6$ cm/s to $3.6\text{e-}7$ cm/s was observed for all the samples excluding S1B2-D. The higher hydraulic conductivity of S1B2-D can be again attributed to the accumulation of coarser particles at this depth. According to the empirical equation for calculating hydraulic conductivity (Taylor 1948), the highest hydraulic conductivity was expected to be associated with S2B1-U, which has the largest particles and D_{50} . However, the hydraulic conductivity is highly sensitive to homogeneity and voids arrangement inside the sample's structure (Budhu 2015). Therefore, the observed discrepancy can be attributed to heterogeneity inside the samples' mass, which is common in tailings. It is also worth mentioning that the hydraulic conductivities presented in Table 3-2 are the hydraulic conductivity in vertical (gravitational) direction.

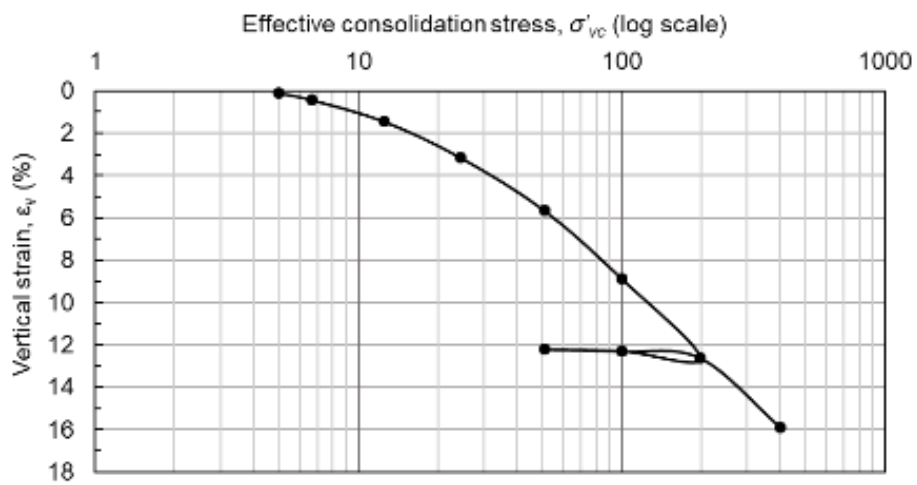
One-dimensional consolidation tests were conducted on the FCR samples as per ASTM D2435. Based on initial interpretation, Borehole 2 at Site 1 is closer to the discharge point and the samples are expected to be coarser than samples from Borehole 1. Consequently, consolidation tests were not conducted on samples from Site 1 Borehole 2 (S1B2). The consolidation test results for S1B1 and S2B1 samples were summarized in Table 3-3. Based on Table 3-3, the compression index ranges from 0.134 and 0.453 and swell index ranges from 0.003 to 0.013. The coefficient of consolidation ranges from 0.75 to 2.36 cm²/min. Figure 3-4 (a-f) presents the consolidation curves for the fine coal refuse samples at different sites and depths.

Table 3-3. Consolidation test results

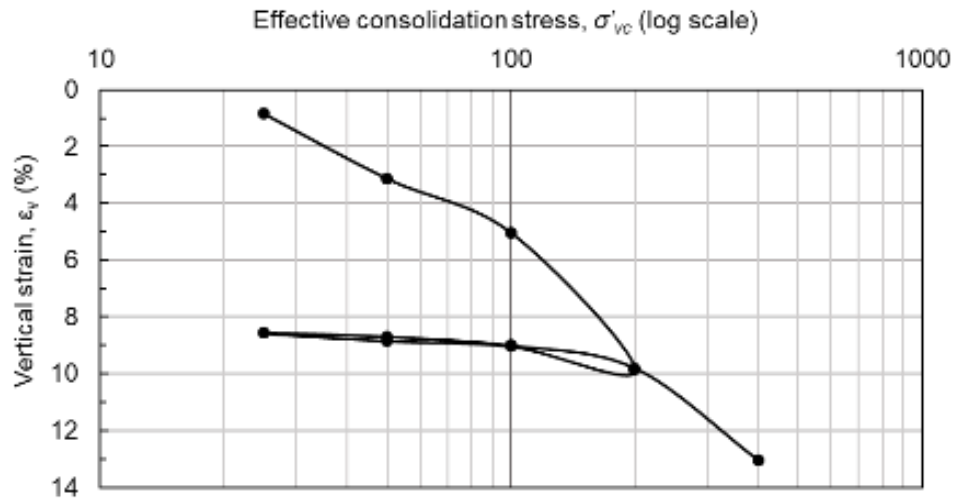
| Sample | Compression Index, C_c | Swell Index, C_s | Coefficient of consolidation, C_v cm^2/min |
|--------|--------------------------|--------------------|---|
| S1B1-S | 0.234 | 0.005 | 1.06 |
| S1B1-U | 0.134 | 0.003 | 1.70 |
| S1B1-D | 0.200 | 0.013 | 1.17 |
| S2B1-S | 0.242 | 0.007 | 0.75 |
| S2B1-U | 0.453 | 0.010 | 2.36 |
| S2B1-D | 0.200 | 0.013 | 0.89 |



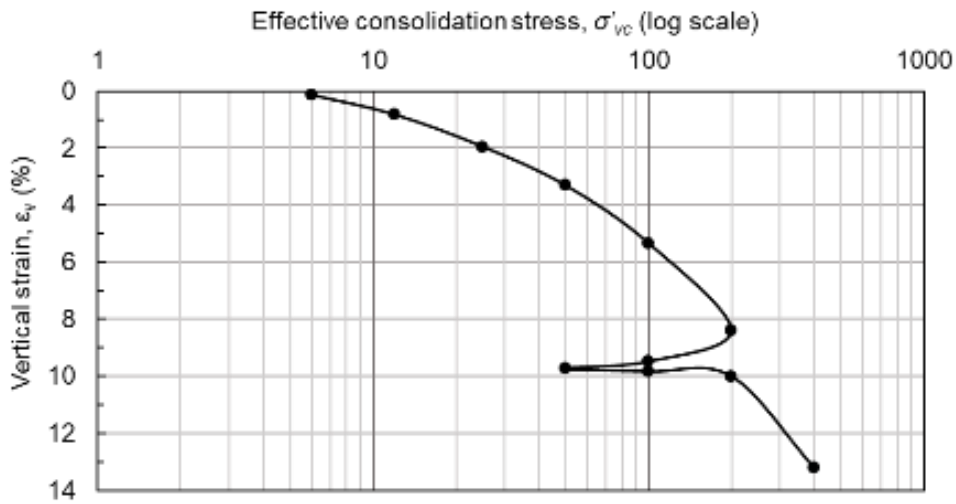
(a) S1B1-S



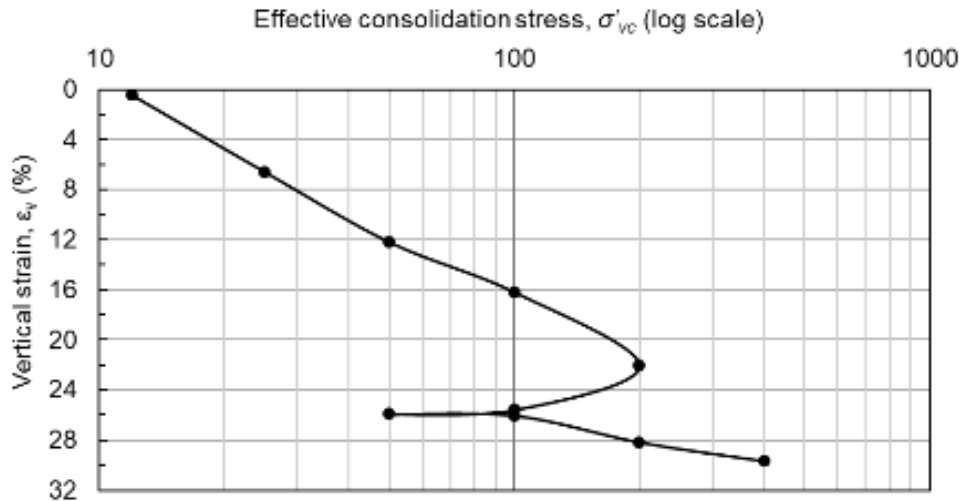
(b) S1B1-U



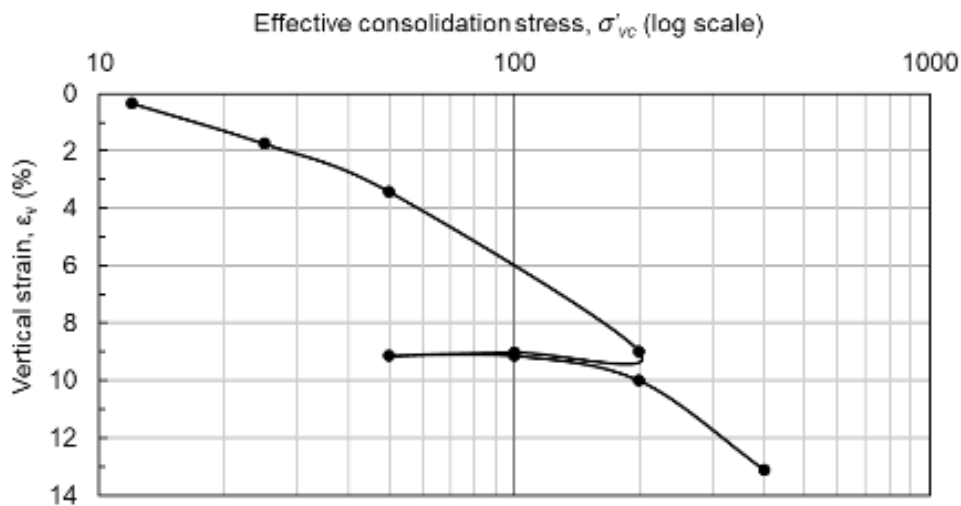
(c) S1B1-D



(d) S2B1-S



(e) S2B1-U



(f) S2B1-D

Figure 3-4. Consolidation curves for the fine coal refuse samples at different sites and depths

Figure 3-5 shows that the coefficient of consolidation of the fine coal refuse samples has a linear negative association with their percentages of fine contents passing sieve #200. As the percentage of fine content increases, the rate of consolidation of coal slurry decreases. The mean coefficient of consolidation decreases by 0.3 times as the fine content of coal refuse increases by 10%. The coefficient of determination, R^2 , for this regression model is 0.94, indicating a strong linear correlation between the coefficient of consolidation and the fine content percentage. One out of six sets of data points were excluded from this regression model and treated as an outlier. This specific coal refuse sample was classified as well-graded sand with silts (SW-SM) whereas the rest of the samples fall into the categories of silty sand (SM) and silt (ML). The coefficient of consolidation, C_v , for SW-SM was found to divert from that of SM and ML. While the physical

mechanism was not fully understood, it is recommended that this regression model should only be used for coal refuse in the categories of SM and ML. C_v (in cm^2/min) for SM and ML can be estimated using Equation (3-1).

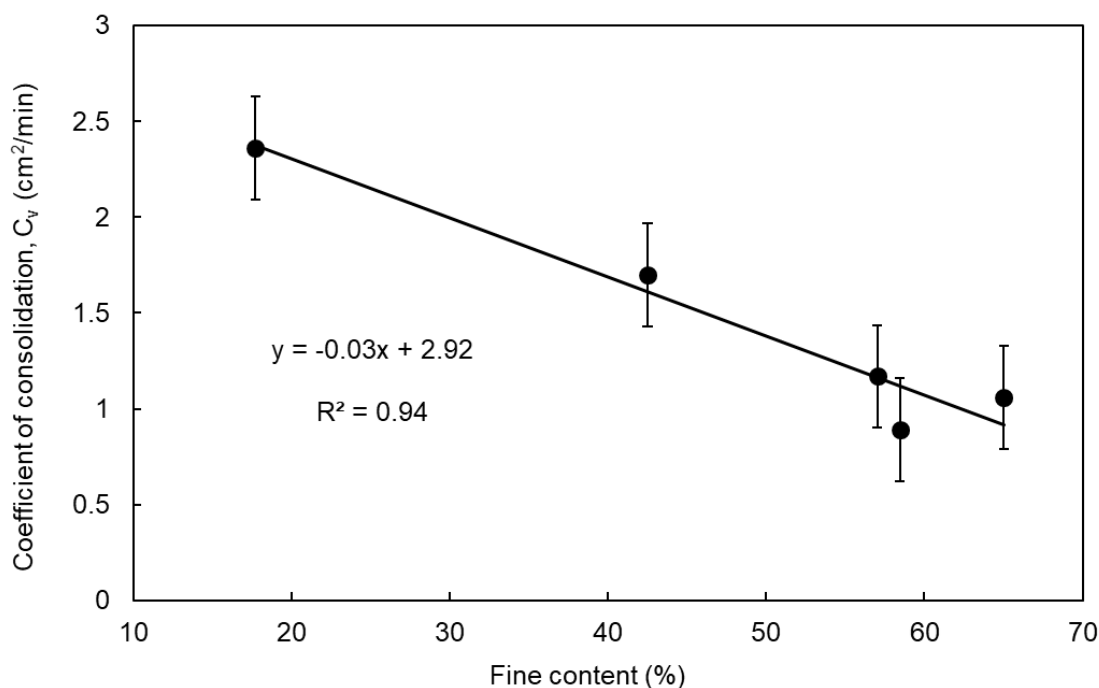


Figure 3-5. A linear relationship between the coefficient of consolidation of the fine coal refuse samples and the percentage of fine content

$$C_v = -0.03 \% \text{Fines} + 2.92 \quad (3-1)$$

3.3 Static Triaxial Test Results

Static triaxial tests were conducted on representative samples to determine the shear strength properties of the specimens under monotonic loading. Staged triaxial approach on a single specimen was practiced in this study, as sufficient number of representative and identical samples were not available. All the samples from S1 and S2 impoundments were tested under consolidated-undrained (CU) condition and consolidated-drained (CD) condition, respectively. It was of interest to evaluate shear strength properties of FCR in both short-term (i.e., undrained) and long-term (i.e. drained) conditions. The index properties of the tested samples, including initial void ratio and initial unit weight, were earlier reported in Table 3-2.

Samples were initially saturated using the back pressure technique, as per ASTM D 4767, until a minimum B-value of 96% was reached. Each staged triaxial test consisted of two stages. Samples were first consolidated and then axially loaded under confining pressure of 34.5 kPa in Stage 1. It is noteworthy to mention that the vertical compression in the first stage (i.e., at 34.5 kPa confining pressure) was halted before failure. The first loading stage was continued until the threshold of the maximum deviatoric stress, where the change in deviatoric stress became minimal.

This practice prevented complete failure or disturbance of the sample. Then, the axial load was removed and the sample was consolidated under 69 kPa confining pressure and vertically compressed again to reach the maximum deviatoric stress. All the samples showed strain hardening behavior during loading so that deviatoric stress kept slightly increasing at large strains. This behavior was also observed in other studies on coal refuse material (Qiu and Seg0 2001). The typical behavior of coal slurry samples observed in CU and CD tests in terms of deviatoric stress versus axial strain, excess pore pressure versus axial strain, stress path in q - p' space, and shear strength envelope are presented for four samples. Figure 3-6 and Figure 3-7 depict the staged CU triaxial test results of S1B2-U and S1B1-D, respectively. Figure 3-8 shows staged CD triaxial results of S2B1-U and S2B1-D. Therefore, drained and undrained mechanical behavior of FCR at shallow and deep depth under shear could be investigated.

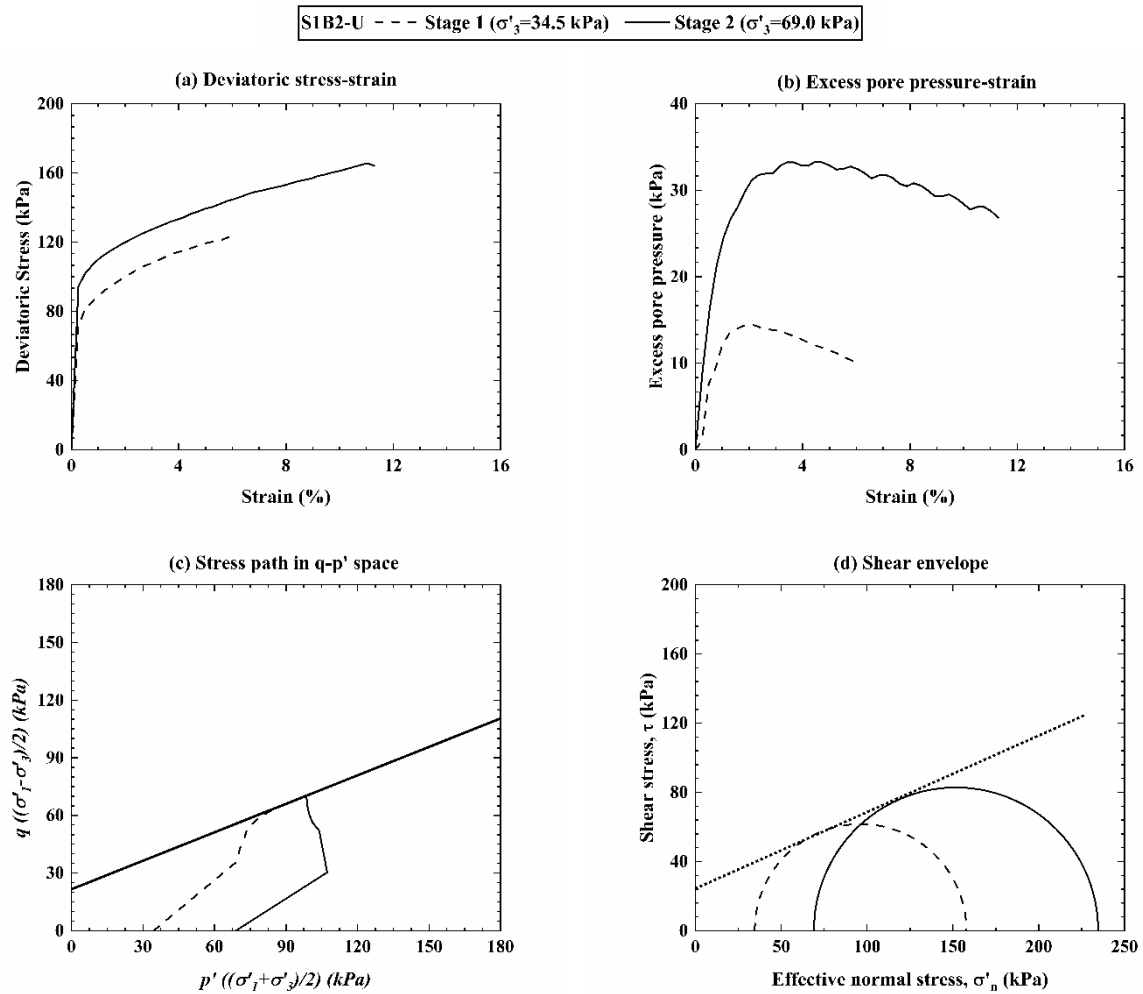


Figure 3-6. Staged CU triaxial test results (S1B2-U)

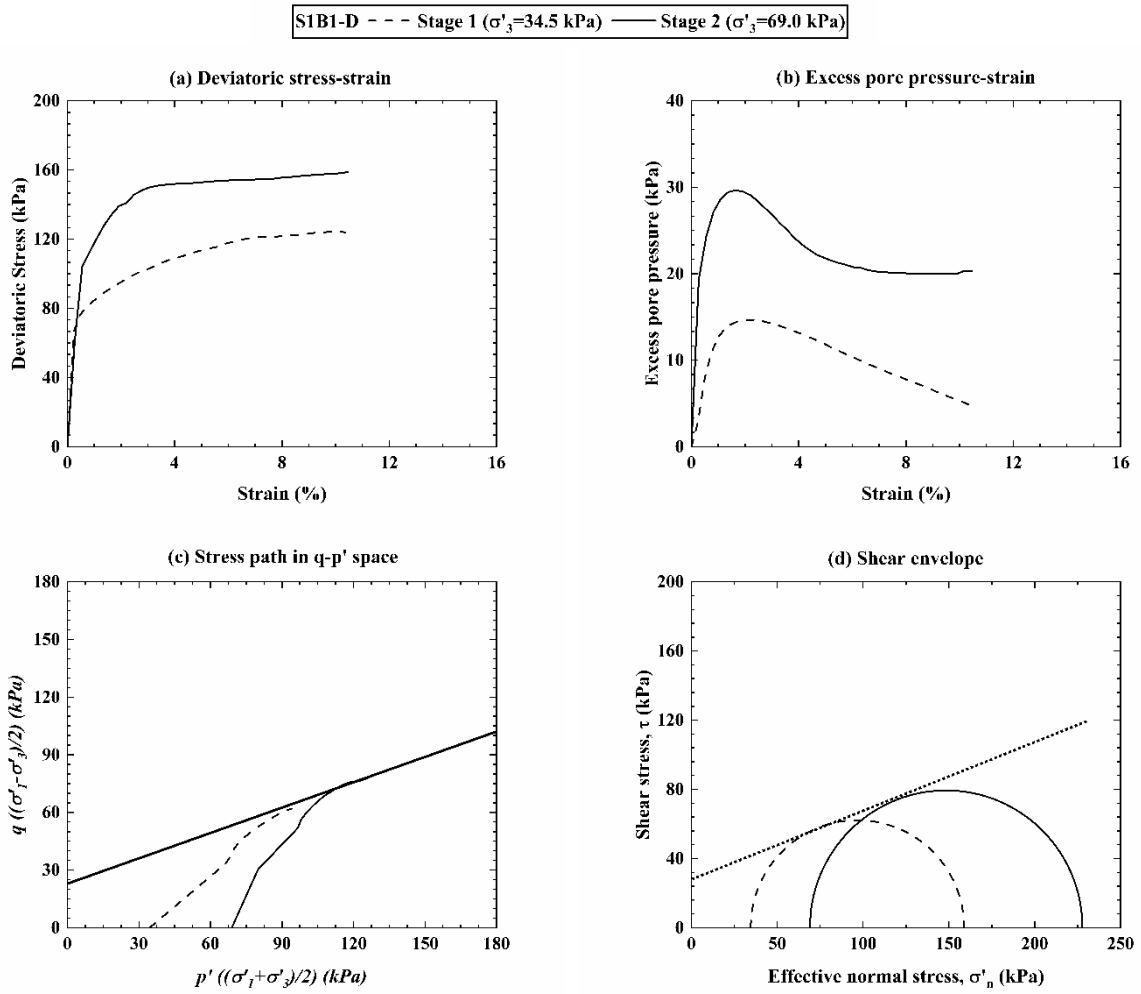


Figure 3-7. Staged CU triaxial test results (S1B1-D)

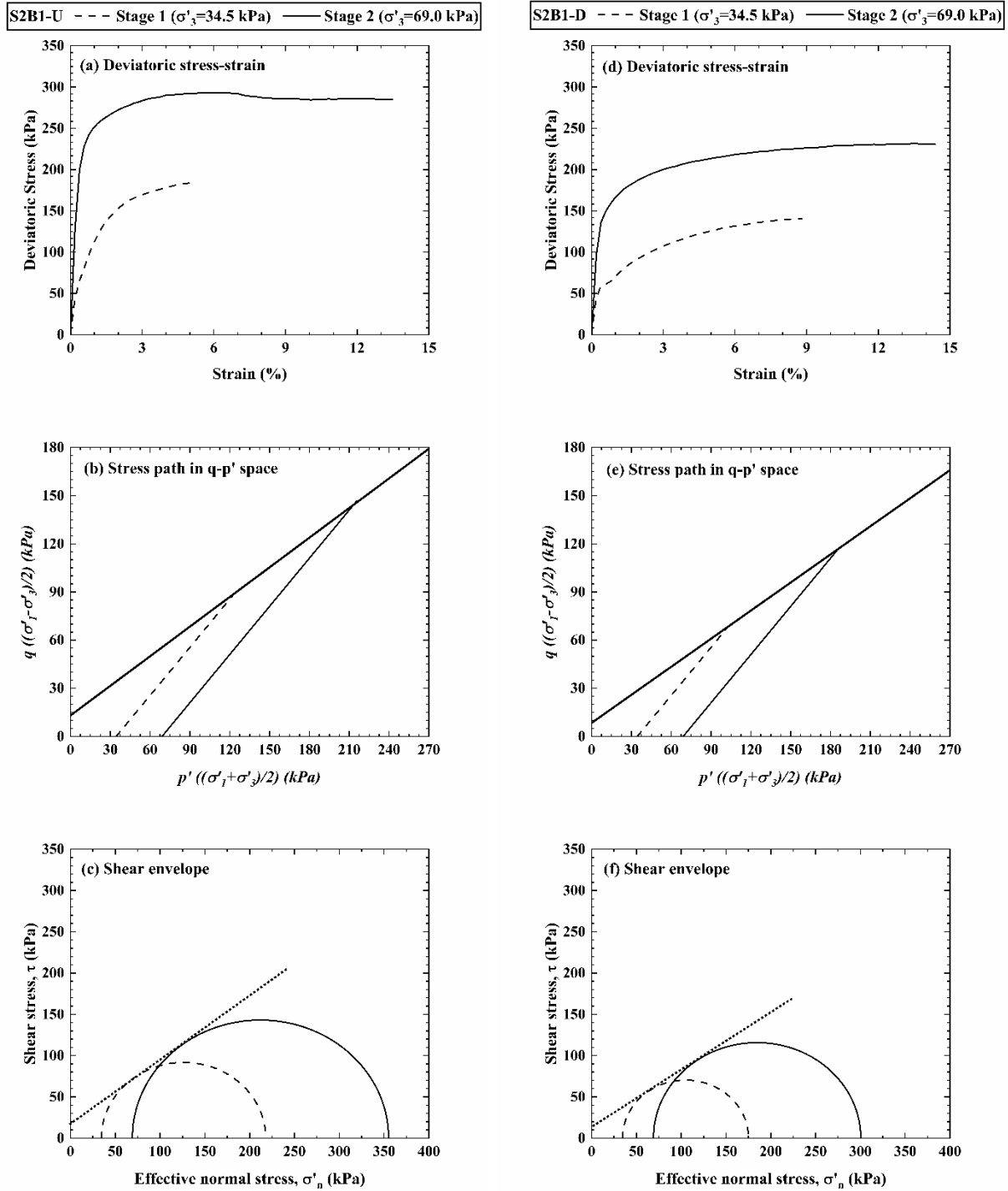


Figure 3-8. Staged CD triaxial tests results (S2B1-U and S2B1-D)

Figure 3-6 presents the mechanical response of S1B2-U under staged CU triaxial static loading. Figure 3-6 (a) shows strain hardening behavior of the sample and reinforcing effect of confining pressure, as higher confining pressure resulted in higher deviatoric stress. The maximum deviatoric stress reached approximately 120 kPa and 165 kPa at 6% and 11% axial strain under

34.5 kPa and 69 kPa confining pressure, respectively. Similarly, higher pore pressure was developed within the sample at higher confining pressure, as shown in Figure 3-6 (b). Peak pore pressure of 15 kPa and 33.5 kPa was observed below 4% axial strain under 34.5 kPa and 69 kPa confining pressure, respectively; then, pore pressure began decreasing. The stress path was plotted in q - p' space per Lambe's (1964) definition, as in Figure 3-6 (c). The slope of the shear envelope in q - p' space is equal to $\tan\alpha = \sin\phi'$, while the intercept is equal to $m = c'\cos\phi'$. The stress path in the first stage relatively resembled the typical stress path seen for over-consolidated soils, as the sample was consolidated under higher effective stress than 34.5 kPa in field. However, the stress path in the second stage showed the typical path seen for normally consolidated soils, as 69 kPa was higher than the consolidation stress in field for S1B2-U. The effective Mohr's circles along with shear envelope were also plotted, as in Figure 3-6 (d). The effective shear strength properties, c' and ϕ' , are later presented and discussed in Table 3-4.

The mechanical response of S1B1-D under staged CU triaxial static loading is presented in Figure 3-7. The strain hardening behavior of the sample S1B1-D was less intense than that of S1B2-U, see Figure 3-7 (a). The reason could be attributed to the larger amount of small particles in S1B2-U that led to higher compressibility of the sample. The maximum deviatoric stresses observed for S1B1-D were 120 kPa and 160 kPa both occurred at approximately 11% axial strain under 34.5 kPa and 69 kPa confining pressure, respectively. The peak pore pressures of 15 kPa and 30 kPa were observed under 34.5 kPa and 69 kPa confining pressure, respectively. The stress path observed for S1B1-D was similar to the stress path expected for over-consolidated soils, as the sample had been consolidated by higher effective stress according to the depth of the sample in field, see Figure 3-7 (c). Effective Mohr's circles are also displayed in Figure 3-7 (d).

The mechanical response of S2B1-U and S2B1-D under staged CD triaxial static loading is shown in Figure 3-8. According to Figure 3-8 (a) and (d), the higher confining pressure was, the higher maximum deviatoric stress was achieved. Consolidated drained condition led to higher maximum deviatoric stress compared to the results observed in consolidated undrained tests. For example, the maximum deviatoric stress achieved by S2B1-U and S2B1-D were approximately 290 kPa and 230 kPa, respectively, under 69 kPa confining pressure. The stress paths shown in Figure 3-8 (b) and (e) represented the drained path, which is a straight line. Lastly, Figure 3-8 (c) and (f) show the shear envelopes for S2B1-U and S2B1-D, which show higher internal friction angle and lower cohesion compared with those under CU condition.

Table 3-4 presents the effective shear strength properties of all the FCR specimens. The cohesion for all the specimens tested under CU condition falls within 13.8 kPa to 25.5 kPa, while the cohesion of the samples tested under CD condition ranges from 13.1 kPa to 16.5 kPa. In terms of internal friction angle, two samples from impoundment S2, tested under CD condition, showed higher values compared to CU test results. Furthermore, higher friction angle (i.e. 38°) was observed for S2B1-D compared to that of S2B1-U (i.e. 36°). Among the results obtained from impoundment S1, S1B2-D showed the highest internal friction angle (i.e. 31°), which can be attributed to the higher concentration of coarse particles at this location. The slope (α) and intercept (m) of the failure envelope in q - p' space are also provided in Table 3-4. The observations in this study were found within the range reported by Hegazy et al. (2004), who conducted statistical analysis on shear strength properties of coal refuse that were determined using laboratory and in-

situ testing. Considering all the results, the FCR's shear strength properties are relatively scattered and dependent on its location and depth.

Table 3-4. Staged triaxial test results

| Test | Sample | c' (kPa) | ϕ' (deg.) | m (kPa) | α (deg.) |
|------|--------|------------|----------------|-----------|-----------------|
| CU | S1B1-U | 13.8 | 29 | 12 | 25.9 |
| CU | S1B1-D | 25.5 | 26 | 22.9 | 23.7 |
| CU | S1B2-U | 24.8 | 30 | 21.5 | 26.6 |
| CU | S1B2-D | 20.7 | 31 | 17.7 | 27.2 |
| CD | S2B1-U | 16.5 | 36 | 13.3 | 30.4 |
| CD | S2B1-D | 13.1 | 38 | 10.3 | 31.6 |

3.4 Resonant Column Test Results

The shear moduli of the FCR samples were determined by resonant column tests on representative samples. The torsional resonant column approach is commonly used to characterize the maximum shear modulus of soil at low shear strain. The shear strain applied to samples in the torsional resonant column ranges from 10^{-5} % to 10^{-2} %. The sample's behavior is considered elastic within this low range of shear strain. Each sample was tested under three confining pressures of 34.5, 69, and 103 kPa. The key outputs of the resonant column tests are shear wave velocity, shear modulus, and damping ratio.

Figure 3-9 presents the normalized shear modulus, defined as the shear modulus divided by the corresponding maximum shear modulus, at 69 kPa confining stress. The hollow and solid markers represent the samples at deeper and shallower depth, respectively. Normalized shear modulus showed minimal change over the shear strain range, therefore, the results at 34.5 kPa and 103 kPa were not shown in order to avoid overlap of the data points. The observations are in agreement with previous studies (e.g. Seed and Idriss 1970; EPRI 1993; Darendeli 2001), which showed negligible influence of confining pressure on normalized shear modulus at low shear strain level that was less than 10^{-3} %, see Figure 3-9. The modulus reduction curve could not be established for the FCR, as the shear modulus was only examined for low shear strain that was less than 10^{-3} %. The effect of aging and time were not investigated in this study. However, the observed shear stiffness properties such as shear modulus might vary over time as shown by Kim and Novak (1963) and Anderson and Stokoe (1978). The normalized shear modulus obtained in cyclic DSS tests are also embedded in Figure 3-9 and will be discussed in the following section. Initial void ratio and unit weight of the samples used in the resonant column tests are presented in Figure 3-10 (d).

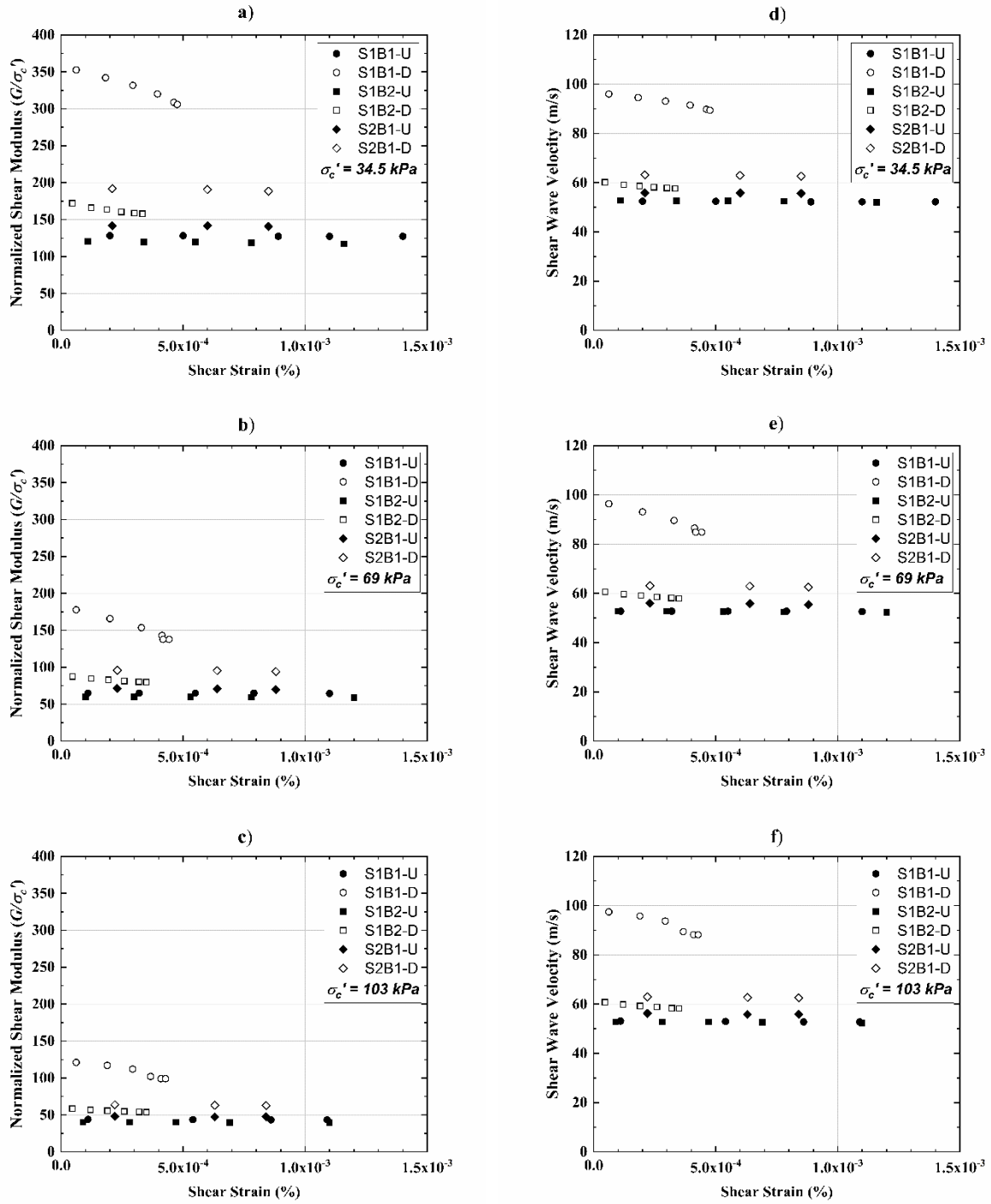


Figure 3-9. Shear modulus and shear wave velocity of the FCR samples

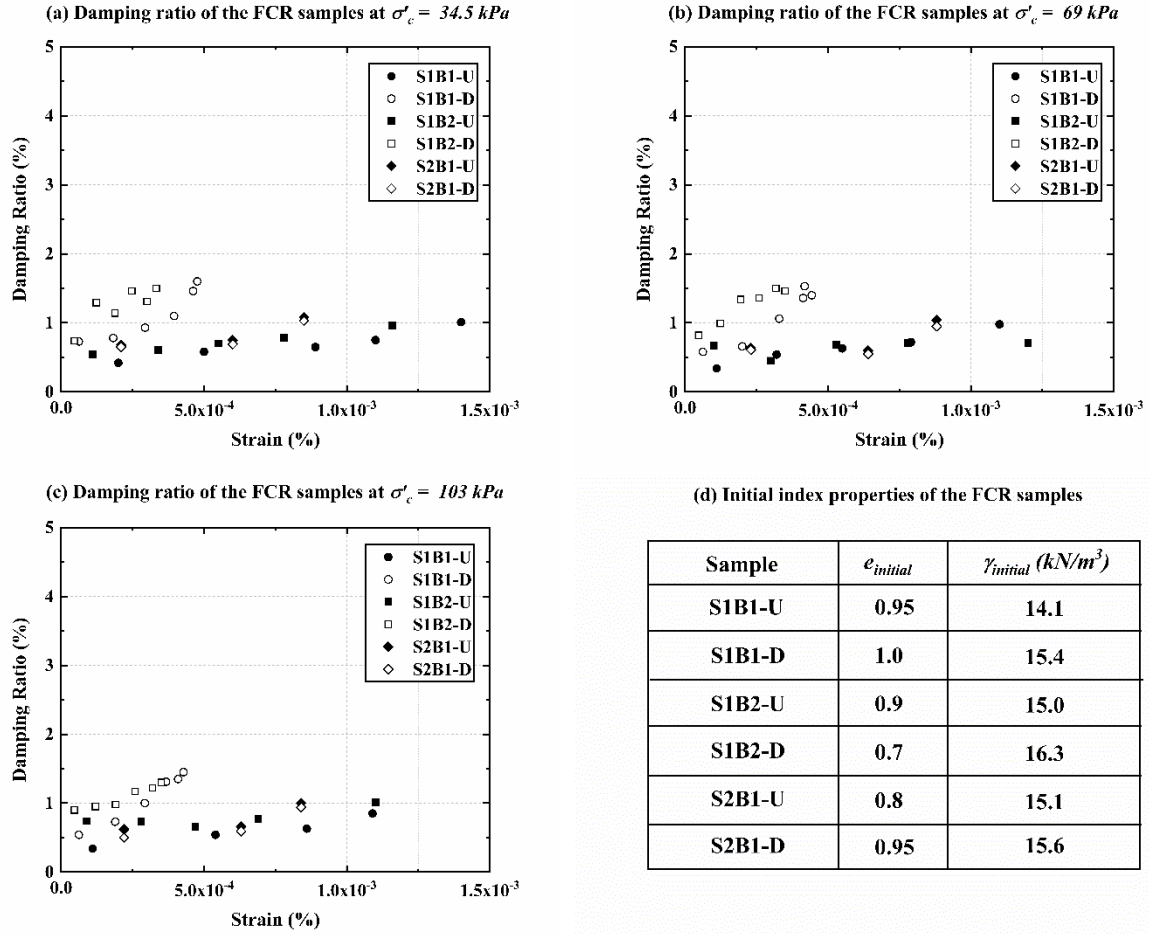


Figure 3-10. Damping ratio of FCR samples and their initial index properties

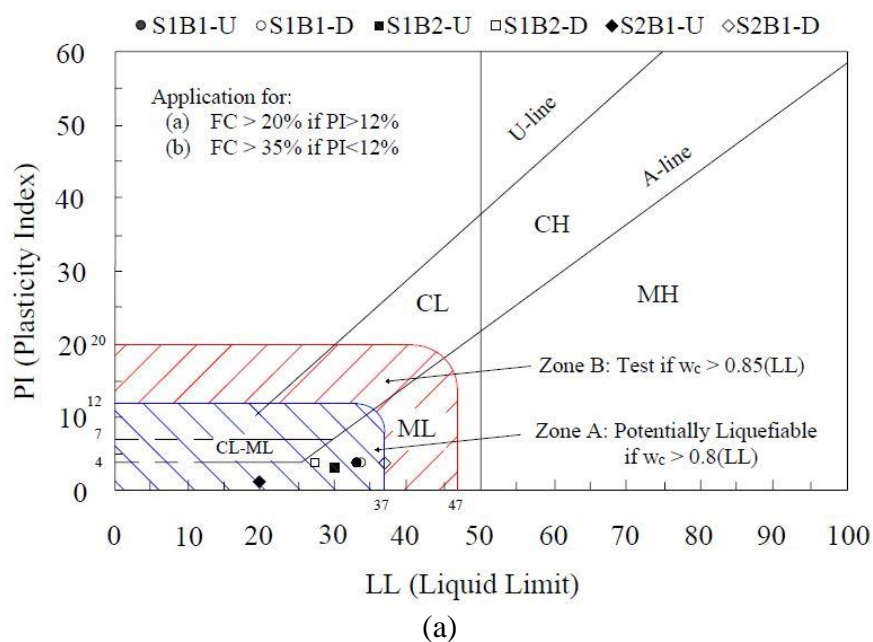
The samples collected from greater depth, S1B1-D, S1B2-D, and S2B1-D, shown by the hollow markers in Figure 3-9, showed higher absolute shear modulus and shear wave velocity than the samples at shallower depth. However, higher reduction was observed for S1B1-D and S1B2-D samples, as shear strain increased, this behavior was found out of the proposed limits shown in Figure 3-9. The sample S1B1-D showed significantly greater shear modulus and shear wave velocity (i.e. 90 to 100 m/s) than those of other samples. The sample S1B1-D seemed to have coarser particle size distribution than other samples, resulting in stiffer material. However, the S1B1-D gradation shown in Figure 3-2 is not the largest. The reason is that the samples used for resonant column and particle size distribution analysis were within the same depth range (i.e. 10.5 m to 12 m), but were not the same sample. This discrepancy emphasizes the scattered physical properties of FCR in the field even in small ranges of depth and distance. However, the higher stiffness observed for deeper samples was consistent with higher shear strength observed for the samples taken from deeper depths in triaxial testing. Except for S1B1-D, other examined samples demonstrated close values in terms of shear modulus in the range of 4.1 to 6.9 MPa.

The damping ratios of all the samples under three different confining pressures are displayed in Figure 3-10. The effect of confining pressure was found minimal due to the large

amount of fines content and low induced shear strain. The damping ratio also increased by increasing shear strain regardless of applied confining pressure. Overall, damping ratio of the FCR samples was found to be within the range of 0.6% to 2%, which is in agreement with other studies on FCR (e.g., Zeng et al. 2008).

3.5 Liquefaction Susceptibility and Cyclic Behavior Characterization

The liquefaction potential of FCR is of great importance, as liquefaction occurrence can result in significant loss in strength and stability of coal slurry impoundments. Accordingly, liquefaction susceptibility of FCR should be assessed under seismic loading conditions. The liquefaction potential per soil type can be evaluated by index properties such as Atterberg limits and water content. Seed et al. (2003), Bray and Sancio (2006), and Idriss and Boulanger (2008) have presented empirical criteria to determine the liquefaction potential of soils based on index properties, including liquid limit (LL), plasticity index (PI), and water content (w). The index properties of the FCR samples at U (upper) and D (deeper) depths, shown in Table 3-2, were plotted in the recommended figures by Seed et al. (2003) and Bray and Sancio (2006), see Figure 3-11. As shown in Figure 3-11, all the samples fall within the area marked as potentially liquefiable by both criteria. Liquefaction potential assessment per soil type using the approach by Idriss and Boulanger (2008) is described later in detail. Cyclic DSS tests were conducted on reconstituted S1B2-D sample at different CSRs to determine the liquefaction resistance of FCR and assess the undrained cyclic behavior of FCR. Duplicate tests were conducted until validity of the results was ensured. The void ratios of the tested samples, which were prepared by slurry deposition approach, were approximately 0.6~0.7 after consolidation and before cyclic loading.



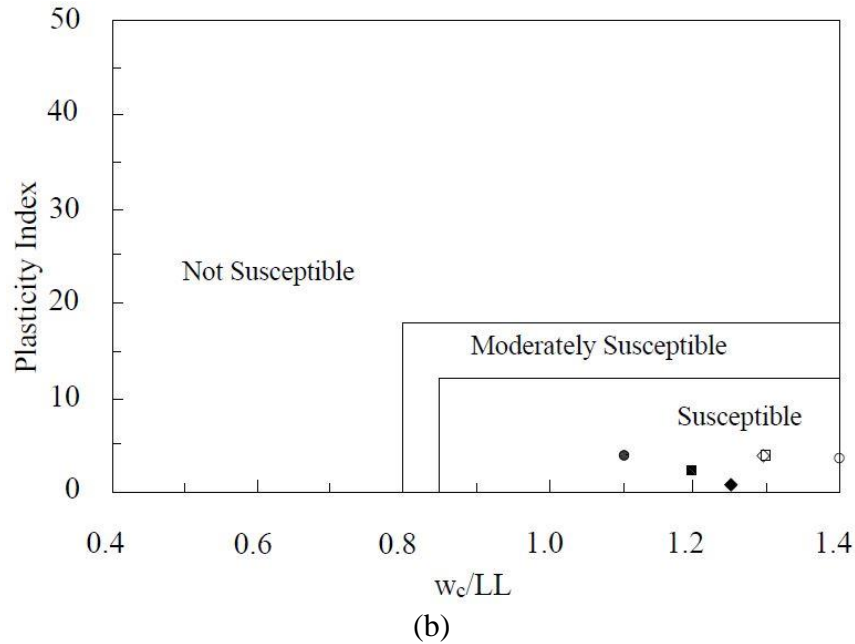


Figure 3-11. Liquefaction susceptibility assessment criteria proposed by
 a) Seed et al. (2003) b) Bray and Sancio (2006)

Figure 3-12 shows the cyclic resistance of FCR prepared by the slurry deposition method and consolidated under a vertical stress of 60 kPa with void ratio after consolidation ranging approximately between 0.6 to 0.7. Higher number of cycles were required to liquefy the sample as the CSR decreased. The relation between CSR and number of cycles (N) to failure (defined in this study as 5% DAS) can be expressed as $CSR = a \times (N_{5\%DAS})^{-b}$. The relation and corresponding fitted line are presented in Figure 3-12. The power fit (b-value) was found to be 0.16.

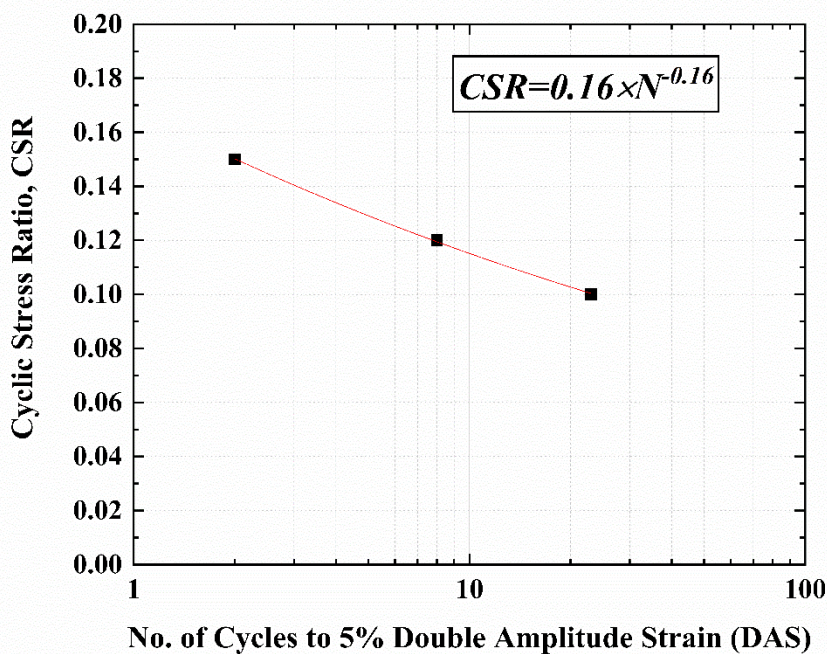


Figure 3-12. Relationship of cyclic stress ratio (CSR) with number of cycles (N) to reach 5% DAS

Figures 3-13 to 3-15 present the results obtained in cyclic DSS test on the FCR samples at CSR of 0.15, 0.12, and 0.1, respectively. The initial void ratio of the samples before cyclic loading is also shown in the figures. The subfigures (a) and (b) summarize the undrained cyclic response of the FCR samples, and the subfigure (c) clearly shows the development of shear strain against number of cycles; the developed double amplitude strain (DAS) can be calculated by summing the positive and negative peak shear strain at each cycle. The subfigure (d) displays the shear modulus reduction during the cyclic loading. The shear modulus, calculated based on the dissipated energy during each cycle, is directly calculated and reported by the device. According to Figure 3-13, the FCR sample reached 5% DAS in almost two cycles when cyclically loaded by CSR of 0.15. The void ratio of the sample before and after consolidation was 0.94 and 0.73, respectively. The pore pressure ratio, which is traditionally considered as a parameter of evaluating liquefaction occurrence, also increased to 0.55 in approximately two cycles. The shear modulus in the first two cycles were plotted in Figure 3-13 (d) to show the decreasing trend of shear modulus. Figure 3-14 shows the results of cyclic DSS test at CSR of 0.12. The void ratio of the sample before and after consolidation was 1.02 and 0.69, respectively. The sample reached 5% DAS after 8 cycles. According to the shear stress-strain loops, the sample behavior is relatively plastic, as large strain is developed rapidly in the first cycle. The shear stress-strain loops are slightly shifted to the left direction. However, the 5% DAS failure criterion was assumed to properly eliminate any potential dependence of the cyclic resistance to the directionality and bias in the shear stress-strain loops (Price et al. 2017). The pore pressure ratio (r_u) increased to 0.7 after 8 cycles.

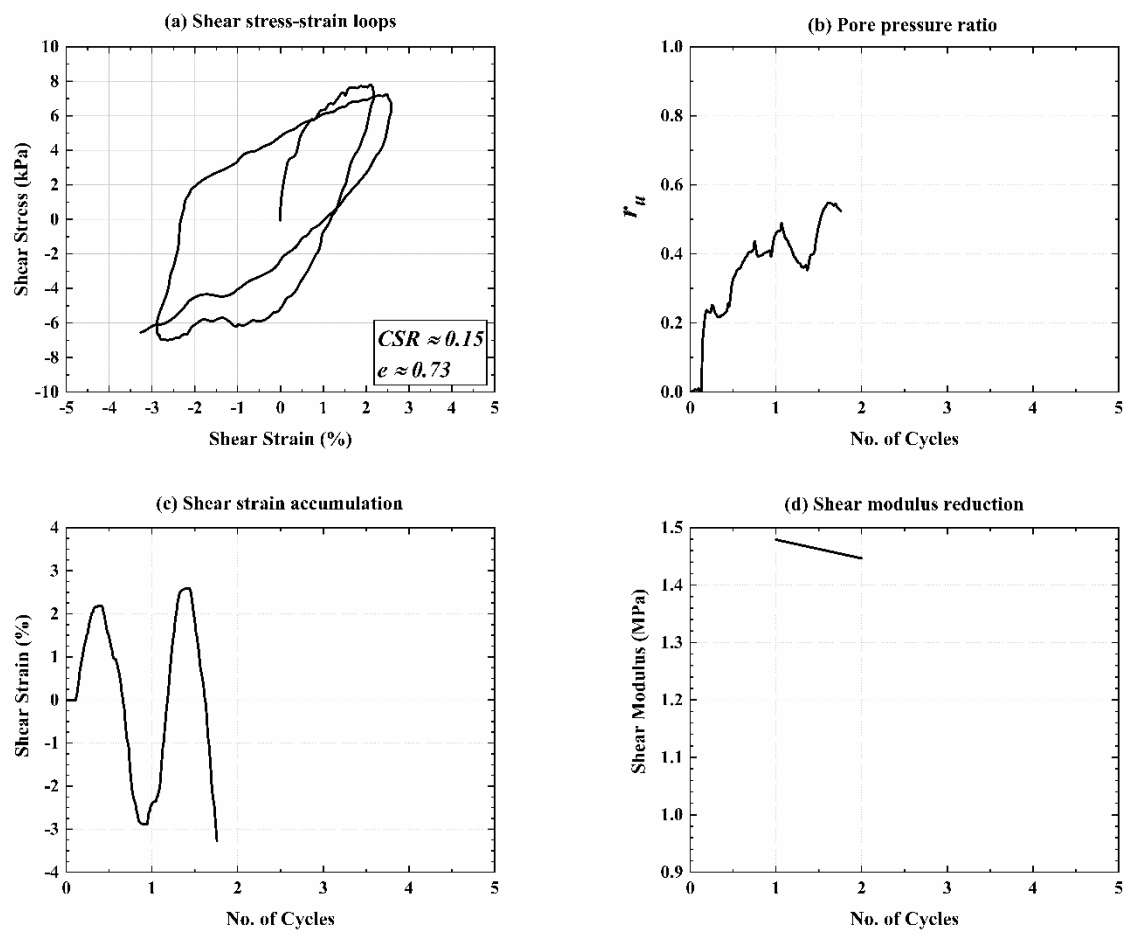
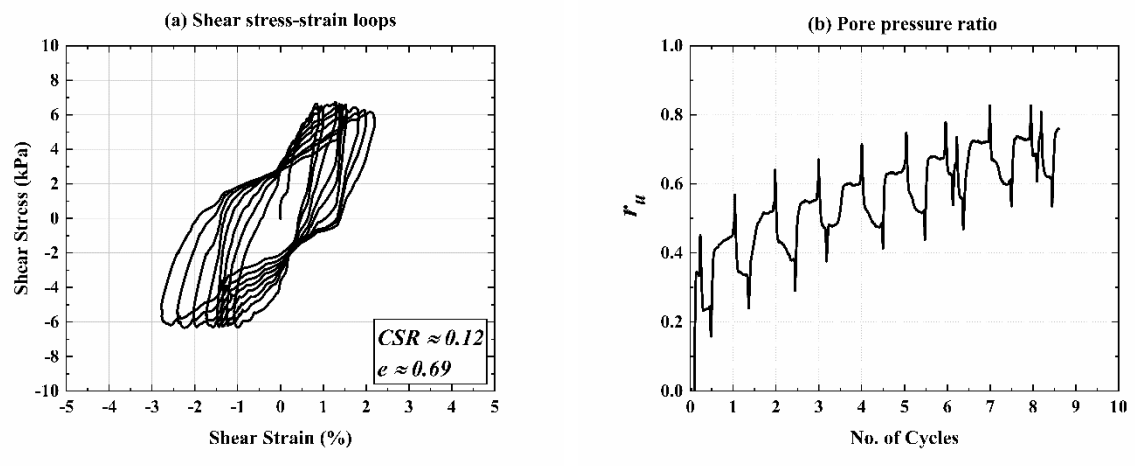


Figure 3-13. Cyclic DSS test results at CSR~0.15



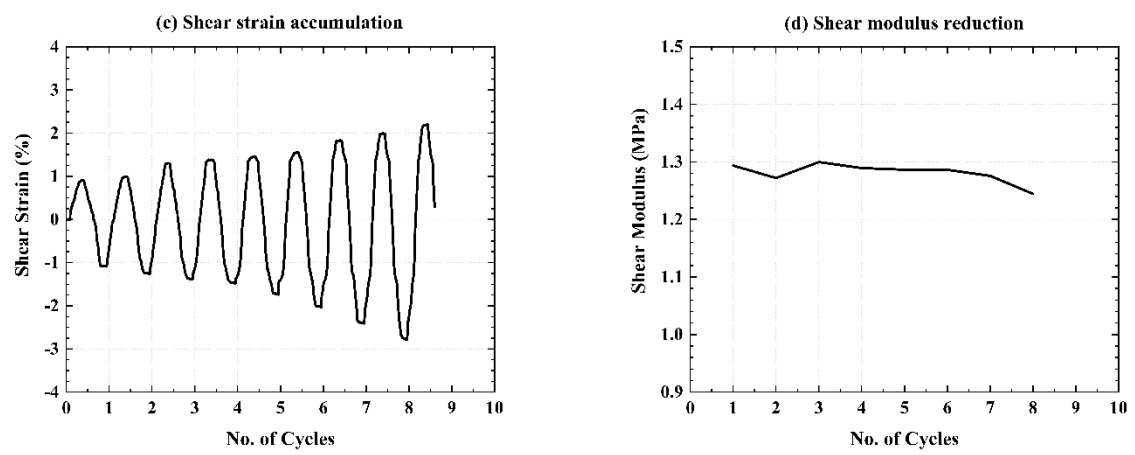


Figure 3-14. Cyclic DSS test results at CSR~0.12

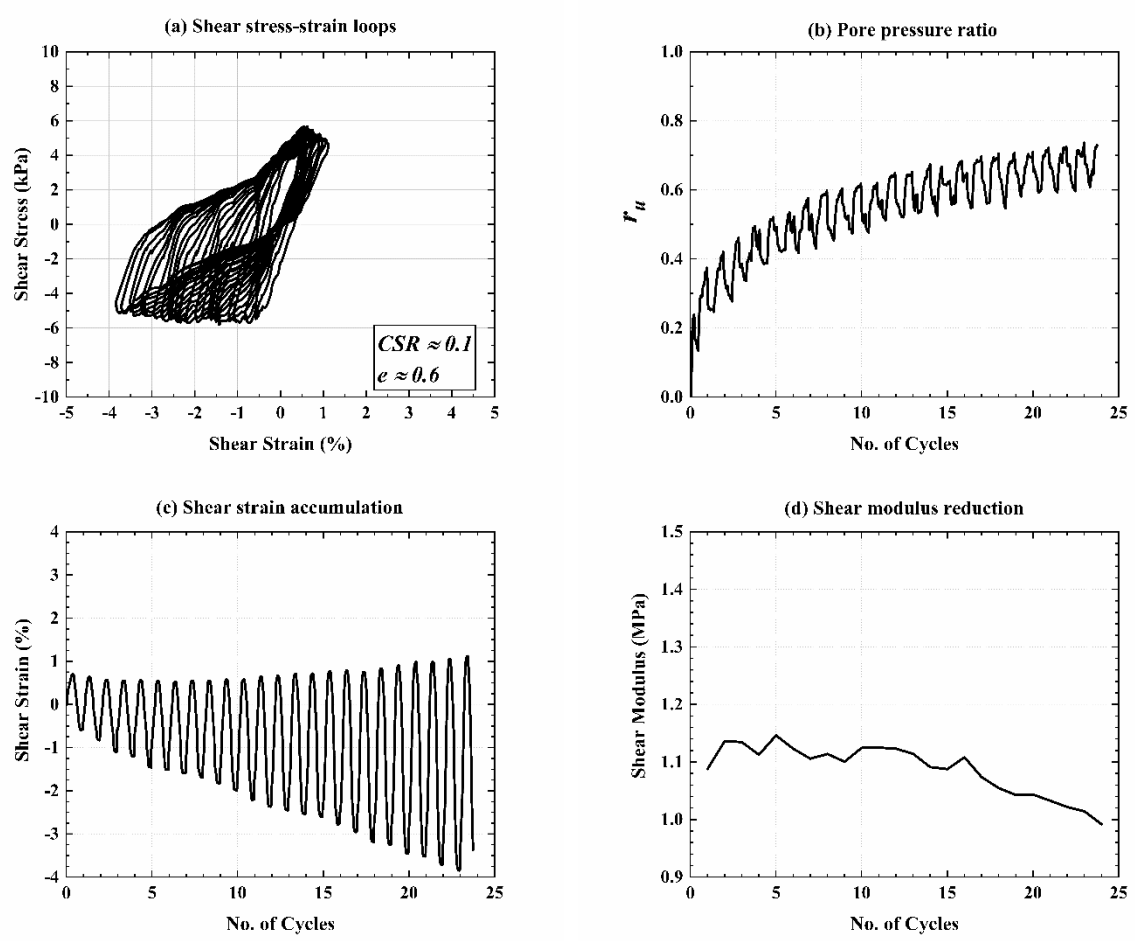


Figure 3-15. Cyclic DSS test results at CSR~0.1

Similar behavior was observed for the FCR sample under CSR of 0.1, as the shear stress-strain loops were wide and shifted, and considerable amount of pore pressure was developed in the first few cycles, as shown in Figure 3-15. The void ratio of the sample before and after consolidation was 0.78 and 0.6, respectively. The 5% DAS was reached after approximately 23 cycles of cyclic loading, and the final pore pressure ratio was equal to 0.7. As shown in Figure 3-15 (d), significant shear modulus reduction occurred in the last few cycles. The specimen generated a considerable amount of pore water pressure in the first cycle, as shown in Figure 3-13 (a), Figure 3-14 (a), and Figure 3-15 (a), while the rate of pore water pressure generation reduced in the following cycles. The axial strain during the cyclic loading was smaller than 0.05%, which ensured that the device was able to maintain the constant volume during cyclic loading. As far as the shear modulus obtained from cyclic DSS testing, the average shear modulus calculated at the beginning of the cyclic DSS tests was approximately 1.3 MPa. The results are embedded in Figure 3-9, which shows the obtained shear modulus is within the proposed limits for sands (Seed and Idriss 1970; EPRI 1993) and low plasticity silty sands (Darendeli 2001). In comparison with the range of G_{max} observed in resonant column tests (4.1 MPa – 6.9 MPa), lower shear modulus was seen for FCR at higher shear strain.

The wide shear stress-strain loops and large shear strain development without reaching 100% pore pressure ratio (r_u) is commonly observed in clay-like material. The b value (i.e. the power fit on the CSR-N plot in Figure 3-12) is also within the range of clay-like material (Idriss and Boulanger, 2008). However, the cyclic response was expected to be sand-like because of the extremely low plasticity index of 2 associated with S1B2-D, see Table 3-2. The uncertainties in characterizing the cyclic response of FCR compelled the authors to try to assess this characteristic using empirical criteria.

In order to further investigate the cyclic behavior of the FCR sample, an empirical criterion proposed by Idriss and Boulanger (2008) was adopted, as shown in Figure 3-16. The transition of cyclic behavior from sand-like to clay-like is shown against plasticity index. The hatched region is the transitional area where the cyclic behavior is between sand-like and clay-like behavior. Furthermore, the solid lines are the conservative limits proposed by Idriss and Boulanger (2008). The cyclic resistance ratios (CRRs) of material assuming clay-like and sand-like behavior can be determined by the equations proposed by Idriss and Boulanger (2008). Equations (3-2) and (3-3) determine the sand-like and clay-like CRR of soils, respectively.

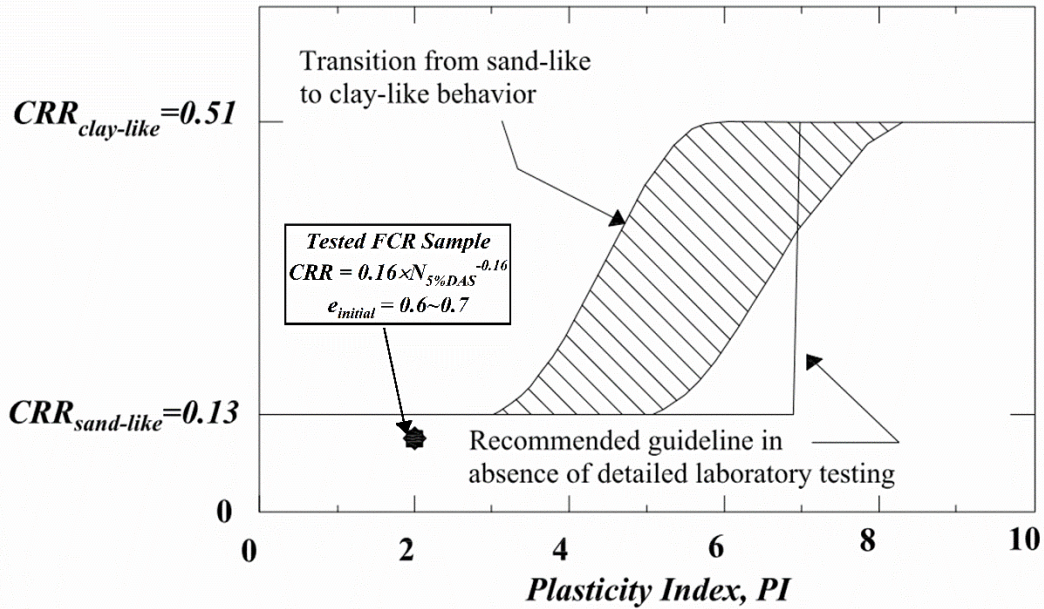


Figure 3-16. Cyclic behavior of the FCR based on Idriss and Boulanger (2008) criterion

$$CRR_{M=7.5, \sigma'_{vc}=1} = \exp\left(\frac{(N_1)_{60cs}}{14.1} + \left(\frac{(N_1)_{60cs}}{126}\right)^2 - \left(\frac{(N_1)_{60cs}}{23.6}\right)^3 + \left(\frac{(N_1)_{60cs}}{25.4}\right)^4 - 2.8\right) \quad (3-2)$$

$$CRR_{M=7.5, \sigma'_{vc}=1} = 0.8 \times \frac{S_u}{\sigma'_{vc}} \quad (3-3)$$

In-situ and laboratory tests are needed to determine the properties required in the equations. Then, the cyclic behavior of the material can be characterized according to plasticity index. The CRR relationship in Equations (3-2) and (3-3) are empirical relationships developed for a wide range of soils and stress conditions. These empirical correlations, also known as “simplified” procedure, are easy to use. However, there is a considerable uncertainty in the estimated cyclic resistance ratios (CRR) from these empirical correlations. In particular, these correlations have been primarily developed for sand and sand-like materials and their applicability to estimating CRR for FCR is uncertain. The study presented in this paper aims to give an insight on the accuracy of using the simplified procedures to estimate CRR for FCR. This is achieved by comparing the CRR estimated from the simplified procedures and the CRR from cyclic DSS tests.

The clean sand-equivalent, overburden-corrected SPT number $((N_1)_{60cs})$ for the sample tested in the cyclic DSS tests (i.e. S1B2-D) was adopted to empirically calculate the sand-like CRR of the sample, per Equation (3-2). Although loading conditions are different between SPT and cyclic DSS tests, this comparison could enable us to understand the accuracy of the simplified SPT-based procedures in estimating CRR for the FCR. This comparison may also help practicing engineers to determine whether the commonly used SPT-based simplified procedures can be used for liquefaction triggering evaluation of FCR. According to the SPTs conducted in the study, the corrected SPT number $((N_1)_{60})$ was estimated to be 6.9. Subsequently, the clean sand equivalent

value $((N_I)_{60cs})$ was calculated based on the approach proposed by Idriss and Boulanger (2008) given 40% fines content, according to Figure 3-2. Therefore, the $(N_I)_{60cs}$ and corresponding $CRR_{\text{sand-like}}$ were 12.5 and 0.13, respectively. Furthermore, the undrained shear strength of the sample was estimated to be 80.4 kPa using the triaxial test results. Idriss and Boulanger (2008) also proposed to decrease the $CRR_{M=7.5, \sigma'_{vc}=1}$ calculated by Equation (3-3) by 20% for tailings, therefore, $CRR_{M=7.5, \sigma'_{vc}=1}$, which is $CRR_{\text{clay-like}}$, was determined to be 0.51.

The CRR calculated from the above empirical correlations were compared against the CRR obtained from the cyclic DSS tests. The $CRR_{M=7.5}$ of the S1B2-D, which is the CSR that liquefies the sample in 15 cycles, was calculated by adopting the power equation developed in Figure 3-12. Therefore, the $CRR_{M=7.5}$ of the S1B2-D with PI of 2 (as seen in Table 3-2) was determined to be 0.1 based on the CSR-N power equation. The $CRR_{M=7.5}$ was converted to $CRR_{M=7.5, \sigma'_{vc}=1}$ by applying the overburden correction factor (K_σ). The overburden correction factor (K_σ) was 1.04 using the correlations by Idriss and Boulanger (2008) and the corresponding $CRR_{M=7.5, \sigma'_{vc}=1}$ was almost 0.1. The CRRs of FCR from the two methods is shown in Figure 3-16. The empirical correlations by Idriss and Boulanger (2008) estimate the CRR of FCR generally well, assuming the FCR has sand-like behavior. However, as described earlier, the stress-strain loops and the pore-water-pressure generation resemble those of clay-like behavior. According to the estimated values, sand-like cyclic behavior is expected for the tested FCR (Figure 3-16). As seen in Figure 3-16, the estimated $CRR_{M=7.5, \sigma'_{vc}=1}$ is noticeably close to the transitional zone where the behavior of the material changes from sand-like to clay-like over a small range of PI. Therefore, observing clay-like cyclic response of the FCR in cyclic DSS is not a surprise. Eventually, the FCR can be classified as a material that has transitional cyclic behavior from sand-like to clay-like behavior.

Post-liquefaction shear strength characteristics of the liquefied FCR, which had experienced 5% DAS, were evaluated by conducting a static shearing immediately after the cyclic loading. The post-liquefaction shear strength and stiffness properties are key characteristics to evaluate the stability of tailings dams after seismic events. Although the static DSS is not the best approach to determine the post-liquefaction shear strength, as the potential void redistribution after liquefaction in field cannot be sufficiently captured in a relatively uniform sample in the DSS equipment, the basic shear behavior of the liquefied material can still be characterized. The strain-controlled shear stress was applied to the sample at the rate of 1.4% per hour, the test was continued up to 30% shear strain. Figure 3-17 shows the shear stress and pore pressure ratio (r_u) against shear strain during the post-cyclic static loading for all three samples that were previously tested under different CSRs. The liquefied FCR samples were found considerably soft so that the post-liquefaction modulus and shear strength were significantly low. For instance, the secant shear modulus of the liquefied FCR samples, at 5% shear strain, was within 40 kPa to 70 kPa.

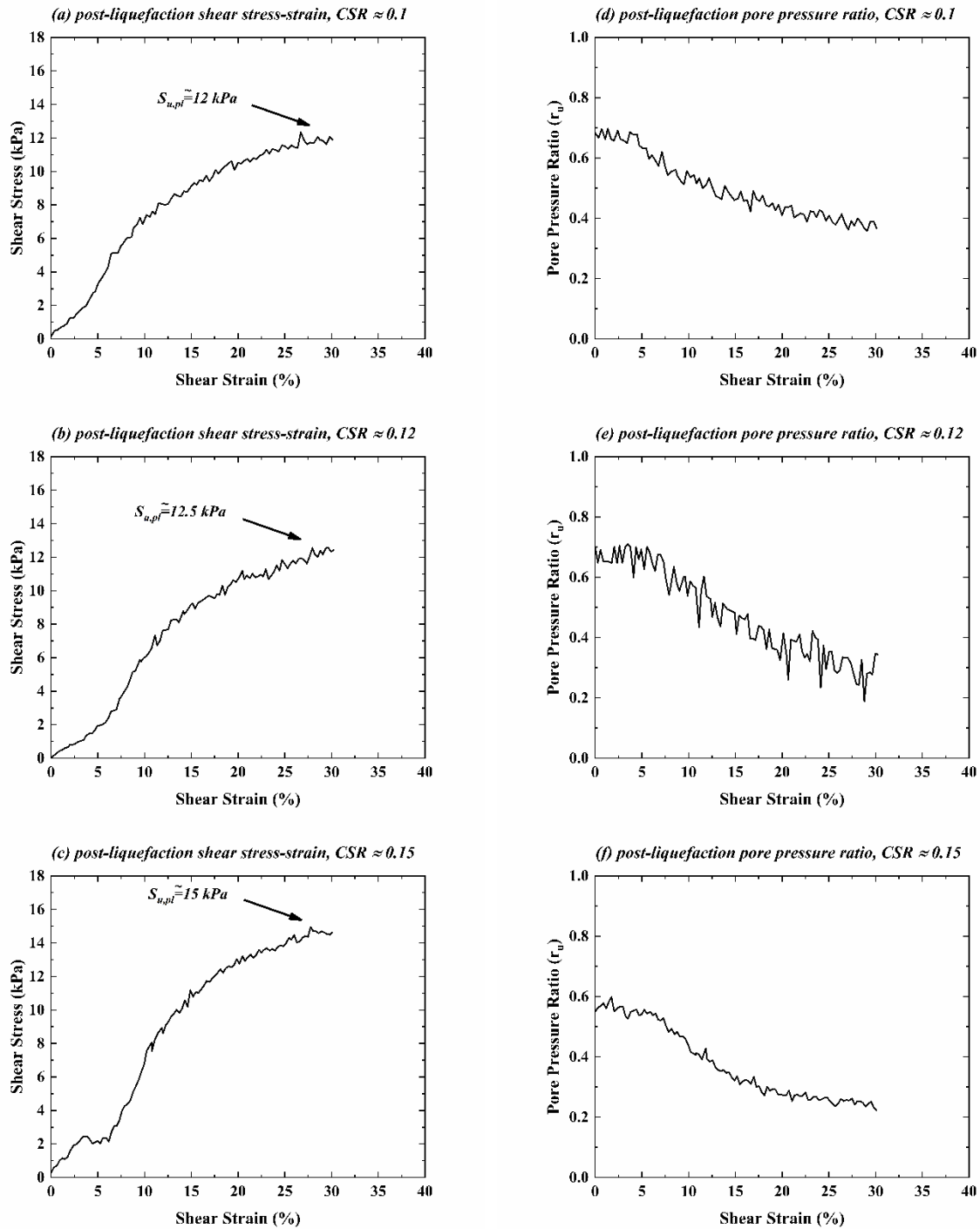


Figure 3-17. Post-liquefaction shear strength characteristics of FCR

Further in the static loading, when the shear strain increased, shear strength began to recover. Eventually, the peak post-liquefaction shear strength ($S_{u,pl}$) were 12 kPa, 12.5 kPa, and 15 kPa for the samples cyclically loaded by CSR of 0.1, 0.12, and 0.15, respectively. The increasing trend in $S_{u,pl}$ as the CSR increased can be attributed to higher void redistribution, subsequently,

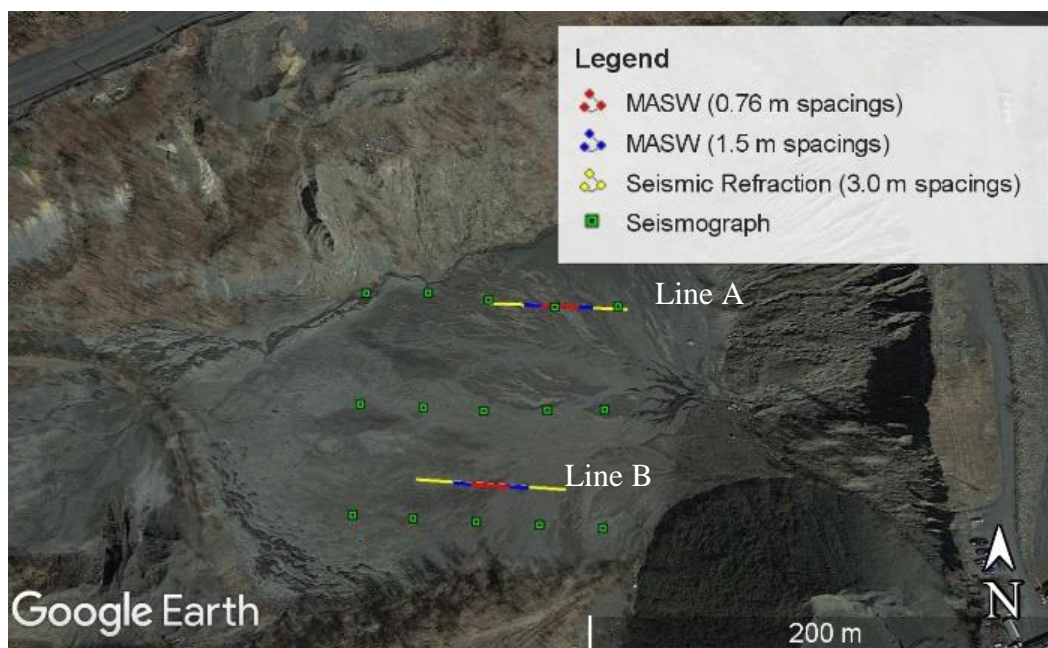
higher densification induced to the sample that was subjected to higher CSR. Considering the figures of pore pressure ratios, the samples showed dilative behavior during the static shearing, as the pore pressure ratio that had developed during the cyclic loading phase decreased during the static shear phase.

CHAPTER 4. SEISMIC SURVEY AND SEISMIC MONITORING

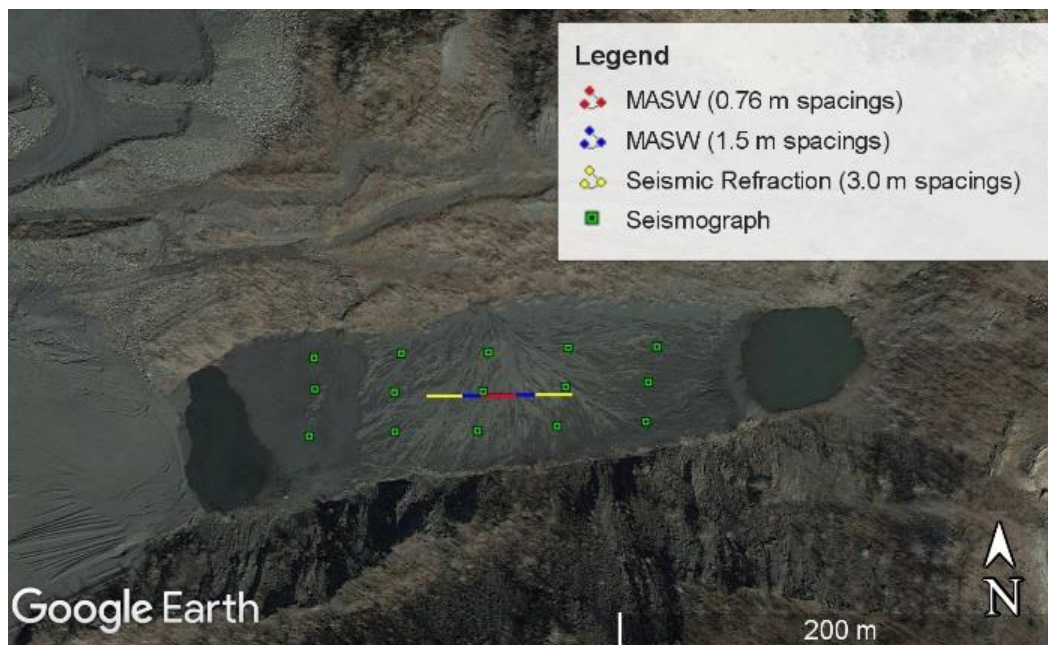
This chapter presents in situ seismic survey and seismic monitoring that were used to determine the basic mechanical properties of in situ coal tailings such as the shear wave velocity, compressional wave velocity, Poisson's ratio, Young's modulus, and small-strain shear modulus; these field tests contribute to the scarce database of in situ coal slurry characteristics. The properties derived from this study are compared with those derived from the standard penetration test (SPT) to show the effectiveness of the seismic investigations in reviewing the in situ properties of coal tailings. A prediction equation for peak particle velocity is also developed specifically for coal tailings. The peak particle velocity obtained in this study is used to evaluate the cyclic stress ratio due to mine blasting. The liquefaction resistance of coal tailings is then evaluated using the simplified procedure presented by Andrus and Stokoe (2000).

4.1 Methodology of Seismic Survey

The seismic survey, which included multichannel analysis of surface waves (MASW) and seismic refraction, was conducted to characterize the in situ properties of fine coal tailings. The MASW was performed to determine the one-dimensional shear wave velocities, and the seismic refraction survey was performed to determine the two-dimensional compressional wave velocities. Figure 4-1 (a) shows the layouts of the seismic lines for the seismic survey at Site 1, which is an active impoundment with on-going deposition of coal tailings, whereas Figure 1 (b) shows the layouts of seismic lines at Site 2, which is an inactive impoundment where the coal tailings deposition has ceased.



(a) Site 1 (an active impoundment)



(b) Site 2 (an inactive impoundment)

Figure 4-1. Layouts of seismic lines and seismographs for seismic survey and monitoring

As shown in Figure 4-1 (a-b), three sets of seismic lines were laid out at various locations in the impoundments, namely Site 1 Line A, Site 1 Line B, and Site 2. Each set of seismic lines included a seismic refraction line with 3.0 m geophone spacings, a MASW line with 0.76 m geophone spacings, and a MASW line with 1.5 m geophone spacings. Twenty-four geophones were deployed for each seismic line as shown in Figure 4-2 (a). Geophones, as shown in Figure 4-2 (b), are instruments that measure ground velocity due to seismic or dynamic event. Figure 4-2 (c) shows a seismogram record and Figure 4-2 (d) shows the data acquisition processes for both seismic refraction and MASW surveys. Since the coal tailings flow in the longitudinal direction of each impoundment from one end that is closer to the coal preparation plant to the other end, the coarser coal tailings are likely to be deposited at the upstream end. Therefore, the seismic lines were laid out in the longitudinal direction to observe the changes of wave velocities across the impoundment. The seismic lines with smaller geophone spacing (the MASW lines with 0.76 m spacings) were designed to give better resolution of the subsurface coal tailings profiles. The seismic excitation for the MASW method was induced by a drop of sledge hammer on the ground surface inside each impoundment. A sledge hammer (as shown in Figure 4-3) was used because ambient noise was insufficient in the impoundments for a passive MASW survey, which utilizes ambient noise as an impact power, to be conducted. In the seismic refraction survey, small explosive charges were used to induce the seismic excitation (as shown in Figure 4-4) because the seismic energy induced by a sledge hammer was insufficient to overcome the energy dissipation in the soft fine coal tailings.



(a) Layout of a seismic line of 12 geophones



(b) A geophone



(c) Seismogram records



(d) Data acquisition by Vibra Tech, Inc.

Figure 4-2. Seismic refraction and MASW testing



(a) A sledge hammer



(b) Generation of shear waves by a sledge hammer

Figure 4-3. MASW testing on July 6, 2017



(a) A drilled hole and the explosives



(b) Generation of primary waves by the blasting of a small explosive charge

Figure 4-4. Seismic refraction testing on July 31, 2017

4.2 Methodology of Seismic Monitoring

Seismic monitoring was carried out on July 6, 2017. Fifteen Geosonics 3000LCP Blasting Seismographs (as shown in Figure 4-5 (b)) were deployed by Vibra-Tech Engineers, Inc. in each impoundment to measure the ground displacements induced by the blasting events. The ground displacement data were collected by the data acquisition system (Figure 4-6 (a-b)). The layouts of the seismographs are shown in Figure 4-1 (a-b). In Site 1, the seismographs were spaced 53.3 m apart in the North/South direction and 30.5 m apart in the East/West direction. In Site 2, the seismographs were spaced 18.3 m apart in the North/South direction and 39.6 m apart in the East/West direction. All seismographs were buried around 15 cm into the ground (Figure 4-5 (a)) and their locations were tracked by a global positioning system (GPS) as shown in Figure 4-5 (c).



(a) A seismograph was buried 15 cm (6 inches) into the ground



(b) A seismograph



(c) A GPS

Figure 4-5. Deployment of seismographs and location tracking



(a) A data acquisition system



(b) Inner view of the data acquisition system

Figure 4-6. Measurements of ground velocities induced by artificial blasting

Two single blast holes were drilled by Eichelbergers Inc one day before the seismic monitoring and their locations are shown in Figure 4-7. The details of the blast hole locations are listed in Table 4-1. The explosive charges were installed by Pennex Powder Company in the morning before the seismic monitoring was conducted (as shown in Figure 4-8). The purpose of the two blast holes was to impart ground motion energy to the fine coal tailings in the impoundments. Each blast hole has nominal 25.4 cm diameter to depth of 12.2 m and then nominal 20.3 cm diameter to depth of 21.3 m. The drilling was done using percussion air rotary techniques. Since the blast holes were drilled in waste rock from past stripping operations, PVC pipes with outside diameter of 20.3 cm were used as casings along the entire depth to prevent the blast holes from caving in and the migration of explosives into voids. Ammonium nitrate/fuel oil (ANFO) with density of 0.85 g/cc was used as the explosive for blasting. Two-pound Pentex 908 cast boosters were placed at the top and bottom of each explosive column. The charge weight for Site 1 and 2 were 385.5 kg and 317.5 kg, respectively. The stemming height of the borehole was at least 8.5 m with 1.9 cm crushed stone.



Figure 4-7. Plan view of the blast hole locations

Table 4-1. Details of blast holes

| Site | Name | Diameter, D cm (in) | Depth, z m (ft) | Elevation m (ft) | GPS Coordinates |
|------|--------------|--------------------------|----------------------|---------------------|---------------------------------|
| 1 | Blast hole 1 | 20.3 (8) | 0.0-21.3 (0-70) | 457 (1498) | 40°58'54.90"N 75°56'16.13"W |
| 2 | Blast hole 2 | 20.3 (8) | 0.0-21.3 (0-70) | 453 (1487) | 40°58'54.90"N, 75°56'16.13"W |



Figure 4-8. A blast hole for ground motion generation during the seismic monitoring on July 6, 2017

The first (for Site 1) and second (for Site 2) blasting events occurred at 12:00 PM and 1:00 PM, respectively. At each site, the seismographs were programmed to turn on 4 minutes before the detonation. All the seismographs were retrieved after the blast events to collect the ground vibration records. Ground velocities measured using these seismographs were then used to evaluate the liquefaction potential of the coal tailings when subjected to blast events and to develop a vibration attenuation equation for the coal tailings. Figure 4-9 (a) shows a photo of the blast hole after the artificial blasting event. The deep blast hole had prevented the generation of the fly rocks. However, some cracks were formed on the ground surface due to the blast as depicted in Figure 4-9 (b). A foot was placed next to the crack to show the scale of the crack.



(a) A blast hole



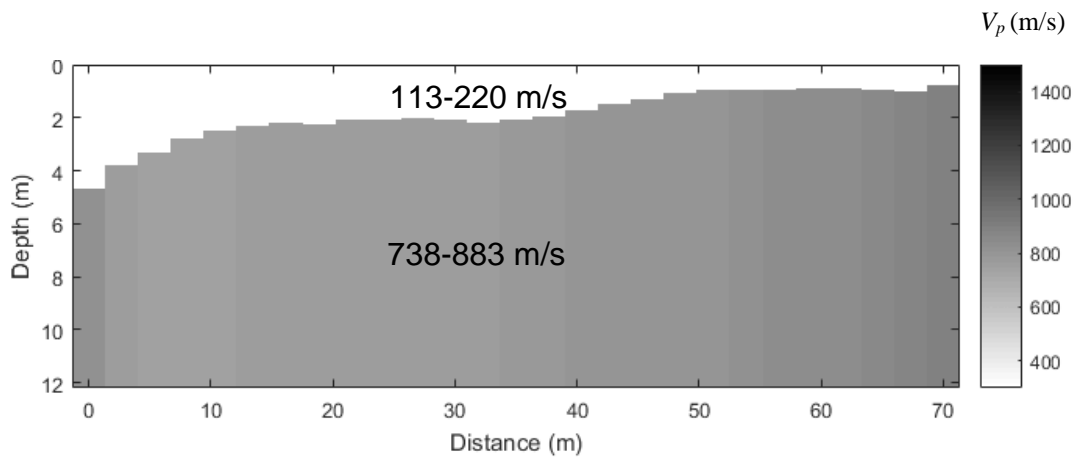
(b) Cracks formed due to blasting

Figure 4-9. Photos showing the impacts of artificial blasting

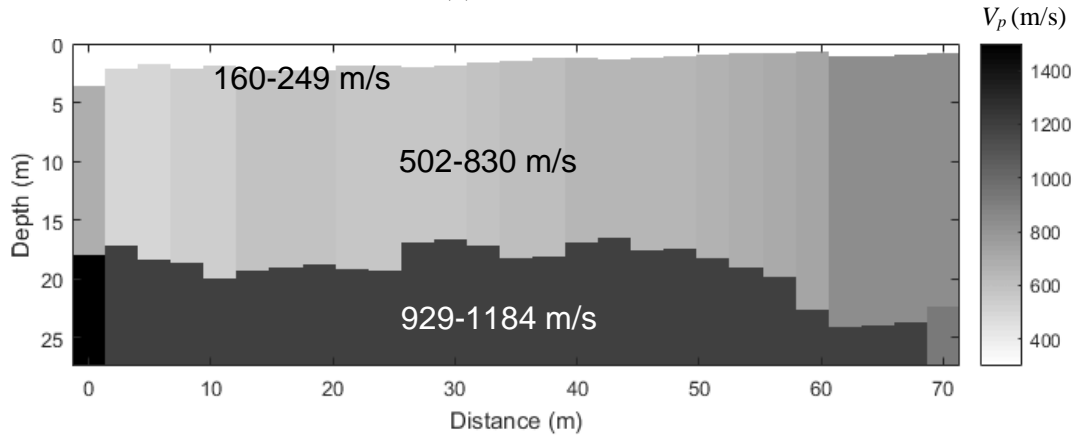
4.3 Results, Analyses, and Discussion

4.3.1 *Compressional Wave Velocity from Seismic Refraction Survey*

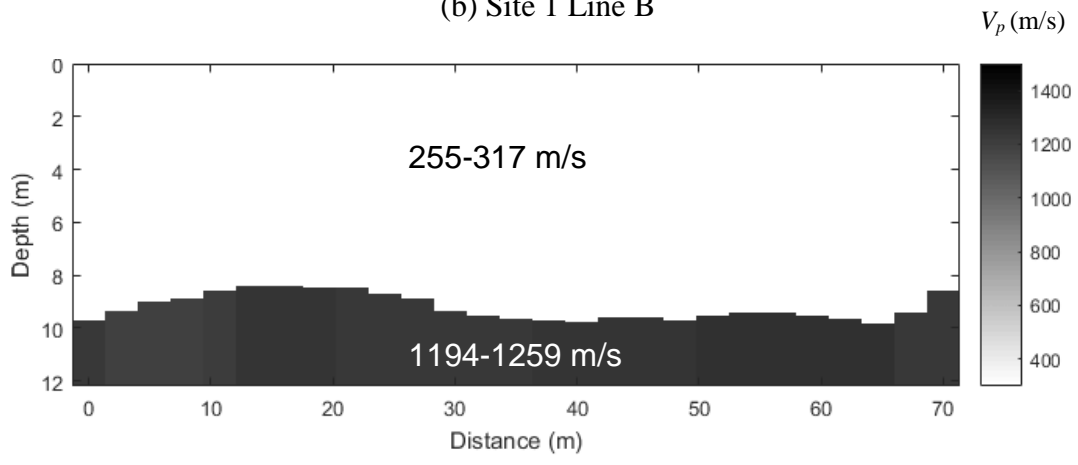
The seismogram records collected from the seismic refraction testing are reduced to derive the two-dimensional compressional wave velocity profiles of the fine coal tailings. The compressional wave velocity is a direct measure of the stiffness, hardness, and degree of compaction of the material (Kramer 1996; Khandelwal and Ranjith 2010; Ilori et al. 2013). The compressional wave velocity profiles are shown in Figure 4-10 (a-c). Based on Figure 4-10, a two-layer compressional wave velocity profile is yielded for Site 1 Line A, three-layer profile for Site 1 Line B, and two-layer profile for Site 2. The profile yielded for Site 1 Line B (30 m) is thicker than that for Site 1 Line A (12 m). Figure 4-10 (a-b) show the small variation of coal tailings strata in the same impoundment as noted by the ranges of compressional wave velocity on the profiles. Such variation may have been caused by the variation of coal slurry discharges in the multi-decade operation.



(a) Site 1 Line A



(b) Site 1 Line B



(c) Site 2

Figure 4-10. Two-dimensional compressional wave velocity profiles determined in the two coal tailings impoundments

The descriptions of the coal tailings that correspond to the ranges of compressional wave velocity are included in Table 4-2. The values in Table 4-2 are developed based on the information obtained during the seismic survey and the wave velocities of typical soils. The range of compressional wave velocity for unconsolidated fine coal tailings is based on the seismic survey conducted in this study. The range for water saturated fine coal tailings is obtained from the standard guide listed for water in ASTM D5777 (2011) and Allen et al. (1980). For the weathered and unweathered bedrocks, the values are those presented by Bourbié et al. (1987). Table 4-2 shows that the water saturated fine coal tailings layers have high compressional wave velocities. These high values of compressional wave velocities do not necessarily indicate high strength of the fine coal tailings but are due to the fully-saturated fine coal tailings. This is because water is highly incompressible, leading to high values of compressional wave velocities ($V_p > 1400$ m/s) in the layers. As shown in Figure 4-10 (c), due to the deep groundwater table at Site 2, the compressional wave velocity of the dry and unconsolidated fine coal tailings is successfully captured; the recorded compressional wave velocity ranges between 255 m/s and 317 m/s.

Table 4-2. Descriptions of the subsurface profile of the fine coal tailings impoundments

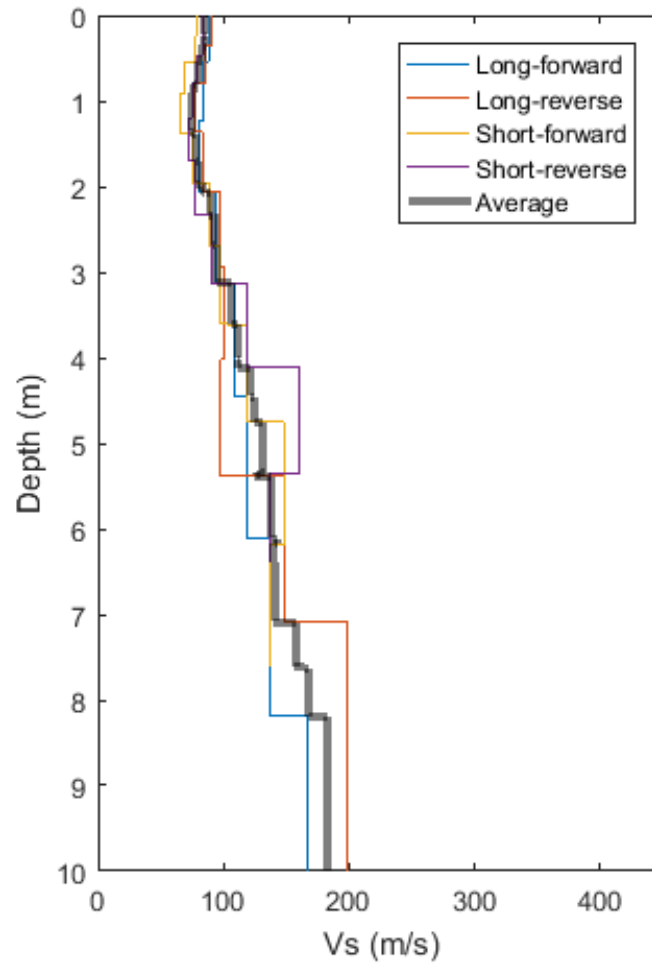
| Description of Coal Tailings | Compressional Wave Velocity, V_p (m/s) |
|------------------------------------|--|
| Unconsolidated fine coal tailings | 113-883 |
| Water saturated fine coal tailings | 1400-1665 |
| Weathered bedrock | 1500-2200 |
| Unweathered bedrock | 3500-6000 |

The depth of groundwater table determined from the field testing that was conducted concurrently in the same impoundment is compared to that estimated from the compressional wave velocity profiles. The groundwater depth was measured by lowering a tape into a borehole. Based on the field measurement, the groundwater table was at 1.1 m below the ground surface at Site 1. Although it is typically understood that the soils are fully saturated below groundwater table, the coal tailings layer (Figure 4-10 (a-b)) merely reaches the compressional wave velocity of about 830 to 883 m/s at the depth of 1.1m instead of the value of 1400 m/s. The deviation of the compressional wave velocity profiles from the measured groundwater depth may be due to the unsaturated coal tailings layer below groundwater table. This observation is further supported by the degrees of saturation of the fine coal tailings determined in the laboratory testing. As shown in Table 3-2, the saturation degrees for the samples from depths below groundwater table at Site 1 range from 73% to 94%. As a result, the range of compressional wave velocity determined in this study is lower than 1400 m/s as a 100% degree of saturation is necessary for the compressional wave velocity to reach 1400 m/s. It has been reported that soils may not be fully saturated at depths below groundwater table due to the seasonal fluctuation of the groundwater table and/or the decays of organic matters that release gasses to the voids of soils (Bonnet and Meyer 1988; Holzer and Bennett 2003; Camp III et al. 2010). These two reasons are perhaps more critical to coal tailings as the groundwater table in the impoundment may be greatly impacted by the operation status of the impoundments (i.e. either active or inactive), and the organic matters in coal tailings are

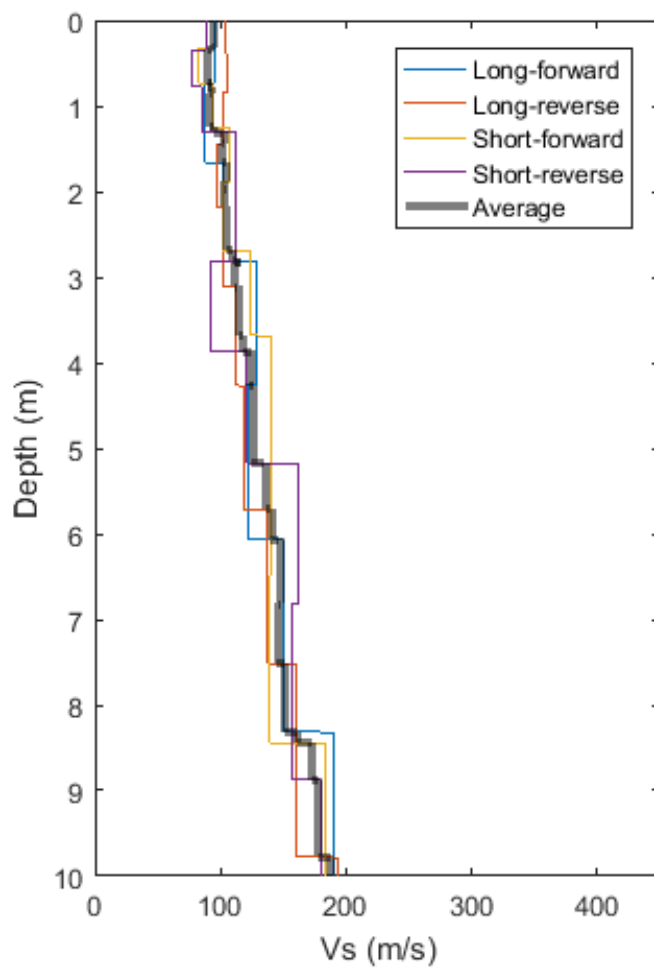
relatively higher than typical mineral soils. Research in Ottawa sands by Allen et al. (1980) shows a sharp increase in the compressional wave velocity approaching 1400 m/s only when the degree of saturation is near 100%. Compressional wave velocity can therefore be used as an indicator of the degree of saturation of the coal tailings (Naesgaard et al. 2007; Hossain et al. 2012). Since the degree of saturation greatly affects the liquefaction resistance of coal tailings, compressional wave velocity can be used to evaluate the critical zones of coal tailings susceptible to liquefaction.

4.3.2 Shear Wave Velocity from Multichannel Analysis of Shear Waves (MASW)

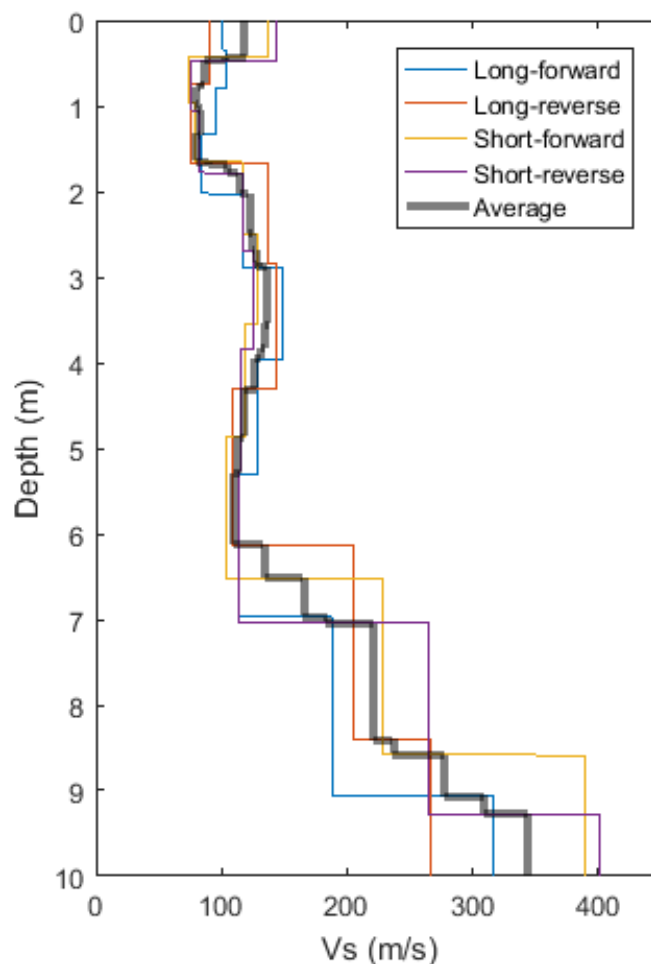
The seismogram records collected from the MASW testing are reduced to derive the one-dimensional shear wave velocity profiles of the fine coal tailings. The shear wave velocity profiles are plotted in Figure 4-11 (a-c). The seismic lines of 1.5 m spacings (long seismic lines), both forward and reverse, were deployed to obtain subsurface information of deeper depths. The seismic lines of 0.76 m spacings (short seismic lines), both forward and reverse, were deployed to obtain high-resolution subsurface information. An average shear wave velocity, V_{s_avg} , profile is determined based on four of the overlapping seismic lines (namely, long-forward, long-reverse, short-forward, and short-reverse). V_{s_avg} at a given depth is calculated by averaging four of the V_s values at that depth.



(a) Site 1 Line A



(b) Site 1 Line B



(c) Site 2

Figure 4-11. Shear wave velocity profiles determined for the coal tailings

The fine coal tailings can be classified into different seismic site classes as shown in Table 4-3 (International Code Council 2009). The profile names are slightly modified to match the context discussed in this report. Based on the ranges of shear wave velocity in Table 4-3, the two profiles in Site 1 (Figure 4-11 (a-b)) have similar trend and are interpreted as soft coal tailings at shallower depth transitioning to stiff coal tailings at deeper depth. The profile in Site 2 (Figure 4-11 (c)) is interpreted as soft coal tailings at shallower depth transitioning to stiff and then very dense coal tailings and soft rock at deeper depth.

Table 4-3. Seismic site classification of fine coal tailings (International Code Council 2009)

| Coal Tailings Profile Name | Shear Wave Velocity, V_s (m/s) | N-value |
|--|----------------------------------|---------------------|
| Soft coal tailings | <183 | $N < 15$ |
| Stiff coal tailings | 183-366 | $15 \leq N \leq 50$ |
| Very dense coal tailings and soft rock | 366-762 | $N > 50$ |
| Rock | 762-1524 | N/A |
| Hard rock | >1524 | N/A |

N-values provided by the International Code Council (2009) that correspond to various coal tailings profiles are included in Table 4-3. Based on the shear wave velocity profile for Site 2 (Figure 4-11 (c)), the fine coal tailings are considered soft above the depth of 8.5 m (based on both the long-forward and long-reverse seismic lines) and the N-value should be lower than 15 as shown in Table 4-3. The long-forward and long-reverse seismic lines were selected instead of the average seismic line because a long seismic line can provide subsurface information at deeper depths. Since a short seismic line only provides subsurface information at a higher resolution at shallower depths, the average seismic line, which has considered the short seismic lines, was not used to define the profile transitions at deeper depths. In this study, a standard penetration test (SPT) was conducted concurrently with the seismic survey at the midpoint of the seismic line at Site 2. The N-values were recorded as 2 at depth of 4.6 m and 2 at depth of 7.6 m. The N-values (N=2) recorded in SPT for soft coal tailings fall in the range of N-values (N<15) provided by the International Code Council (2009), showing that the interpretation of coal tailings strata based on the N-values was consistent with that based on the shear wave velocity profiles.

4.3.3 Determination of Poisson's Ratio, Young's Modulus, and Small-strain Shear Modulus from Compressional and Shear Wave Velocities

The Poisson's ratio, Young's modulus, and small-strain shear modulus of the fine coal tailings are derived based on the shear wave velocity profiles from the MASW testing and the compressional wave velocity profiles from the seismic refraction testing, as shown in Equations (4-1) to (4-3) (Kramer 1996).

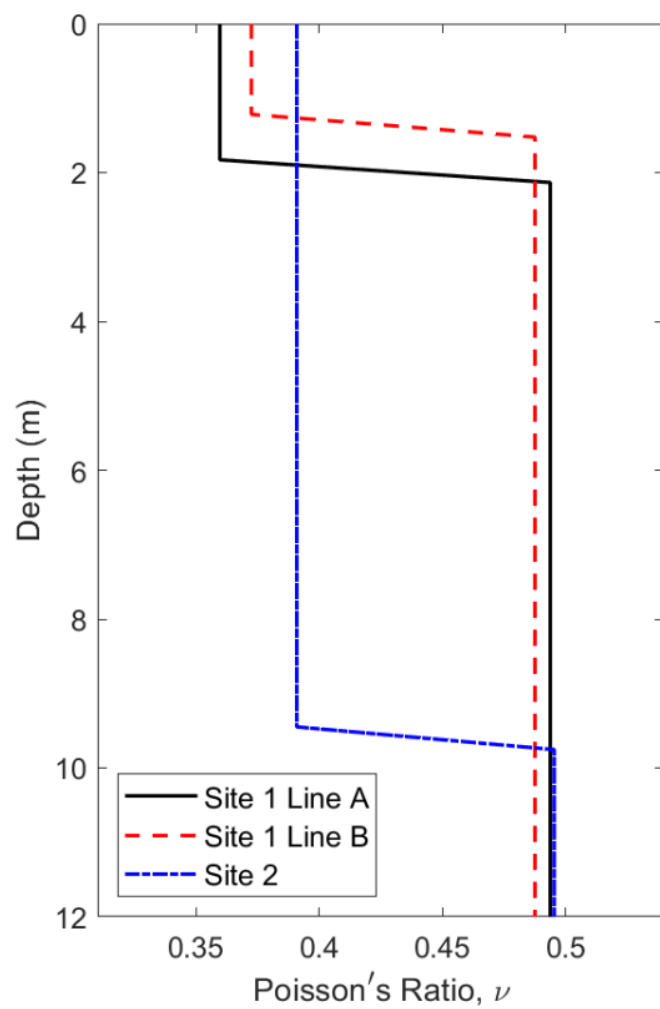
$$\text{Young's modulus, } E = \rho V_s^2 \left(\frac{3V_p^2 - 4V_s^2}{V_p^2 - V_s^2} \right) \quad (4-1)$$

$$\text{Poisson's ratio, } \nu = \frac{V_p^2 - 2V_s^2}{2(V_p^2 - V_s^2)} \quad (4-2)$$

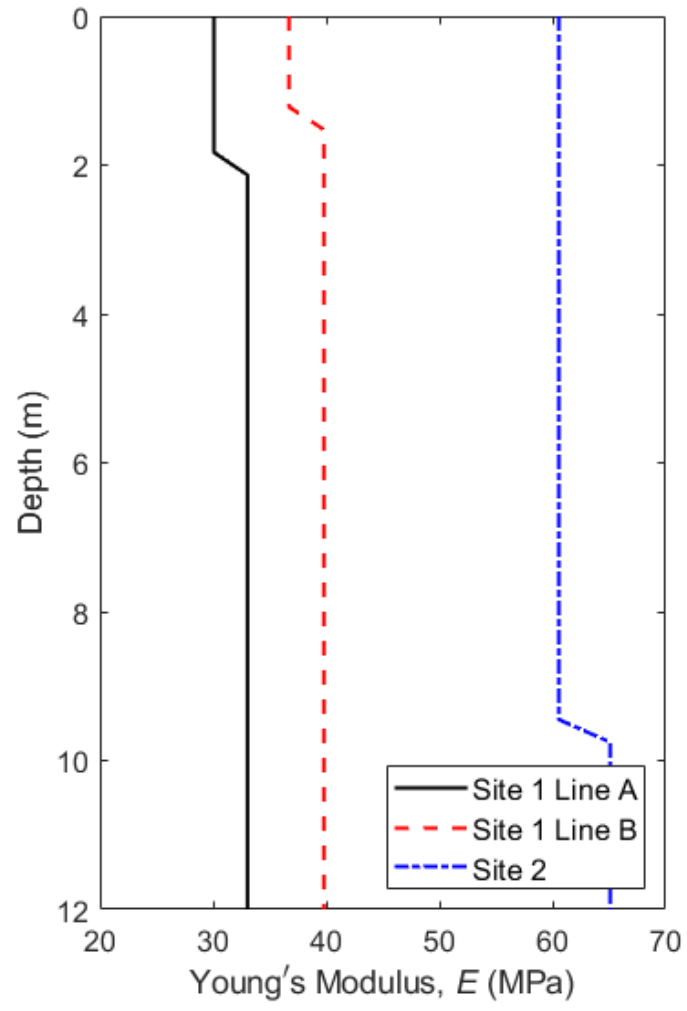
$$\text{Small - strain shear modulus, } G_{max} = \rho V_s^2 \quad (4-3)$$

where ρ is density, V_p is the compressional wave velocity, and V_s is the shear wave velocity of the fine coal tailings.

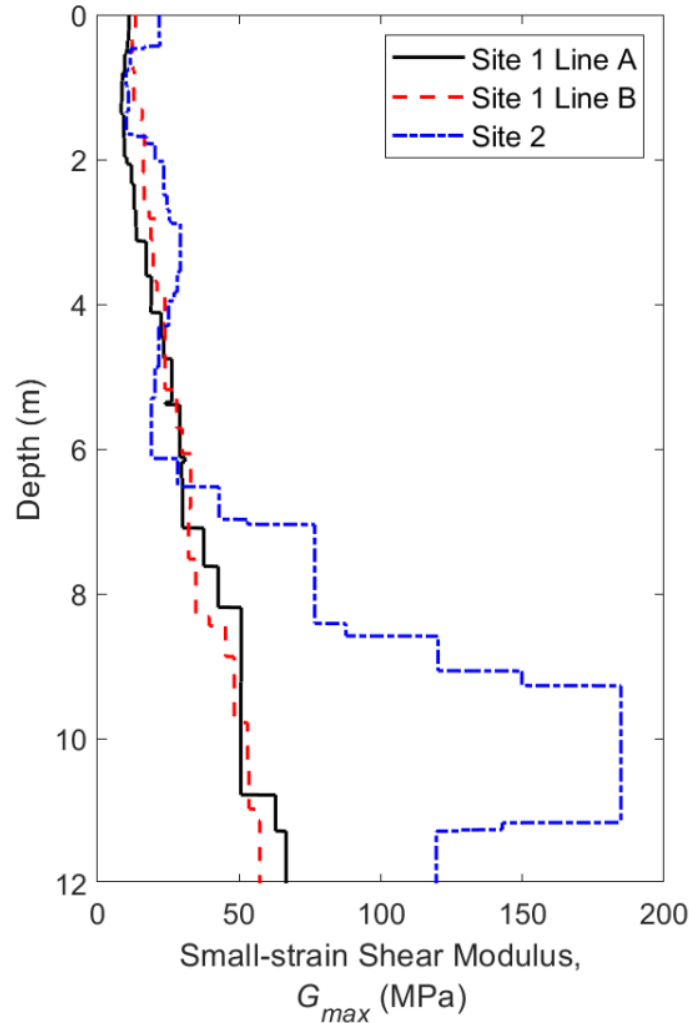
Figure 4-12 (a) shows the profile of the Poisson's ratio for all the three seismic lines, Figure 4-12 (b) for the Young's modulus, and Figure 4-12 (c) for the small-strain shear modulus. As shown in Figure 4-12 (a-c), the profiles of the Poisson's ratio, Young's modulus, and small-strain shear modulus of Site 1 Lines A and B are consistent with each other. The Poisson's ratios as shown in Figure 4-12 (a) are all in the range of 0.35 to 0.49. The Poisson's ratio of the dry and unconsolidated coal tailings is determined to be about 0.39. Based on the field measurement, the groundwater table was at the depth of 1.1 m below ground surface at Site 1 as mentioned earlier. It is reasonable that the Poisson's ratios of Site 1 (as shown in Figure 4-12 (a)) suddenly increase to 0.49 at the depth of approximately 1.5 m to 2 m as the Poisson's ratio can be assumed to be 0.5 for groundwater due to its high incompressibility. The Poisson's ratio of 0.49 can therefore be used to represent the depth of groundwater table but not necessarily the fully-saturated coal tailings layer. As presented in Figure 4-12 (b), the Young's modulus of the fine coal tailings at Site 2 is approximately twice of that of the tailings at Site 1 (i.e., 60 MPa versus 30 MPa). For the profile shown in Figure 4-12 (c), the small-strain shear modulus increases with depth continuously except for Site 2 that the small-strain shear modulus starts to decrease from the depths of 11 m to 12 m. This reduction is not considered reliable due to the deeper inversion in the final models of the MASW data and therefore it cannot be used to represent the actual field condition. Based on Figure 4-12 (c), the small-strain shear modulus of the unconsolidated coal tailings is determined to be in the range of 10 to 50 MPa.



(a) Poisson's ratio



(b) Young's modulus



(c) Small-strain shear modulus

Figure 4-12. The Poisson's ratio, Young's modulus, and small-strain shear modulus determined for the fine coal tailings along the depths

N-values recorded in the SPT are used to validate the Young's modulus derived from the compressional and shear wave velocity profiles at Site 1. The N-values are 2 at depth of 4.6 m and 2 at depth of 7.6 m at Site 1. The N-values are corrected to N_{60} , which is 1.86 and 2.08 at depths of 4.6 m and 7.6 m, respectively. The Young's modulus can be calculated as a function of N_{60} from Equation (4-4) (Coduto 2001).

$$E_s = \beta_0 \sqrt{OCR} + \beta_1 N_{60} \quad (4-4)$$

where E_s is high-strain Young's modulus, β_0 and β_1 are correlation factors, which vary for various soil types, OCR is overconsolidation ratio, and N_{60} is the SPT N-value corrected for field procedures.

Based on the results of consolidation testing that was conducted in this study, the preconsolidation stress is approximately the same as the effective stress for the coal tailings samples, resulting in OCR of 1 for the coal tailings. Since the coal tailings samples are classified as silty sand (SM) or low-plasticity silt (ML), β_0 is taken as 2500 kPa and β_1 as 600 kPa (Coduto 2001). Based on Equation (4-4), E_s is calculated to be 3.62 MPa and 3.75 MPa at depths of 4.6 m and 7.6 m, respectively. The Young's modulus estimated from Equation (4-4) is a high-strain modulus because it is derived from SPT, which is a high-strain penetration test with strain to the order of 10^{-1} (Sabatini et al. 2002). Hence, the high-strain Young's modulus, E_s , needs to be corrected to the corresponding shear strain before it can be compared to the small-strain Young's modulus, E , estimated from the seismic survey with shear strain to the order of 10^{-6} . Based on the relationship between shear modulus and shear strain that was proposed by Seed and Idriss (1970) and Idriss (1990), the reduction of shear modulus for sand when shear strain changed from 10^{-6} to 10^{-1} is approximately 94%. Sett (2010) reasoned that the relationship of Young's modulus reduction with strain followed the same relationship of shear modulus vs. shear strain. Therefore, in this paper, 94% reduction of Young's modulus is adopted when the strain increased from 10^{-6} to 10^{-1} . Using 94% reduction in modulus, high-strain E_s is corrected to small-strain E of 62.4 MPa and 64.7 MPa at depths of 4.6 m and 7.6 m, respectively. The values were consistent with the Young's modulus of 60 MPa estimated from the seismic survey for Site 2. The values of Young's modulus from SPT and seismic survey at Site 1 were not compared because the SPT location did not overlap with the seismic lines at Site 1. The SPT was carried out at the center of the impoundment as shown in Figure 2-8, whereas the seismic lines were spread north and south of the midline of the impoundment as shown in Figure 4-1(a) due to the existence of ponded water during the field testing.

4.3.4 Peak Particle Velocity and Vibration Attenuation Equation

Peak particle velocity (*PPV*) can be used to evaluate the ground acceleration induced by either blasting or earthquake motion. Although the attenuation equations are site specific, past research has developed general equations that can be used in various blasting applications (ISEE 2011). Though the equations have been developed for coal mines, construction sites, and quarries, there is no general attenuation equation that has been developed for coal tailings. A general equation is needed for coal tailings specifically to evaluate the liquefaction potential of coal tailings impoundments.

Ground motions in the fine coal tailings were induced by blasting near the impoundments and recorded by seismographs. A total of 30 seismographs were deployed in the impoundments but only 28 data points of peak particle velocity were collected as two other seismographs experienced malfunction. The *PPV* is plotted against the scaled distance (*SD*), as shown in Figure 4-13. The *SD* is calculated as a function of the distance (*D*) between the blast location and the point of interest, and the charge weight (*W*) as presented in Equation (4-5). The square-root scaling is used for *W* since the charges used in this study are cylindrical (Kumar et al. 2013). The *PPV* is inversely proportional to the *SD* and the relationship is described through the power law as

presented in Equation (4-6). The intercept, a , is a curve fitting coefficient that is related to the degree of confinement, rock strength, and explosive parameters, and the slope, b , represents the attenuation rate of vibration based on geologic conditions (ISEE 2011).

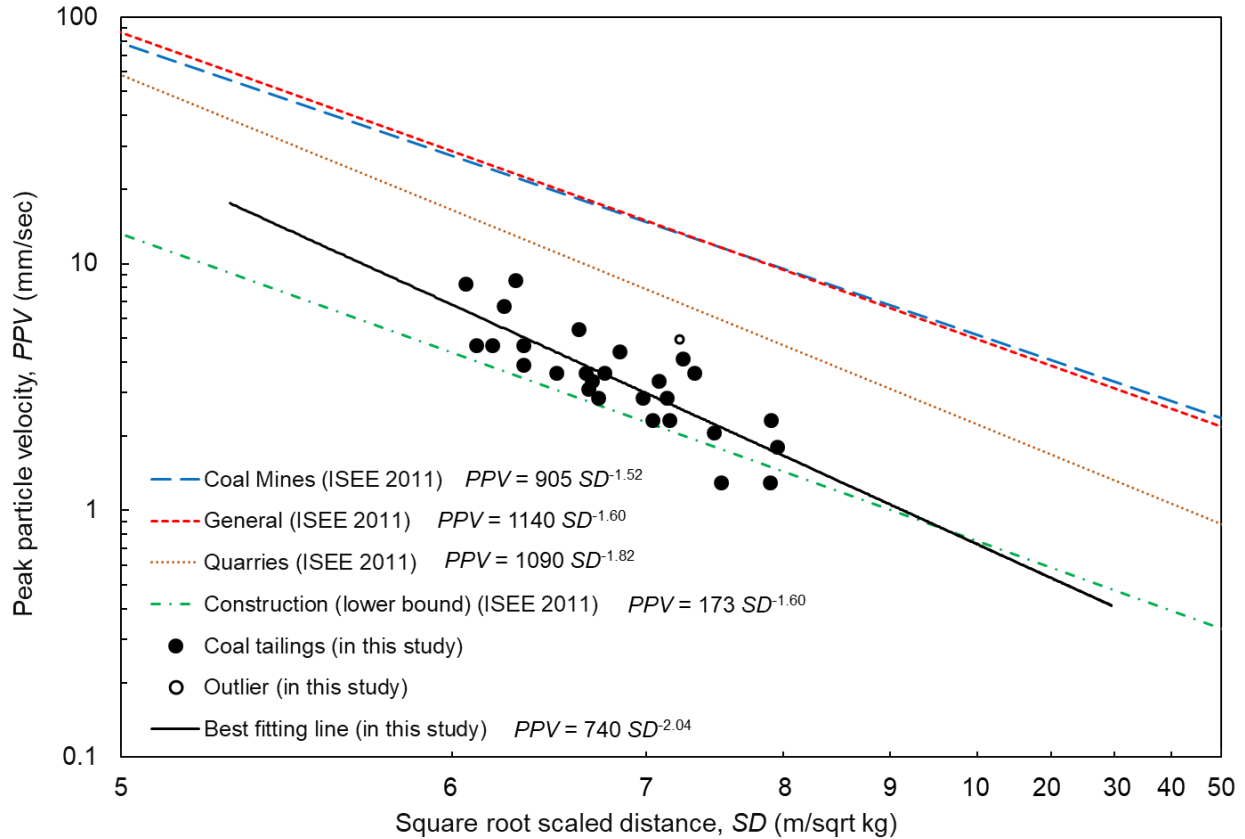


Figure 4-13. *PPV* prediction equation for fine coal tailings and its comparisons with other general attenuation equations by ISEE (2011)

$$SD = \frac{D}{\sqrt{W}} \quad (4-5)$$

$$PPV = a \times SD^b \quad (4-6)$$

The 28 datapoints are statistically analyzed. The fit and diagnosis test infers that there is an unusual and influential data point, which is plotted as an empty circle in Figure 4-13. The removal of this outlier improves 6% of the coefficient of determination, R^2 , from 0.63 to 0.69. An equation is then developed and fitted for the coal tailings. As presented in Equation (4-7), a is determined to be 740 and b is -2.04. Though R^2 of at least 0.70 is typically recommended by ISEE (2011) in developing the vibration attenuation equations, the prediction equation with R^2 of 0.69 could still be used to provide rough estimations of *PPV*, considering that the sample size, n , is small ($n < 30$). A larger sample size may improve R^2 . However, the P-value estimated for this

dataset is less than 0.001, indicating that there is a statistical evidence showing that the logarithm of PPV and logarithm of SD are linearly associated at the significance level of 0.01.

$$PPV = 740 SD^{-2.04} \quad (4-7)$$

The attenuation equation developed in this study is then compared to the general equations developed for various mining sites as depicted in Figure 4-13. The slope of the best fit line for the site with coal tailings is the highest among all, indicating that the vibration attenuation rate is the highest for coal tailings. Since the attenuation rate is based on the site conditions, the slurry-like coal tailings are believed to be responsible for the high rate of attenuation. However, the attenuation equation is based on SD values ranging from 6 to 8 m/sqrt kg; its application to higher SD values (10 to 100 m/sqrt kg) needs to be verified.

4.3.5 Liquefaction Resistance of Coal Tailings

The liquefaction resistance of the coal tailings is evaluated from the shear wave velocity profiles based on the simplified procedure presented by Andrus and Stokoe (2000). While this simplified procedure is typically used for evaluating the liquefaction resistance of soils against earthquake loads, it can be adapted and utilized for loads induced by bench blasting, which consists of a series of detonation. The cyclic stress ratio (CSR) of an earthquake load is commonly calculated as 65% of the peak horizontal ground surface acceleration, a_{max} (Andrus and Stokoe 2000). However, it is reasonable to use 100% of the a_{max} to calculate the CSR of bench blasting. This is because the delay time between holes for the bench blasting is typically within a few milliseconds, resulting in a stress loading that approximates a sinusoidal function with a_{max} as the amplitude. In the case of a single detonation, it is assumed that 65% of a_{max} can still be used. The a_{max} can be estimated from Equation (4-8) (ISEE 2011) using the PPV measured in the field or that predicted by the vibration attenuation equation as shown in Equation (4-7).

$$a_{max} = \frac{2\pi f PPV}{9810} \quad (4-8)$$

After calculating a_{max} , the CSR is estimated using Equations (4-9) for the factor of safety of coal tailings against liquefaction due to mine blasting. The shear stress reduction coefficient, r_d , can be estimated from the chart by Idriss (1999). The total vertical stress, σ_v , and vertical effective stress, σ'_v , can be calculated from the unit weight of coal tailings and the depth of groundwater table. The depth of groundwater table can be estimated from the Poisson's ratio if seismic surveys were carried out instead of drilling. The moist unit weight of coal tailings is taken as 15.0 ± 1.1 kN/m³ based on the laboratory results from this study.

$$CSR = 1.0 \left(\frac{a_{max}}{g} \right) \left(\frac{\sigma_v}{\sigma'_v} \right) r_d \quad (4-9)$$

To estimate the cyclic resistance ratio, CRR , of coal tailings, the shear wave velocity, V_s , is first corrected to account for the overburden stress. The corrected shear wave velocity, V_{sI} , and the magnitude scaling factor, MSF , are then used to calculate CRR using Equation (4-10) (Andrus and Stokoe 2000). V_{sI}^* , which serves as an upper limit of V_{sI} for the liquefiable coal tailings, is

correlated with the amount of fines content, FC , in the coal tailings. The coal tailings with V_{s1} greater than 200 m/s is assumed to be non-liquefiable (Andrus and Stokoe 2000). In the mining industry, the total amount of explosives used in the entire blast is typically less than 100,000 kg, hence the earthquake magnitude in Richter scale (M_L) is less than 5.0 (Arkansas Geological Survey 2015). At low earthquake magnitudes, the Richter magnitude scale (M_L) is consistent with the moment magnitude scale (M_w) (Kramer 1996). Hence, the MSF was taken as 1.82 as the M_w is less than 5.2 (Idriss 1999).

$$CRR = \left\{ a \left(\frac{V_{s1}}{100} \right)^2 + b \left(\frac{1}{V_{s1}^* - V_{s1}} - \frac{1}{V_{s1}^*} \right) \right\} MSF \quad (4-10)$$

The factor of safety, FS , for the coal tailings to resist liquefaction is then evaluated as the ratio of CRR to CSR as shown in Equation (4-11).

$$FS = \frac{CRR}{CSR} \quad (4-11)$$

Based on the simplified procedure, the CRR and the FS for the coal tailings to resist liquefaction due to vibrations from bench blasting are calculated and plotted in Figure 4-14 (a) and 4-14 (b), respectively. As depicted in Figure 4-14 (a), the resistance of the coal tailings against cyclic liquefaction increases with increasing depth. The data points are plotted in circular (Line A) and triangular (Line B) markers for Site 1 and square markers for Site 2. The trend of increasing resistance is more obvious for the coal tailings at Site 1. However, for Site 2, the cyclic resistance ratio also increases with depth but starts to decrease at depth of 4 m. In the regression analyses, given the null hypotheses that the slopes are equal to zero, the P-values determined for the plots in Figure 4-14 (a) and 4-14 (b) are both less than 0.001, concluding that CRR and FS are linearly associated with the depth at the significance level of 0.01 despite of high variability in the plots.

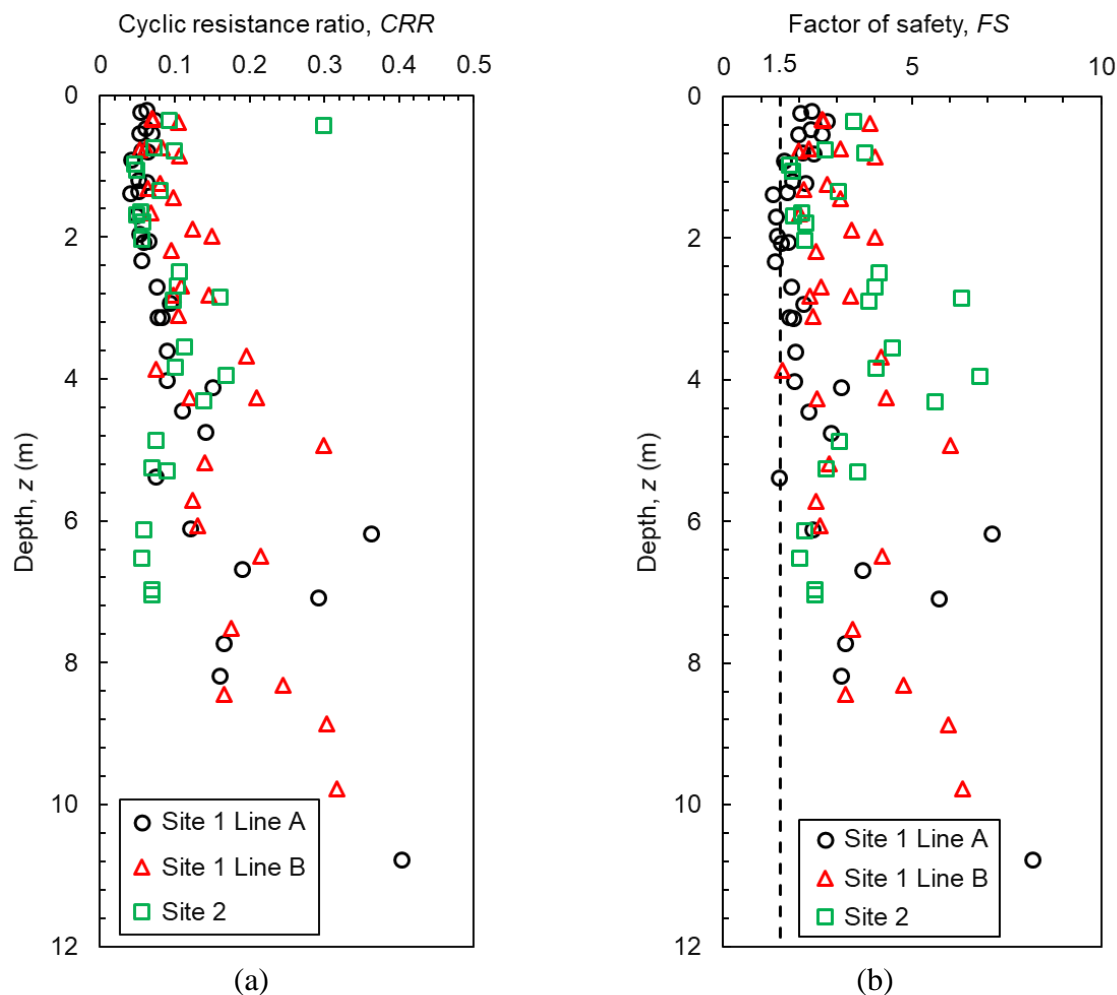


Figure 4-14. Plots of (a) the calculated CRR and (b) the FS of the coal tailings upon blast loading, and the CSR is based on Equation (4-9)

Based on Figure 4-14 (b), where 100% of a_{max} is used in calculating FS , the lower bound of the calculated FS fall under FS of 1.5 (i.e. a typical design factor for liquefaction), indicating that the coal tailings are prone to liquefaction hazards during bench blasting. Taking account that the blasting loads in this study are lower than that typically induced during mine blasting, the coal tailings are likely to be subjected to liquefaction or loss of shear strength upon strong blasting events.

The CRR is plotted against the percentage of FC in the coal tailings as shown in Figure 4-15. Every CRR data point in Figure 4-15 represents the average value that is computed from all CRR values for a specific percentage of FC at a specific depth range. As the percentage of FC increases, the CRR in the depth group larger than 4 m tends to increase. A more drastic increase of CRR at depth deeper than 8 m is observed.

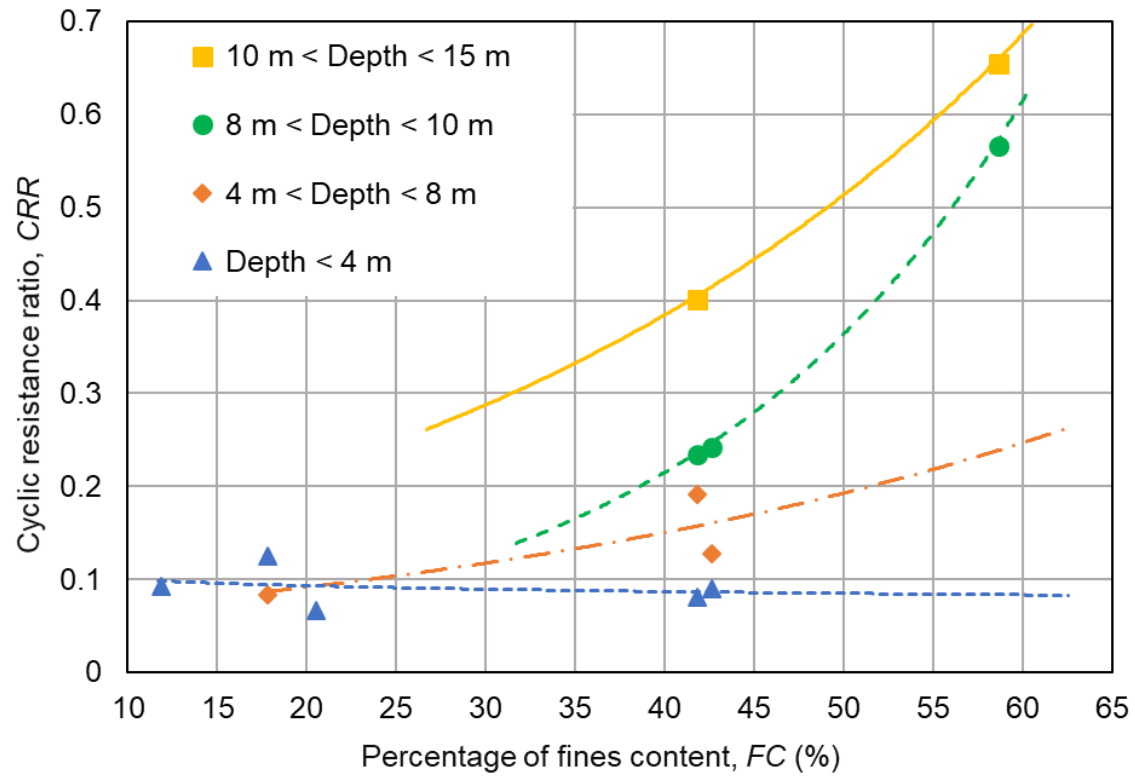


Figure 4-15. CRR of the coal tailings over a wide range of percentages of FC

CHAPTER 5. NUMERICAL MODEL

This chapter presents the numerical modeling and use of PM4Silt plasticity model to capture the liquefaction behavior and seismic stability of an upstream impoundment.

5.1 Geotechnical Properties and Model Generation

Construction of upstream coal slurry impoundments is usually started with a starter dam that underlies the proceeding dikes, which are constructed over time to retain deposited coal slurry behind the impoundment. Therefore, a coal slurry impoundment mainly consists of three sections: coal slurry, dikes, and starter dam all underlain by bedrock as shown in Figure 5-1. Table 5-1 shows the basic geotechnical properties used in numerical modeling in Fast Lagrangian Analysis of Continua (FLAC) commercial software.

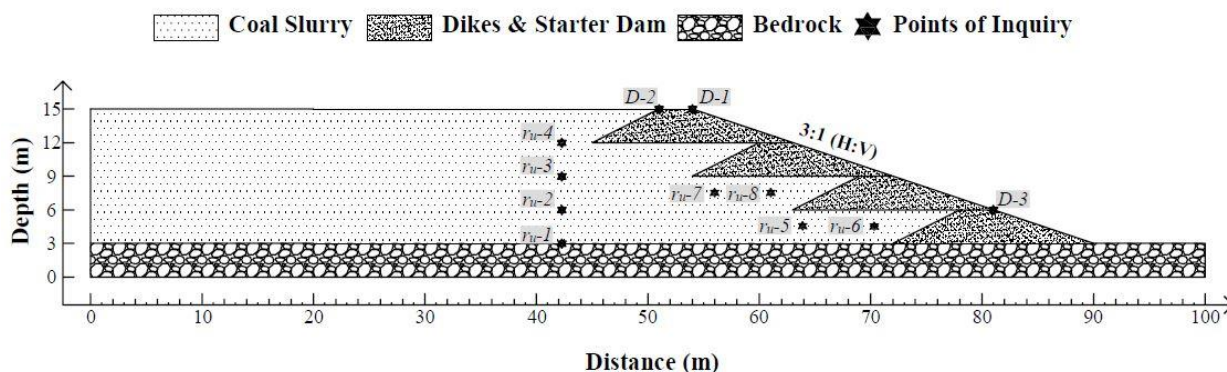


Figure 5-1 Upstream construction of tailings dam (model configuration)

Table 5-1 Geotechnical properties of the impoundment sections

| Material | Coal Slurry | Dikes | Starter Dam | Bedrock |
|------------------------------|-------------|---------|-------------|---------|
| Density (kg/m ³) | 1190 | 1700 | 1700 | 2400 |
| Bulk Modulus (Pa) | 3.6e7 | 4.5e8 | 4.5e8 | 2.9e10 |
| Shear Modulus (Pa) | 1.2e7 | 2.1e8 | 2.1e8 | 1.3e10 |
| Cohesion (kPa) | 21 | 10 / 7 | 10 / 7 | - |
| Friction Angle (°) | 30 | 35 / 32 | 35 / 32 | - |

The properties of coal slurry, shown in Table 5-1, were adopted from Salam et al. (2019). Although coal slurry is typically found stratified in both horizontal and vertical direction in impoundments, a homogenous medium was assumed for coal slurry in this study. The reason was that the available plasticity models are not able to properly address the localized loosening and water film phenomenon in layered material (Ziotopoulou and Boulanger 2015). However, the associated shortcoming with the assumption was minimized by assigning the properties of coal slurry located in the vicinity of the dikes to the coal slurry in the simulated model. The seismic

response of the region behind the dike in the main interest in stability analysis, as the failure plane is formed in that region. Therefore, the system behavior can be assumed to be close to field condition. The dikes, starter dam, and bedrock properties were adopted from the studies, in which the cyclic behavior and seismic stability of coal tailings impoundments were evaluated (Byrne and Seid-Karbasi 2003; Zeng et al. 2008; Ferdosi et al. 2015). Two different sets of shear strength properties (i.e. $c' = 10 \text{ kPa}$, $\phi' = 35^\circ$ and $c' = 7 \text{ kPa}$, $\phi' = 32^\circ$) were assigned to the dikes and the started dams representing strong and weak material, respectively.

The common geometry of upstream construction was generated in FLAC^{2D}, as shown in Figure 5-1. The model was 100 m long and 15 m tall including four different types of materials. The simulated coal slurry impoundment consisted of three dikes underlain by a starter dam, each was 3 m high. The slope of the impoundment was 3:1 (H:V) and plane strain condition was assumed to be valid. The bottom boundary was fixed by fixing the nodes in both horizontal and vertical directions, and the side boundaries were also fixed in horizontal direction. Free-field boundary condition was defined during dynamic analysis. The dikes and expected failure zone were kept sufficiently far from the boundaries to minimize the influence of boundaries on the response. Only the coal slurry was considered liquefiable, while a 10 meter wide zone at the left end of coal slurry was considered non-liquefiable to avoid inaccurate free-field boundary calculations on the left side, as recommended by FLAC manual (Itasca 2016). The element size was kept small enough to satisfy proper wave transmission through the model. According to the Lysmer's criteria the largest element dimension was limited to 1 meter to ensure correct wave transmission (Itasca 2016). The pore pressure was also established through the model such that the coal slurry was assumed to be fully saturated and the toe of the dam was the drainage zone.

5.2 Cyclic DSS Tests

Besides the basic geotechnical properties of the materials, the cyclic behavior of coal slurry was characterized in order to calibrate the plasticity models. Therefore, cyclic DSS tests were conducted on the coal slurry samples. Several cyclic DSS tests were conducted on reconstituted coal slurry samples retrieved from the vicinity of a discharge point in a coal slurry impoundment in an Appalachian coalfield, USA. The samples represented the coal slurry behind dikes in the impoundment. The cyclic DSS test was chosen over other laboratory experiments, as the rotation of principal stresses during cyclic loading is better simulated. Although testing undisturbed samples was not possible, slurry deposition method proposed by Kuerbis and Vaid (1988) was employed to prepare coal slurry samples resembling fabric and structure of hydraulically deposited coal slurry in the field. The other advantage of slurry deposition method compared to other reconstitution methods such as dry and wet pluviation is that the segregation of sand and silt particles, which might result in water film phenomenon during loading, is properly prevented (Carraro and Prezzi 2007). The cyclic resistance of coal slurry, in terms of CSR-N curve, was established for the void ratio of 0.6~0.7. The details of sample preparation and testing approach were presented in Chapter 3.

5.3 PM4Silt Plasticity Model Calibration

PM4Silt model requires three primary input parameters as contraction rate parameter (h_{po}), which estimates the plastic volumetric strain rate, shear modulus coefficient (G_0), and undrained shear strength at critical state under earthquake loading ($S_{u,cs,eq}$). Contraction rate parameter is a soil specific input parameter that should be calibrated based on CSR-N curve of the material through laboratory testing. The remaining primary input parameters, G_0 and $S_{u,cs,eq}$, are determined by either empirical equations or in-situ and laboratory tests.

In addition to the primary input parameters, there are twenty secondary input parameters defined in PM4Silt model. The secondary input parameters have default values unless they are assigned different values by user if there are available laboratory or field data. The calibration of the contraction rate parameter for PM4Silt was conducted by using the single element simulation code provided by Boulanger and Ziotopoulou (2013, 2018). The primary input parameters and the adjusted secondary parameters used to approximate the cyclic response of coal slurry by PM4Silt are shown in Table 5-2. Comprehensive cyclic coal slurry properties were presented in Salam et al. (2019). Three secondary parameters were modified in order to better represent the coal slurry samples used in the cyclic DSS tests. They are initial void ratio (e_0), constant volume effective friction angle ($\phi_{cv'}$), and a parameter that regulates the undrained shear strength exceedance potential ($n^{b,wet}$). Initial void ratio and constant volume friction angle were obtained from Salam et al. (2019).

Table 5-2 PM4Silt input parameters

| Model | PM4Silt | |
|----------------------------|---------------|--------|
| Primary Input Parameters | $S_{u,cs,eq}$ | 15 kPa |
| | G_0 | 394 |
| | h_{po} | 0.5 |
| Secondary Input Parameters | e_0 | 0.67 |
| | $\phi_{cv'}$ | 30° |
| | $n^{b,wet}$ | 0.03 |

The CSR-N curve can be numerically established by PM4Silt approximating the experimental CSR-N curve. The calibration processes of PM4Silt is presented in the manual by Boulanger and Ziotopoulou (2018). Figure 5-2 shows the experimental and simulated CSR-N curves. The CSR-N curve on log-scale can be expressed by $CSR = a \times (N_{failure})^{-b}$, where $N_{failure}$ was defined as 5% double amplitude strain (DAS) in cyclic DSS tests. The corresponding equation of each line is also shown in Figure 5-2. The estimated b -value in the PM4Silt simulations is 0.2, while the b -value from the cyclic DSS results is 0.17. Moreover, the difference between experiment and simulation was more pronounced at higher CSR (i.e. CSR=0.15). Considering the slope, the b -values, and the cyclic DSS results, PM4Silt appeared to sufficiently approximate the liquefaction resistance of coal slurry. However, to further investigate the applicability of PM4Silt

in approximating the cyclic response of coal slurry, the shear stress-strain loops and pore pressure ratio from experiment and simulation were compared.

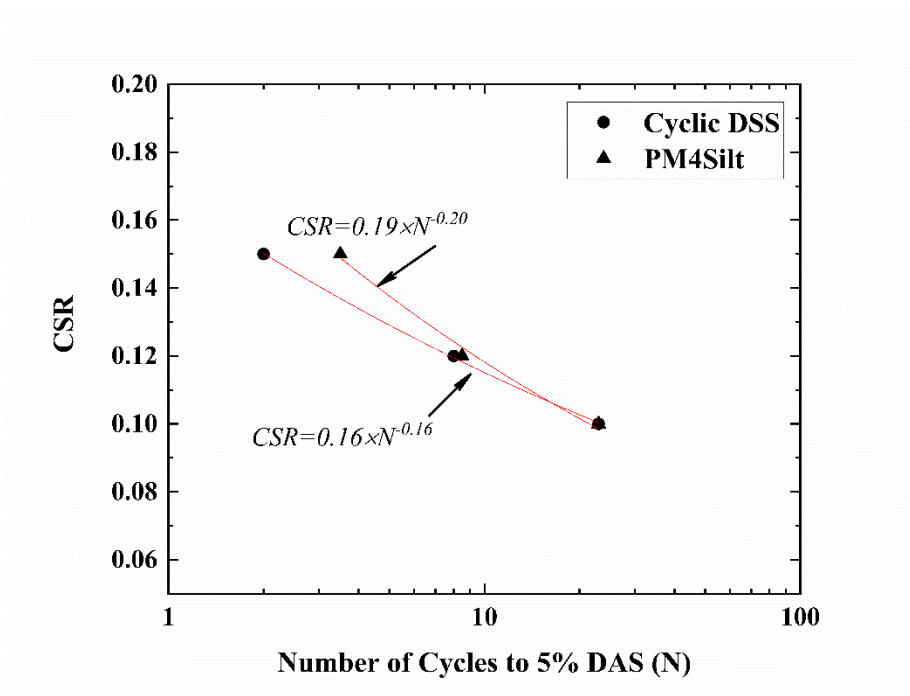


Figure 5-2 Cyclic stress ratio versus number of cycles to 5% double amplitude strain

The approximated stress-strain loops by PM4Silt against the observed loops in cyclic DSS tests for the CSR of 0.12 are presented in Figure 5-3. In addition, the pore pressure ratio (r_u) is shown for PM4Silt along with r_u observed in cyclic DSS tests for the coal slurry sample in Figure 5-4. According to Figure 5-3, the plastic behavior of the coal slurry and the wide shear stress-strain loops could be approximated by PM4Silt. PM4Silt model also estimated the 5% DAS occurrence at comparable number of cycles (i.e. $N=9$). The soil element simulated by PM4Silt experienced progressive and gradual accumulation of shear strain until failure. Close agreement was also observed in the results of pore pressure ratio by PMSilt and cyclic DSS, as the final r_u was approximated 0.7~0.8 from both approaches: cyclic DSS testing and PM4Silt, see Figure 5-4.

Although close approximation of cyclic DSS test results was achieved with PM4Silt, it was of interest to capture the applicability and performance of PM4Silt plasticity model in numerical investigation of a large scale model configuration such as coal slurry impoundment, as coal slurry is composed of sand and silt.

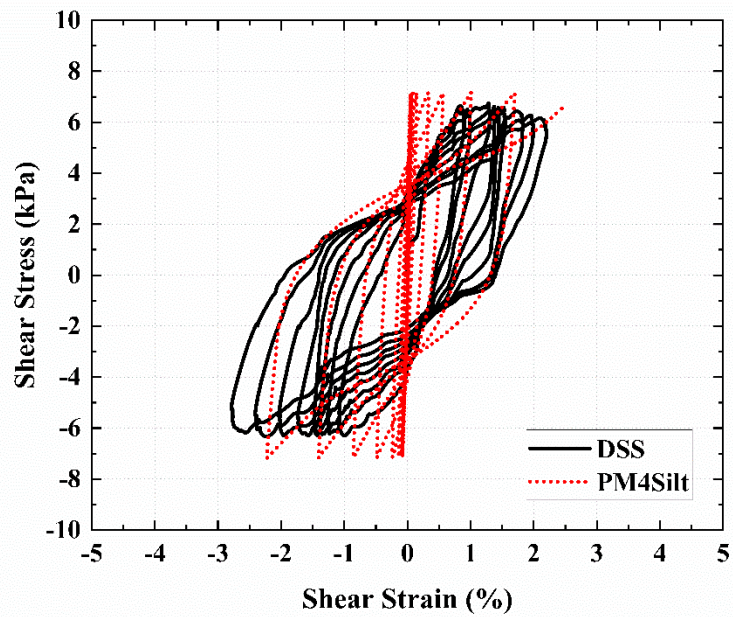


Figure 5-3 Shear stress-strain loops from cyclic DSS and PM4Silt

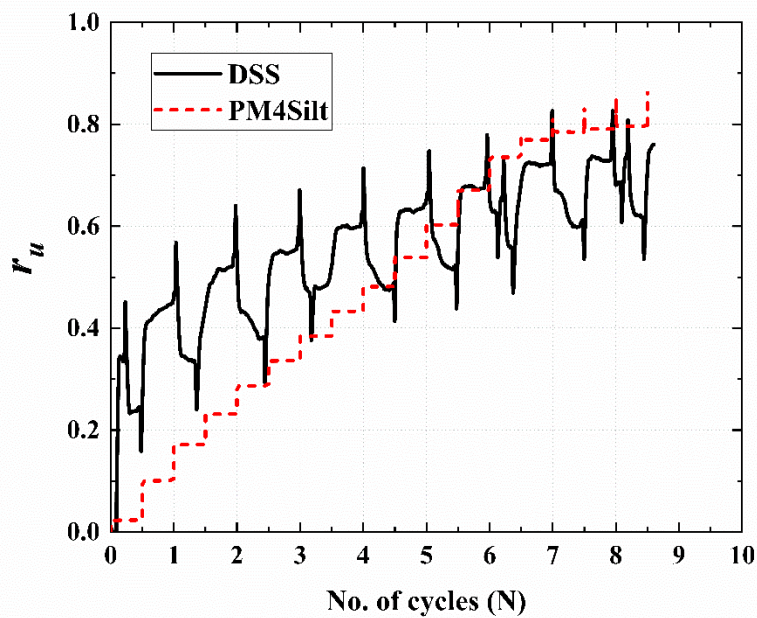


Figure 5-4 Pore pressure ratio from cyclic DSS and PM4Silt

5.4 Dynamic Input Motions

The numerical analysis of slurry impoundment was divided into two stages: 1) static simulation and 2) dynamic simulation. The impoundment model was first constructed by assigning elastic-plastic parameters to the bedrock and the Mohr-Coulomb model parameter to the starter dam, dikes, and coal slurry. These parameters are listed in Table 5-1. Then, the mechanical (stress-strain) and hydro-mechanical (pore water pressure) equilibriums were achieved, and the static stability of the impoundment was assessed. The safety factor for slope stability of the studied upstream impoundment under static condition was found to be 1.88.

In the Stage 2, the seismic stability and performance of coal slurry impoundments under seismic (e.g. an earthquake) and co-seismic (e.g. blast) events were of great interest. In order to assess the behavior of upstream impoundments, which are considered the least stable design in practice, two different input motions representing an earthquake and blast events were selected. Earthquake and blast are different in terms of frequency, duration, induced displacement, and kinetic energy. Mining blasting acceleration history typically has short duration with a high frequency waveform, while an earthquake can last up to minutes and acceleration amplitude is noticeably greater.

An earthquake input motion with peak ground acceleration (PGA) of 0.24g, peak ground velocity (PGV) of 0.092 m/s, and duration of 20 seconds was selected for the upstream impoundment seismic analysis, see Figure 5-5 (a). The dominant frequencies of acceleration and velocity input were found to be 1.6 Hz and 1.0 Hz, respectively, using Fast Fourier Transform (FFT) analysis. A relatively strong and representative blast event that was used in coal mine blasting was also adopted as blast input motion. The peak particle velocity (PPV), which is commonly used to characterize blast intensity, and peak ground acceleration (PGA) were 0.022 m/s and 0.24g, respectively. The motion lasted for 5 seconds, see Figure 5-5 (b). Although the PPV and duration are considerably lower compared to the earthquake motion, the dominant frequency of blast input velocity was 11.2 Hz, which is significantly higher than that of earthquake. The scaled peak acceleration (i.e. $0.65a_{max}$) 0.15g for blast and earthquake, respectively. The input motions of earthquake and blast were separately imposed to the bottom of the model. Pore pressure ratio (r_u) and displacement (D) were monitored and recorded at selected points of interests as shown in Figure 5-1.

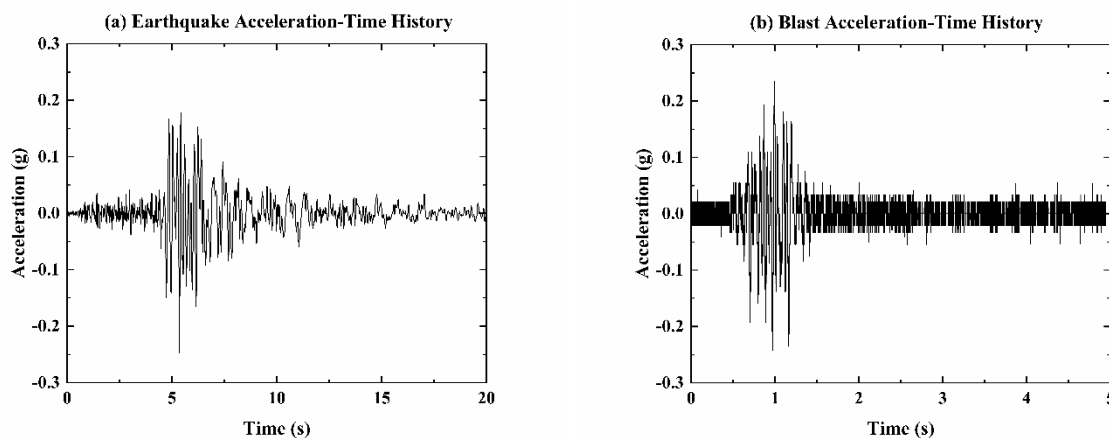


Figure 5-5 Model input motions (a) Earthquake (b) Blast

5.5 Results and Discussion

5.5.1 Shear Bands and Strain Contours

The general performance of the upstream impoundment under an earthquake and blast input motions in terms of shear strain was of great interest. Figure 5-6 shows the shear strain distributions of the tailings dam under earthquake seismic loading for two cases of strong and weak dikes using PM4Silt model. The figure shows the largest shear strain is mobilized approximately from the crest and extends to the top of the starter dam, when dikes have strong shear strength properties. The sliding plane passed through the bottom of starter dam, when weak dikes properties considered. PM4Silt distinctly showed a sliding plane, where developed shear strain was larger than 5%, as shown in Figure 5-6. The maximum shear strain developed during the earthquake were 0.16% and 0.18% in case of strong and weak dikes, respectively.

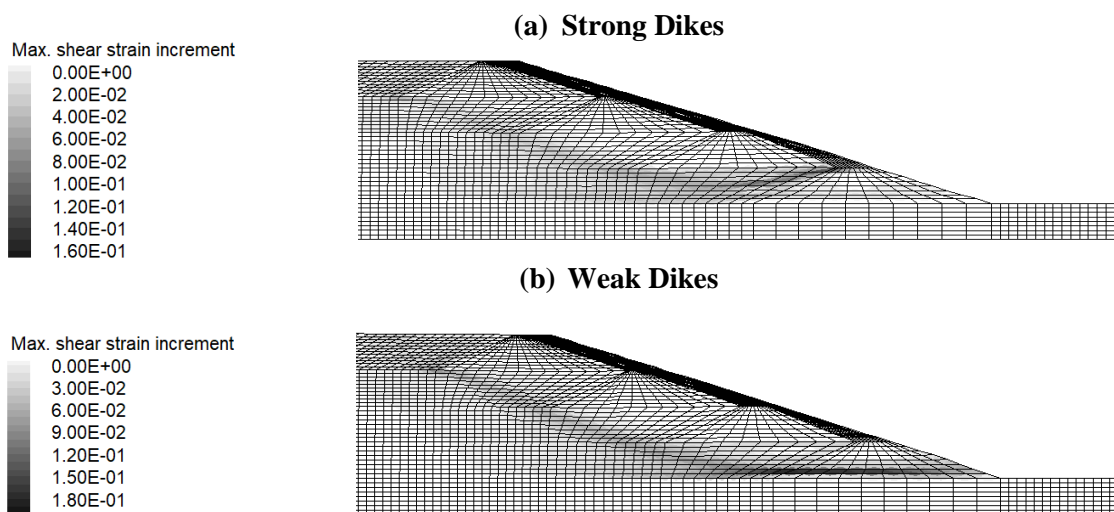


Figure 5-6 Estimated shear strain due to earthquake for strong and weak dikes

According to Figure 5-7, PM4Silt approximated fairly similar pattern of shear strain distribution under blast loading; and the maximum shear strains predicted for strong and weak dikes were relatively close, i.e., 0.01%. In general, the shear strains developed during the earthquake were almost ten times larger than those during the blast. In order to further investigate the seismic performance and stability of the impoundment, the pore pressure ratio (r_u) and displacement (D) at several points of interest as shown in Figure 5-1 are discussed.

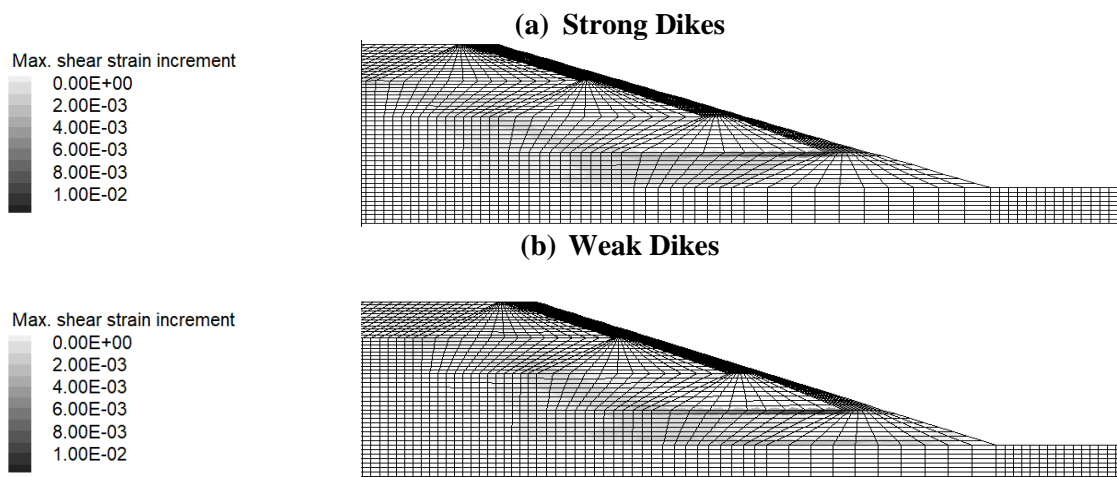
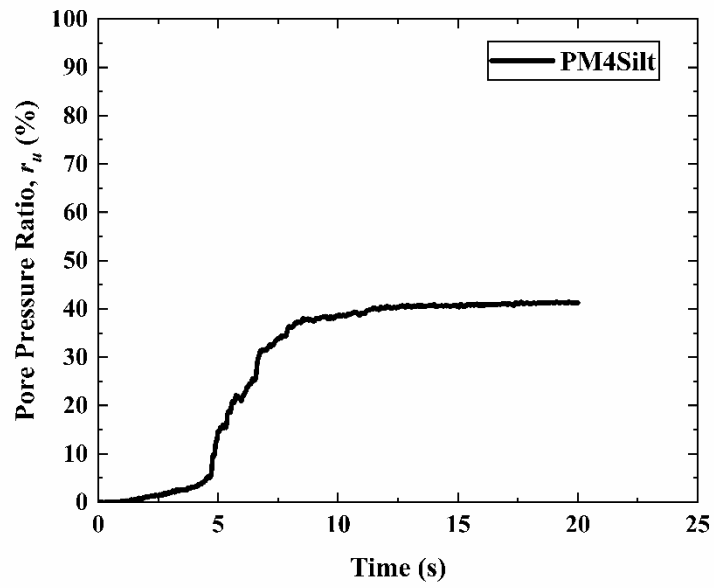
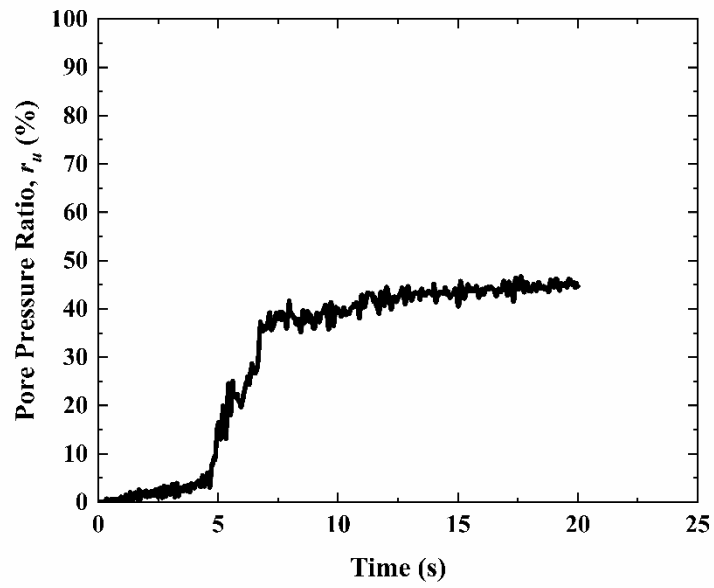


Figure 5-7 Estimated shear strain due to blast for strong and weak dikes

5.5.2 Pore Pressure Ratio

Pore pressure ratio (r_u) has been traditionally considered as a criterion for the occurrence of liquefaction. Accordingly, when r_u is 100%, which means that excess pore pressure has reached the initial effective stress, soil is considered fully liquefied. The pore pressure ratio at different depths at relatively far distance from the dikes were calculated and shown for four cases in Figure 5-8 to Figure 5-11 PM4Silt constitutive plasticity model. The points of interest are marked as r_u-1 to r_u-4 in Figure 5-1 and are located at 12, 9, 6, and 3 m below the surface, respectively. Figure 5-8 (a) through (d) depict the resulting pore pressure ratios due to the earthquake event on the impoundment with strong dikes, while Figure 5-9 (a) through (d) display those for the impoundment with weak dikes. The pore pressure ratio developed at the far distance from the dikes during the earthquake was not noticeably affected by strength of the dikes. The pore pressure ratio increased to almost 40% to 50% at r_u-1 to r_u-3 . This can be attributed to the difficulty of liquefaction occurrence at high confining stress. The point at shallow depth, r_u-4 , showed higher pore pressure and fluctuation during seismic loading, specifically in case of strong dikes, see Figure 5-8 and Figure 5-9. Figure 5-8 and Figure 5-9 show that a rapid increase of r_u occurred at around 5s under earthquake event at the four selected elevations, and the highest pore pressure ratio was observed at shallower depth (i.e. 3 m). r_u reached 70% and 50% at 3 m depth in case of strong and weak dikes, respectively.

(a) Earthquake/ r_u-1 (b) Earthquake/ r_u-2 

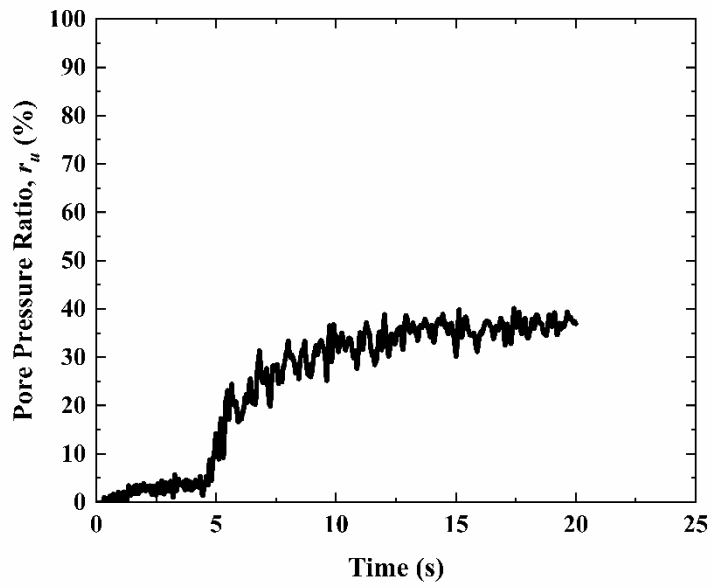
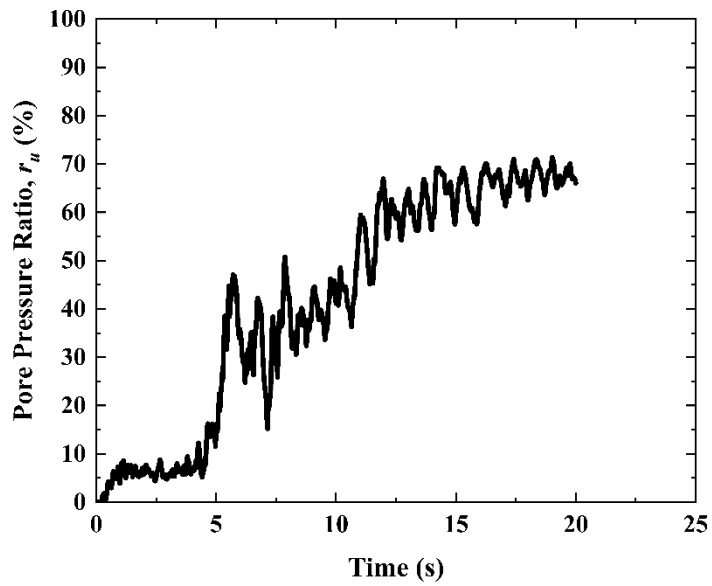
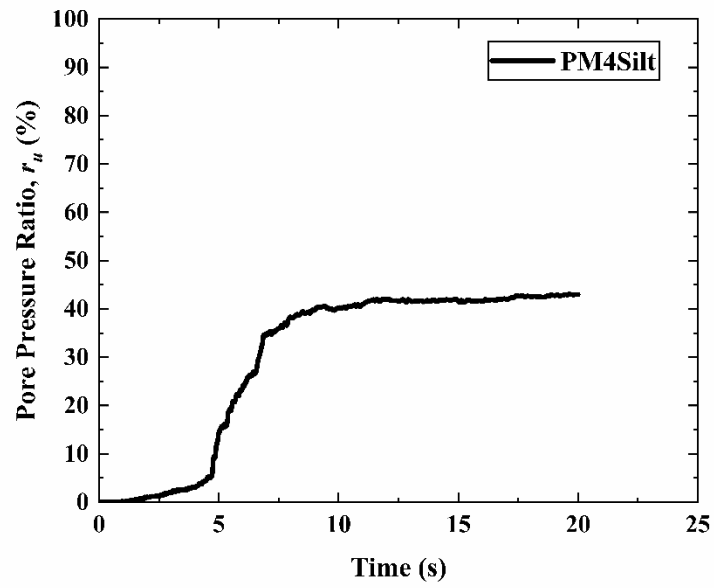
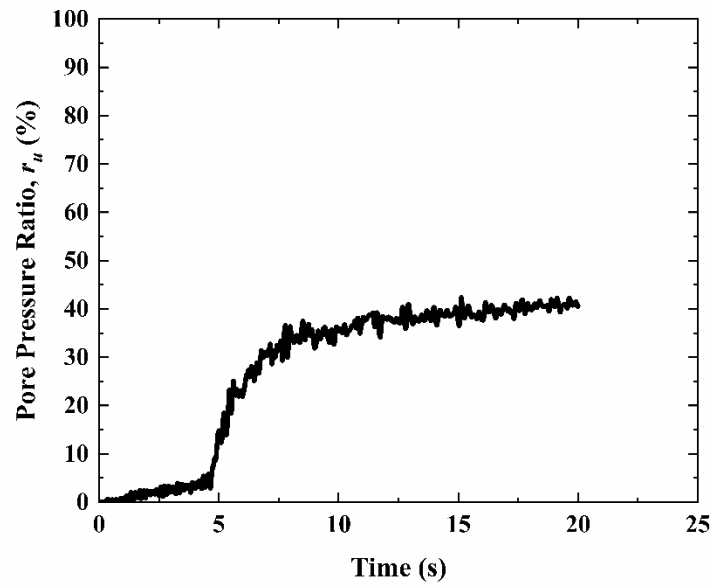
(c) Earthquake/ r_u-3 (d) Earthquake/ r_u-4 

Figure 5-8 Pore pressure ratio generated by earthquake in the model with strong dikes

(a) Earthquake/ r_u-1 (b) Earthquake/ r_u-2 

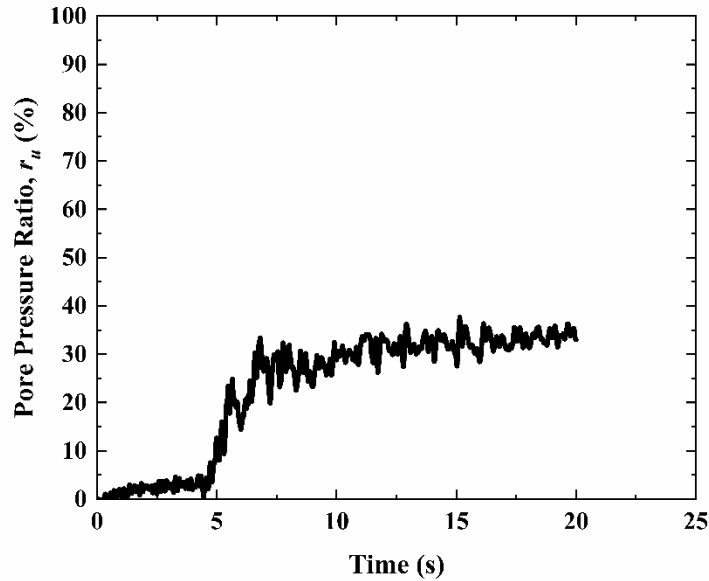
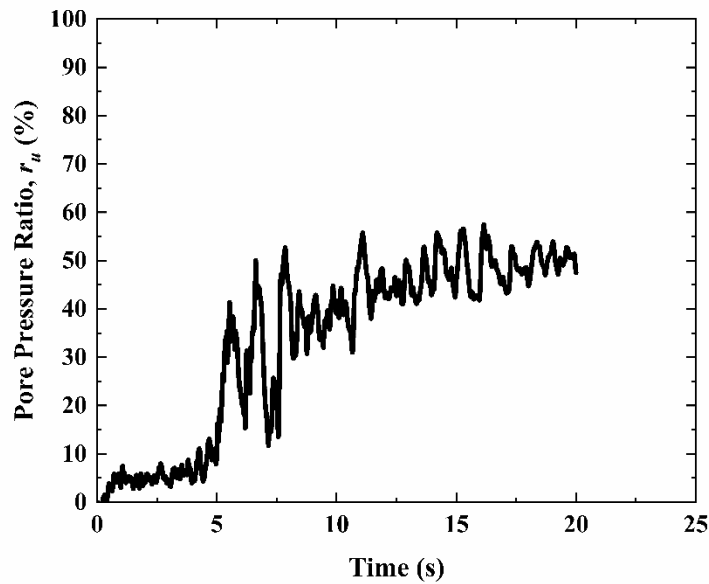
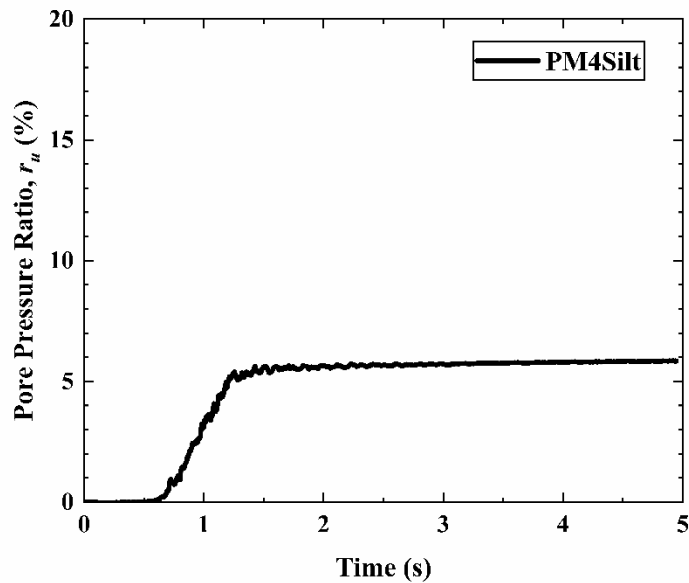
(c) Earthquake/ r_u-3 (d) Earthquake/ r_u-4 

Figure 5-9 Pore pressure ratio generated by earthquake in the model with weak dikes

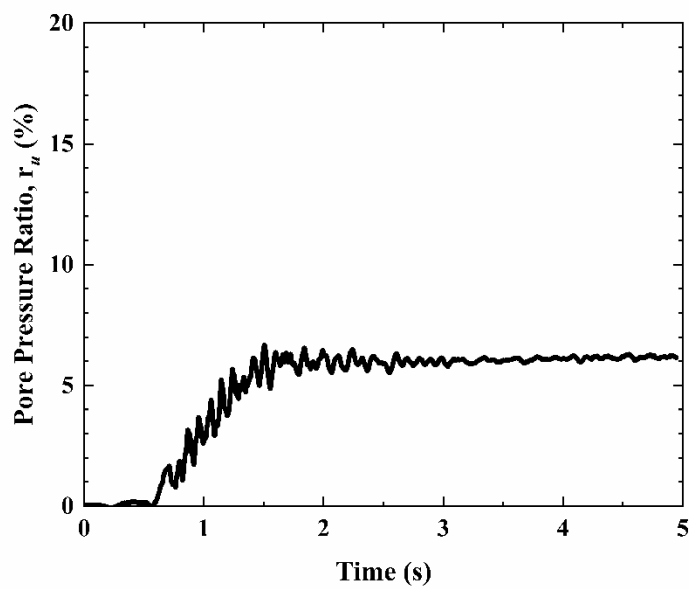
Figure 5-10 and Figure 5-11 show that under blast event the generated pore pressure ratio was significantly lower, compared to that under earthquake, since lower shear stress was induced by the blast. Similar pattern for pore pressure ratio build up was observed for both strong and weak dikes cases. The fluctuation and maximum pore pressure ratio at shallower depth were greater than those at the rest of the points. The pore pressure ratio developed at shallower depth (i.e. r_u-4) was approximately three times higher than that at greater depths such as r_u-3 , r_u-2 , and r_u-1 . This

observance can be again attributed to the difficulty of liquefaction occurrence at higher confining stress.

(a) Blast/ r_u-1



(b) Blast/ r_u-2



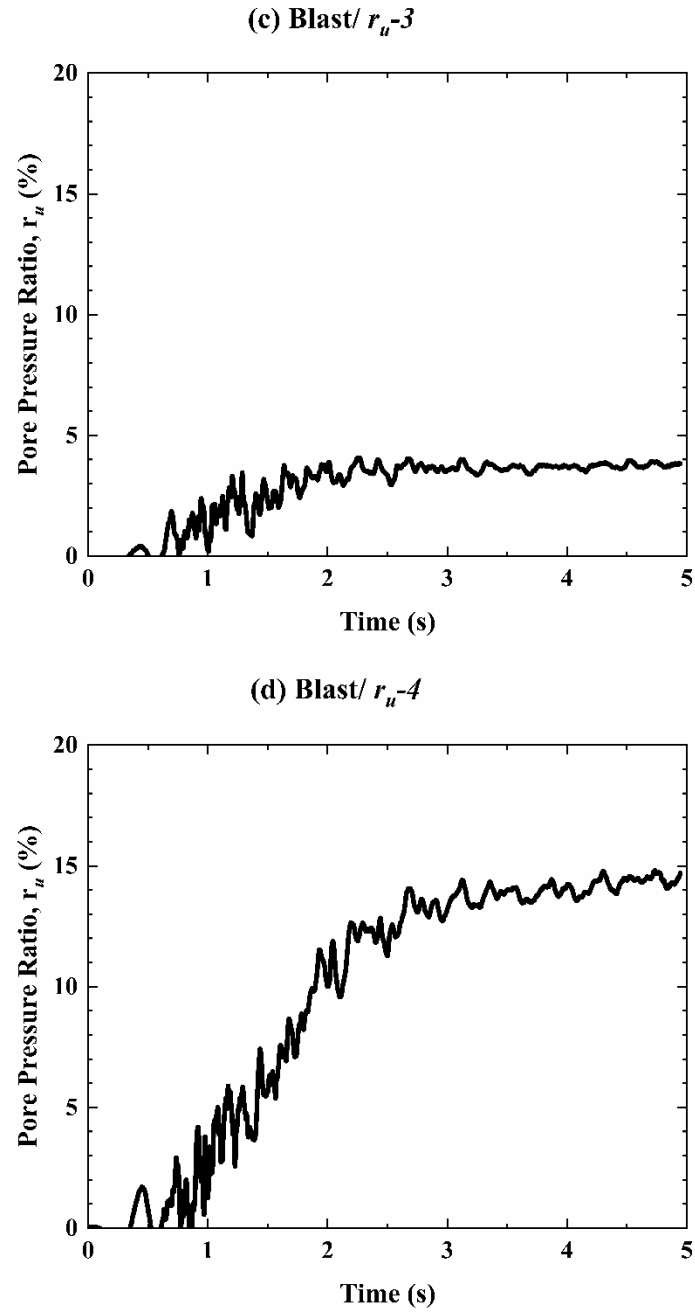
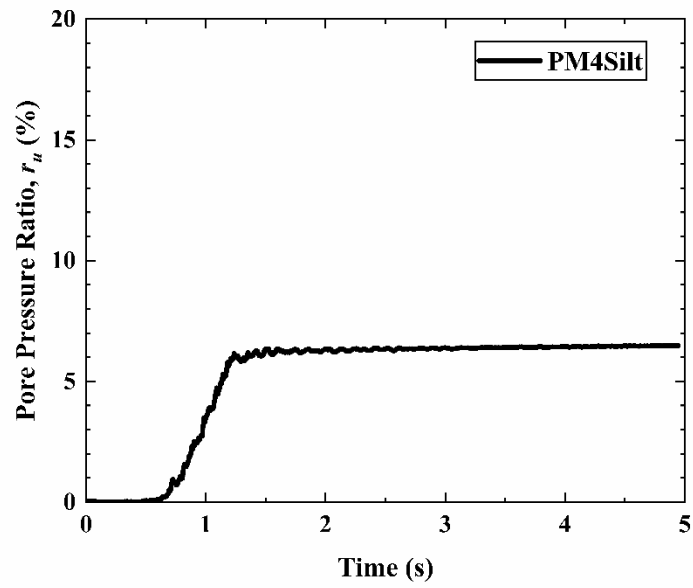
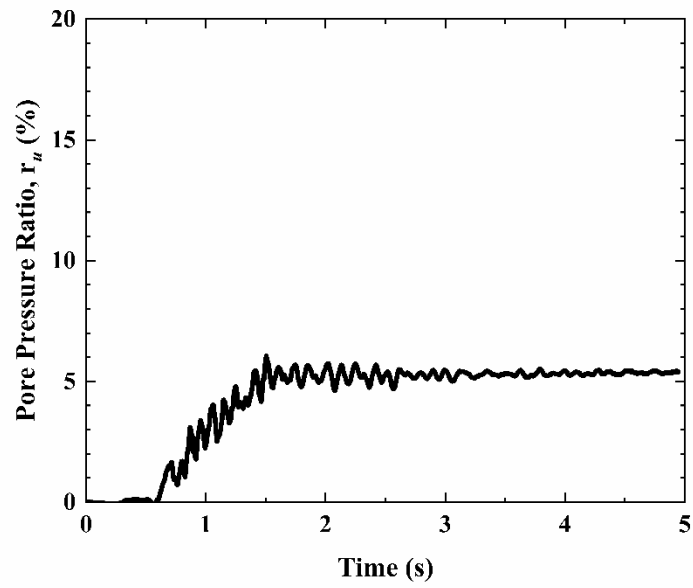


Figure 5-10 Pore pressure ratio generated by blast in the model with strong dikes

(a) Blast/ r_u-1 (b) Blast/ r_u-2 

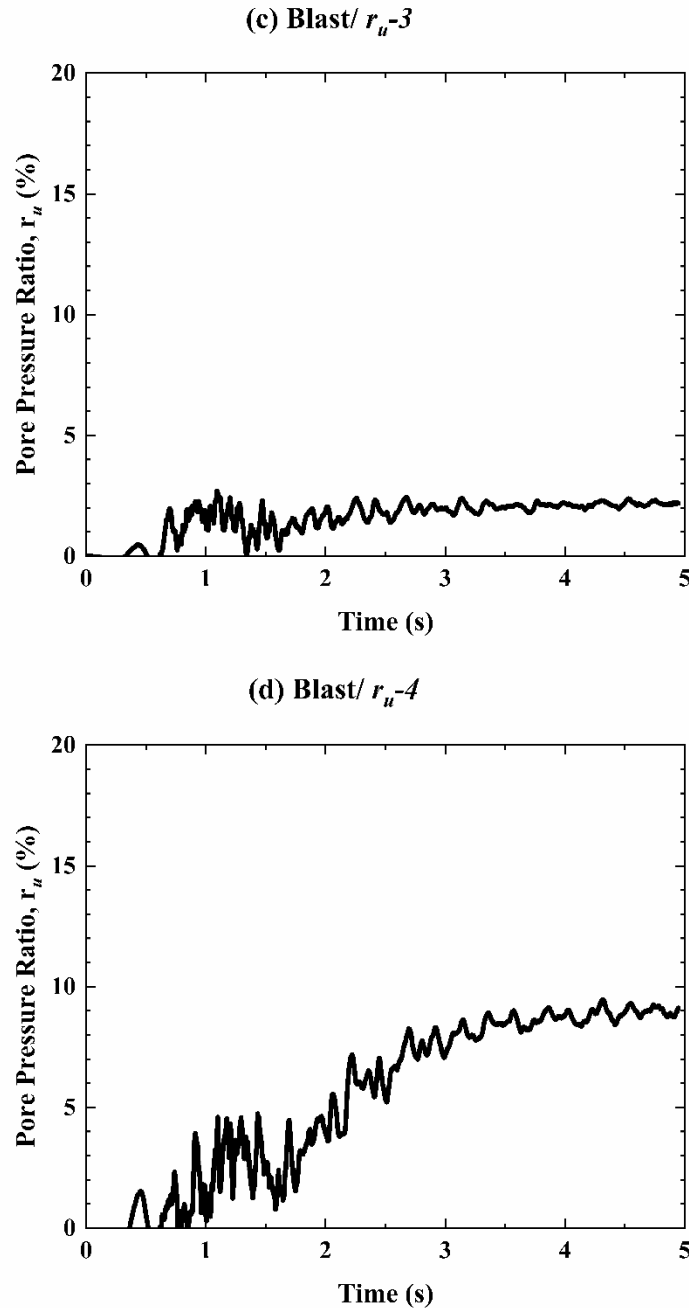


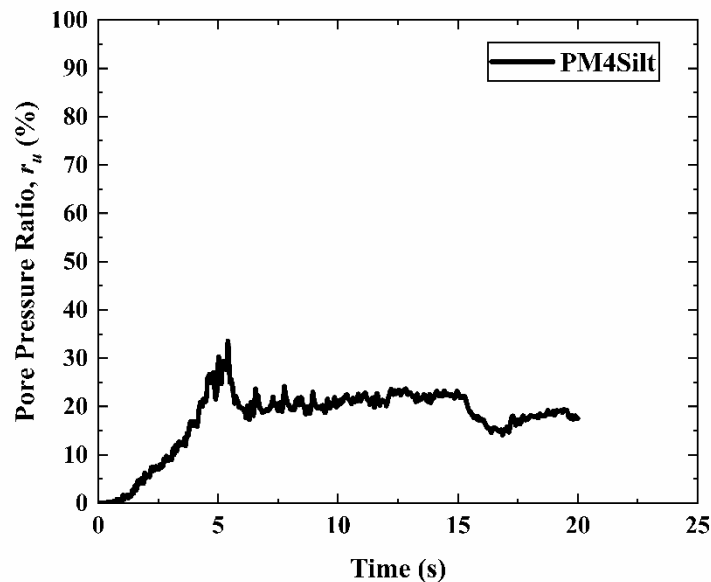
Figure 5-11 Pore pressure ratio generated by blast in the model with weak dikes

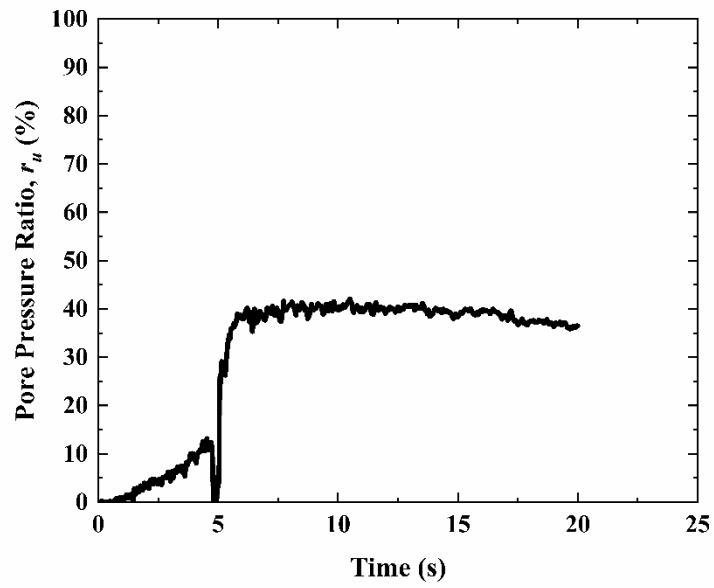
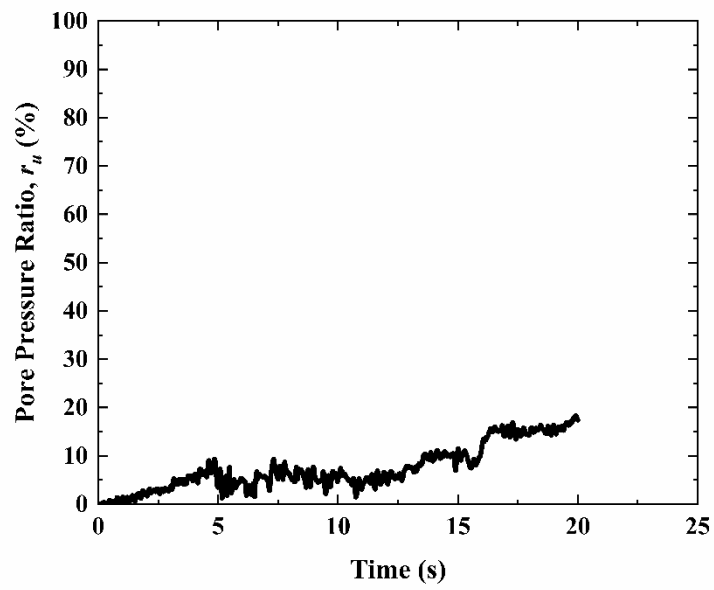
The liquefaction of the coal slurry in the vicinity of the dikes is of great importance, as the coal slurry in those regions serve as a foundation, withstanding the weight of the proceeding dikes. According to Figure 5-6 and Figure 5-7, the failure plane has also been formed in the neighborhood of the dikes. Liquefaction, and subsequently, extensive shear strain can lead to failure or instability of impoundment. Therefore, the liquefaction potential and subsequent volumetric shear strain of coal slurry close to the dikes should be evaluated. Accordingly, the pore pressure ratios of four locations, r_u -5 to r_u -8 shown in Figure 5-1, were monitored. The cyclic behavior and liquefaction

resistance of the locations indicated by r_{u-5} to r_{u-8} are more complex than r_{u-1} to r_{u-4} , as those points are subject to static shear stress ratio (i.e. $\alpha = \frac{\tau_s}{\sigma'_{v0}}$) larger than zero, as they are located under sloping ground, before cyclic loading. The cyclic resistance ratio of sandy soils is a function of relative density and static shear stress. The cyclic mobility behavior of soil is also substantially influenced by the presence of static shear stress (Youd and Idriss 2001). The existing static shear stress ratios before dynamic motion at r_{u-5} to r_{u-8} were 0.32, 0.44, 0.17, and 0.24, respectively. The cyclic resistance ratio of coal slurry decreases when the static shear stress ratio increases. Accordingly, higher pore pressure buildup is expected for the points with higher α . Therefore, higher pore pressure ratio is expected to develop at r_{u-5} and r_{u-6} than that at r_{u-7} and r_{u-8} .

Figure 5-12 to Figure 5-15 show pore pressure ratio due to earthquake and blast event for strong and weak dikes, respectively. Pore pressure ratio approximated by PM4Silt did not exceed 50% in the selected locations. In addition to the effect of static shear stress ratio, the deformation pattern in the investigated region adds to the complexity of pore pressure ratio development trend. According to Figure 5-14 and Figure 5-15, the pore pressure ratio trend closely followed the blast input motion pattern, which had strong spikes at approximately the first second. The sudden increase in pore pressure ratio also occurred at the first second and then r_u either remained constant or showed minimal changes. The pore pressure at the locations of r_{u-5} to r_{u-8} did not exceed 20% under blast loading. Due to higher static shear stress ratio at r_{u-5} and r_{u-6} higher pore pressure ratio was developed compared to r_{u-7} and r_{u-8} in all cases. The effect of static shear stress ratio (α) can be more clearly realized when the generated pore pressure ratio at points with $\alpha=0$ (e.g. r_{u-2}) and $\alpha>0$ (e.g. r_{u-5} and r_{u-6}) at similar depth are compared. For instance, under blast event, higher pore pressure ratio was observed at r_{u-5} and r_{u-6} than that at r_{u-2} , see Figure 5-14 and Figure 5-10.

(a) Earthquake/ r_{u-5}



(b) Earthquake/ r_u-6 (c) Earthquake/ r_u-7 

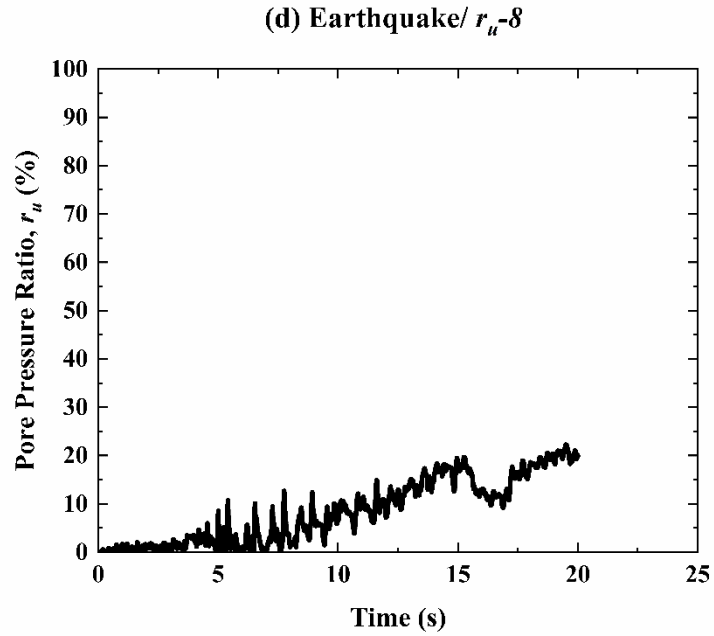
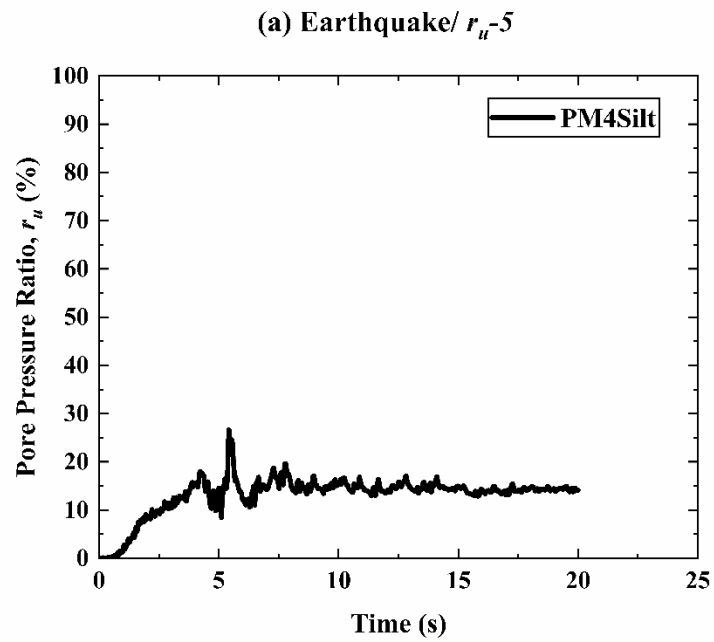
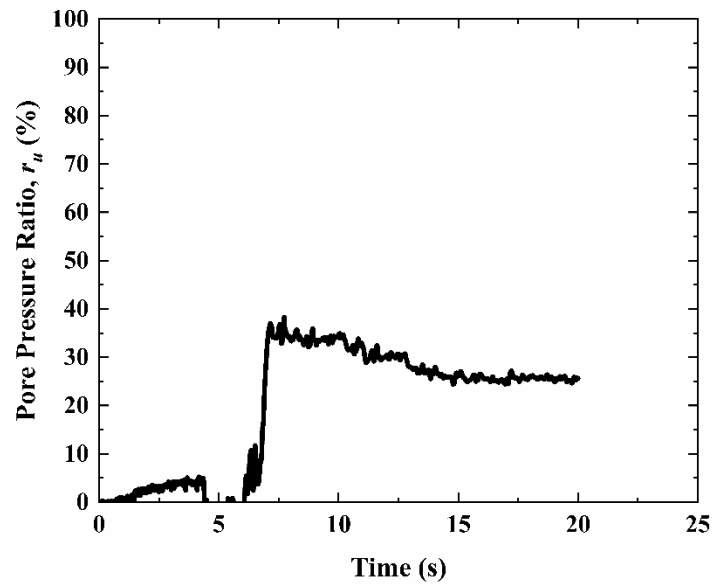
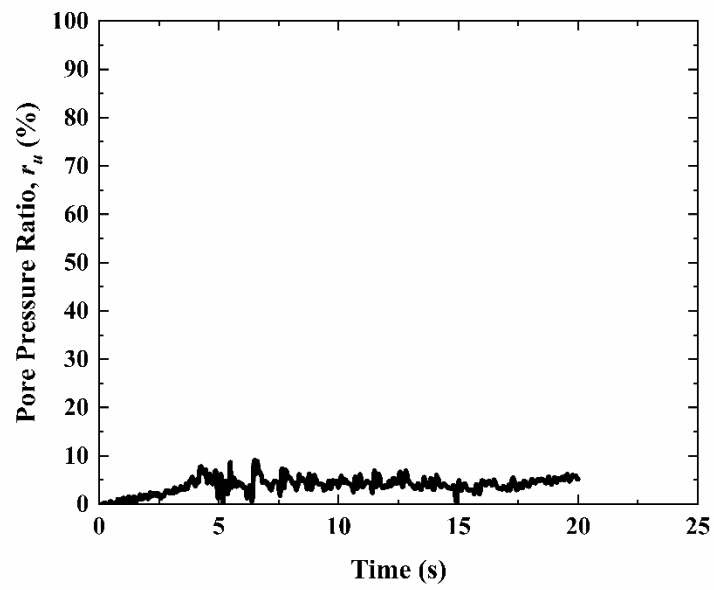


Figure 5-12 Pore pressure ratio generated by earthquake in the model with strong dikes



(b) Earthquake/ r_u-6 (c) Earthquake/ r_u-7 

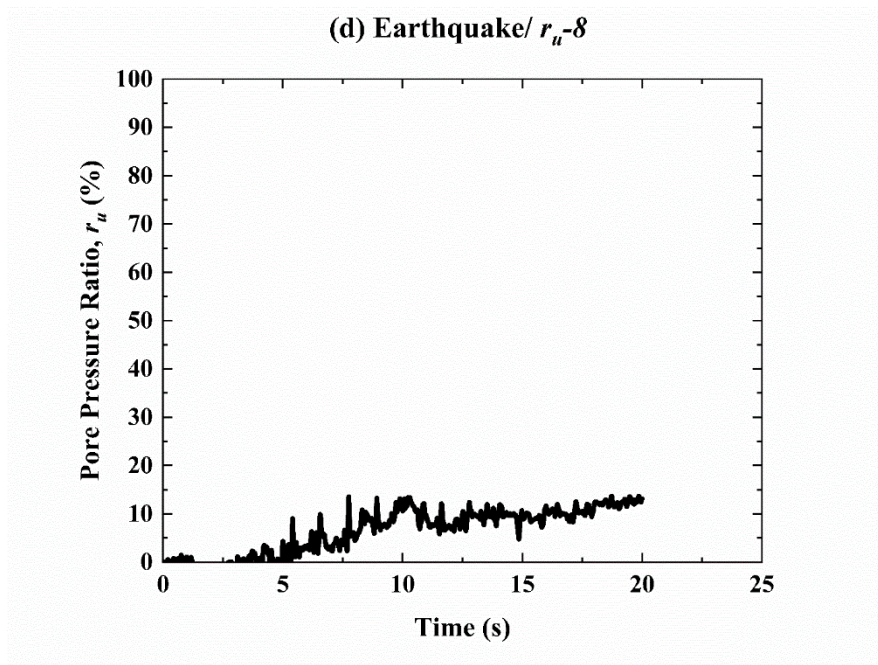
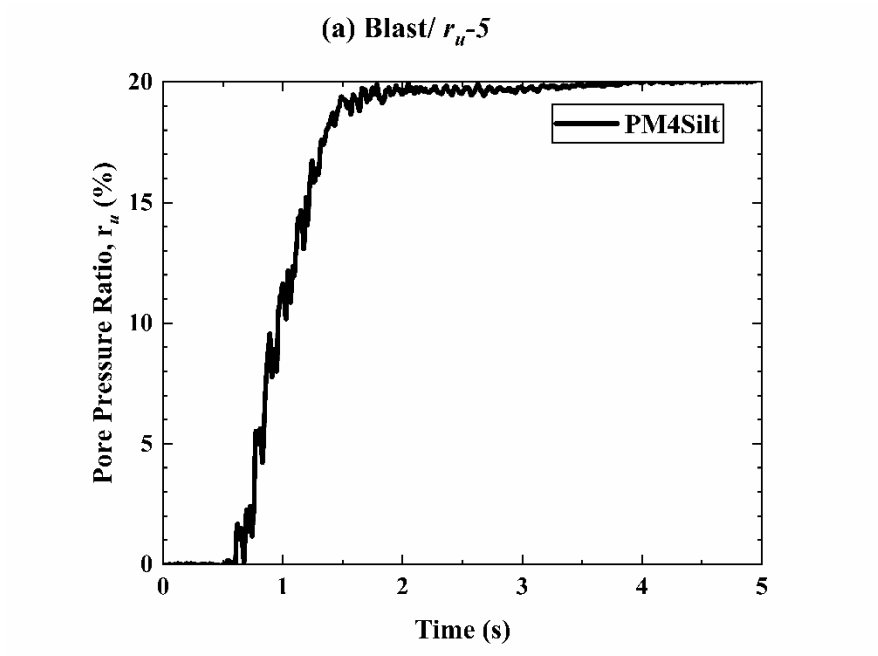
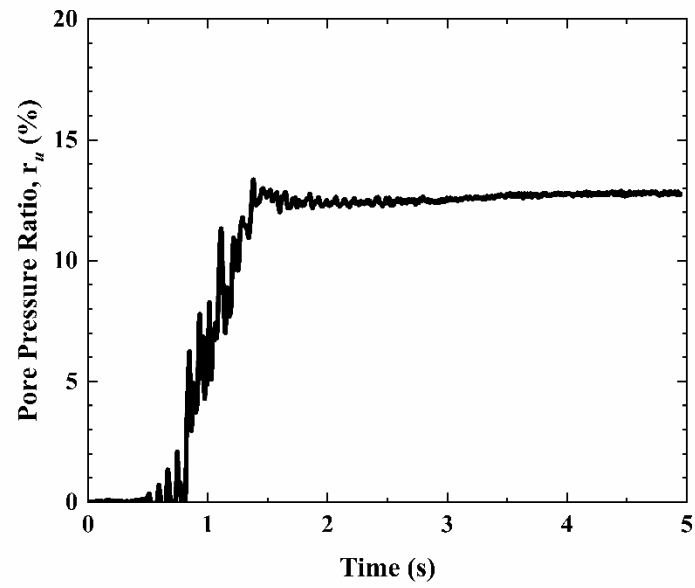
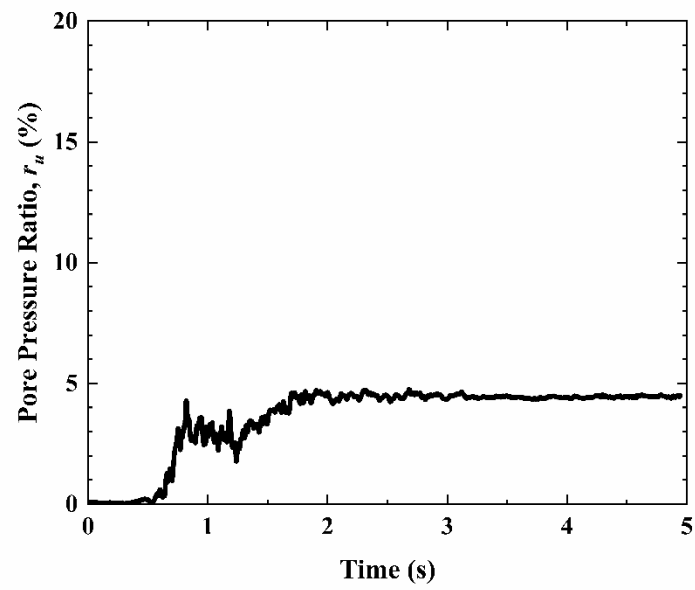


Figure 5-13 Pore pressure ratio generated by earthquake in the model with weak dikes



(b) Blast/ r_u -6(c) Blast/ r_u -7

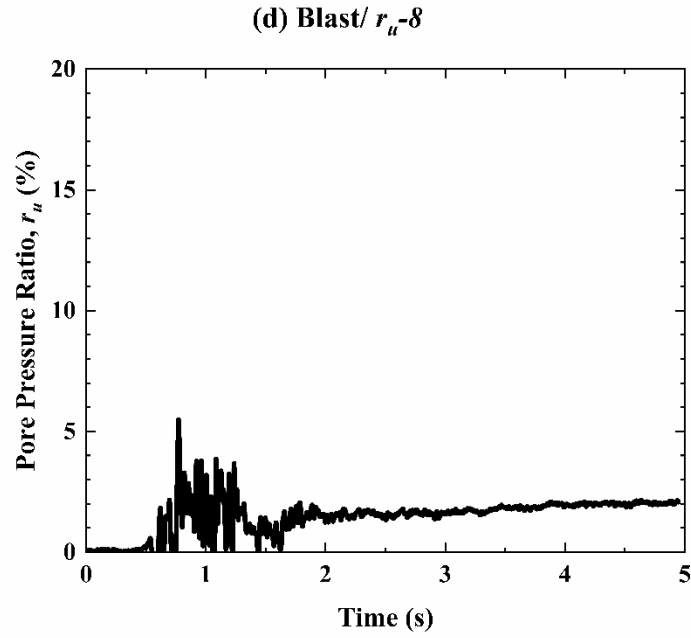
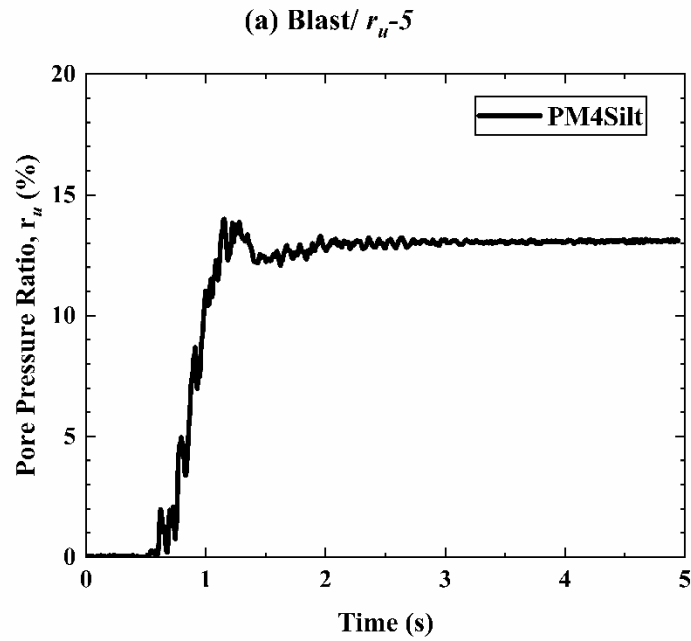
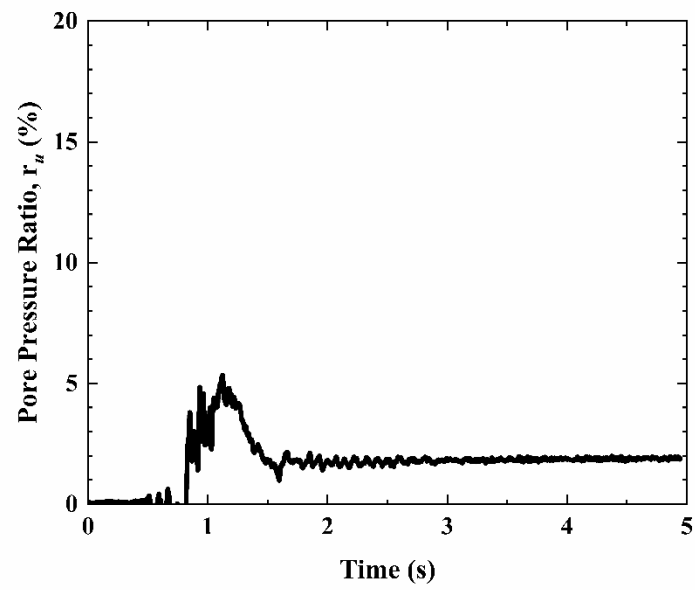
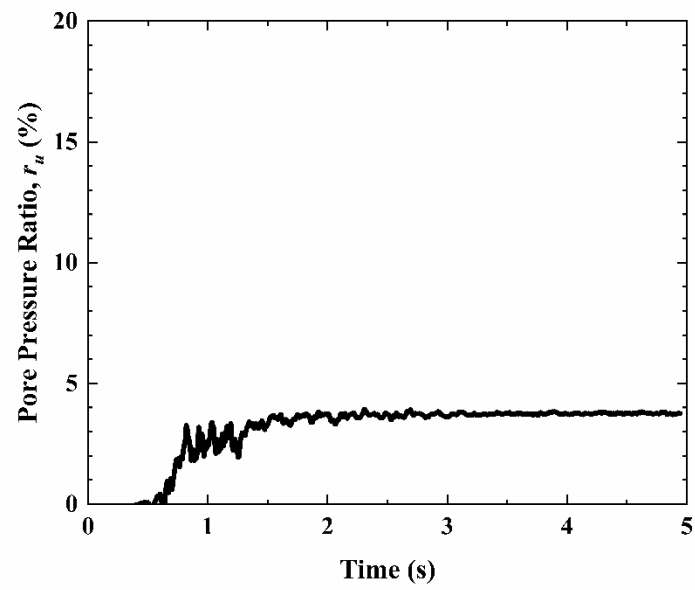


Figure 5-14 Pore pressure ratio generated by blast in the model with strong dikes



(b) Blast/ r_u -6(c) Blast/ r_u -7

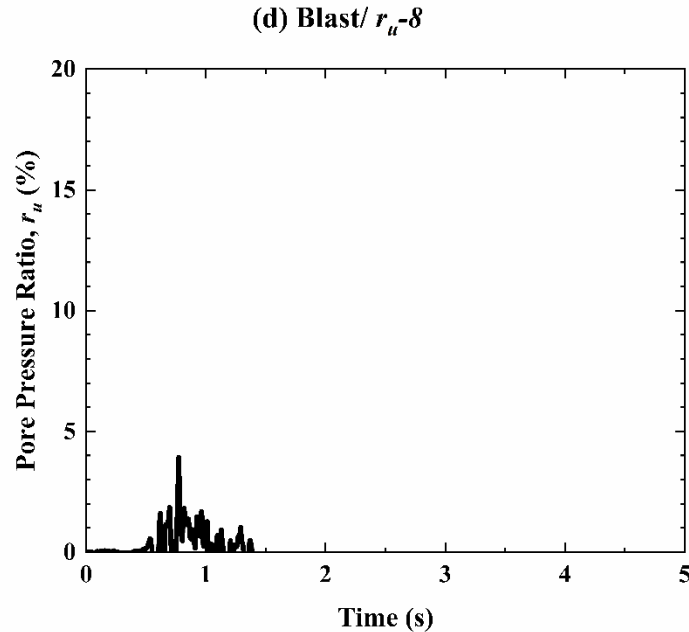
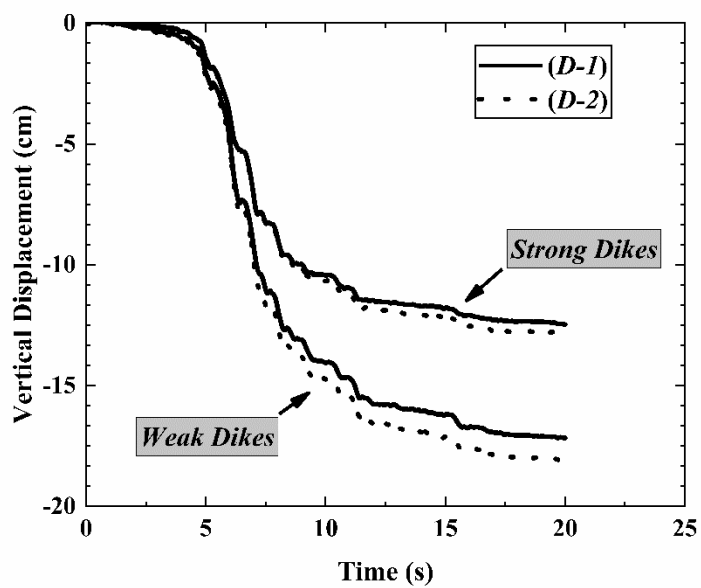


Figure 5-15 Pore pressure ratio generated by blast in the model with weak dikes

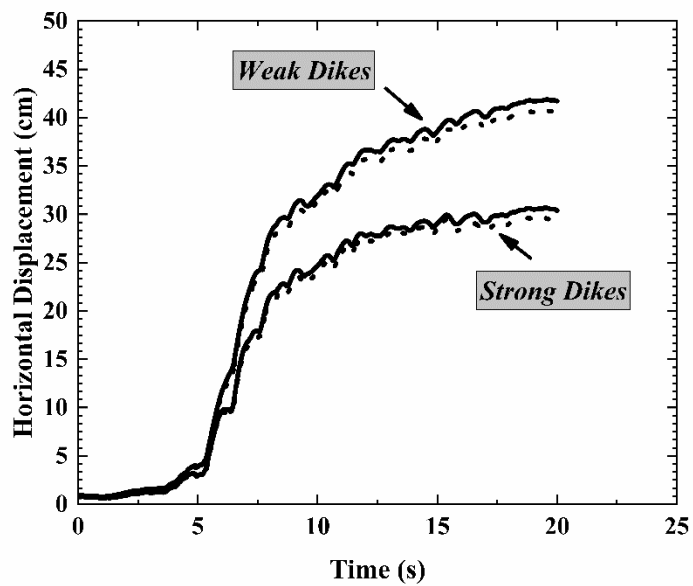
5.5.3 Deformations

Figure 5-16 and Figure 5-17 present the vertical and horizontal displacement of *D-1*, *D-2*, and *D-3*, marked in Figure 5-1, under earthquake and blast seismic loading, respectively. *D-1* and *D-2* are located on the crest of the upstream impoundment. The differential displacement at *D-1* and *D-2* can imply occurrence of tilting at the crest, which is likely since the crest is laid on a liquefiable material. Displacements at *D-3*, as in Figure 16 (c) to (d) and Figure 17 (c) to (d), also has been found the spot, at which high displacement and shear strain is expected, see Figure 5-6 and Figure 5-7. The impoundment with weak dikes experiences larger deformations compared to the impoundment with strong dikes. The difference in vertical and horizontal displacement of the crest is up to approximately 5 cm and 10 cm, respectively. However, the effect of shear strength properties on deformation of slope is clearly pronounced when considering the horizontal displacement of *D-3*, see Figure 5-16 (d). Smaller deformations were observed under blast seismic loading, as expected. In addition, the difference in stability and deformation of the impoundment with strong and the impoundment with strong dikes was minimal, see Figure 5-17. Figure 5-16 (a) and (b) and Figure 5-17 (a) and (b) also show the differential movement of *D-1* and *D-2* was small, therefore, significant tilting was not captured in the studied case.

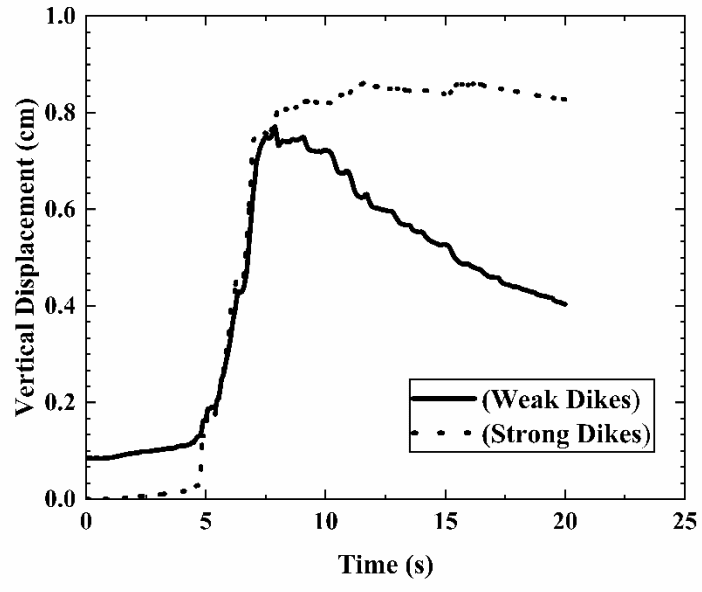
(a) Earthquake/ crest vertical displacement



(b) Earthquake/ crest horizontal displacement



(c) Earthquake/ *D-3* vertical displacement



(d) Earthquake/ *D-3* horizontal displacement

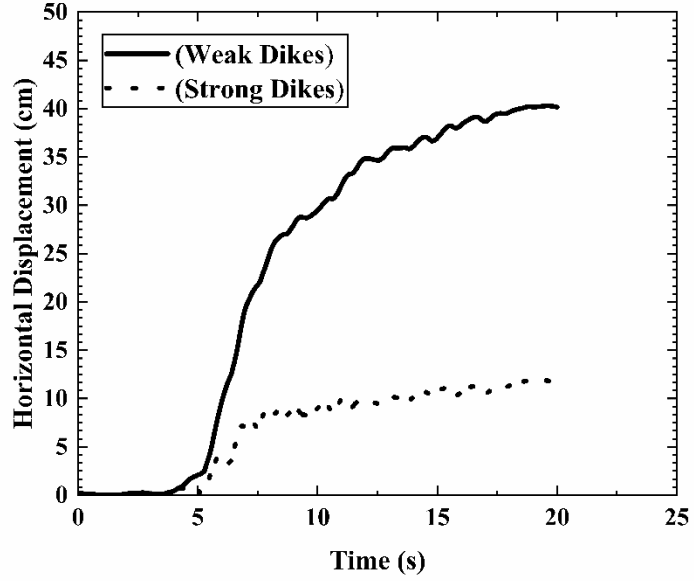
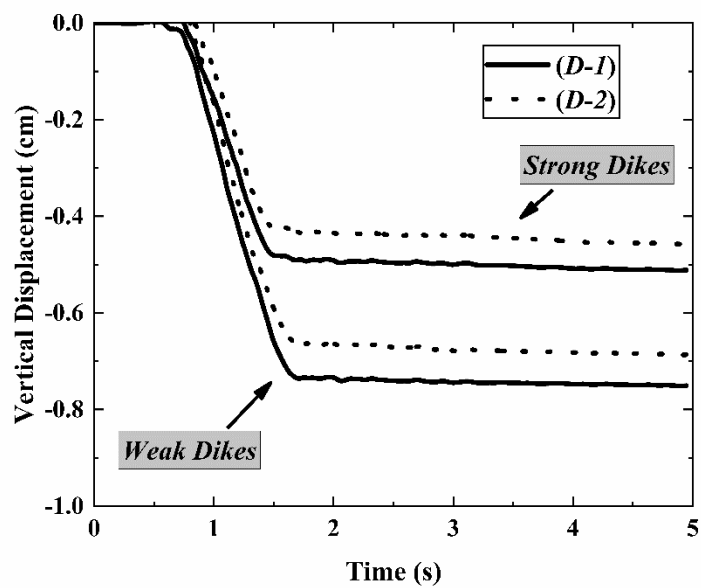
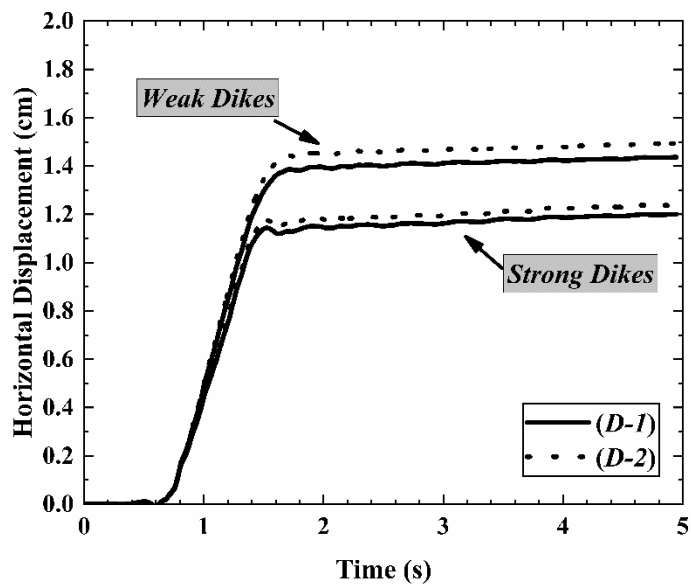


Figure 5-16 Deformations due to earthquake for both models with strong and weak dikes

(a) Blast/ crest vertical displacement



(b) Blast/ crest horizontal displacement



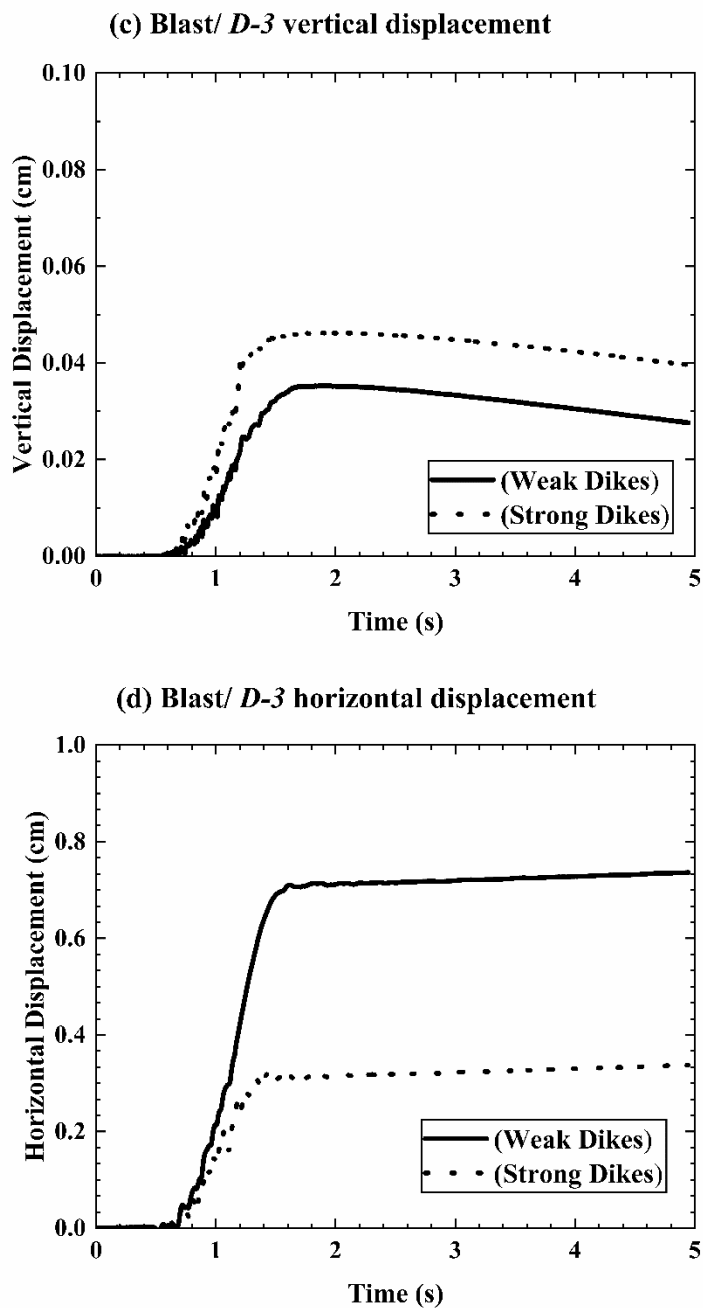


Figure 5-17 Deformations due to blast for both models with strong and weak dikes

5.6 Conclusions

Blast resulted in significantly lower pore pressure ratio compared to the earthquake. The pore pressure ratio generated at far distance from dikes was not noticeably affected by strength of the dikes. The material at shallow depth showed higher pore pressure ratio development during loading. The magnitude of pore pressure ratio generation is greatly affected by ground condition, as the locations under sloping ground are subject to static shear stress ratio.

As far as deformations, blast did not induce large deformations in comparison with earthquake. The impoundment with weak dikes showed noticeably higher deformations on the slope. The effect of shear strength properties of the dikes is more pronounced in case of earthquake. No tilting was observed for the crest, which is half founded on liquefiable material.

CHAPTER 6. CONCLUSIONS AND RECOMMENDATIONS

6.1 Conclusions

6.1.1 Characterization of Static and Dynamic Geotechnical Properties and Behavior of Fine Coal Tailings

Basic geotechnical properties in terms of unit weight, classification, Atterberg limits, specific gravity, hydraulic conductivity, and consolidation were determined to characterize the FCR samples that were obtained from two Appalachian coalfields. All the studied samples were classified as SW-SM, SM, ML, and ML-CL with plasticity index lower than 7. The measured unit weight of the representative samples varied noticeably through depth. Hydraulic conductivity of the tested FCR samples was mostly within a narrow range from $1.0\text{e-}6$ cm/s to $3.6\text{e-}7$ cm/s. However, the FCR sample taken from the location close to the coal slurry discharge point showed higher unit weight and hydraulic conductivity compared to other tested samples, implying the higher accumulation of coarse particles. The coefficient of consolidation ranges from 0.75 to 2.36 cm^2/min .

Staged triaxial tests and resonant column tests were conducted on representative samples taken from different locations and depths in the impoundment. The samples at deeper depth consistently showed higher shear strength and stiffness. The effective cohesion and internal friction angle of the samples tested under CU condition were from 13.8 kPa to 25.5 kPa and 26° to 31° , respectively. Lower cohesion and higher internal friction angle were also observed for the samples tested under CD condition compared to those under CU condition. The effect of confining pressure was found to be negligible on normalized shear modulus at shear strain level less than $10^{-3}\%$. The damping ratio ranged from 0.6% to 2% for the FCR samples.

The liquefaction resistance and cyclic behavior of FCR were assessed by cyclic DSS testing on reconstituted samples. FCR samples, taken from deeper depth in the vicinity of the coal slurry discharge point that may substantially contribute to the failure of impoundments, were prepared per slurry deposition method that resembles the structure and fabric of the FCR in the field. The CSR-N relationship was established. The cyclic resistance ratio (CRR) was close to the values estimated from empirical correlations for sand-like behavior material based on the procedures by Idriss and Boulanger (2008). On the other hand, the shear stress-strain loops and pore pressure ratio exhibited clay-like behavior. Therefore, the FCR cyclic behavior was perceived to be transitioning from sand-like to clay-like. Furthermore, the post-liquefaction shear behavior of FCR showed a dilative response, as pore pressure ratio showed a decreasing trend from the beginning of the static loading. The undrained shear strength of FCR after liquefaction was found to range from 12 kPa to 15 kPa. It was also noticed that higher CSR induced higher densification, consequently, slightly higher post-liquefaction peak shear strength was observed compared to those liquefied with lower CSR.

6.1.2 Seismic Investigation of Coal Tailings Using Multichannel Analysis of Surface Waves, Seismic Refraction, and Seismic Monitoring

In this study, seismic surveys, which include seismic refraction and the multichannel analysis of surface waves (MASW) methods, and the seismic monitoring of ground vibrations are conducted in two coal tailings impoundments in the Appalachian coalfields in the United States. Based on the seismogram records from the MASW and seismic refraction survey, the shear wave velocity and compressional wave velocity profiles are determined for the coal tailings, respectively. Combining both the wave velocity profiles, Poisson's ratio, Young's modulus, and small-strain shear modulus, which are important for stability assessment of coal tailings dams, are derived. Based on the *PPV* data from seismic monitoring, a vibration attenuation equation for peak particle velocity is developed specifically for coal tailings. The liquefaction resistance of coal tailings is evaluated using the *PPV* from seismic monitoring and the shear wave velocity from seismic survey. The main findings from this study are presented as follows.

- 1) With the aid of a sledge hammer in the active MASW survey and small explosive charges in the seismic refraction survey, the seismic surveys can effectively determine the strata of the coal tailings. The interpretation of the coal tailings strata based on the shear wave velocity from MASW is consistent with that based on the N-values from SPT.
- 2) The seismic refraction survey successfully determines the compressional wave velocity profiles of coal tailings and captures the thick and unsaturated layers of coal tailings below the groundwater table. Hence, the compressional wave velocity can only be used to estimate the depth of the fully-saturated coal tailings but not the groundwater depth.
- 3) The Poisson's ratio can be used to determine the groundwater depth. The depth of groundwater table measured from a borehole is congruent with the trend of the Poisson's ratio profile, where the groundwater depth can be estimated using Poisson's ratio of approximately 0.49. The Poisson's ratio of the fine coal tailings is determined to be 0.39.
- 4) The Young's modulus of the soft fine coal tailings for the inactive site is higher than that for the active site (i.e., 60 MPa versus 30 MPa), indicating that the coal tailings deposited in the inactive site are slightly stiffer than that in the active site. The Young's moduli derived from the seismic surveys are consistent with that estimated based on the N_{60} of SPT.
- 5) For the coal tailings, the *PPV* is correlated with *SD* through the power rule. The curve fitting results in the intercept, a , of 740 and slope, b , of -2.04. The slope, b , for coal tailings is the highest among other general equations, inferring the highest rate of vibration attenuation. However, the attenuation equation is based on *SD* values ranging from 6 to 8 m/sqrt kg; its application to higher *SD* values (10 to 100 m/sqrt kg) needs to be verified.
- 6) From the liquefaction evaluation of the coal tailings, the *CRR* is shown to have a strong association with depth. In general, the average in situ *CRR* of the coal tailings increases with the depth and with the percentage of *FC*. The increasing rate of *CRR* against the percentage of *FC* is also more drastic at depth deeper than 8 m.
- 7) When 100% of a_{max} is used in calculating the *CSR* of bench blasting, the lower bound of the calculated *FS* falls under the typical design factor of 1.5, indicating that the coal tailings

are prone to liquefaction or a reduction in shear strength when subjected to typical mine blasting.

A detailed in-situ seismic investigation that is effective in determining the in-situ properties of coal tailings and evaluating the liquefaction potential of the coal tailings subjected to ground vibrations due to mine blasting should therefore be performed to assess the potential risks of the current impoundment sites. While the coal tailings properties presented in this study are site-specific, the described methodology of the seismic investigation can be applied to other coal tailings impoundments to reassess the in-situ coal tailings properties in other regions.

6.1.3 Numerical Models

Seismic stability of an upstream impoundment was studied by a novel plasticity constitutive model, PM4Silt, which is able to capture cyclic behavior of non-plastic to low plasticity silts and clays. The applicability and ability of the plasticity model was first assessed by approximating laboratory cyclic DSS results. Then the model was further calibrated for coal slurry material.

PM4Silt was found a proper choice to simulate cyclic behavior of coal slurry, as the pore pressure ratio and number of cycles to liquefaction predicted by PM4Silt was in close agreement with the laboratory observation. The seismic stability and performance of an upstream impoundment with strong and weak dikes in terms of shear strength properties were evaluated. An earthquake and a blast were considered as input motions.

Blast resulted in significantly lower pore pressure ratio compared to the earthquake. The pore pressure ratio generated at far distance from dikes was not noticeably affected by strength of the dikes. The material at shallow depth showed higher pore pressure ratio development during loading. The magnitude of pore pressure ratio generation is greatly affected by ground condition, as the locations under sloping ground are subject to static shear stress ratio.

As far as deformations, blast did not induce large deformations in comparison with earthquake. The impoundment with weak dikes showed noticeably higher deformations on the slope. The effect of shear strength properties of the dikes is more pronounced in case of earthquake. No tilting was observed for the crest, which is partially founded on liquefiable material.

6.2 Recommendations

The results of this study show that dynamic loadings of the coal tailing dams impact the stability of impoundments. The procedures used in this study can be used to perform preliminary assessment of the stability of coal tailings impoundments based on simple site testing and sampling as well as limited laboratory testing. For the cases where the factor of safety is marginal, it is warranted to perform onsite investigations of the material properties of the tailings and dams using seismic techniques. The results of field testing and numerical modeling of the dams including detailed geometry and topography of the site allow for a more suitable analysis of potential risks under earthquake and blast shock loading. In the light of the recent instability of the impoundment

dam of Vale mining in Brazil which resulted in fatalities and property damage, it is prudent to develop a comprehensive plan for examination of known tailing ponds and risk assessment to be proactive in mitigation of possible issues. This also allows for creation of a database or a list of tailings impoundments along with the risk index pertinent to their stability under static and dynamic loadings.

REFERENCES

- Ajmera, B., Brandon, T., & Tiwari, B. 2015. Cyclic strength of clay-like materials. In Proc., 6th Int. Conf. on Earthquake Geotechnical Engineering, Christchurch, New Zealand.
- Allen, F.A., Richart Jr, F.E., and Woods, R.D. (1980). Fluid wave propagation in saturated and nearly saturated sands. *Journal of Geotechnical Engineering*, 106(GT3), pp.235-254.
- Almes, R.G., and Butail, A. (1976). Coal refuse: its behavior related to the design and operation of coal refuse disposal facilities. In *Proceedings of the Seventh Ohio Valley Soils Seminar on Shales and Mine Wastes: Geotechnical Properties, Design and Construction*, pp.9.
- Al-Qasimi, E.M., Charlie, W.A., and Woeller, D.J. (2005). Canadian liquefaction experiment (CANLEX): Blast-induced ground motion and pore pressure experiments. *Geotechnical Testing Journal*, 28(1), pp.9-21.
- American Society for Testing and Materials, C. 2006. Standard test method for sieve analysis of fine and coarse aggregates. ASTM C136-06. Philadelphia, USA
- American Society for Testing and Materials, D. 1963. Standard test method for particle-size analysis of soils. ASTM D422-63. Philadelphia, USA
- Anderson, D. G., & Stokoe, K. H. 1978. Shear modulus: a time-dependent soil property. In *Dynamic geotechnical testing*. ASTM International.
- Andrus, R.D., and Stokoe II, K.H. (2000). Liquefaction resistance of soils from shear-wave velocity. *Journal of Geotechnical and Geoenvironmental Engineering*, 126(11), pp.1015-1025.
- Arkansas Geological Survey. (2015). Equivalent energy of earthquakes. *Geohazards, Earthquakes*, accessed June 27, 2018 at URL <http://www.geology.ar.gov/geohazards/eq_geninfo.htm>
- ASTM. (2011). Standard guide for using the seismic refraction method for subsurface investigation. (D5557). American Society for Testing and Materials (ASTM) International, West Conshohocken, Pennsylvania.
- Azam, S. and Li, Q. (2010). Tailings dam failures: a review of the last one hundred years. *Geotechnical News*, 28(4), pp.50-54.
- Beatty, M., & Byrne, P. M. (1998, August). An Effective Stress Model for Predicting Liquefaction Behaviour of Sand. In *Geotechnical Earthquake Engineering and Soil Dynamics III*(pp. 766-777). ASCE.
- Blight, G.E. and Fourie, A.B. (2005). Catastrophe revisited—disastrous flow failures of mine and municipal solid waste. *Geotechnical and Geological Engineering*, 23(3), pp.219-248.
- Boulanger, R. W., and Ziotopoulou, K. (2013). Formulation of a sand plasticity plane-strain model for earthquake engineering applications. *Soil Dynamics and Earthquake Engineering*, 53, 254-267.
- Boulanger, R. W., and Ziotopoulou, K. (2017). “PM4Sand (version 3.1): A sand plasticity model for earthquake engineering applications.” Report No. UCD/CGM-17/01, Center for Geotechnical Modeling, Department of Civil and Environmental Engineering, University of California, Davis, CA, March, 114 pp.
- Boulanger, R. W., and Ziotopoulou, K. (2018). “PM4Silt (Version 1): A silt plasticity model for earthquake engineering applications.” Report No. UCD/CGM-18/01, Center for Geotechnical Modeling, Department of Civil and Environmental Engineering, University of California, Davis, CA.
- Bonnet, G., and Meyer, M. (1988). Seismic refraction tests above water table. *Journal of Geotechnical Engineering*, 114(10), pp.1183-1189.

- Bourbié, T., Coussy, O., and Zinszner, B. (1987). *Acoustics of porous media*, Gulf Publishing Company, Book Division, Houston, Texas.
- Bray, J. D., & Sancio, R. B. 2006. Assessment of the liquefaction susceptibility of fine-grained soils. *Journal of Geotechnical and Geoenvironmental Engineering*, 132(9), 1165-1177.
- Budhu, M. 2015. *Soil mechanics fundamentals*. John Wiley & Sons.
- Busch, R.A., Backer, R.R., Atkins, L.A. and Kealy, C.D. (1975). Physical property data on fine coal refuse. US Department of Interior Bureau of Mines Report of Investigation, 8062.
- Byrne, P. M., & Seid-Karbasi, M. 2003. Seismic stability of impoundments. In 17th Annual Symposium, Vancouver Geotechnical Society.
- Camp, W.M. III, Camp, H.C., and Andrus, R.D. (2010). Liquefaction mitigation using air injection. *International Conferences on Recent Advances in Geotechnical Earthquake Engineering and Soil Dynamics*. 26.
- Carraro, J. A. H., & Prezzi, M. 2007. A new slurry-based method of preparation of specimens of sand containing fines. *Geotechnical Testing Journal*, 31(1), 1-11.
- Castillo, J., Hallman, D., Byrne, P., & Parra, D. (2005). "Dynamic analysis of heap leach pad under high phreatic levels." In *Proceedings of 27th Mining convention*, Arequipa, Peru.
- Castro, G. 2003. Evaluation of seismic stability of tailings dams. In *Proceedings of the 12th Pan-American Conference on Soil Mechanics and Geotechnical Engineering*, Cambridge, MA (pp. 16-23).
- Castro, G., & Troncoso, J. 1989. Effects of 1989 Chilean earthquake on three tailings dams. In *Proceedings of the Fifth Chilean Conference on Seismology and Earthquake Engineering*, Santiago, Chile.
- Charlie, W.A., Bretz, T.E., Schure, L.A., and Doehring, D.O. (2013). Blast-induced pore pressure and liquefaction of saturated sand. *Journal of Geotechnical and Geoenvironmental Engineering*, 139(8), pp.1308-1319.
- Charlie, W.A., Lewis, W.A., and Doehring, D.O. (2001). Explosive induced pore pressure in a sandfill dam. *Geotechnical Testing Journal*, 24(4), pp.391-400.
- Coduto, P. D. (2001) *Foundation Design: Principles and Practices*. 2nd Edition. Prentice-Hall, Inc., Upper Saddle River, New Jersey.
- Cowherd, D.C., and Corda, I.J. (1998). Seismic considerations for upstream construction of coal refuse dams," *Proceedings, 1998 Annual Conference*, Las Vegas, Association of State Dam Safety Officials, Lexington, KY., pp. 523-534.
- D'appolonia Engineering, Inc. (2009). *Engineering and Design Manual: Coal Refuse Disposal Facilities*, prepared for the U.S. Mine Safety and Health Administration, Pittsburgh, PA.
- Dafalias, Y. F., and Manzari, M. T. (2004). "Simple plasticity sand model accounting for fabric change." *Journal of Engineering Mechanics*, 130(6), 622-634.
- Darendeli, M. B. 2001. Development of a new family of normalized modulus reduction and material damping curves. PhD Dissertation, University of Texas A&M.
- Dobry, R., & Alvarez, L. 1967. Seismic failures of Chilean tailings dams. *Journal of Soil Mechanics & Foundations Div.*
- Electric Power Research Institute 1993. *Guidelines for site specific ground motions*, Rept. TR102293, 1-5, Pala Alto, California.
- Ferdosi, B., James, M., & Aubertin, M. (2015). "Effect of waste rock inclusions on the seismic stability of an upstream raised tailings impoundment: a numerical investigation." *Canadian Geotechnical Journal*, 52(12), 1930-1944.

- Genes, B.E., Keller, T.O., and Laird, J.P. (2000). Steady state liquefaction susceptibility of high hazard upstream-constructed coal refuse disposal facilities. Proceedings, Tailings Dams 2000, Las Vegas, ASDSO/USCOLD, pp. 47-58.
- Geremew, A. M., & Yanful, E. K. 2012. Dynamic properties and influence of clay mineralogy types on the cyclic strength of mine tailings. *International Journal of Geomechanics*, 13(4), 441-453.
- Grangeia, C., Ávila, P., Matias, M., and Da Silva, E.F. (2011). Mine tailings integrated investigations: the case of Rio tailings (Panasqueira Mine, Central Portugal). *Engineering Geology*, 123(4), pp.359-372.
- Hammond, A.A. (1988). Mining and quarrying wastes: a critical review. *Engineering Geology*, 25(1), pp.17-31.
- Hegazy, Y.A., Cushing, A.G., and Lewis, C.J. (2004). Physical, mechanical, and hydraulic properties of coal refuse for slurry impoundment design. Proceedings of the Second International Conference on Site Characterization, Geotechnical and Geophysical Site Characterization, Viana da Fonseca and Mayne, pp.1285-1292.
- Highter, W.H. and Tobin, R.F. (1980). Flow slides and the undrained brittleness index of some mine tailings. *Engineering Geology*, 16(1-2), pp.71-82.
- Hofmann, B.A., Segó, D.C., and Robertson, P.K. (2000). In situ ground freezing to obtain undisturbed samples of loose sand. *Journal of Geotechnical and Geoenvironmental Engineering*, 126(11), pp.979-989.
- Holzer, T.L., and Bennett, M.J. (2003). Unsaturation beneath a water table. *Environmental and Engineering Geoscience*, 9(4), pp.379-385.
- Hossain, A.M., Andrus, R.D., and Camp III, W.M. (2012). Correcting liquefaction resistance of unsaturated soil using wave velocity. *Journal of Geotechnical and Geoenvironmental Engineering*, 139(2), pp.277-287.
- Huang, Y., Li, J., & Gamini, W. 1987. Strength and consolidation characteristics of fine coal refuse. Report to Office of Surface Mining, Department of Interior.
- Idriss, I. M. (1990). Response of soft soil sites during earthquakes." Proceedings, Symposium to Honor Professor H. B. Seed, BiTech Publishers, Vancouver, BC, Canada, pp.273-289.
- Idriss, I. M., & Boulanger, R. W. 2008. Soil liquefaction during earthquakes. Earthquake Engineering Research Institute.
- Idriss, I.M., (1999). An update to the Seed-Idriss simplified procedure for evaluating liquefaction potential. Proceedings, TRB Workshop on New Approaches to Liquefaction, FHWA-RD-99-165, Federal Highway Administration.
- Ilori, A.O., Okwueze, E.E., and Obianwu, V.I. (2013). Evaluating compaction quality using elastic seismic P-wave. *Journal of Materials in Civil Engineering*, 25(6), pp.693-700.
- International Code Council, Inc. (2009). International Building Code. International Code Council Publications, Illinois.
- International Commission on Large Dams (ICOLD). (2001). Tailings dams - risk of dangerous occurrences, lessons learnt from practical experiences (Bulletin 121). Paris: International Commission on Large Dams (ICOLD).
- Ishihara, K. (1984). Post-earthquake failure of a tailings dam due to liquefaction of pond deposit.
- Ishihara, K., Yasuda, S., & Yokota, K. 1981. Cyclic strength of undisturbed mine tailings.
- Itasca Consulting Group. (2017). Fast Lagrangian analysis of continua, Version 8.0.
- James, M., Aubertin, M., Wijewickreme, D., & Wilson, G. W. 2011. A laboratory investigation of the dynamic properties of tailings. *Canadian Geotechnical Journal*, 48(11), 1587-1600.

- James, M. (2009). "The use of waste rock inclusions to control the effect of liquefaction in tailings impoundments." Ph.D. thesis, Department of Civil, Geological, and Mining Engineering, Ecole Polytechnique de Montreal, Montréal, Que.
- Kalinski, M. E., & Salehian, A. 2016. Estimating the Cyclic and Post-Earthquake Behavior of Coal Mine Tailings at a Site in Eastern Kentucky. In *Geo-Chicago*, pp. 279-288.
- Kalinski, M.E., and Phillips, J.L. (2008). Development of methods to predict the dynamic behavior of fine coal refuse: Preliminary results from two sites in Appalachia. In *Geotechnical Earthquake Engineering and Soil Dynamics IV*, pp.1-10.
- Khandelwal, M., and Ranjith, P.G. (2010). Correlating index properties of rocks with P-wave measurements. *Journal of Applied Geophysics*, 71(1), pp.1-5.
- Kim, T. C., & Novak, M. 1981. Dynamic properties of some cohesive soils of Ontario. *Canadian Geotechnical Journal*, 18(3), 371-389.
- Kokusho, T. 2003. Current state of research on flow failure considering void redistribution in liquefied deposits. *Soil Dynamics and Earthquake Engineering*, 23(7), 585-603.
- Kramer, S. L. (1996). *Geotechnical Earthquake Engineering*. Pearson Education, Inc, New York.
- Kuerbis, R., & Vaid, Y. P. 1988. Sand sample preparation-the slurry deposition method. *Soils and Foundations*, 28(4), 107-118.
- Kumar, R., Choudhury, D., and Bhargava, K. (2013). Prediction of blast-induced vibration parameters for soil sites. *International Journal of Geomechanics*, 14(3), pp.04014007.
- Leventhal, A.R. and De Ambrosis, L.P. (1985). Waste disposal in coal mining - a geotechnical analysis. *Engineering Geology*, 22(1), pp.83-96.
- Lin, C.P., Chang, C.C., and Chang, T.S. (2004). The use of MASW method in the assessment of soil liquefaction potential. *Soil Dynamics and Earthquake Engineering*, 24(9-10), pp.689-698.
- Martin, T. E., & Davies, M. P. 2000. Development and Review of Surveillance Programs for Tailings Dams. *Tailings Dams 2000 Proceedings*. Association of State Dam Safety Officials. Las Vegas. March.
- McCutcheon, H.P. (1983). Liquefaction and cyclic mobility of coal refuse material, M.S. Thesis, Carnegie Mellon University, Pittsburgh, PA.
- Michael, P.R., Richmond, M.W., Superfeský, M.J., Stump Jr, D.E. and Chavel, L.K. (2010). Potential of breakthroughs of impounded coal refuse slurry into underground mines. *Environmental and Engineering Geoscience*, 16(3), pp.299-314.
- Naesgaard, E., Byrne, P.M., and Wijewickreme, D. (2007). Is P-wave velocity an indicator of saturation in sand with viscous pore fluid? *International Journal of Geomechanics*, 7(6), pp.437-443.
- National Research Council (US). Committee on Earthquake Engineering, & National Research Council (US). Committee on Earthquake Engineering Research. 1985. *Liquefaction of soils during earthquakes (Vol. 1)*. National Academies.
- Oyanguren, P.R., Nicieza, C.G., Fernández, M.Á., and Palacio, C.G. (2008). Stability analysis of Llerin Rockfill Dam: An in situ direct shear test. *Engineering Geology*, 100(3-4), pp.120-130.
- Park, C.B., Miller, R.D., and Xia, J. (1999). Multichannel analysis of surface waves. *Geophysics*, 64(3), pp.800-808.
- Plant, K. F., & Harriman, T. 2008. Root Cause Analysis of TVA Kingston Dredge Pond Failure on December 22, 2008 Volume I-Summary Report, Volume II-Geological and Field Explorations.
- Polito, C. P., & Martin II, J. R. 2001. Effects of nonplastic fines on the liquefaction resistance of sands. *Journal of Geotechnical and Geoenvironmental Engineering*, 127(5), 408-415.

- Price, A. B., DeJong, J. T., & Boulanger, R. W. 2017. Cyclic loading response of silt with multiple loading events. *Journal of Geotechnical and Geoenvironmental Engineering*, 143(10), 04017080.
- Puri, V.K. and Kostecki, T.R. (2013). Liquefaction of mine tailings. *International Conference on Case Histories in Geotechnical Engineering*. 16.
- Qiu, Y. and Sego, D.C. (2001). Laboratory properties of mine tailings. *Canadian Geotechnical Journal*, 38(1), pp.183-190.
- Rico, M., Benito, G., Salgueiro, A.R., Díez-Herrero, A. and Pereira, H.G. (2008). Reported tailings dam failures: A review of the European incidents in the worldwide context. *Journal of Hazardous Materials*, 152(2), pp.846-852.
- Robertson, P.K., and Campanella, R.G. (1985). Liquefaction potential of sands using the CPT. *Journal of Geotechnical Engineering*, 111(3), pp.384-403.
- Sabatini, P.J., Bachus, R.C., Mayne, P.W., Schneider, J.A. and Zettler, T.E. (2002). *Geotechnical Engineering Circular No. 5 (Evaluation of Soil and Rock Properties)* (No. FHWA-IF-02-034). Washington DC, USA: US Department of Transportation Office of Bridge Technology, Federal Highway Administration.
- Salam, S., Xiao, M., Khosravifar, A., Liew, M., Liu, S., Rostami, J. (2019). "Characterizations of Static and Dynamic Geotechnical Properties and Behaviors of Fine Coal Refuse." *Canadian Geotechnical Journal*.
- Salehian, A. (2013). Predicting the dynamic behavior of coal mine tailings using state-of-practice geotechnical field methods. *Theses and Dissertations - Civil Engineering*. 9. University of Kentucky.
- Seed, H. B. and Idriss, I. M. (1970). Soil moduli and damping factors for dynamic response analysis, Report No. UCB/EERC-70/10, Earthquake Engineering Research Center, University of California, Berkeley, pp.48.
- Seed, H.B., and Idriss, I.M. (1971). Simplified procedure for evaluating soil liquefaction potential. *Journal of Soil Mechanics and Foundations Division*, 97(9), pp.1249-1273.
- Seed, R. B., Cetin, K. O., Moss, R. E., Kammerer, A. M., Wu, J., Pestana, J. M., ... & Faris, A. 2003. Recent advances in soil liquefaction engineering: a unified and consistent framework. In *Proceedings of the 26th Annual ASCE Los Angeles Geotechnical Spring Seminar: Long Beach, CA*.
- Seid-Karbasi, M., & Byrne, P. M. (2004). "Embankment dams and earthquakes." *International Journal on Hydropower & Dams*, 11(2), 96-102.
- Sett, K., Unutmaz, B., Çetin, K.Ö., Koprivica, S. and Jeremić, B., 2010. Soil uncertainty and its influence on simulated G/G_{max} and damping behavior. *Journal of Geotechnical and Geoenvironmental Engineering*, 137(3), pp.218-226.
- Sivathayalan, S., & Vaid, Y. P. 2004. Cyclic resistance and post liquefaction response of undisturbed in-situ sands. In *Proceedings of the 13th world conference on earthquake engineering*.
- Taylor, D. 1948. *Fundamentals of soil mechanics*. Chapman and Hall, Limited; New York.
- Teng, W.C. 1962. *Foundation Design*, Prentice-Hall, Inc., Englewood Cliffs, N.Y.
- Thacker, B. K., Ullrich, C. R., Athanasakes, J. G., & Smith, G. 1988. Evaluation of a coal refuse impoundment built by the upstream method. In *Hydraulic Fill Structures* (pp. 730-749). ASCE.
- Ullrich, C. R., Thacker, B. K., & Roberts, N. R. 1991. *Dynamic Properties of Fine-Grained Coal Refuse*.
- Vick, S. G. 1990. *Planning, design, and analysis of tailings dams*. BiTech.

- Wijewickreme, D., Sanin, M. V., & Greenaway, G. R. 2005. Cyclic shear response of fine-grained mine tailings. *Canadian Geotechnical Journal*, 42(5), 1408-1421.
- Zamiran, S., Salam, S., Osouli, A., & Ostadhassan, M. 2015. Underground Disposal of Fine Coal Waste. In 49th US Rock Mechanics/Geomechanics Symposium. American Rock Mechanics
- Zeng, X., Goble, J.A. and Fu, L. (2008). Dynamic properties of coal waste refuse in a tailings dam. In *Geotechnical Earthquake Engineering and Soil Dynamics IV*, pp.1-14.
- Zeng, X., Wu, J., & Rohlf, R. 1998a. Modeling the seismic response of coal-waste tailings dams. *Geotechnical News*, 6(6), 29-32.
- Zeng, X., Wu, J., & Rohlf, R. A. 1998b. Seismic Stability of Coal-Waste Tailing Dams. ASCE.
- Ziotopoulou, K., & Boulanger, R. W. (2016). "Plasticity modeling of liquefaction effects under sloping ground and irregular cyclic loading conditions." *Soil Dynamics and Earthquake Engineering*, 84, 269-283.
- Ziotopoulou, K., & Montgomery, J. (2017). "Numerical modeling of earthquake-induced liquefaction effects on shallow foundations." In *Proceedings of the 16th World Conference on Earthquake Engineering*, Paper (No. 2979, pp. 9-3).

APPENDIX I

Geophysical Investigation Report

Geophysical Investigation
Coal Refuse Impoundments
Jeddo Coal
Ebervale, PA

Prepared for:

Ming Xiao, PhD, PE
Associate Professor of Civil Engineering
231P Sackett Building
The Pennsylvania State University
University Park, PA 16802

Prepared by:

Vibra-Tech Engineers, Inc.
109 E. First Street
Hazleton, Pennsylvania 18201

October 24, 2017

TABLE OF CONTENTS

| | |
|--|-----------|
| INTRODUCTION | 1 |
| SCOPE AND CONDITIONS OF SURVEY | 1 |
| LIMITATIONS OF GEOPHYSICAL METHODS | 1 |
| MASW DATA ACQUISITION PROCEDURE | 2 |
| BACKGROUND | 3 |
| ANALYSIS PROCEDURE..... | 4 |
| DISCUSSION OF MASW DATA | 5 |
| SEISMIC REFRACTION DATA ACQUISITION PROCEDURE | 6 |
| ANALYSIS PROCEDURE..... | 7 |
| FACTORS AFFECTING SEISMIC VELOCITY | 7 |
| DISCUSSION OF SEISMIC REFRACTION DATA | 8 |
| CONCLUSION | 8 |
| APPENDIX A..... | 10 |
| APPENDIX B..... | 11 |
| APPENDIX C | 12 |
| APPENDIX D..... | 13 |

Geophysical Investigation
Coal Refuse Impoundments
Jeddo Coal
Ebervale, PA

October 24, 2017

INTRODUCTION

Multi-Channel Analysis of Surface Waves (MASW) and Seismic Refraction testing was carried out by Vibra-Tech Engineers, Inc. at the coal refuse impoundments Jeddo 8 and Jeddo 14 of Jeddo Coal in Ebervale, PA. The fieldwork for this project was carried out on July 31 and August 1, 2017.

The purpose of the investigation was to utilize the MASW method to assess the propagation velocity of shear waves and the seismic refraction method to assess the propagation velocity of compressional waves through the refuse material. The results of this study will be utilized to study the coal refuse's seismic behavior.

SCOPE AND CONDITIONS OF SURVEY

The measurements consisted of twelve (12) MASW spreads and three (3) seismic refraction spreads that were located about the Jeddo 8 and Jeddo 14 coal refuse impoundments. There was one location in the Jeddo 8 impoundment and two locations in the Jeddo 14 impoundment, one in the north end and one in the south end of the impoundment, where data was collected. In each of the three locations where MASW data was collected, a forward and reverse 5-foot spacing spread and a forward and reverse 2.5-foot spacing spread were collected totaling four (4) spreads at each location. The mid-point of each MASW and seismic refraction spread were the same at each location. A plan view showing the approximate location of the MASW and seismic refraction investigation lines is presented in Appendix-A of this report in Figure 1a and Figure 1b.

The Jeddo 14 refuse impoundment was inherently noisy because the mine actively releases into the impoundment. Periods of relative quiet within this environment were utilized for the collection of MASW data. This resulted in the collection of MASW data that ranged in clarity and quality from good to fair.

LIMITATIONS OF GEOPHYSICAL METHODS

Geophysical Methods are indirect methods of subsurface investigation subject to both natural limits and interpretational errors. Vibra-Tech Engineers, Inc. does not guarantee that the interpreted subsurface conditions will completely coincide with the geological conditions that actually exist. The methods and equipment described in this report represent standard accepted practices employed by the engineering geophysical industry. The interpretations made in this report are representative of the data on the day of the acquisition. Vibra-Tech Engineers, Inc. cannot be held responsible for changes in subsurface conditions as a result of natural or man-made phenomena.

One limitation of the seismic refraction method is that the compressional wave velocity of groundwater (+/- 5000 ft/sec) is similar to that of some types of weathered rock. Unconsolidated soil materials located below the water table will appear to have the same velocity as weathered rock.

Under certain circumstances a subsurface layer may not be detected by the seismic refraction method. One such instance would be a velocity inversion. This occurs when a lower layer has a lesser seismic velocity than the overlying material. An example of this would be a soft shale which underlies a hard sandstone. The interface between the sandstone and the shale could not be mapped. The seismic refraction method will only map those layers which become progressively harder with depth.

Another instance where a subsurface layer may not be detected is when this layer has insufficient velocity contrast or insufficient thickness with respect to the overlying and underlying materials. This situation is called a "hidden layer" in the geophysical literature. Correlation of the seismic data with drill hole logs will normally identify the presence and thickness of these layers. Hidden layers are often indicated on the seismogram by analyzing second and third arriving events.

One limitation of the MASW (Multi-channel Analysis of Surface Waves) method is that the depth of investigation is limited by the length of the acquisition spread. There is a general rule of thumb that surface waves sample to an approximate depth of their wavelength divided by two. In surface wave surveying, it is assumed that the longest wavelength that can be sampled is as long as the spread length.

In addition to possessing inherent depth limitations, the MASW method is also limited in the interpretation of shear velocities at shallow levels near the ground surface. The resolution of MASW surveying at shallow depths is controlled by the length of the MASW spread, with shorter spread lengths providing greater resolution near the ground surface.

MASW DATA ACQUISITION PROCEDURE

A twenty-four channel, Geometrics Strataview seismograph was used to record active source MASW data collected at the site. Active source denotes the active or intentional manner in which seismic energy is transmitted into the ground. The instrument was set to acquire seismic records of 2048 ms in length, with a sample interval of 1,000 μ s. No pre-acquisition filters were used on the data.

On each of the investigation lines, spreads of twenty-four 4.5 Hz vertical geophones were placed along the ground surface. Both a five-foot spacing and a 2.5-foot spacing between geophones were utilized in the collection of MASW data, yielding 115 and 57.5 foot long spreads, respectively. As a useful rule of thumb, the MASW depth of investigation is approximately equal to half of the spread length. The locations of the MASW spreads run were largely controlled by the length of available open terrain encountered at the project area as the site had areas of pooled water from previous rainfall. As an example, the MASW lines in Jeddo 14 were collected in the north and south end of the site as those areas were not under water.

Seismic energy was transmitted into the ground adjacent and in-line with the beginning and end of the geophone spread. Offset distances to this seismic source measured 20 feet away from both the beginning (forward) and end (reverse) of the geophone spread for 5-foot array, and 10 feet for the 2.5-foot geophone spacing array. The seismic energy source was a light explosive charge buried in the ground. The travel time of the seismic energy, from the source point to each geophone, was stored in the seismograph's internal memory then transferred to disk for later analysis.

BACKGROUND

Multi-channel Analysis of Surface Waves (MASW) is a seismic method for near-surface characterization of the shear wave velocity of the sub-surface. It utilizes Rayleigh-type surface waves to determine the variation of shear wave velocity with depth. The Rayleigh Wave (R-Wave) is the dominant component of surface waves, and is often referred to as the “ground-roll”. Shear wave velocity (V_s) can be calculated by the mathematical inversion of the dispersive phase velocity of surface waves. The method uses 1.1 times the phase velocity for an estimate of V_s . Shear wave velocity is a direct indication of the stiffness of the material, where higher wave velocities is associated with higher stiffness.

When the ground surface is disturbed by an impact, two types of waves propagate in the system: body waves, and surface waves. Body waves travel in the body of the earth system and consist of shear waves and compressional waves. Surface waves propagate near the surface of the earth and are the focus of the MASW method. The ground motion associated with Rayleigh waves has been described as a motion that traces a retrograde-elliptical path throughout one complete cycle.

In an isotropic media, the velocity of surface waves does not vary with the frequency (wavelength) of the surface wave. However, if the stiffness of a site varies with depth, the velocity of the Rayleigh wave will vary with frequency. The variation of R-wave velocity with frequency is called dispersion, and a plot of surface wave velocity versus wavelength is called a dispersion curve.

Surface wave energy decays quite rapidly with depth. As a general rule of thumb, surface waves sample to an approximate depth of their wavelength divided by two. This means that the longer wavelength, lower-frequency surface waves travel deeper and thus contain more information about deeper velocity structure, while shorter wavelength, higher-frequency surface waves travel shallower and thus contain more information about shallower velocity structure.

Many of the concepts utilized in the explanation of the MASW method in this report are obtained from the publications of Soheil Nazarian and Kenneth Stokoe, whose work focuses largely on the spectral analysis of surface waves in the evaluation of roadways. In their work, In Situ Determination of Elastic Moduli of Pavement Systems By Spectral-Analysis-of-Surface-Wave Method: Practical Aspects¹, Nazarian and Stokoe discuss many of the practical and theoretical aspects of the method. In addition, the explanation of the MASW method also relied on the publication of Debra Underwood and Koichi Hayashi, Seismic Wave Surveying With Geometrics, Inc. Seismographs and SeisImager/SW, Geometrics Inc. Short Course Notes.²

¹ Nazarian, S. & Stokoe III, K.H. (1985). In Situ Determination of Elastic Moduli of Pavement Systems by Spectral-Analysis-of-Surface-Wave Method: Practical Aspects (Report No. FHWA/TX-86/13+368-1F). Austin, TX: Texas State Department of Highways and Public Transportation.

² Underwood, D.H. and Hayashi, K. (2005), Seismic Surface Wave Surveying With Geometrics, Inc. Seismographs and SeisImager/SW Software, Geometrics, Inc. Short Course Notes, San Jose, California and London, United Kingdom.

ANALYSIS PROCEDURE

Data files obtained in the field were imported and converted from SEG-2 data to KGS format into the Surfseis MASW software manufactured by the Kansas Geological Survey. Surfseis is a Windows based software for the analysis of multi-channel surface wave data.

The first step in the processing of the MASW data deals with the extraction of the dispersion curve from discrete 1-D seismic data sets, or shot-gathers. The dispersion curves are imaged through a wavefield-transformation method that directly converts the multi-channel record into a dispersion pattern where phase velocity is plotted versus frequency. The fundamental mode of the Rayleigh wave is then extracted and separated from the remainder of the dispersion images. This stripping of the unwanted portions of the wave-train allows further analysis of the fundamental mode of the Rayleigh Wave.

Following the transformation from the waveform record into the dispersion curve image, the initial S-wave velocity model is calculated. Vs velocities determined up to this point are not actual velocities of the subsurface layers, but are apparent Vs velocities. The existence of a layer with high or low velocity at the ground surface affects measurement velocities of the underlying layers. A method for evaluating Vs from apparent Vs is provided by the inversion process.

Inversion consists of the determination of the depth of each layer and the actual shear wave velocity of each layer from the apparent R-Wave velocity versus wavelength information. The mathematical process iteratively modifies the initial model of Vs to minimize the difference from the observed data. The inversion process is an iterative one in which a shear wave velocity profile is assumed and a theoretical dispersion curve is constructed. The observed and calculated dispersion curves are compared and necessary changes are made in the assumed shear wave velocity profile until the two curves match within a reasonable tolerance. The results of the inversion process generate a series of 1-D MASW profiles

Appendix-B of this report presents a set of figures for each of the twelve (12) MASW investigation lines collected in the study area. In each of the three locations MASW data was collected, a forward and reverse 5-foot spacing spread and a forward and reverse 2.5-foot spacing spread were collected totaling four (4) spreads at each location. The final Vs profiles are shown in **Combined Vs Velocity (ft/s) versus Depth (ft) Plots** (Figure 2, Figure 3, and Figure 4) of each MASW spread at each location shown to the same scale.

The first figure for each MASW line location in Appendix-B presents the seismic data, or **Multi-channel Waveform Record** (Figure 5 – Figure 16). This record captures the character and magnitude of ground vibrations as they travel through the geophone spread. This seismic data is referred to as a shot gather in geophysical literature. Following the multi-channel waveform record is the **Dispersion Curve Image** (Figure 5a – Figure 16a). This image is obtained directly from the original waveform record through a process where surface waves on the shot gather are converted into images of multi-mode dispersion curves. In these color coded dispersion curve images, phase velocity in feet per second (ft/sec) is plotted vs. frequency, in Hertz (Hz). The maximum amplitude for each frequency was picked on the dispersion curve image, and is represented by a series of dots.

Following the transformation from the waveform record into the dispersion curve image, The **Initial Model of Vs** (Figure 5b – Figure 16b) with depth was calculated. The initial model of Vs is presented as a plot of S-wave velocity versus depth. The initial Vs model is calculated from the one-third wavelength approximation represented by the green circles pictured. Vs velocities determined up to this point are

not actual velocities of the subsurface layers, but are apparent Vs velocities. The existence of a layer with high or low velocity at the ground surface affects measurement velocities of the underlying layers. A method for evaluating Vs from apparent Vs is provided by the inversion process.

Inversion consists of the determination of the depth of each layer and the actual shear wave velocity of each layer from the apparent R-Wave velocity versus wavelength information. The mathematical process is based on the Least-Squares Method and simply stated, iteratively modifies the initial model of Vs to minimize the difference from the observed data. The inversion process is an iterative one in which a shear wave velocity profile is assumed and a theoretical dispersion curve is constructed. The observed and calculated dispersion curves are compared and necessary changes are made in the assumed shear wave velocity profile until the two curves match within a reasonable tolerance. The **Final Vs Profile** (Figure 5c – Figure 16c) is generated in the inversion process. Results of this inversion is shown in Appendix-B following the initial model of Vs. The values utilized in the calculation of the Final Vs Profile are shown in table form (Figure 5d – Figure 16d) following the final Vs profile.

DISCUSSION OF MASW DATA

The Vs for each MASW spread location is presented in Appendix-B of this report. The calculated shear wave velocity for each MASW spread location is plotted versus depth. The values utilized in the profiles are also presented in table form.

A total of twelve (12) MASW investigation lines were run in the investigation area. The locations of the MASW spreads run were largely controlled by the available open terrain encountered at the project area because of previous rainfall. The midpoints of the MASW spreads all coincided with the midpoint of the seismic refraction spread in the same location. The location of these MASW investigation lines can be referenced in the Appendix-A plan. The following table presents MASW line specifics:

| MASW Line Nomenclature | Line Location | Length (feet) | Forward or Reverse Shot |
|------------------------|--------------------|---------------|-------------------------|
| File 54 | North End Jeddo 14 | 115 | Forward |
| File 55 | North End Jeddo 14 | 115 | Reverse |
| File 56 | North End Jeddo 14 | 57.5 | Reverse |
| File 57 | North End Jeddo 14 | 57.5 | Forward |
| File 58 | South End Jeddo 14 | 115 | Forward |
| File 60 | South End Jeddo 14 | 115 | Reverse |
| File 61 | South End Jeddo 14 | 57.5 | Reverse |
| File 62 | South End Jeddo 14 | 57.5 | Forward |
| File 63 | Jeddo 8 | 115 | Forward |
| File 64 | Jeddo 8 | 115 | Reverse |
| File 65 | Jeddo 8 | 57.5 | Reverse |
| File 66 | Jeddo 8 | 57.5 | Forward |

The following table presents a general classification of materials along with their respective average shear wave velocity ranges.

| PROFILE NAME | AVERAGE PROPERTIES IN TOP 100 FEET (SOIL SHEAR WAVE VELOCITY, V_s) (ft/s) |
|--------------------------------------|---|
| Hard Rock | $V_s > 5,000$ |
| Rock | $2,500 < V_s \leq 5,000$ |
| Very dense Coal Refuse and Soft Rock | $1,200 < V_s \leq 2,500$ |
| Stiff Coal Refuse profile | $600 \leq V_s \leq 1,200$ |
| Soft Coal Refuse profile | $V_s < 600$ |

As seen in the Combined V_s Velocity (ft/s) versus Depth (ft) Plot in Figure 2, the Jeddo 8 MASW results from a depth of 0 to 20 feet yielded V_s velocities of 250 ft/s to 400 ft/s. Velocities from a depth of 20 feet to 30 feet range from 400 ft/s to 800 ft/s. At depths of 30 feet to 40 feet velocities range from 1030 ft/s to 1300 ft/s. At depths below 40 feet the MASW data was not considered reliable due to the deeper velocity inversions in the final models. This profile is interpreted as a soft coal refuse at shallower depths moving to a stiff and then very dense coal refuse/soft rock at deeper depths.

As seen in the Combined V_s Velocity (ft/s) versus Depth (ft) Plot in Figure 3, the Jeddo 14 North End MASW results from a depth of 0 to 13 feet yielded V_s velocities of 220 ft/s to 400 ft/s. Velocities from a depth of 13 to 25 feet range from 400 ft/s to 500 ft/s. At depths of 25 feet to 45 feet velocities range from 500 ft/s to 675 ft/s. At depths below 45 feet the MASW data was not considered reliable due to the deeper velocity inversions in the final models. This profile is interpreted as a soft coal refuse at shallower depths moving to a stiff coal refuse at deeper depths.

As seen in the Combined V_s Velocity (ft/s) versus Depth (ft) Plot in Figure 4, the Jeddo 14 South End MASW results from a depth of 0 to 12 feet yielded V_s velocities of 250 ft/s to 350 ft/s. Velocities from a depth of 12 to 27 feet range from 350 ft/s to 550 ft/s. At depths of 27 feet to 40 feet velocities range from 550 ft/s to 670 ft/s. At depths below 40 feet the MASW data was not considered reliable due to the deeper velocity inversions in the final models. This profile is interpreted as a soft coal refuse at shallower depths moving to a stiff coal refuse at deeper depths.

Seismic Refraction Data Acquisition Procedure

Standard shallow seismic refraction techniques were used for this survey. A twenty-four channel, Geometrics Strataview seismograph was used to record the field data. The instrument was set to acquire seismic records of 512 ms in length with a sample interval of 500 μ s. No pre-acquisition filters were used on the data. Three (3) seismic refraction spreads were collected at Jeddo Coal. One spread in the Jeddo 8 impoundment and two spreads in the Jeddo 14 impoundment, one in the north end and one in the south end of the impoundment.

On each of the traverse lines, spreads of twenty-four geophones (Mark Products L-10A, 14 Hz), with 10-foot spacing between geophones, were placed along the ground surface. At the beginning, end, and

three points interior to the spread, seismic energy was transmitted into the ground. Additional shot points were also recorded from points offset from either end of the spreads. The seismic energy source was a light explosive charge buried in the ground. The travel time of the seismic energy, from the source point to each geophone, was stored in the seismograph's internal memory then transferred to disk for later analysis.

Analysis Procedure

The first step in analyzing the seismic refraction data was to pick the onset of the compressional wave arrival for each shot point-geophone pair. The onset of the compressional wave arrivals for the recorded data on this project was picked using Interpex's Firstpix Software that enabled the enhancement of each individual seismic trace.

Appendix-C shows the suite of records for the three spreads. The onset of the compressional wave arrival is marked with a computer generated tick mark. The arrival times were then plotted as a function of the shot point-geophone field geometry to produce the correct **Travel Time Curves** (Figure 17 – Figure 19) for analysis. The travel time curves were then analyzed using the Generalized Reciprocal Method (GRM). This produced an **Elevation and Velocity Profile** (Figure 17a – Figure 19a) of the layers present at those locations. After the elevation model is a table showing velocities and depths at each geophone location (Figure 17b – Figure 19b) and also a table of the reciprocal time estimates (Figure 17c – Figure 19c). Appendix-D provides a short discussion of how the seismic refraction technique works along with a brief explanation of the GRM.

Factors Affecting Seismic Velocity

The compressional wave velocity is a direct measure of the strength, hardness, and degree of compaction of the material. Unconsolidated soil overburden would have a low velocity (1,000-2,000 ft/sec), whereas hard, unweathered bedrock would have a high velocity (10,000 ft/sec). We have classified the following material types from the seismic profiles in terms of compressional wave velocity. Based upon Vibra-Tech's experience, field observations, and published work of others, our interpretation of the materials represented by the seismic velocities is as follows:

| Compressional Wave Velocities (kilofeet/second) | Description of Material |
|---|---------------------------------|
| 0.3 – 2.7 | Dry, Unconsolidated Coal Refuse |
| 4.6 – 5.5 | Water Saturated Coal Refuse |
| 4.6-7.3 | Weathered Bedrock |
| 10.7 – 17.7 | Unweathered Bedrock |

Discussion of Seismic Refraction Data

A total of three (3) seismic refraction spreads were run in the project area, consisting of overlapping seismic refraction and MASW spreads. Appendix-A presents an aerial photo showing the location of the seismic refraction spreads located in Jeddo 8 (Figure 1a) and Jeddo 14 (Figure 1b).

In the upper Elevation Profile, the uppermost line displays the topography across the seismic profile. Displayed beneath the topography is the interpreted refracted layer. The refraction layer interface is defined by an undulating horizontal line displayed beneath the topography. This line defines the depth to the top of the underlying layer. In the lower Velocity Profile, the variation in compressional wave velocity of the earth materials across the seismic spread is displayed beneath their respective fields, in feet/second. The values used to construct the velocity and elevation (depth) sections for each of the cross sections are presented in Appendix-C following each of the seismic sections.

As seen in Figure 17a, results of the seismic profiling at the Jeddo 8 location yielded a two-layer model. Layer 1 is a surface layer with a depth of 0 to 30 feet on average that exhibited compressional wave velocities ranging from 835 ft/s to 1040 ft/s. Velocities in this range are indicative of a dry, unconsolidated coal refuse. Layer 2 ranged in seismic travel velocities from 3,918 ft/s through 4128 ft/s and is interpreted as water saturated materials.

As seen in Figure 18a, results of the seismic profiling at the Jeddo 14 North End location yielded a two-layer model. Layer 1 is a surface layer with a depth of 0 to 2 feet on the west end of the spread and deepens to 15 feet on the east end of the spread. Layer 1 exhibited compressional wave velocities ranging from 370 ft/s to 723 ft/s. Velocities in this range are indicative of a dry, unconsolidated coal refuse. Layer 2 ranged in seismic travel velocities from 2422 ft/s through 2897 ft/s and is interpreted as waste rock or more consolidated coal refuse.

As seen in Figure 19a, results of the seismic profiling at the Jeddo 14 South End location yielded a three-layer model. Layer 1 is a surface layer with a depth of 0 to 2 feet on the west end of the spread and deepens to 11 feet on the east end of the spread. Layer 1 exhibited compressional wave velocities ranging from 526 ft/s to 816 ft/s. Velocities in this range are indicative of a dry, unconsolidated coal refuse. Layer 2 ranged in seismic travel velocities from 1646 ft/s through 2724 ft/s and is interpreted as waste rock or more consolidated coal refuse. Layer 2 ranged in thickness from 2 feet through 79 feet on the west end of the spread and 11 feet to 60 feet on the east end of the spread. Layer 3 ranged in seismic velocities from 3046 ft/s through 5258 ft/s. Velocities in this range are typical of weathered bedrock/waste rock material. Depths to the top of Layer 3 ranged from 79 feet on the west end of the spread and 60 feet on the east end of the spread.

CONCLUSION

The three seismic refraction investigation lines and the twelve MASW investigation lines run at Jeddo Coal were able to shed light on the seismic characteristics of the coal refuse in Jeddo 8 and Jeddo 14. Jeddo 8 was investigated to a depth of approximately 40 feet and resulted in Vs velocities of 250 ft/s to 1300 ft/s and compressional wave velocities of 835 ft/s to 4128 ft/s.

The Jeddo 14 North End location was investigated to a depth of approximately 45 feet and resulted in Vs velocities of 220 ft/s to 675 ft/s and compressional wave velocities of 370 ft/s to 2897 ft/s.

The Jeddo 14 South End location was investigated to a depth of approximately 80 feet and resulted in Vs velocities of 250 ft/s to 670 ft/s and compressional wave velocities of 526 ft/s to 5258 ft/s.

Respectfully submitted,
Vibra-Tech Engineers, Inc.



Ryan Jubran
Geological Technician, G.I.T.






Douglas Rudenko, P.G.
Vice President

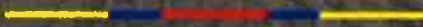
Appendix A

Jeddo 8 Figure 1a

Geophysical Line Locations

Legend

-  115' MASW
-  230' Seismic Refraction
-  57.5' MASW






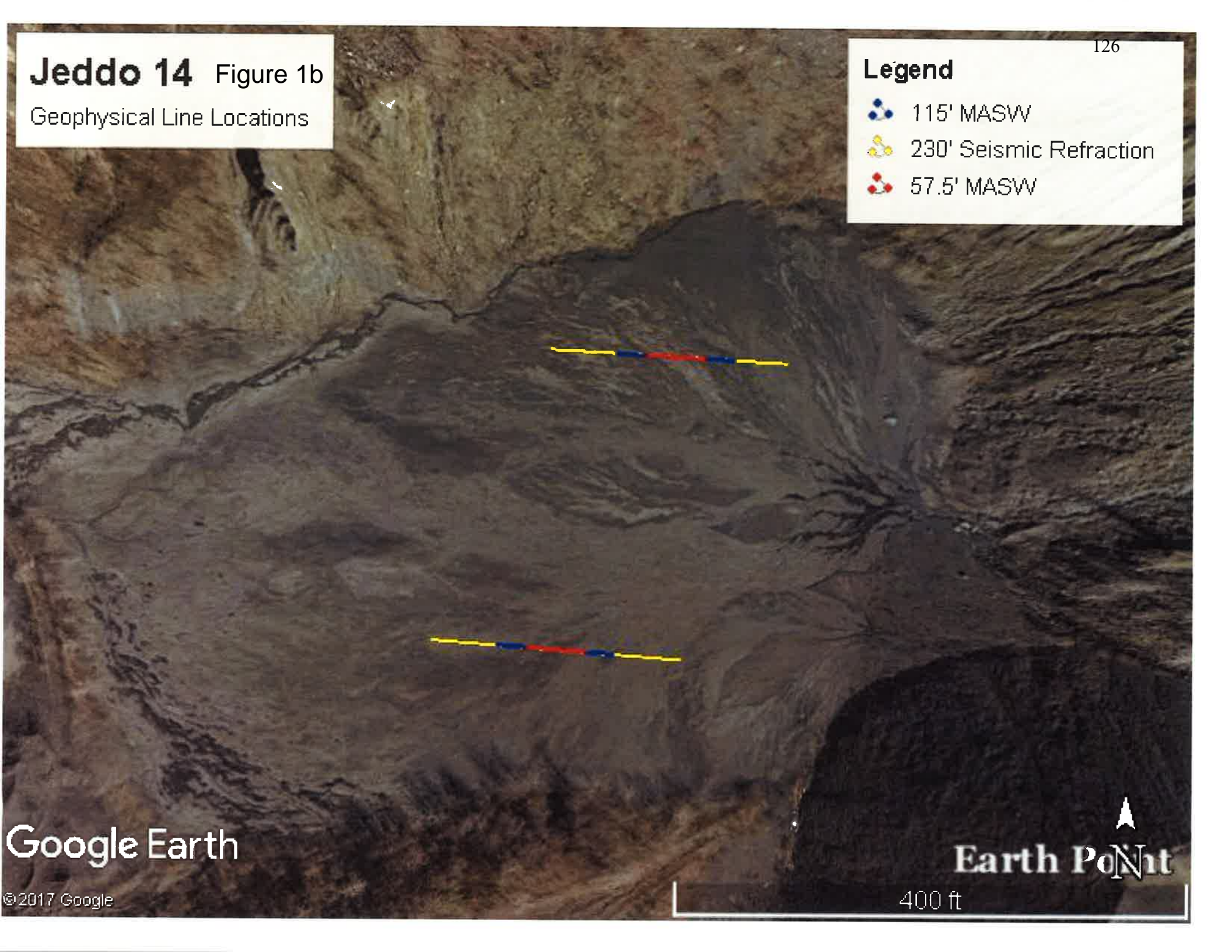
Google Earth

Earth Point 

Jeddo 14 Figure 1b
Geophysical Line Locations

Legend

-  115' MASW
-  230' Seismic Refraction
-  57.5' MASW



Google Earth

© 2017 Google

Earth Point

400 ft

Geophysical Line Locations - Midpoint is Same for all three lines
GPS coordinates are based off of 230' Seismic Refraction Profile

Jeddo 14 North End

Midpoint N40° 59.026 W075°56.738
West End N40° 59.025 W075°56.715
East End N40° 59.027 W075°56.764

Jeddo 14 South End

Midpoint N40° 58.978 W075°56.737
West End N40° 58.980 W075°56.763
East End N40° 58.981 W075°56.789

Jeddo 8

Midpoint N40° 58.922 W075°56.277
West End N40° 58.922 W075°56.302
East End N40° 58.922 W075°56.326

Appendix B

Figure 2

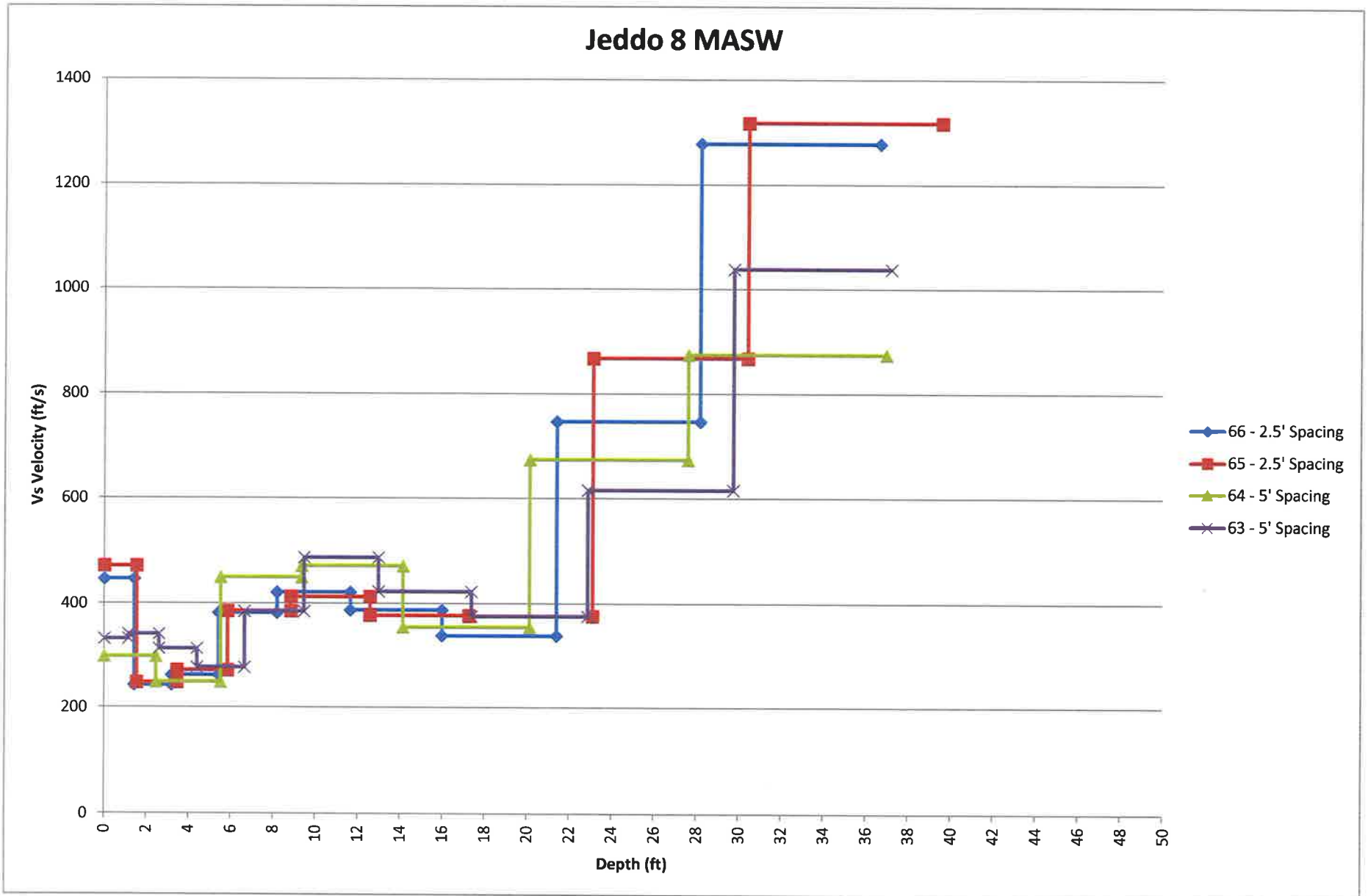


Figure 3

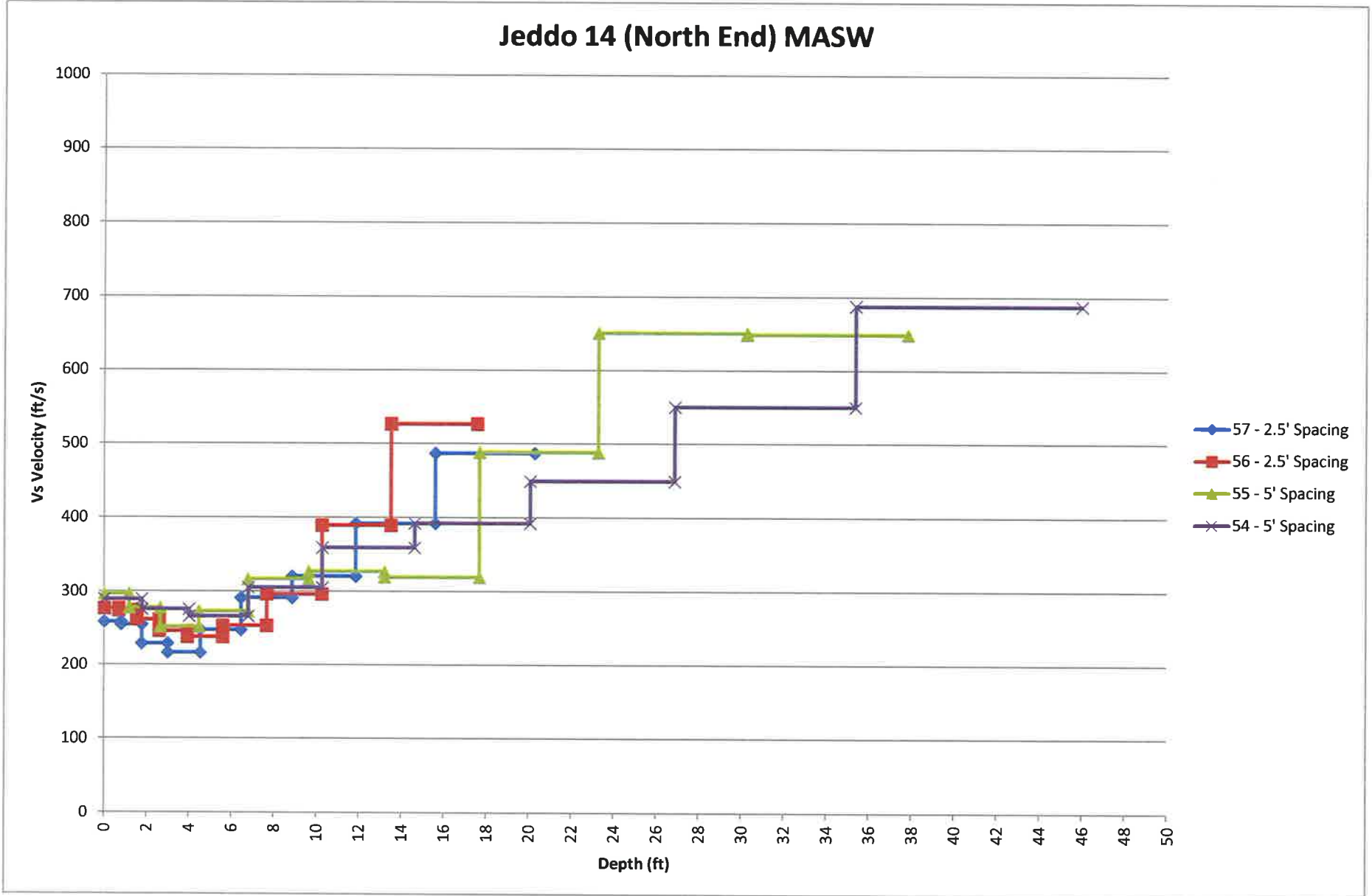


Figure 4

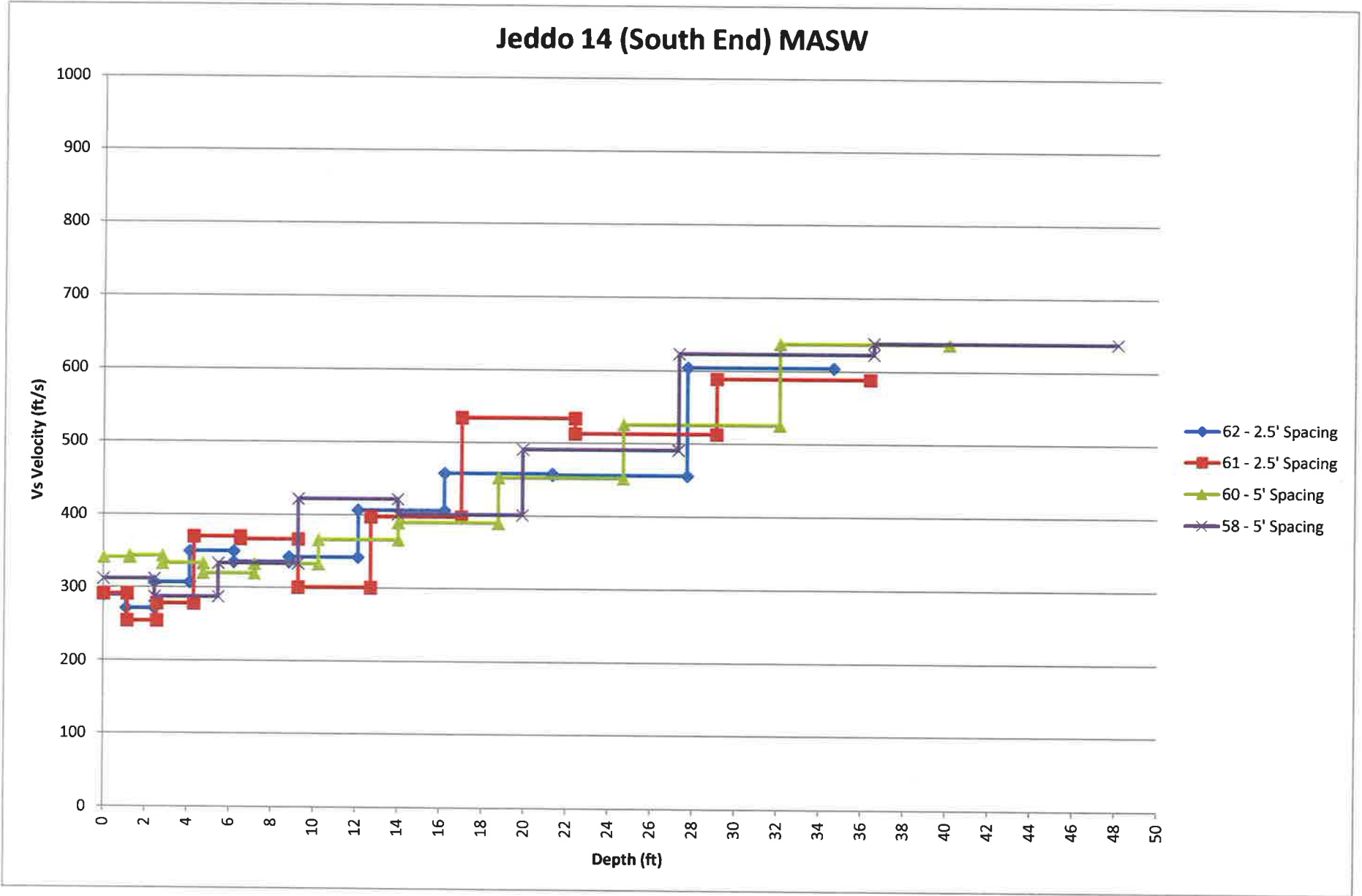


Figure 5

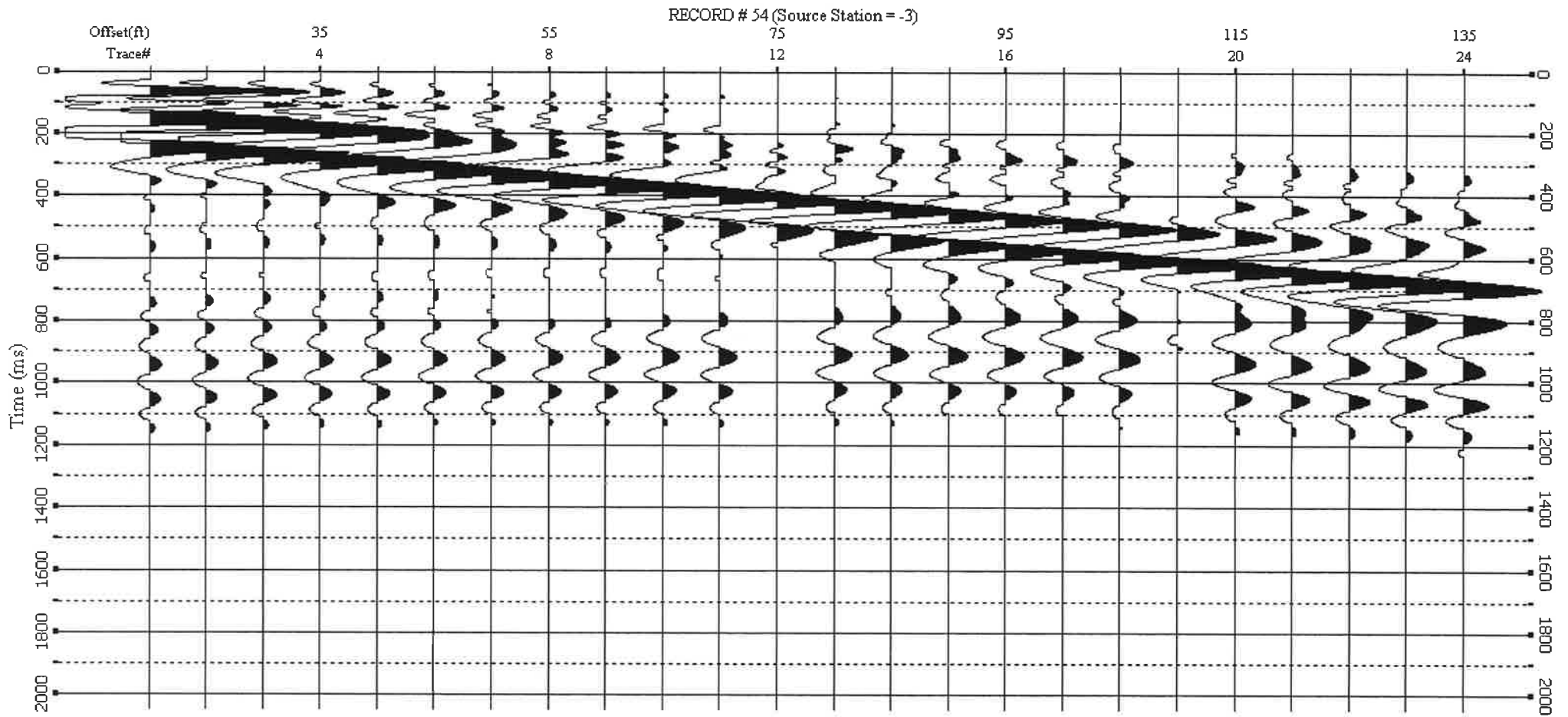


Figure 5a

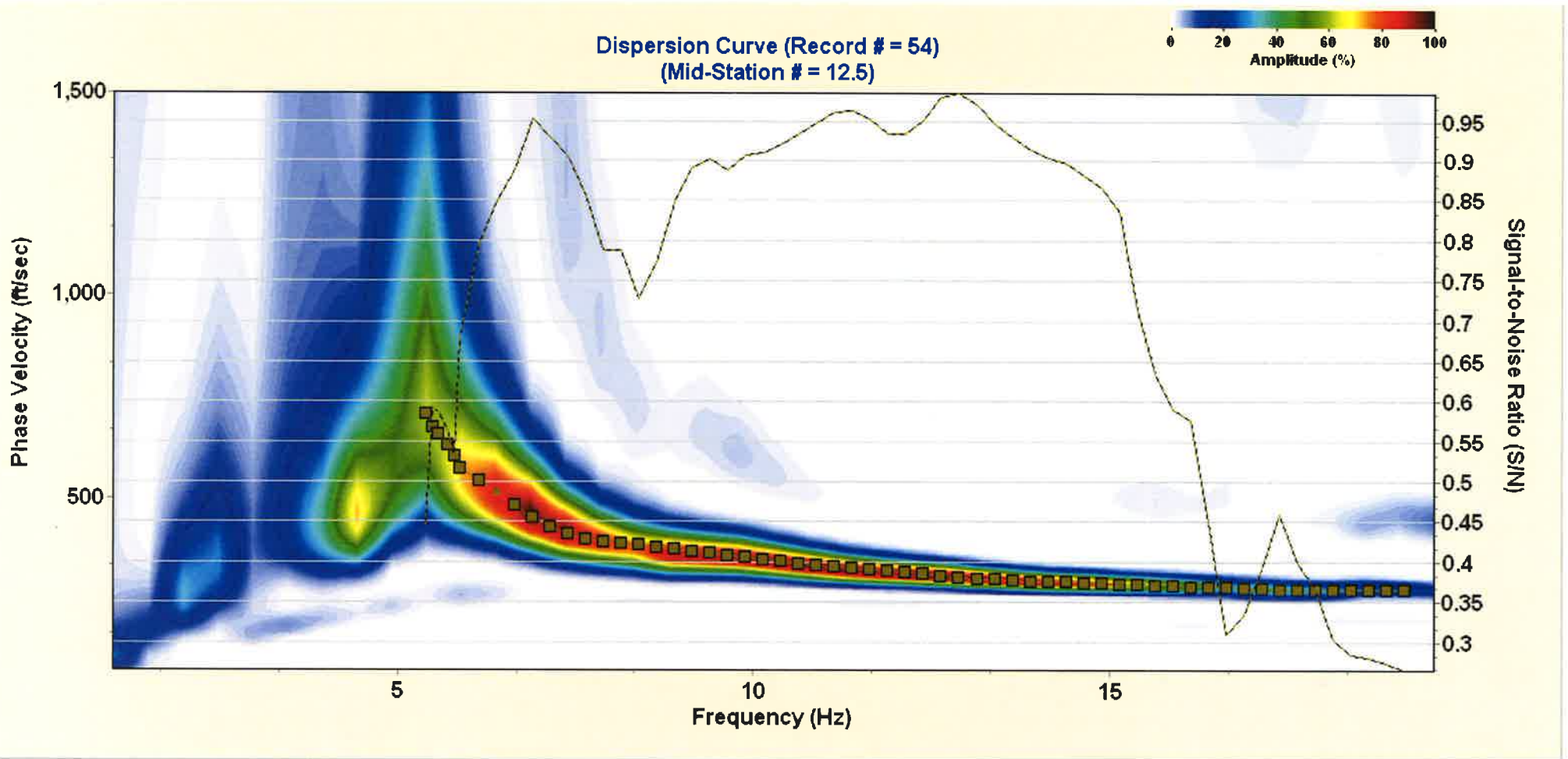


Figure 5b
Velocity Model

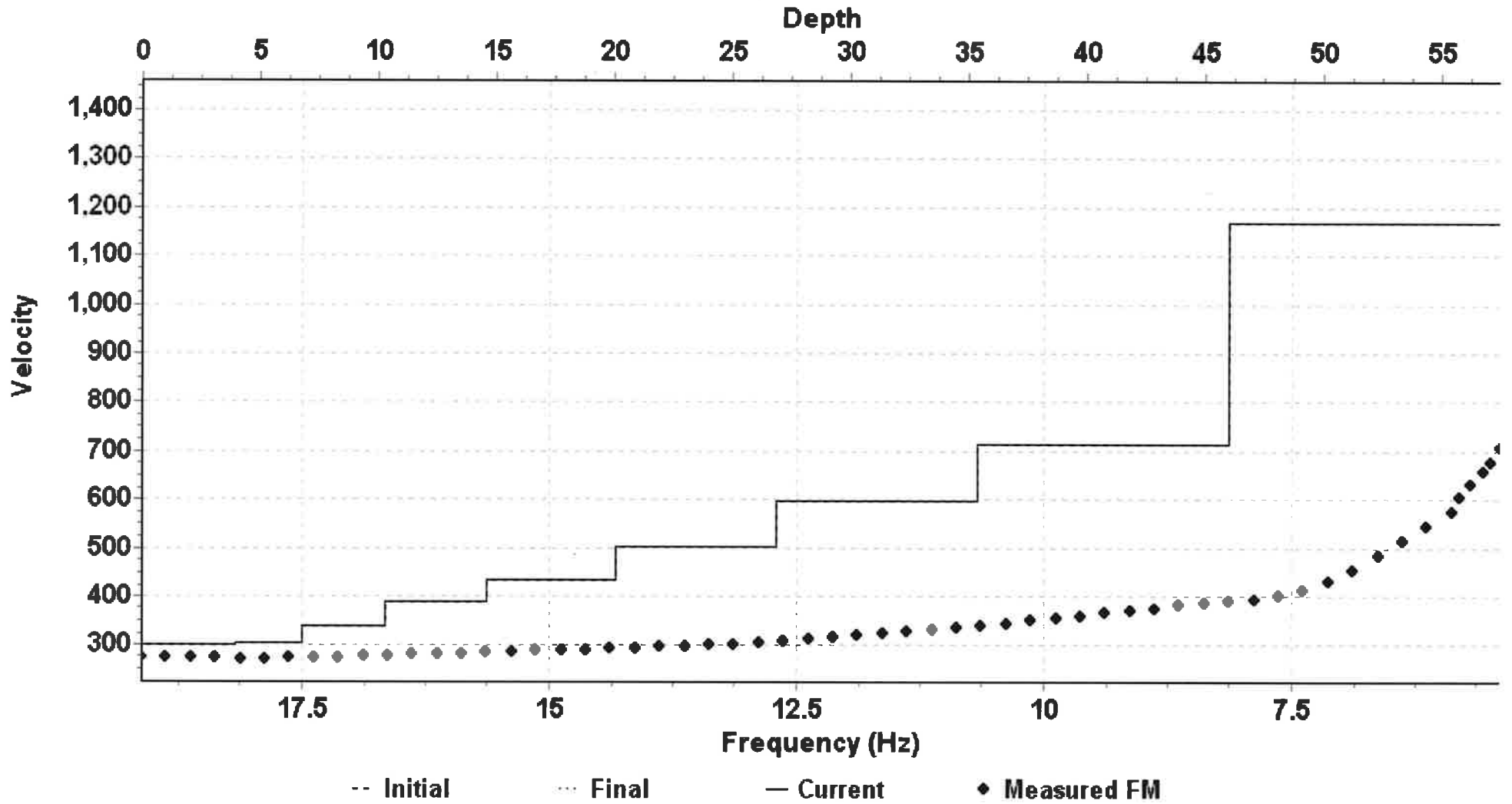


Figure 5c
 10-LAYER VELOCITY MODEL (Record = 54)
 (Mid-Station = 12.5)

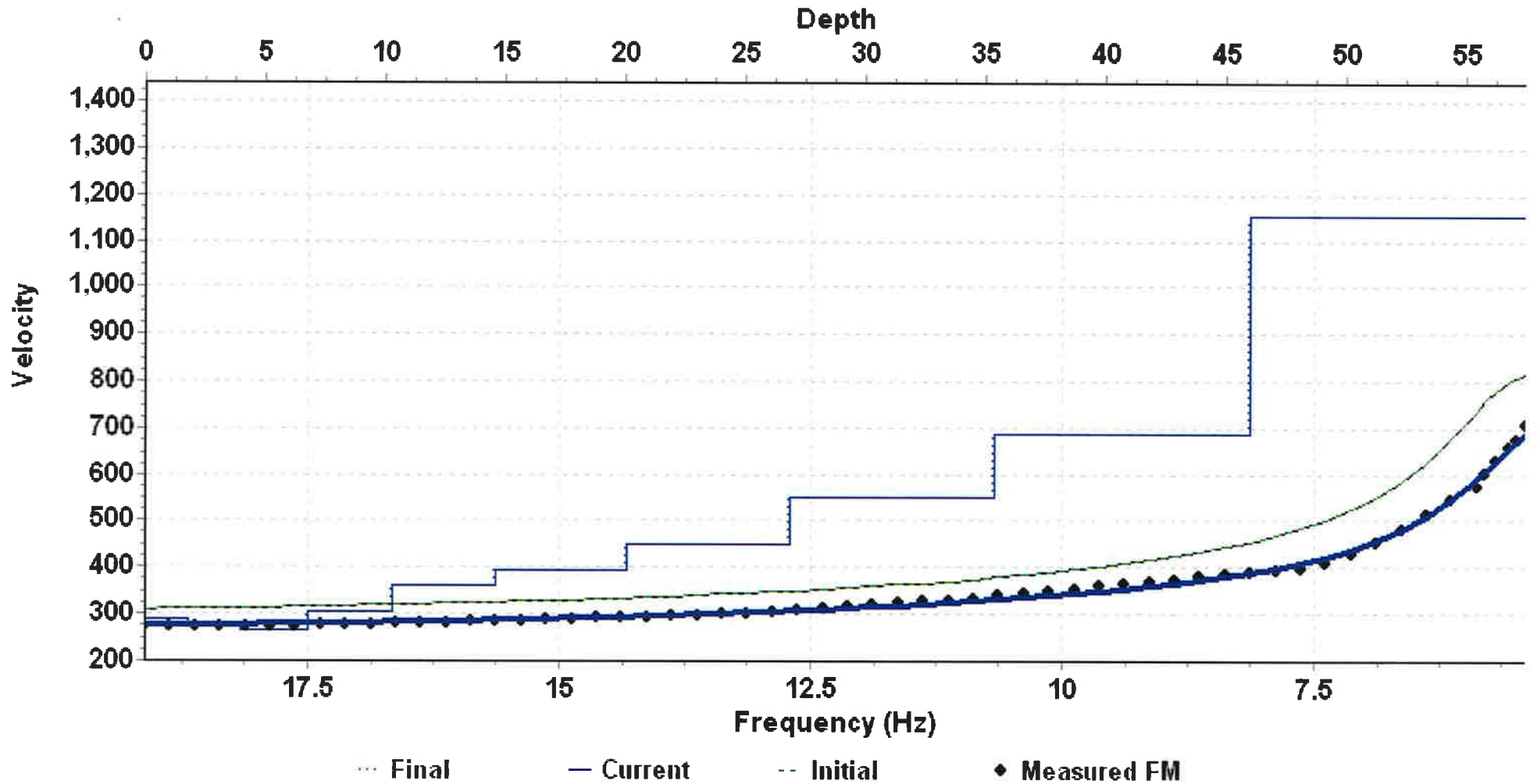


Figure 5d

MASW Line 54

| Layer | Depth (ft) | Vs Velocity (ft/s) |
|--------------|-------------------|---------------------------|
| 1 | -1.782 | 289.32 |
| 2 | -4.01 | 275.674 |
| 3 | -6.795 | 265.985 |
| 4 | -10.276 | 305.234 |
| 5 | -14.627 | 359.121 |
| 6 | -20.066 | 392.197 |
| 7 | -26.865 | 449.314 |
| 8 | -35.364 | 549.851 |
| 9 | -45.987 | 687.68 |
| 10 | -57.484 | 1153.236 |

Figure 6

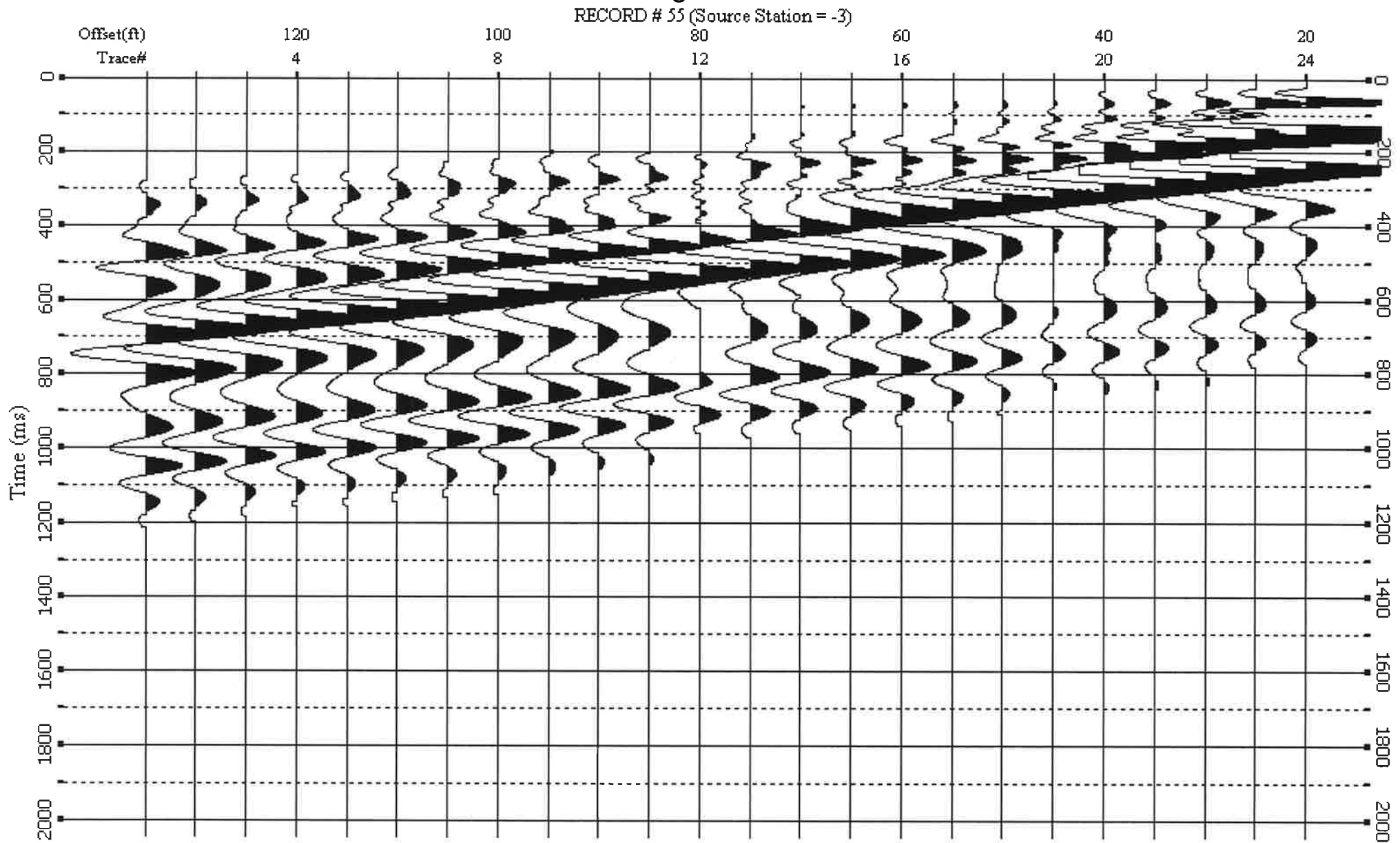
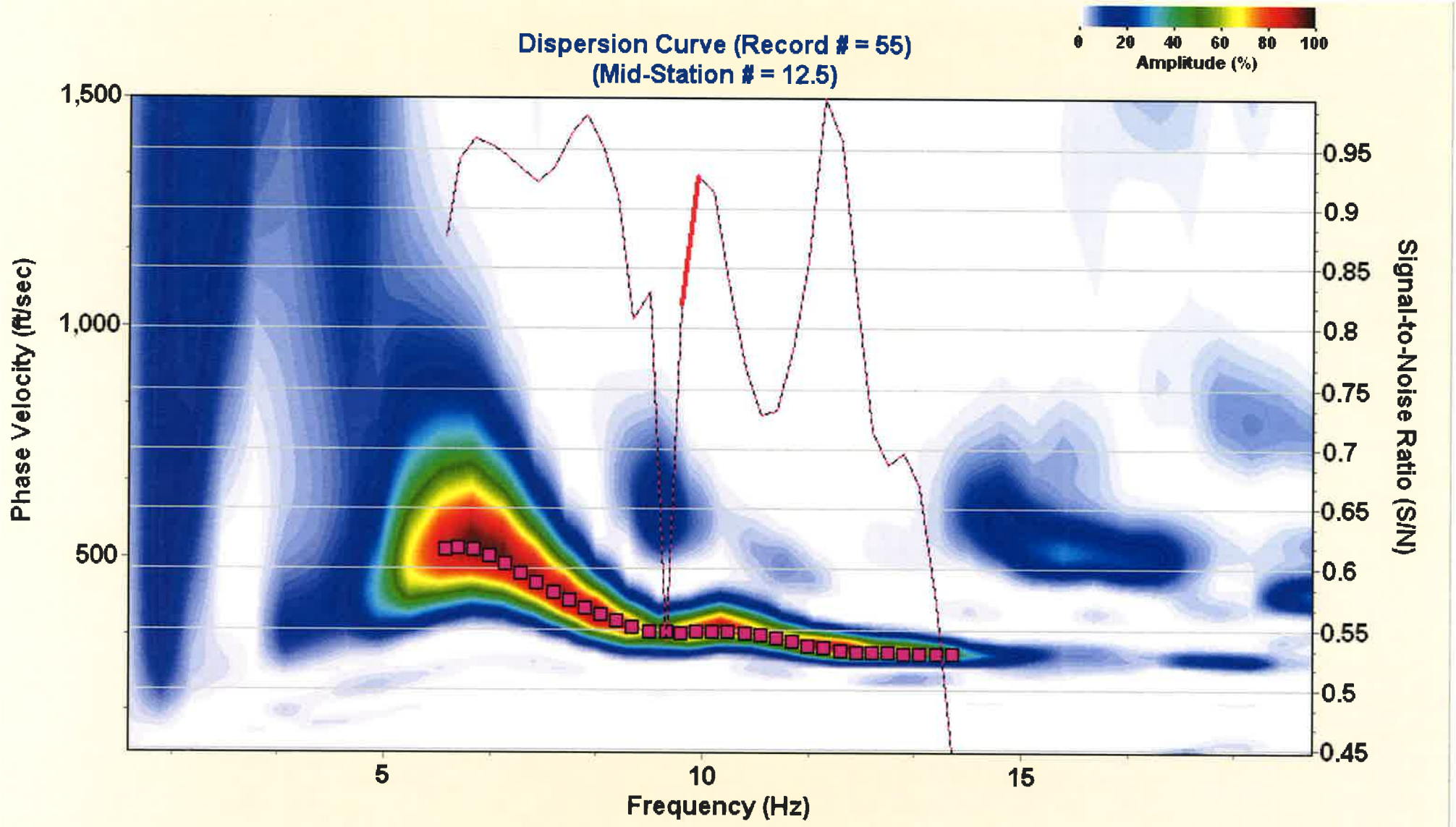
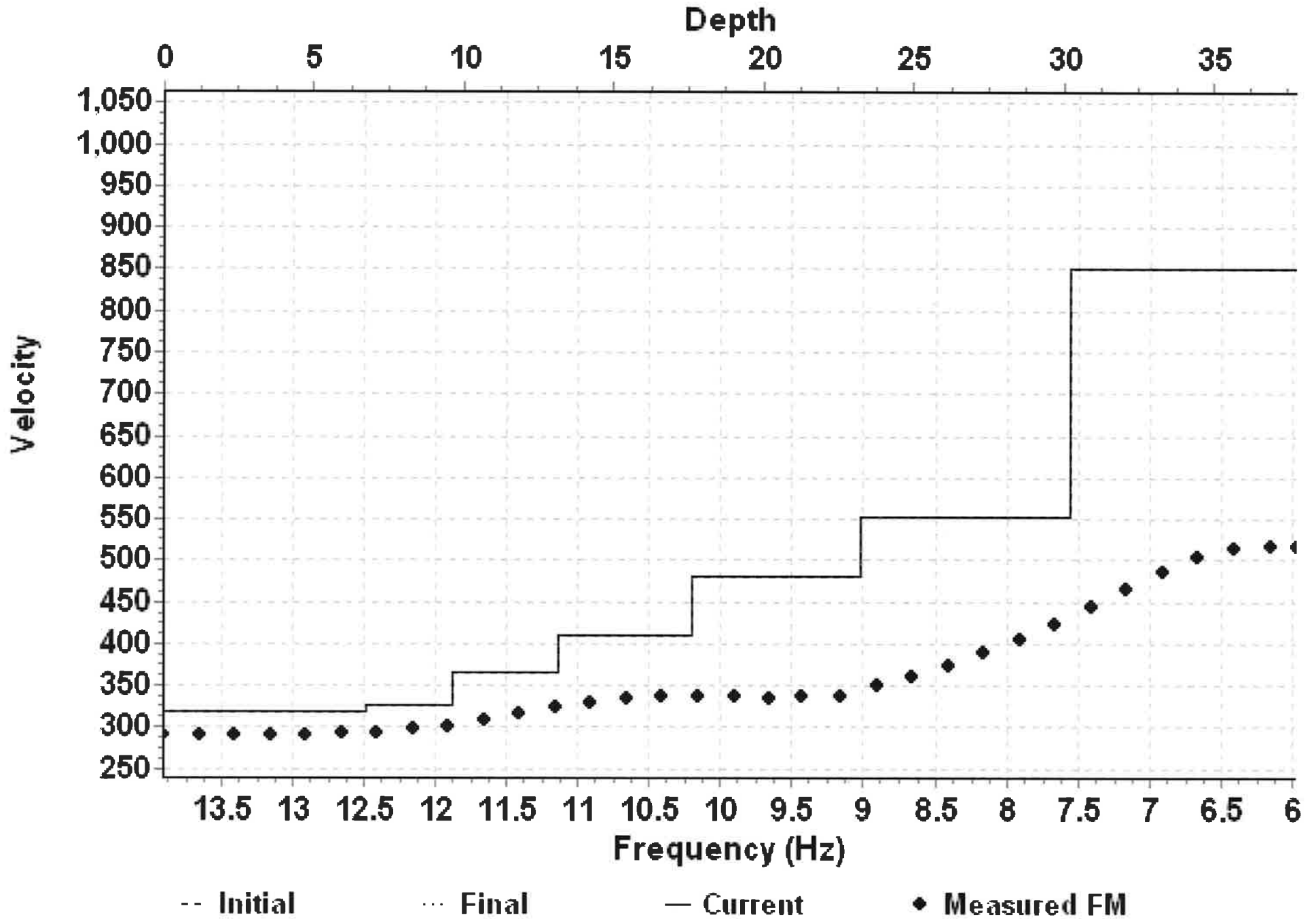


Figure 6a



Velocity Model



**10-LAYER VELOCITY MODEL (Record = 55)
(Mid-Station = 12.5)**

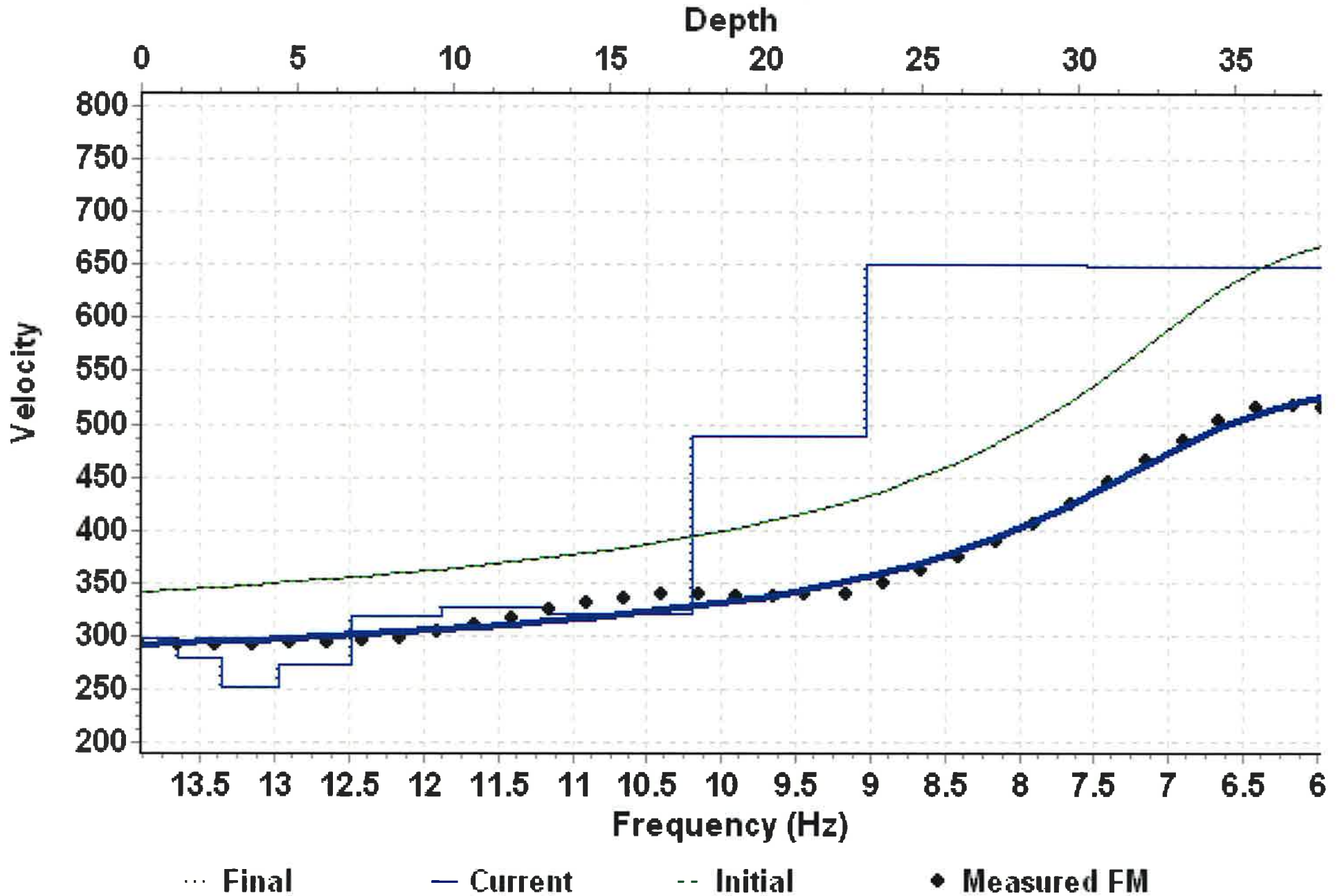


Figure 6d

MASW Line 55

| Layer | Depth (ft) | Vs Velocity (ft/s) |
|--------------|-------------------|---------------------------|
| 1 | -1.172 | 296.762 |
| 2 | -2.638 | 277.921 |
| 3 | -4.47 | 251.497 |
| 4 | -6.76 | 272.844 |
| 5 | -9.622 | 316.741 |
| 6 | -13.2 | 327.039 |
| 7 | -17.672 | 319.434 |
| 8 | -23.263 | 488.269 |
| 9 | -30.251 | 650.769 |
| 10 | -37.814 | 648.839 |

Figure 7

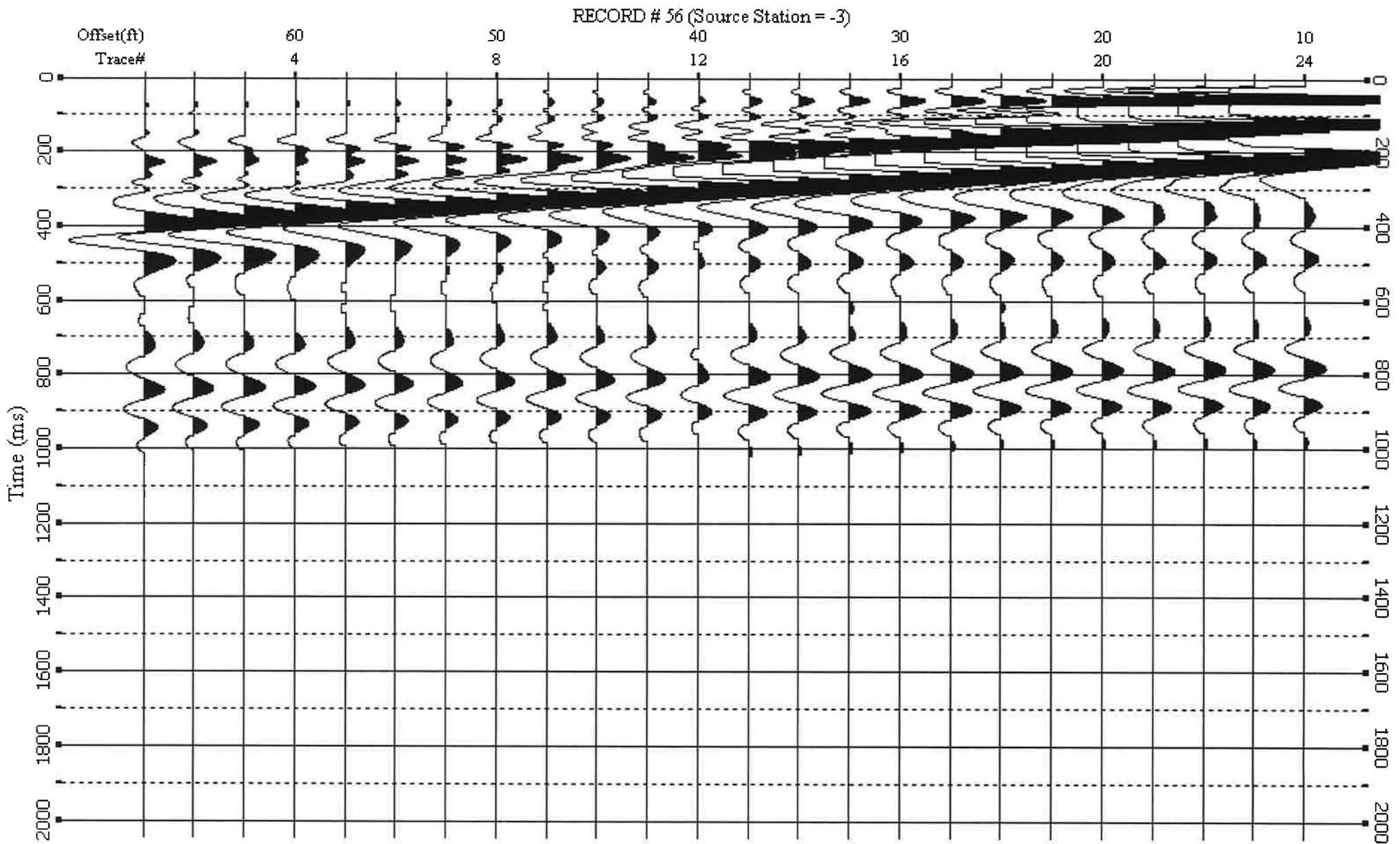
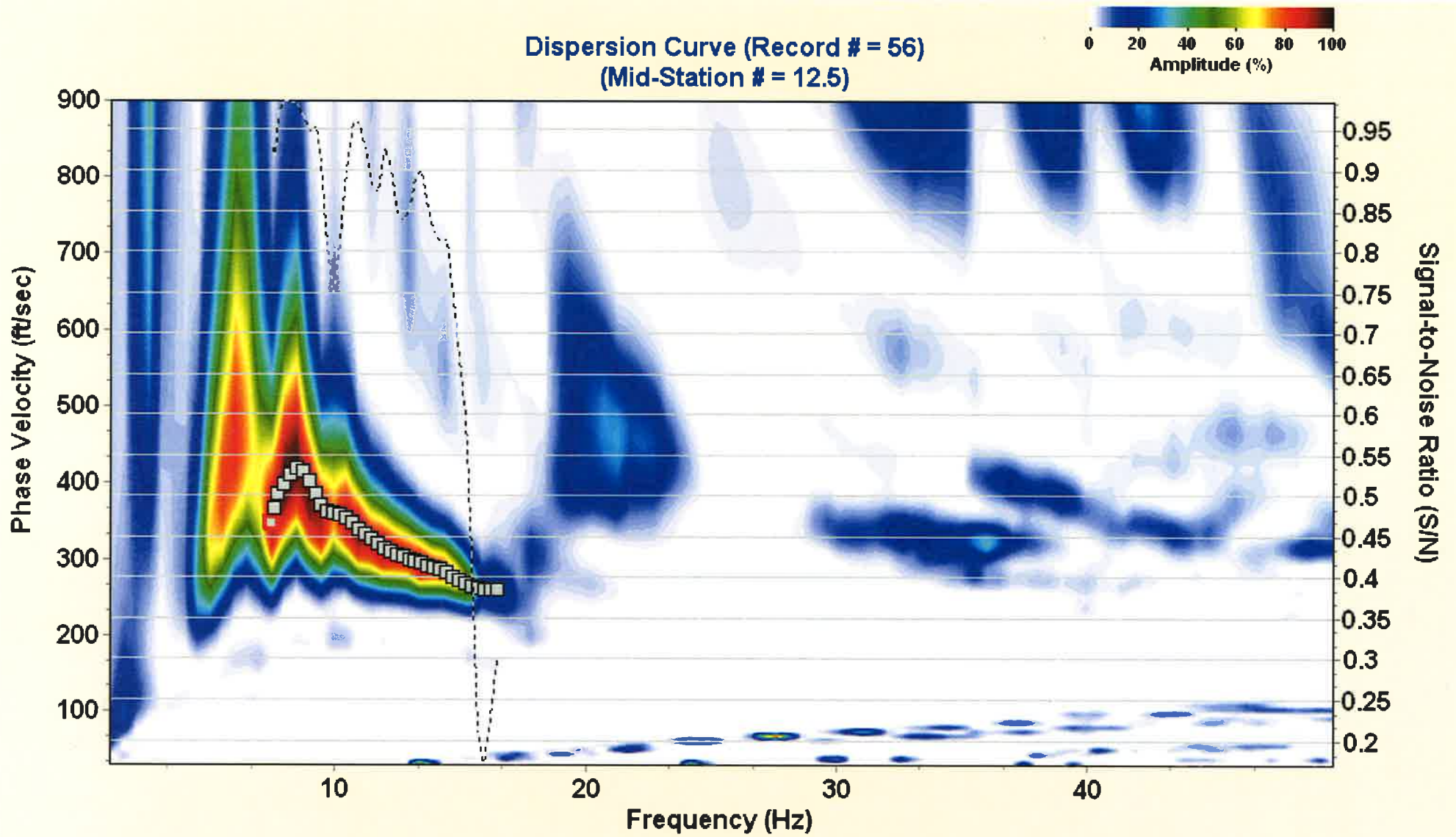


Figure 7a



Velocity Model

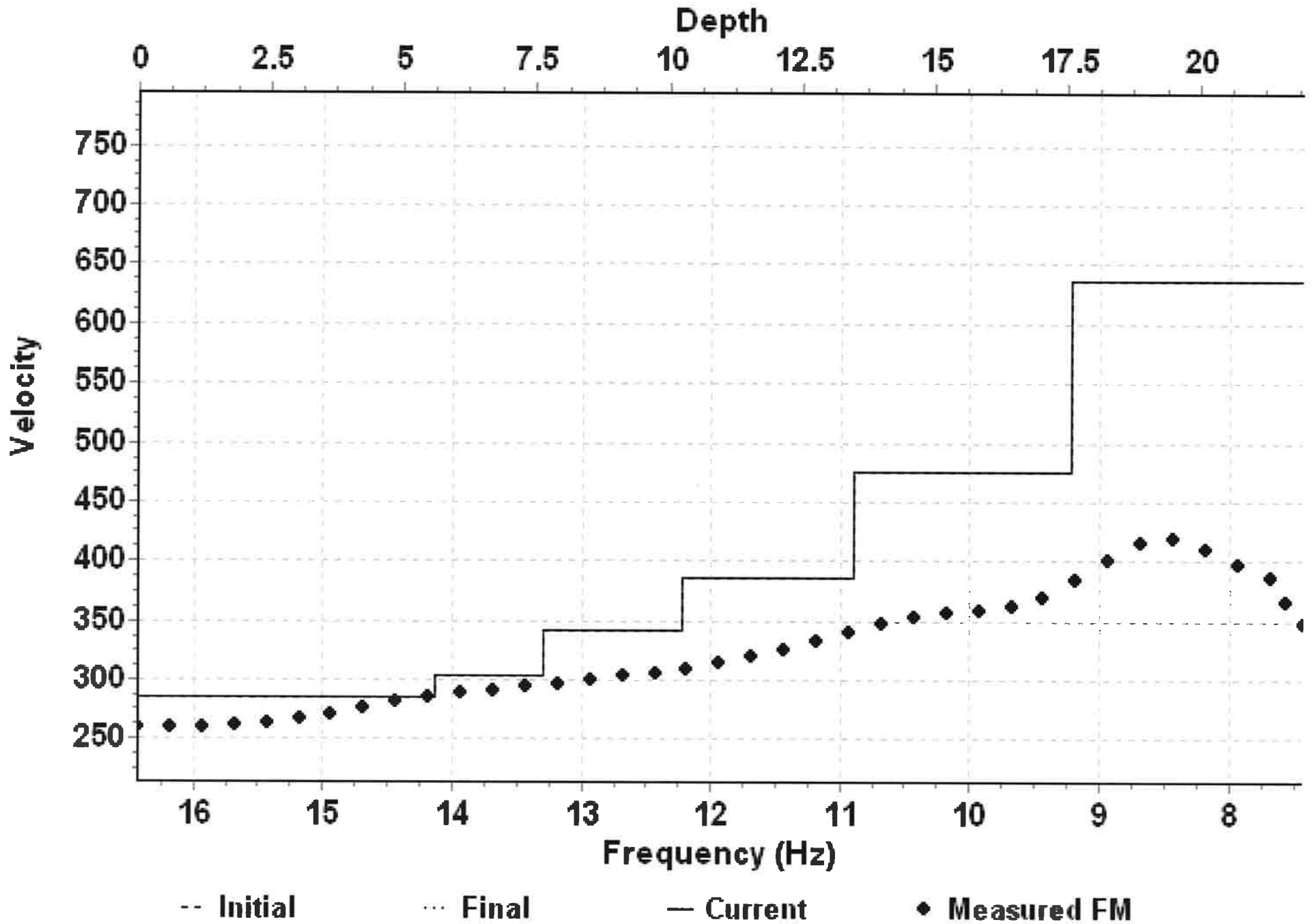


Figure 7c

10-LAYER VELOCITY MODEL (Record = 56)
(Mid-Station = 12.5)

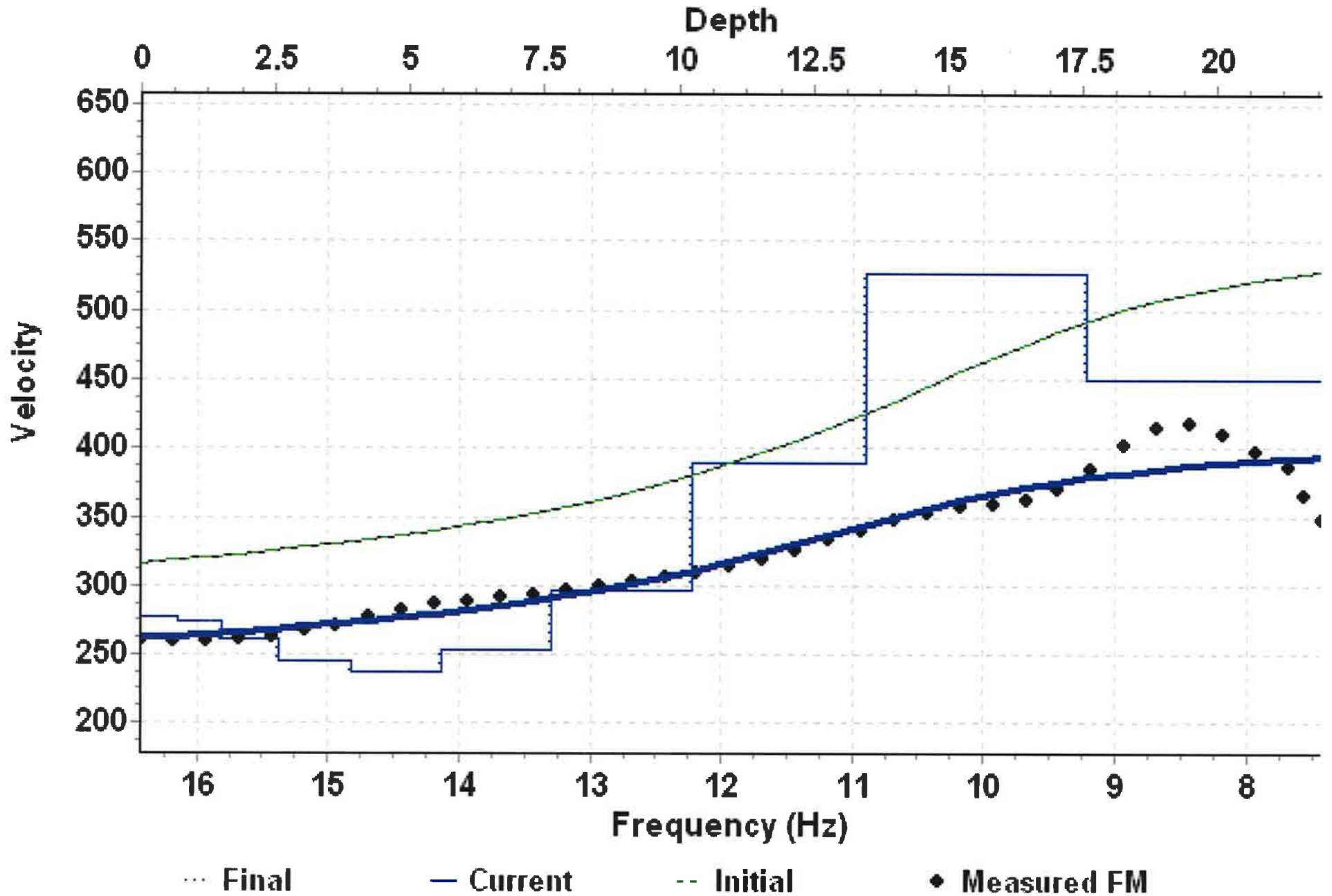


Figure 7d

MASW Line 56

| Layer | Depth (ft) | Vs Velocity (ft/s) |
|--------------|-------------------|---------------------------|
| 1 | -0.681 | 276.649 |
| 2 | -1.532 | 273.713 |
| 3 | -2.595 | 261.378 |
| 4 | -3.924 | 245.606 |
| 5 | -5.586 | 237.535 |
| 6 | -7.663 | 252.888 |
| 7 | -10.259 | 296.184 |
| 8 | -13.504 | 389.345 |
| 9 | -17.561 | 526.241 |
| 10 | -21.951 | 449.206 |

Figure 8

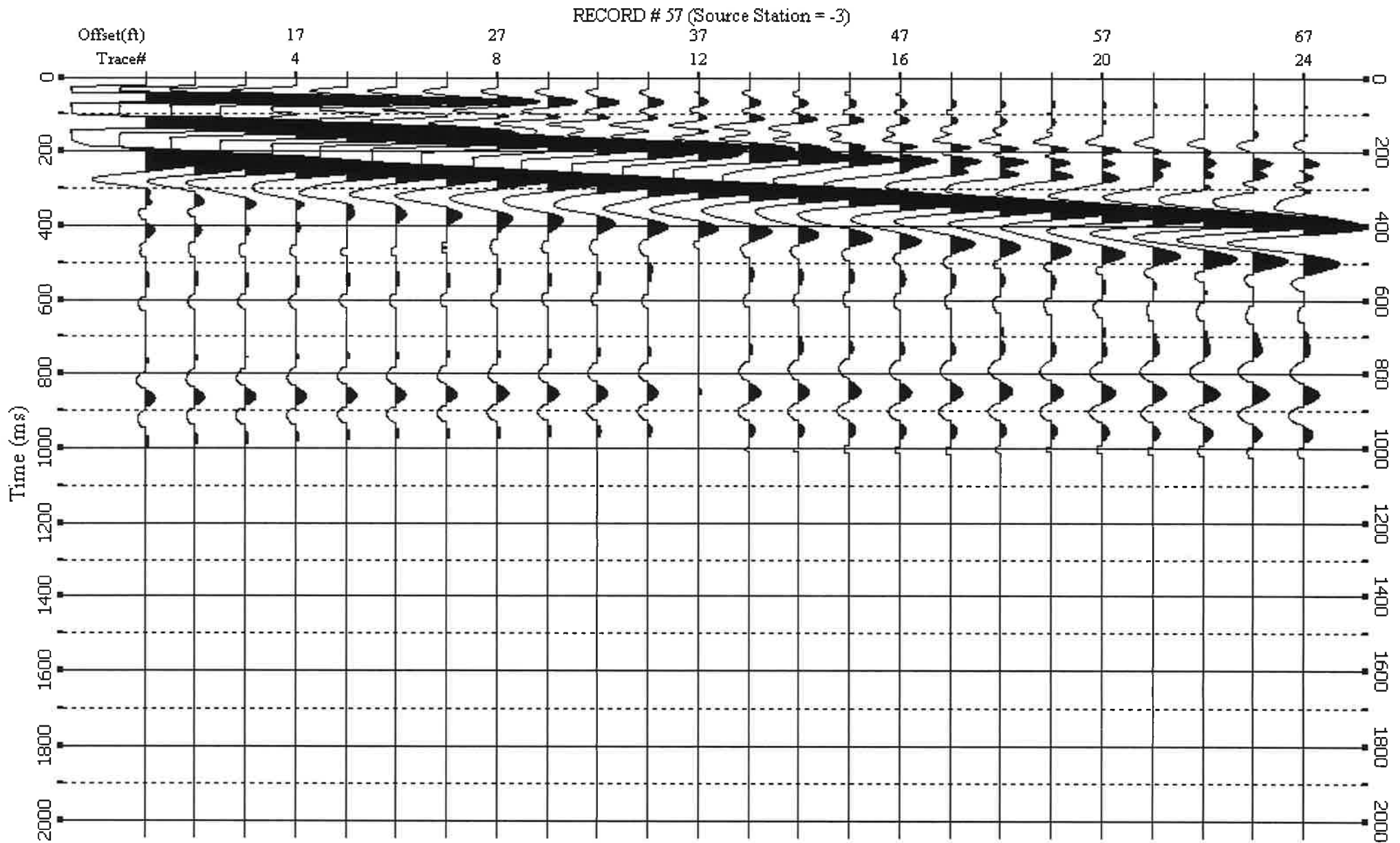


Figure 8a

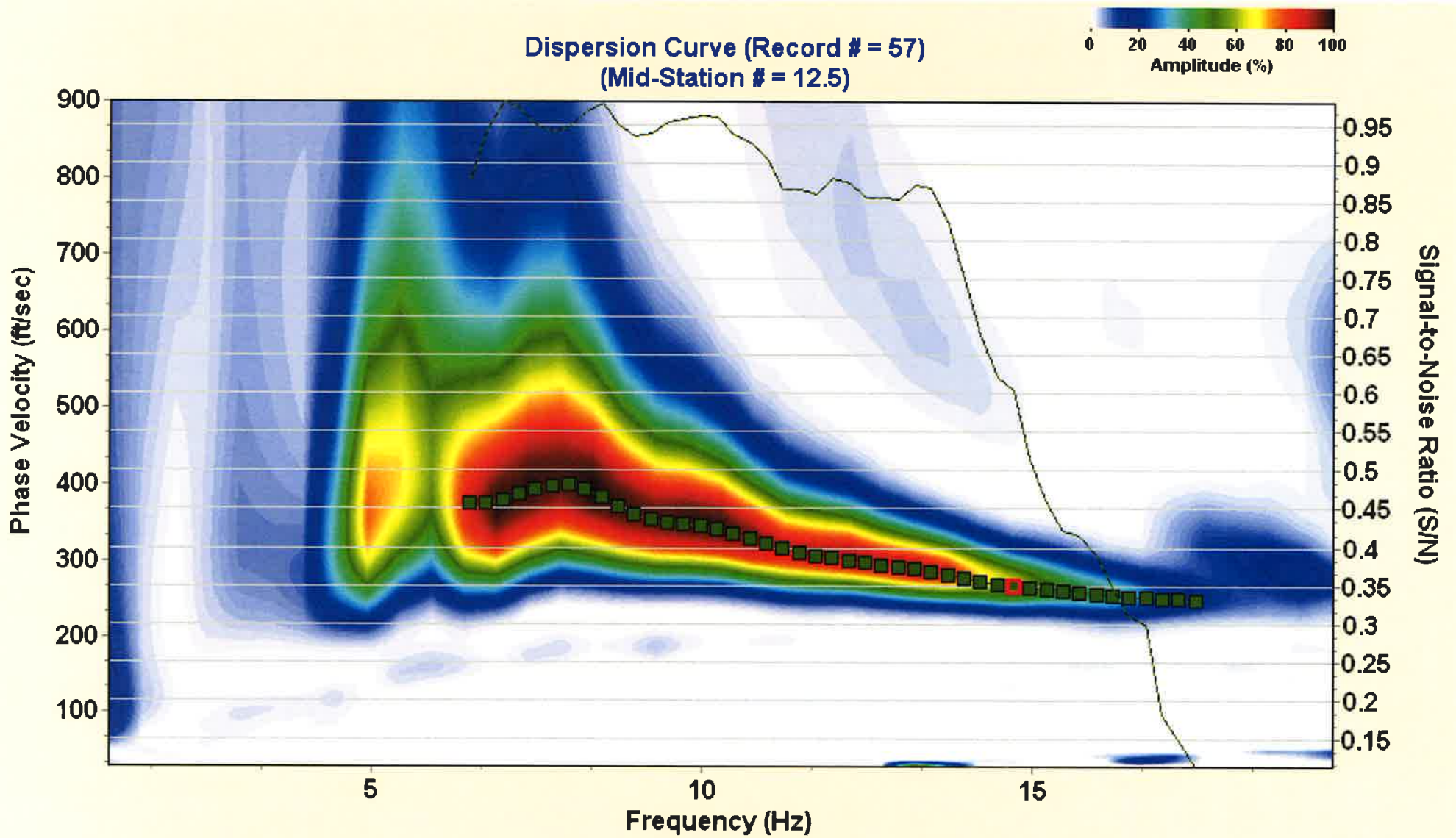


Figure 8b
Velocity Model

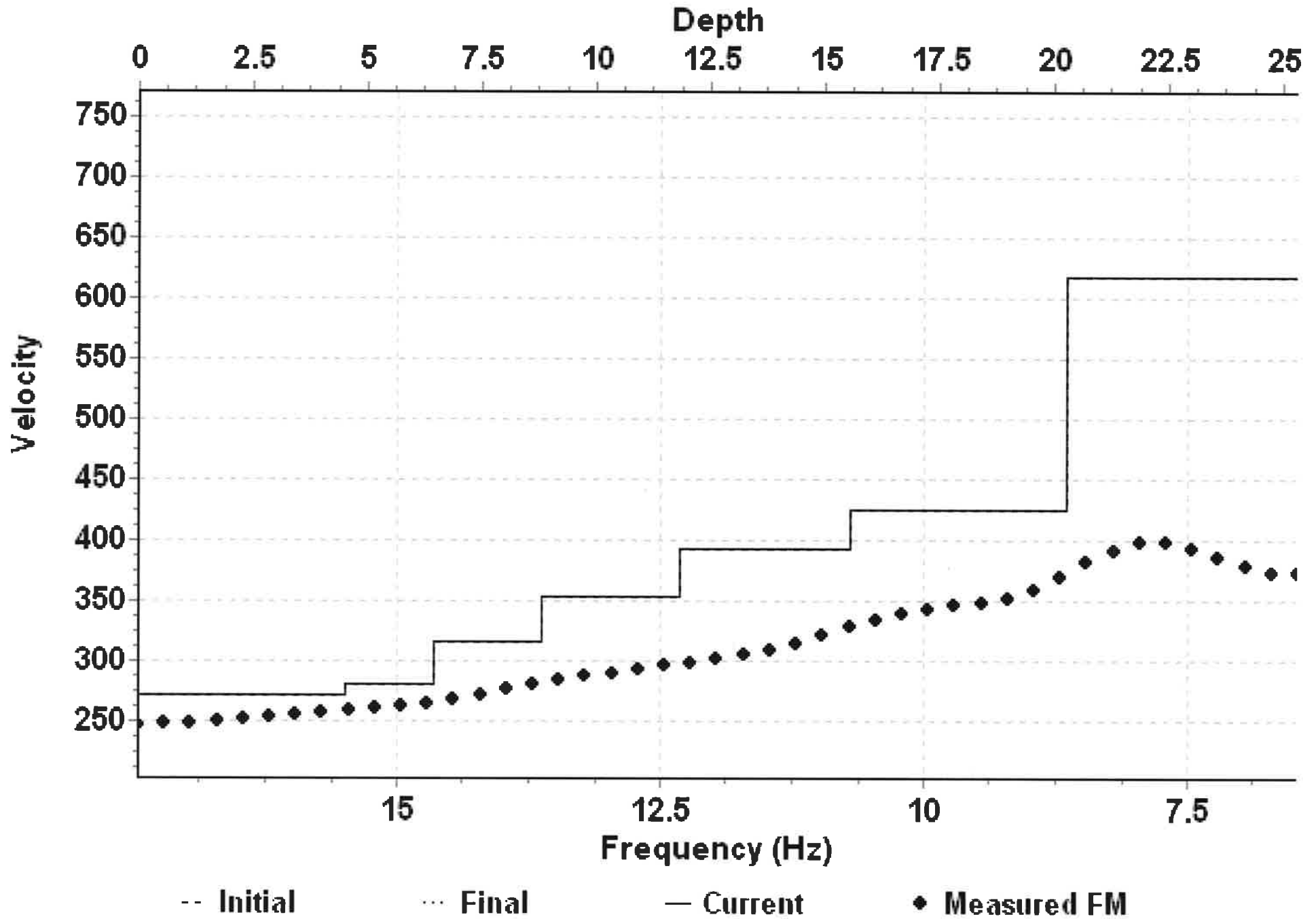


Figure 8c

**10-LAYER VELOCITY MODEL (Record = 57)
(Mid-Station = 12.5)**

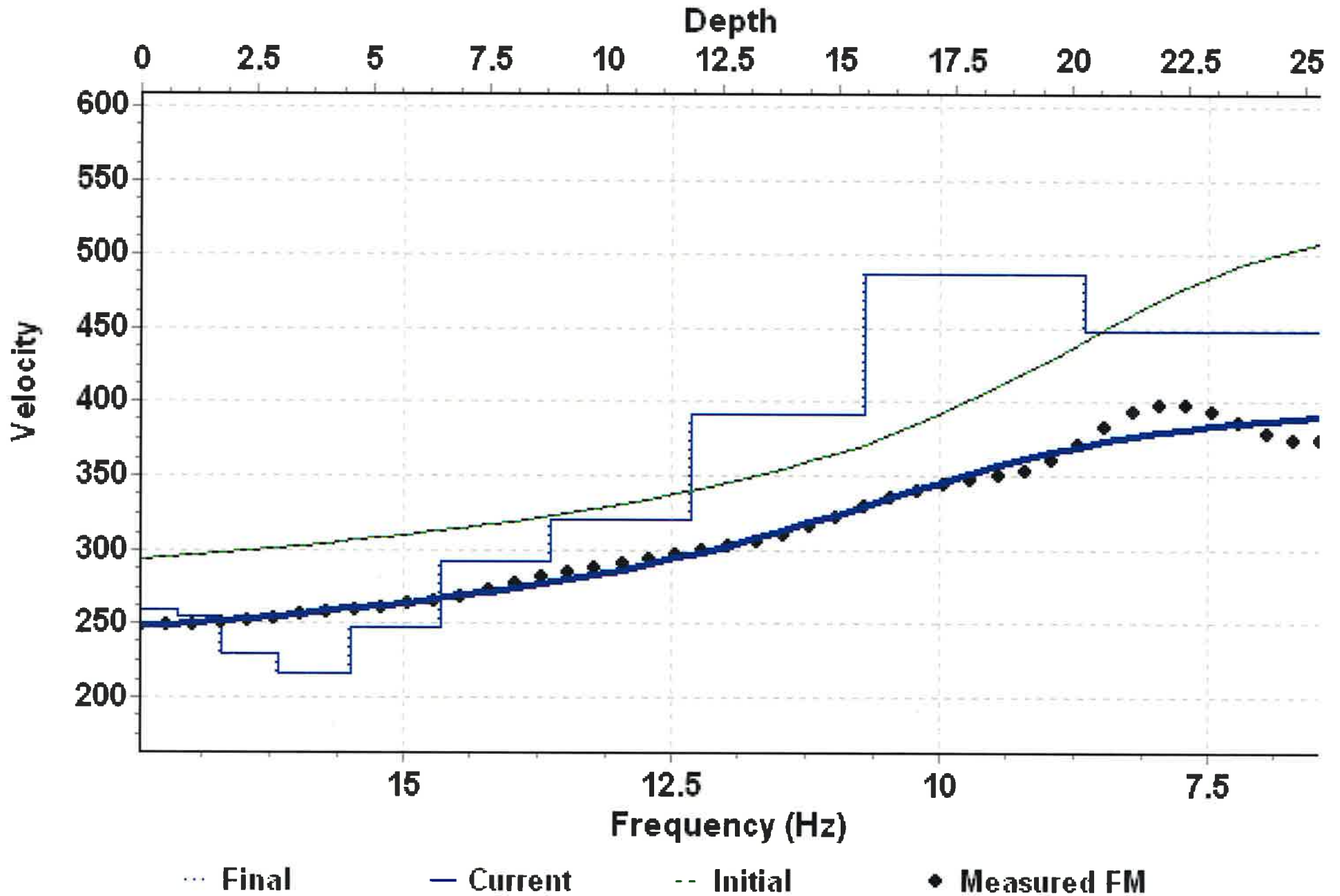


Figure 8d

MASW Line 57

| Layer | Depth (ft) | Vs Velocity (ft/s) |
|--------------|-------------------|---------------------------|
| 1 | -0.786 | 258.615 |
| 2 | -1.768 | 254.668 |
| 3 | -2.996 | 228.629 |
| 4 | -4.531 | 216.42 |
| 5 | -6.45 | 247.283 |
| 6 | -8.848 | 291.515 |
| 7 | -11.846 | 320.597 |
| 8 | -15.593 | 392.129 |
| 9 | -20.277 | 487.159 |
| 10 | -25.346 | 447.806 |

Figure 9

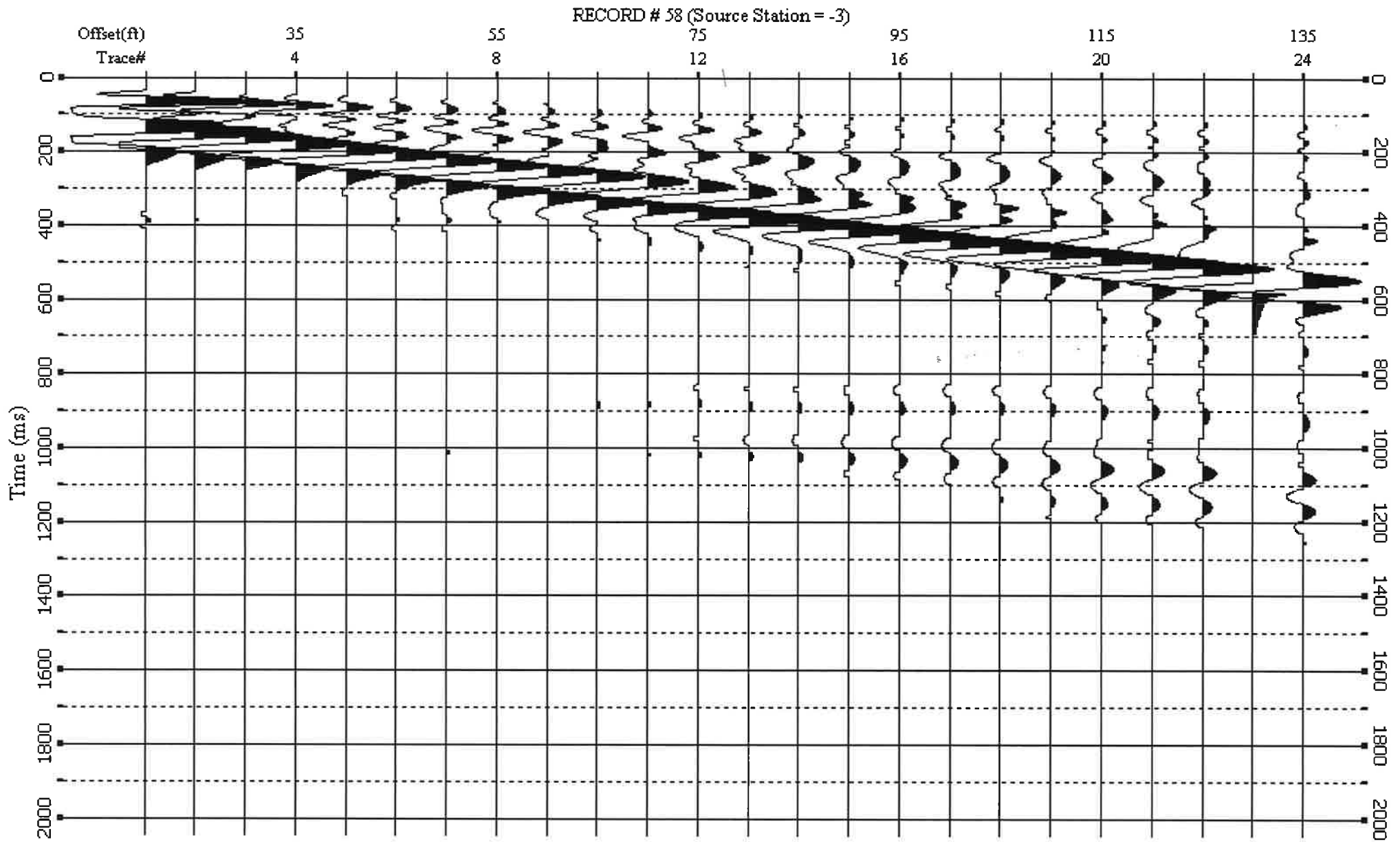
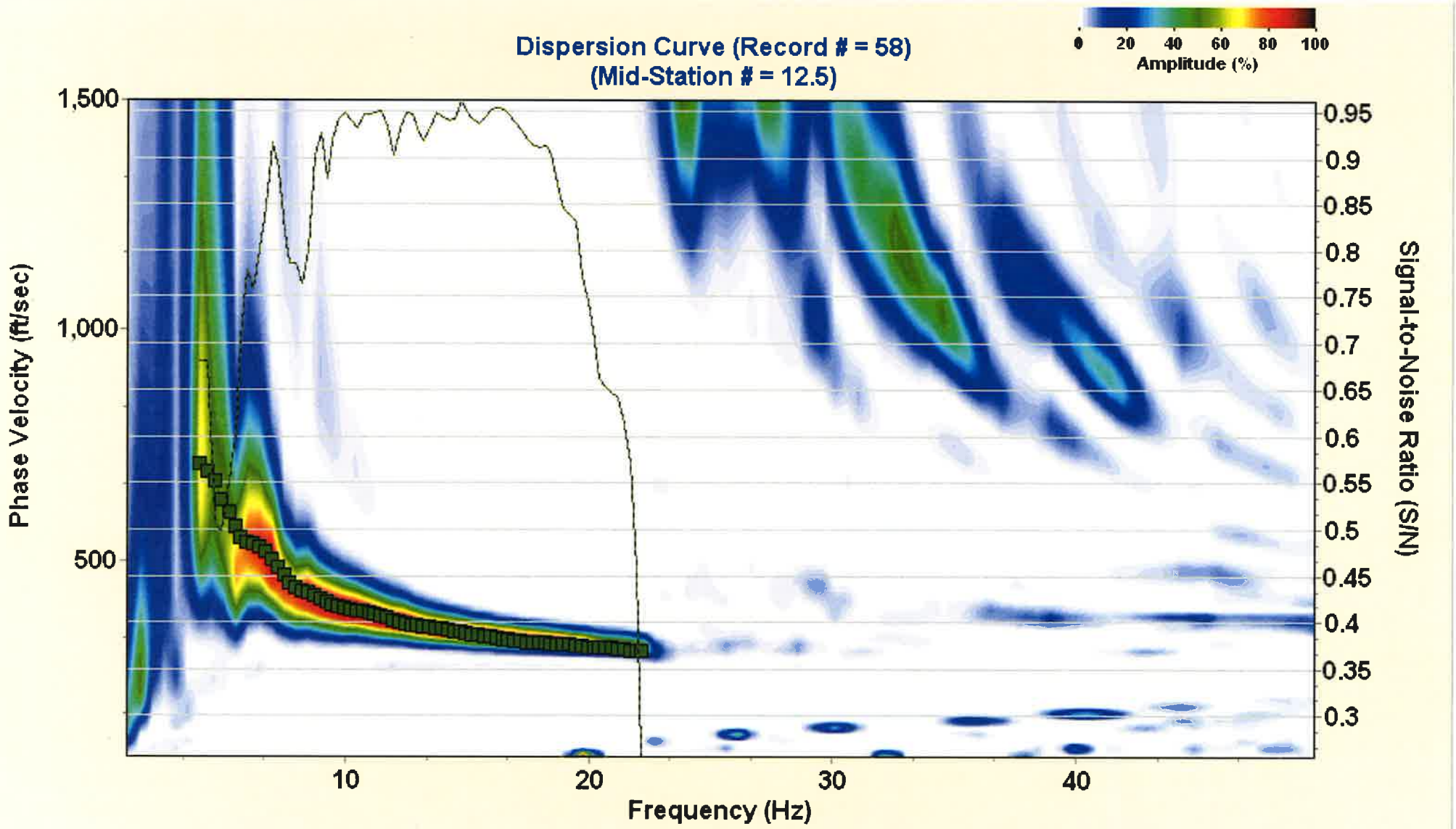
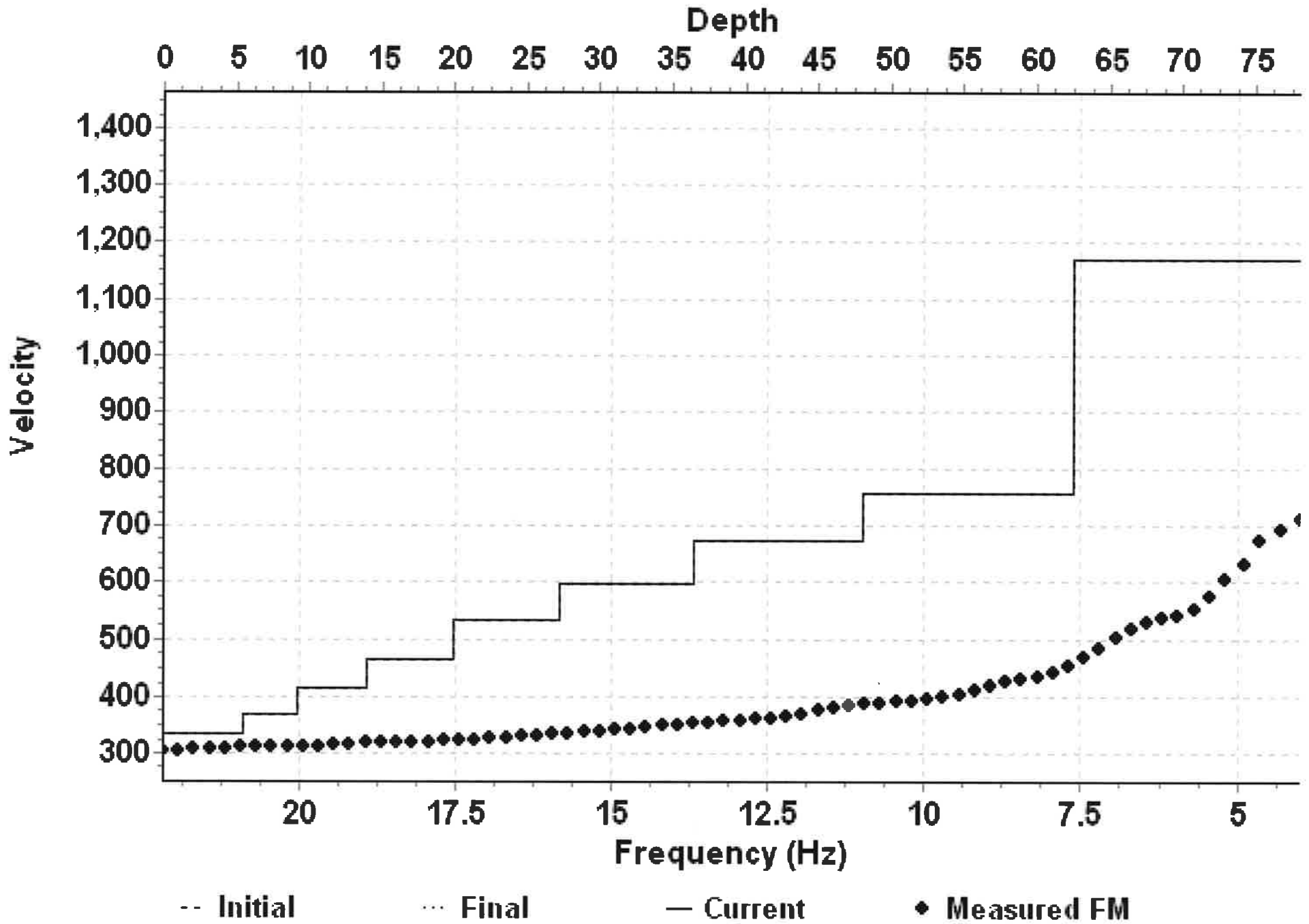


Figure 9a



Velocity Model



10-LAYER VELOCITY MODEL (Record = 58)
(Mid-Station = 12.5)

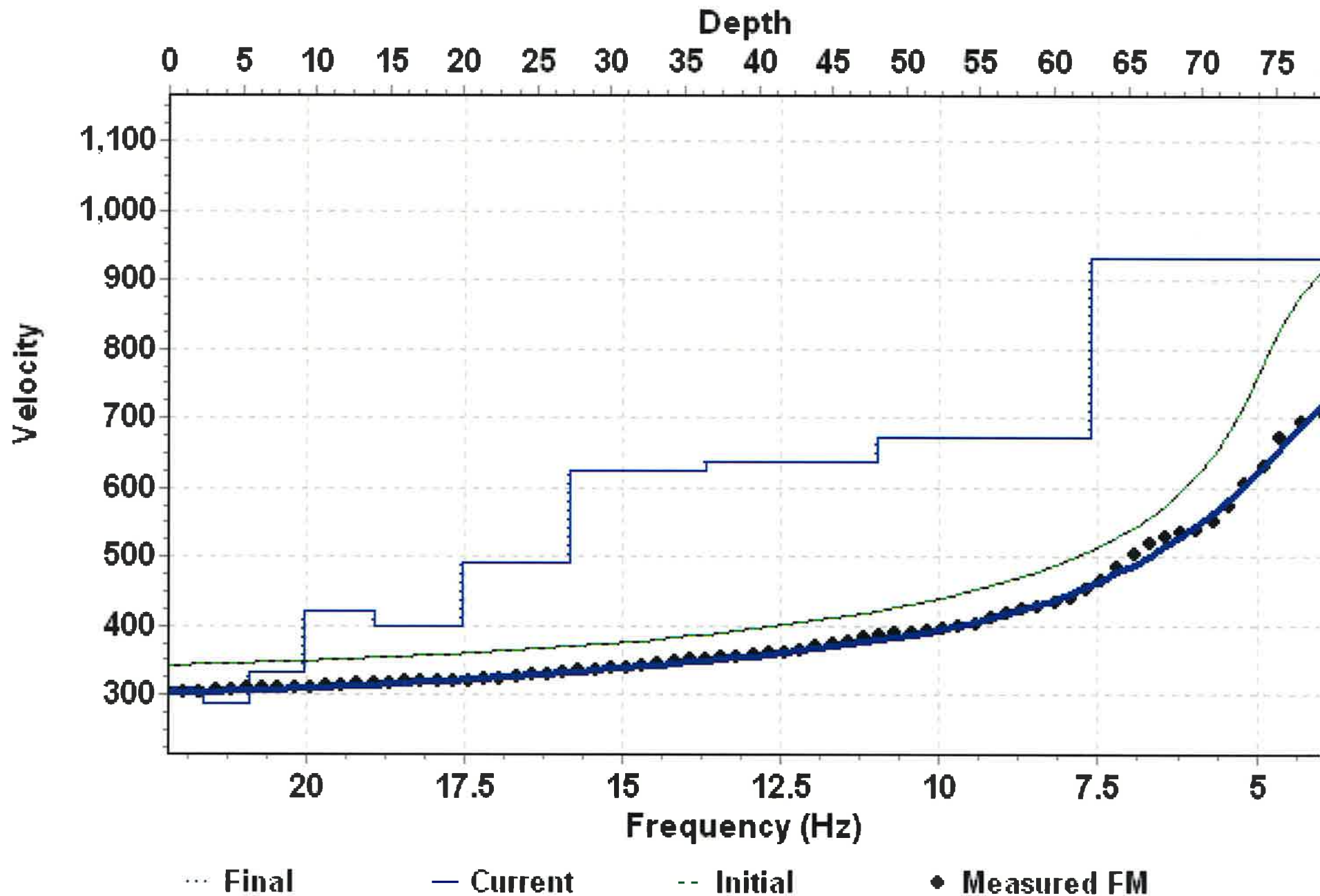


Figure 9d

MASW Line 58

| Layer | Depth (ft) | Vs Velocity (ft/s) |
|--------------|-------------------|---------------------------|
| 1 | -2.424 | 311.616 |
| 2 | -5.454 | 287.358 |
| 3 | -9.241 | 333.126 |
| 4 | -13.975 | 421.825 |
| 5 | -19.892 | 400.859 |
| 6 | -27.289 | 491.027 |
| 7 | -36.535 | 623.137 |
| 8 | -48.092 | 638.568 |
| 9 | -62.539 | 671.944 |
| 10 | -78.174 | 933.562 |

Figure 10

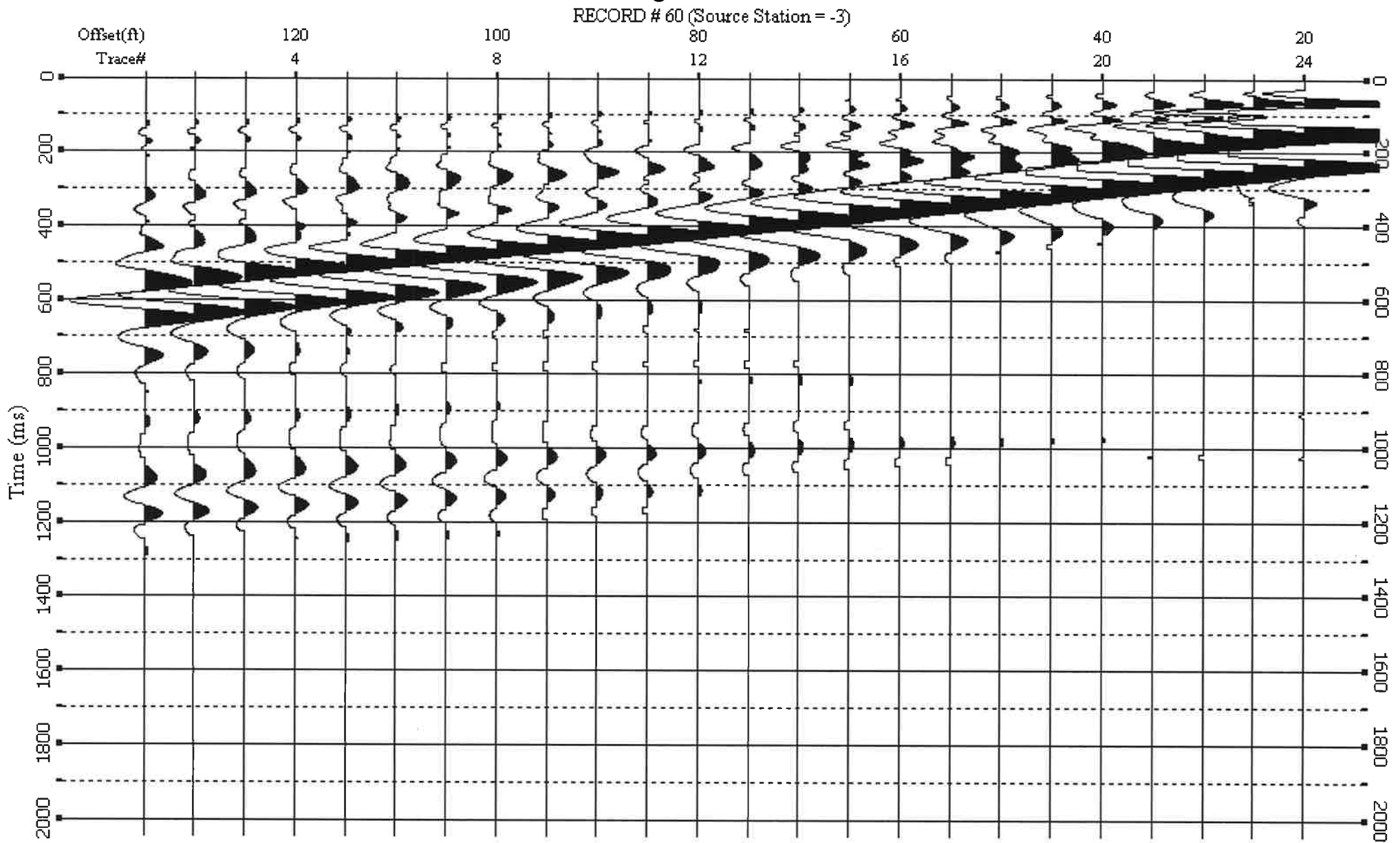


Figure 10a

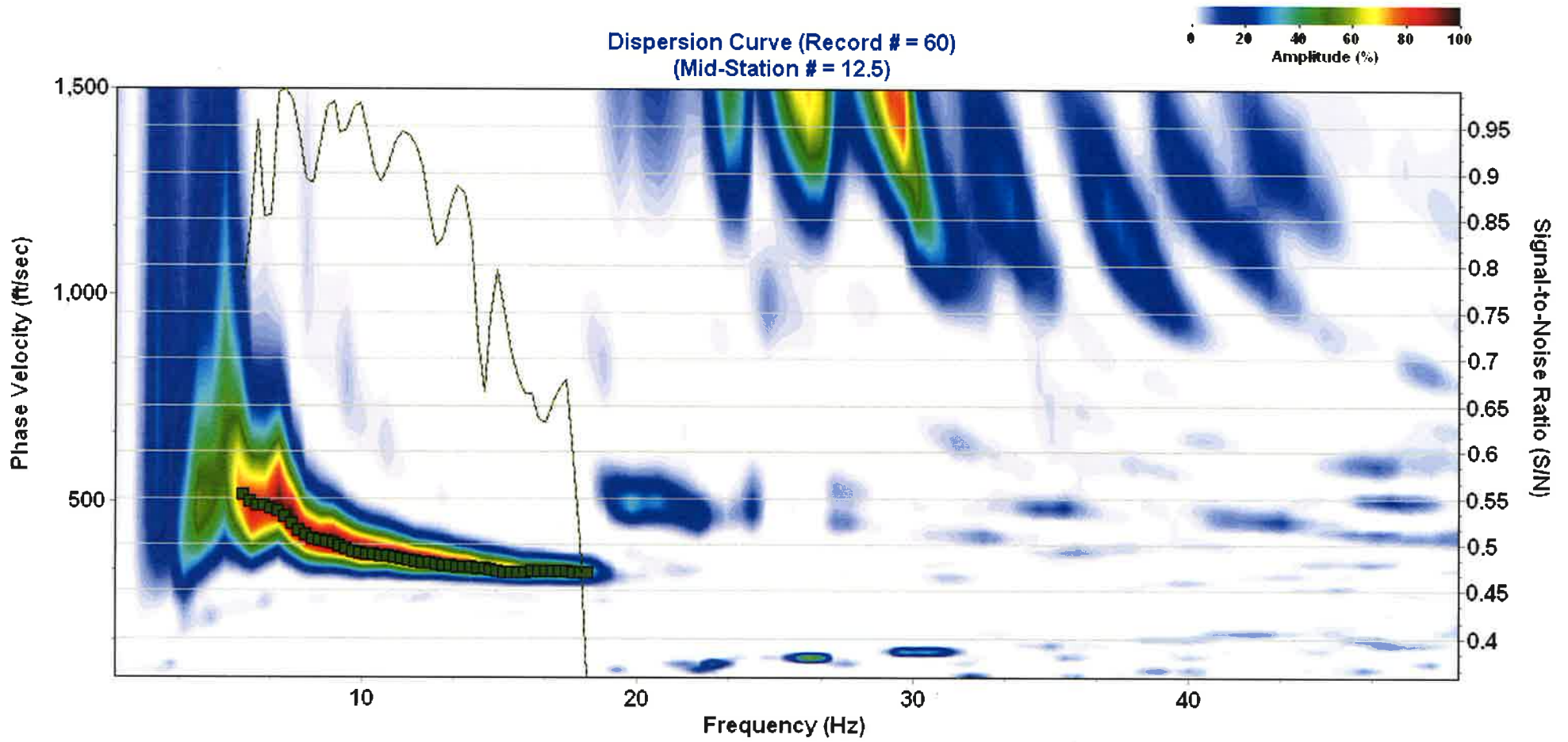


Figure 10b

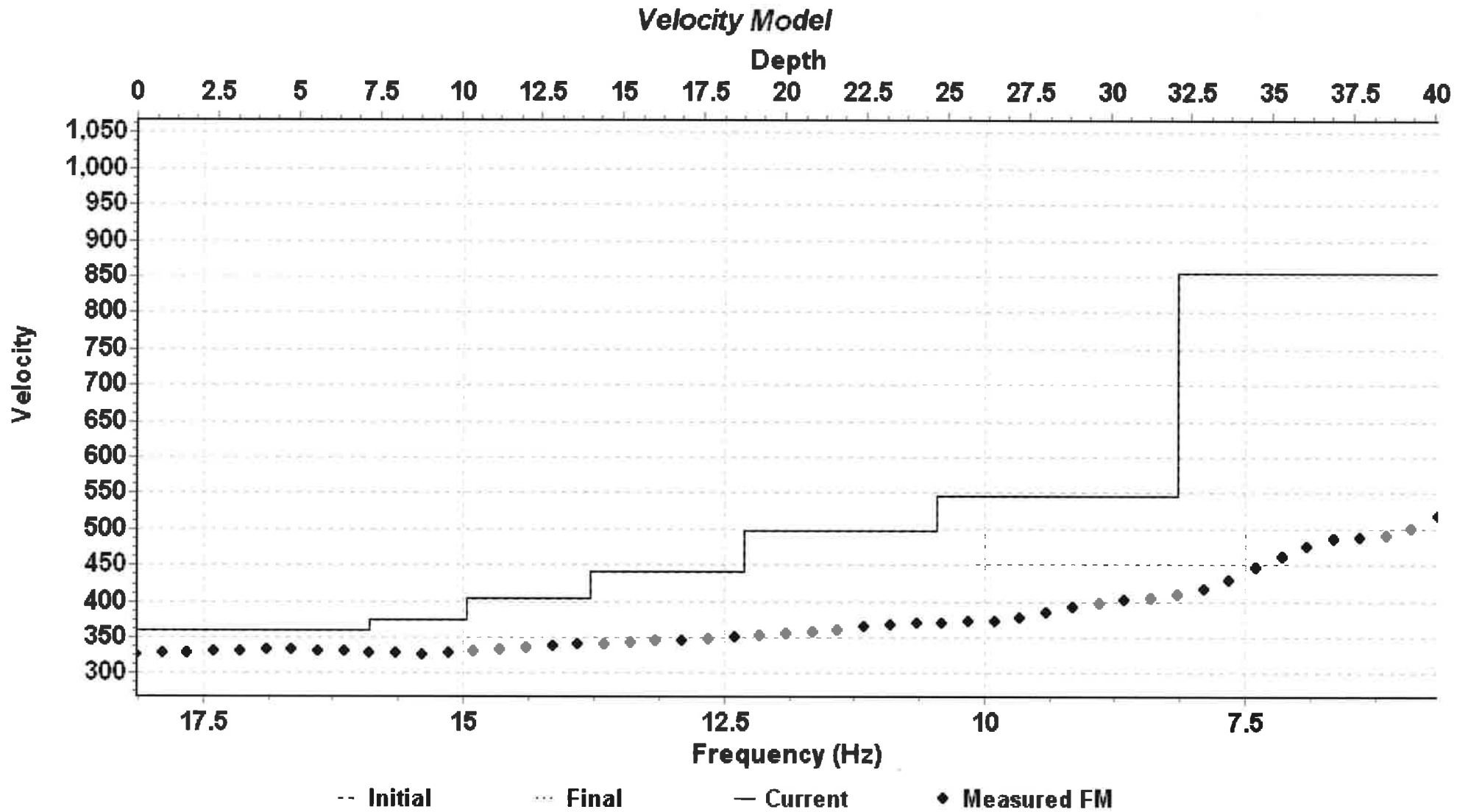


Figure 10c

**10-LAYER VELOCITY MODEL (Record = 60)
(Mid-Station = 12.5)**

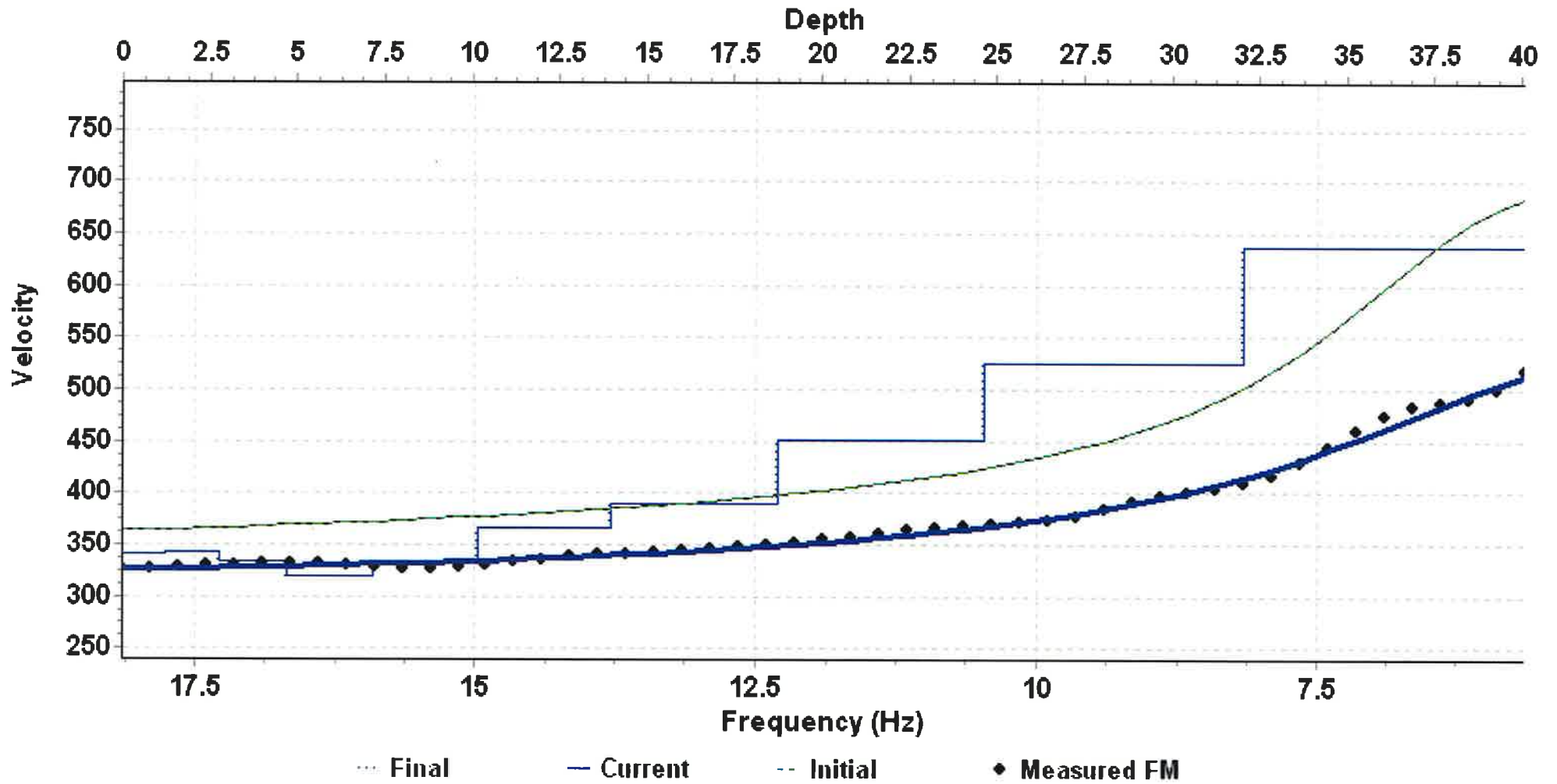


Figure 10d

MASW Line 60

| Layer | Depth (ft) | Vs Velocity (ft/s) |
|--------------|-------------------|---------------------------|
| 1 | -1.243 | 340.944 |
| 2 | -2.797 | 343.376 |
| 3 | -4.74 | 333.165 |
| 4 | -7.169 | 319.631 |
| 5 | -10.205 | 332.685 |
| 6 | -14 | 366.081 |
| 7 | -18.744 | 389.896 |
| 8 | -24.673 | 451.789 |
| 9 | -32.085 | 525.999 |
| 10 | -40.106 | 637.367 |

Figure 11

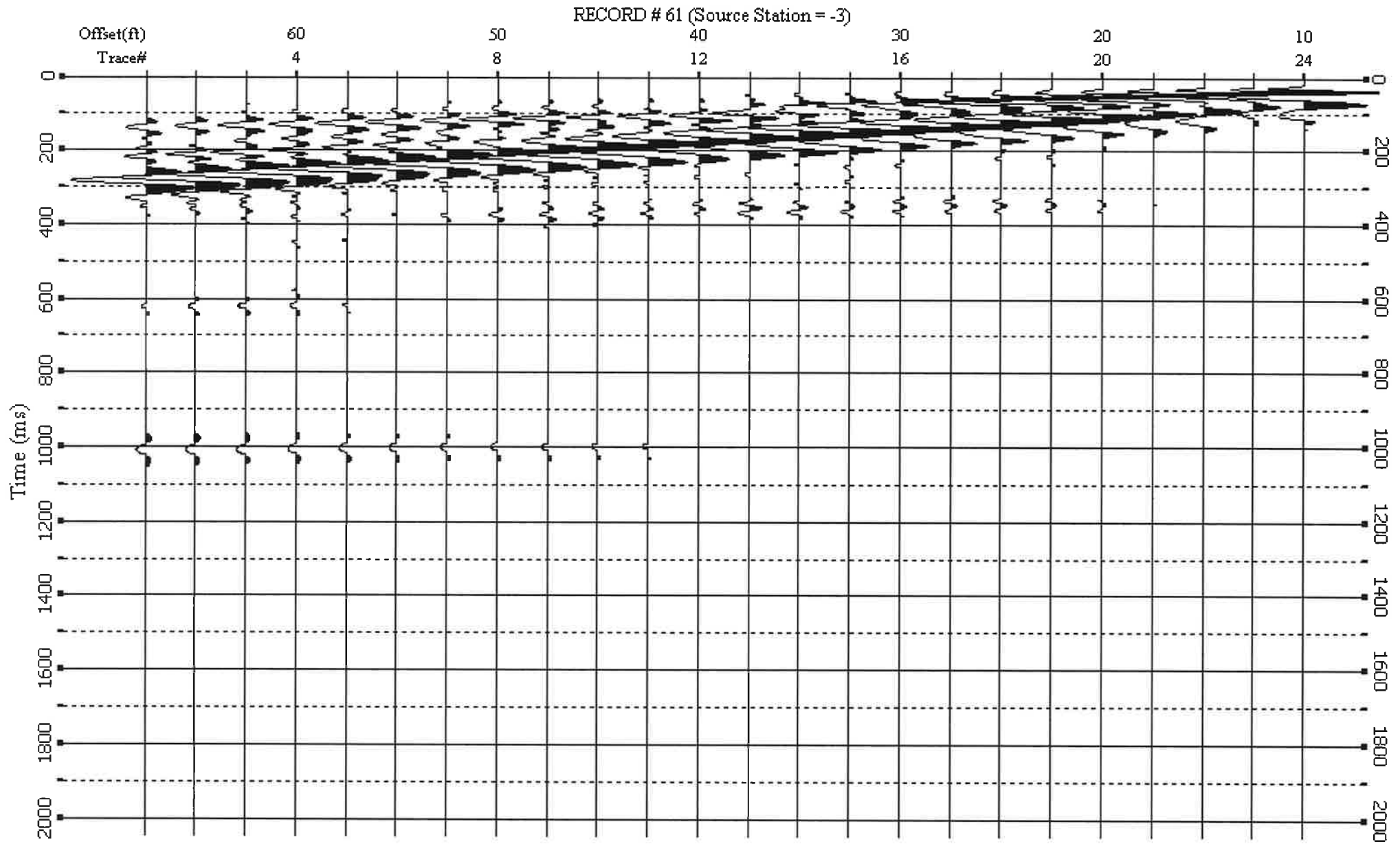


Figure 11a

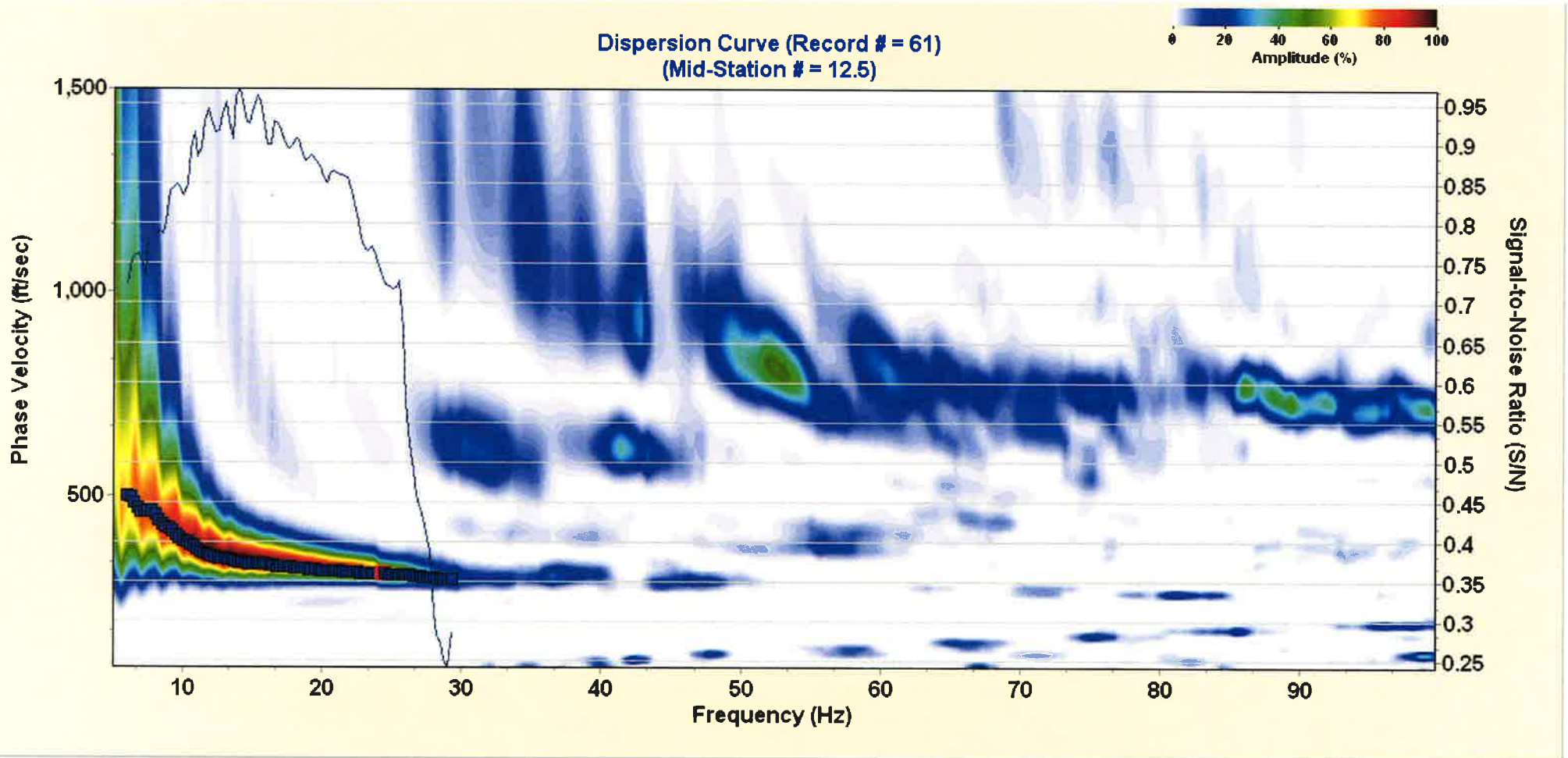


Figure 111b

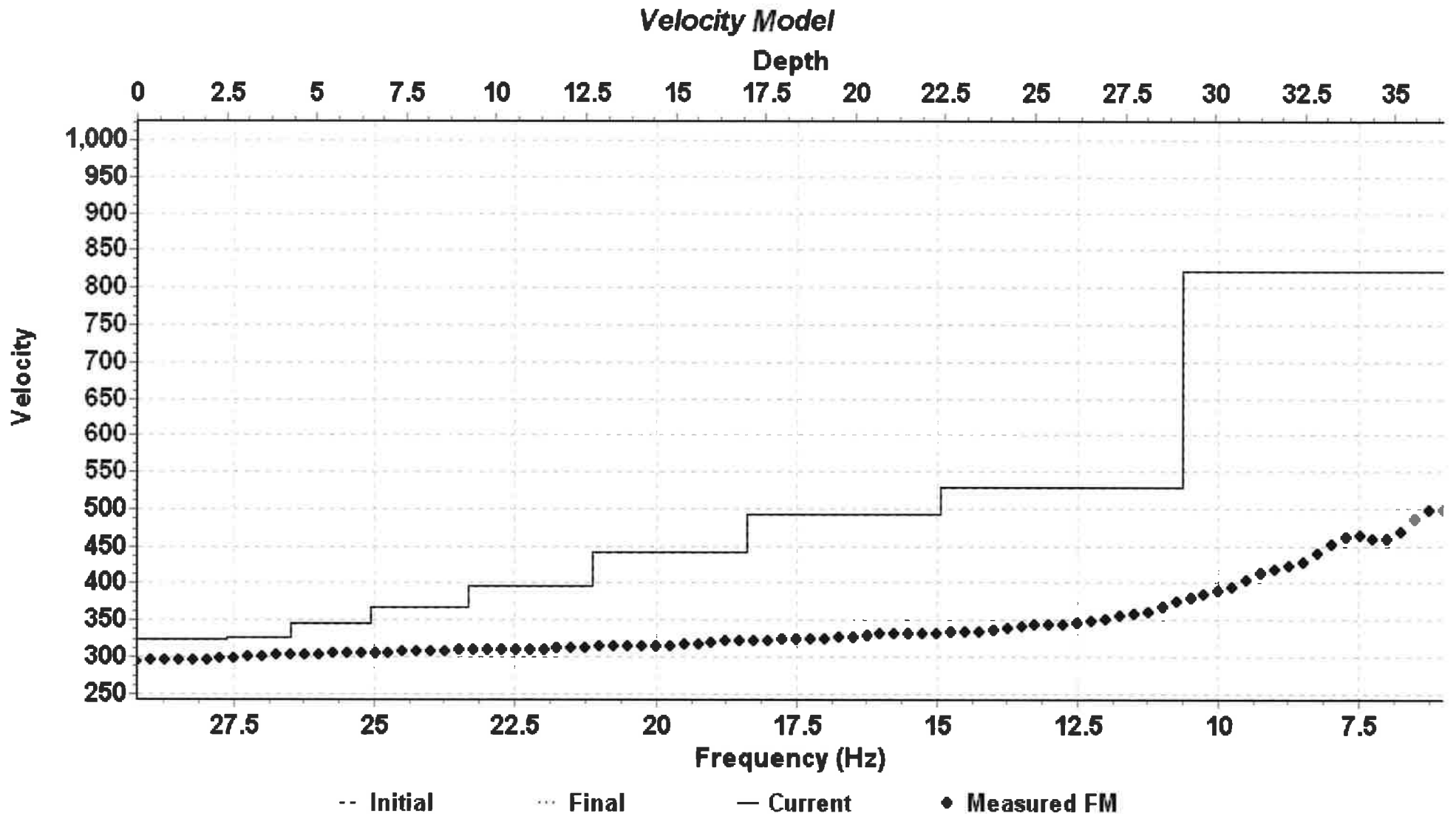


Figure 11c

10-LAYER VELOCITY MODEL (Record = 61)
 (Mid-Station = 12.5)

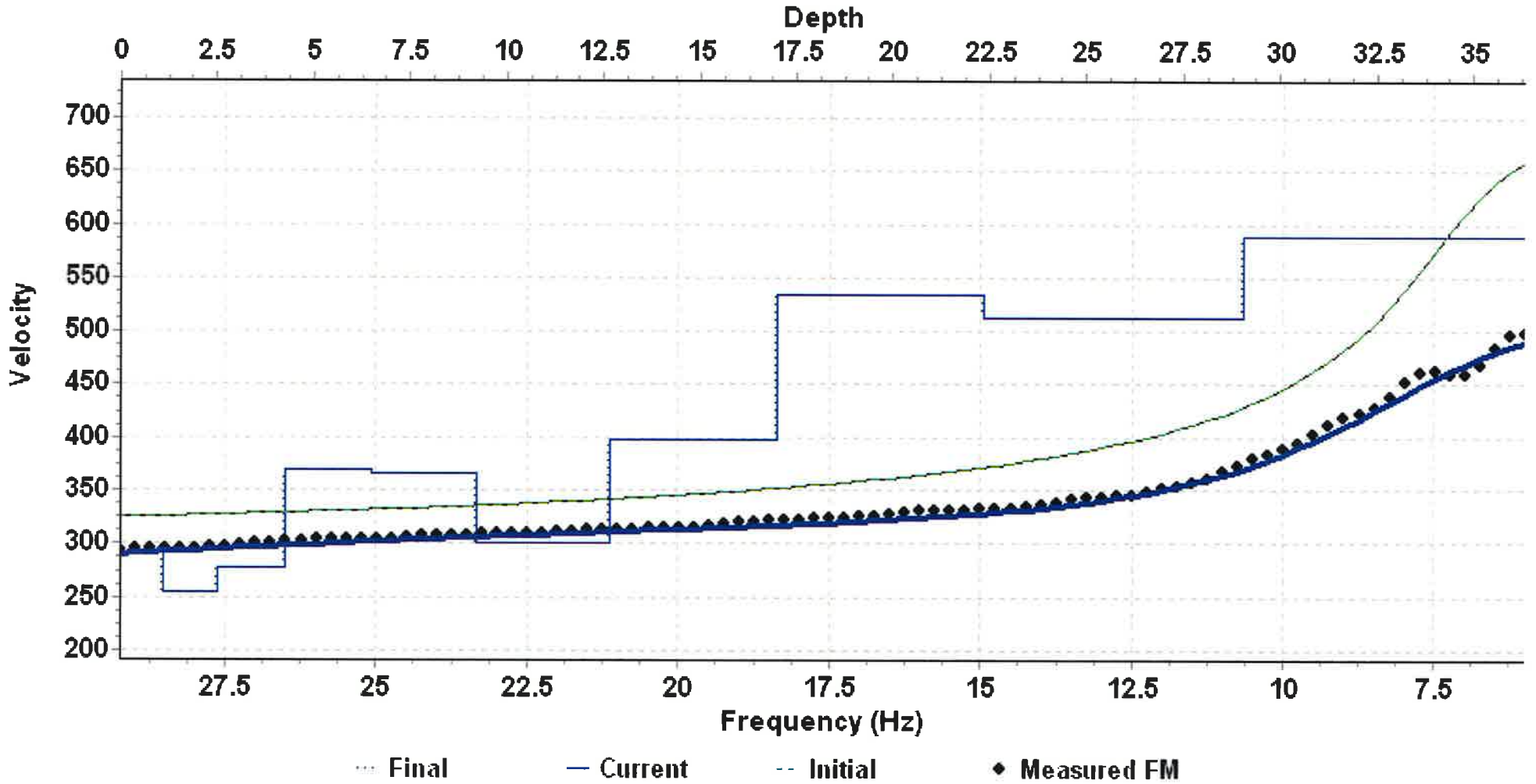


Figure 11d

MASW Line 61

| Layer | Depth (ft) | Vs Velocity (ft/s) |
|--------------|-------------------|---------------------------|
| 1 | -1.127 | 290.95 |
| 2 | -2.536 | 254.36 |
| 3 | -4.298 | 277.922 |
| 4 | -6.5 | 369.769 |
| 5 | -9.252 | 366.296 |
| 6 | -12.693 | 300.473 |
| 7 | -16.994 | 397.364 |
| 8 | -22.37 | 533.807 |
| 9 | -29.09 | 512.593 |
| 10 | -36.362 | 588.491 |

Figure 12

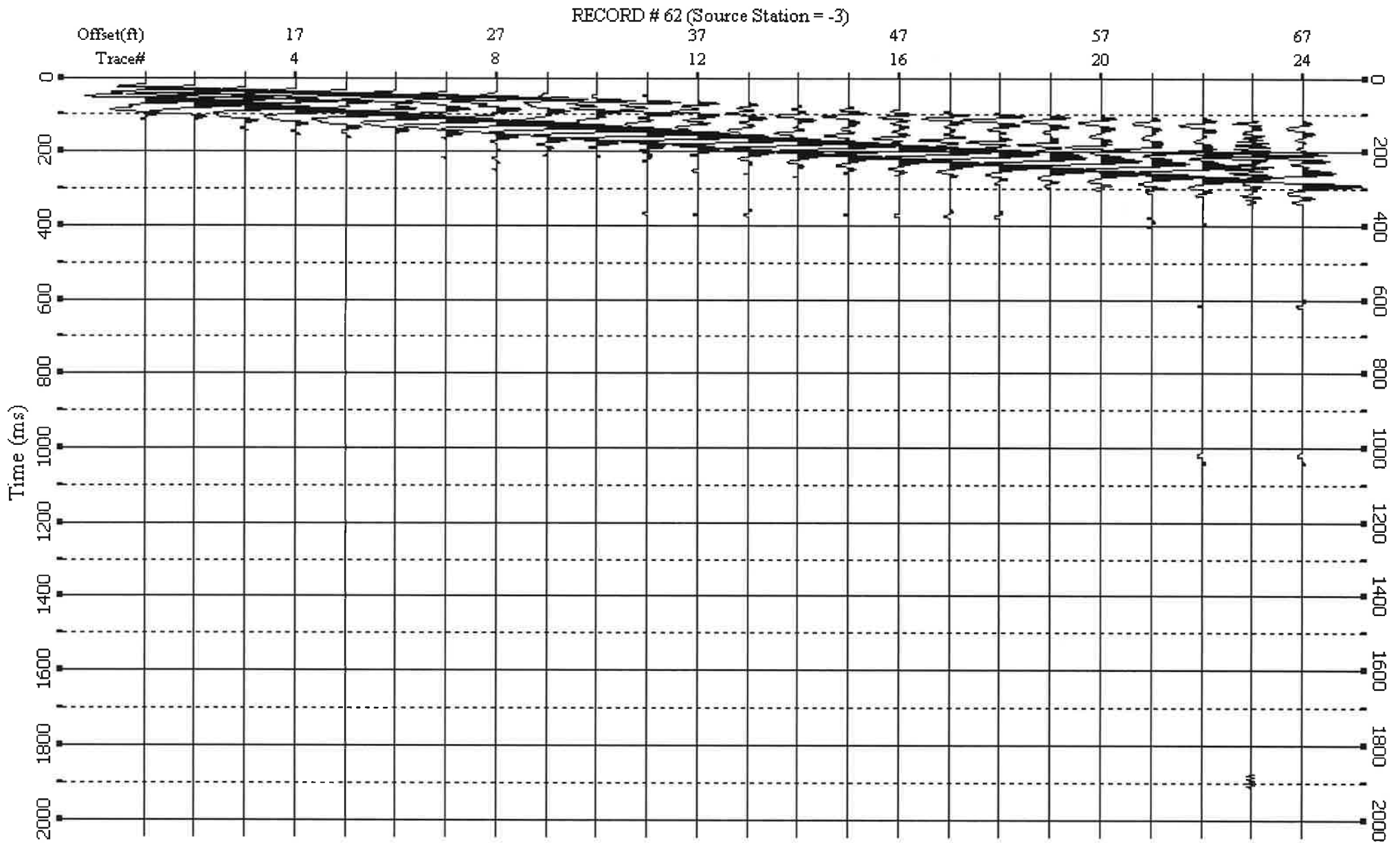


Figure 12a

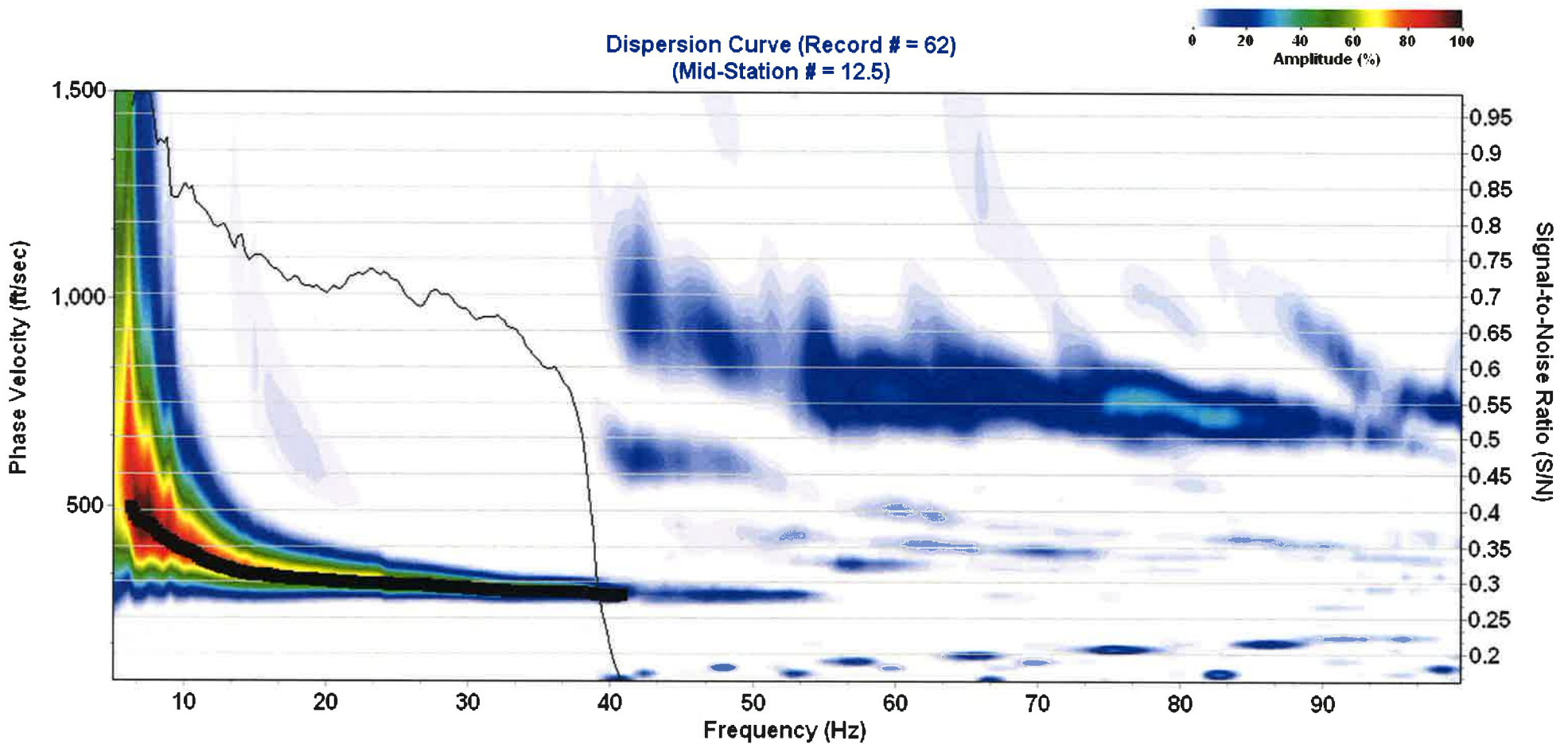


Figure 12b

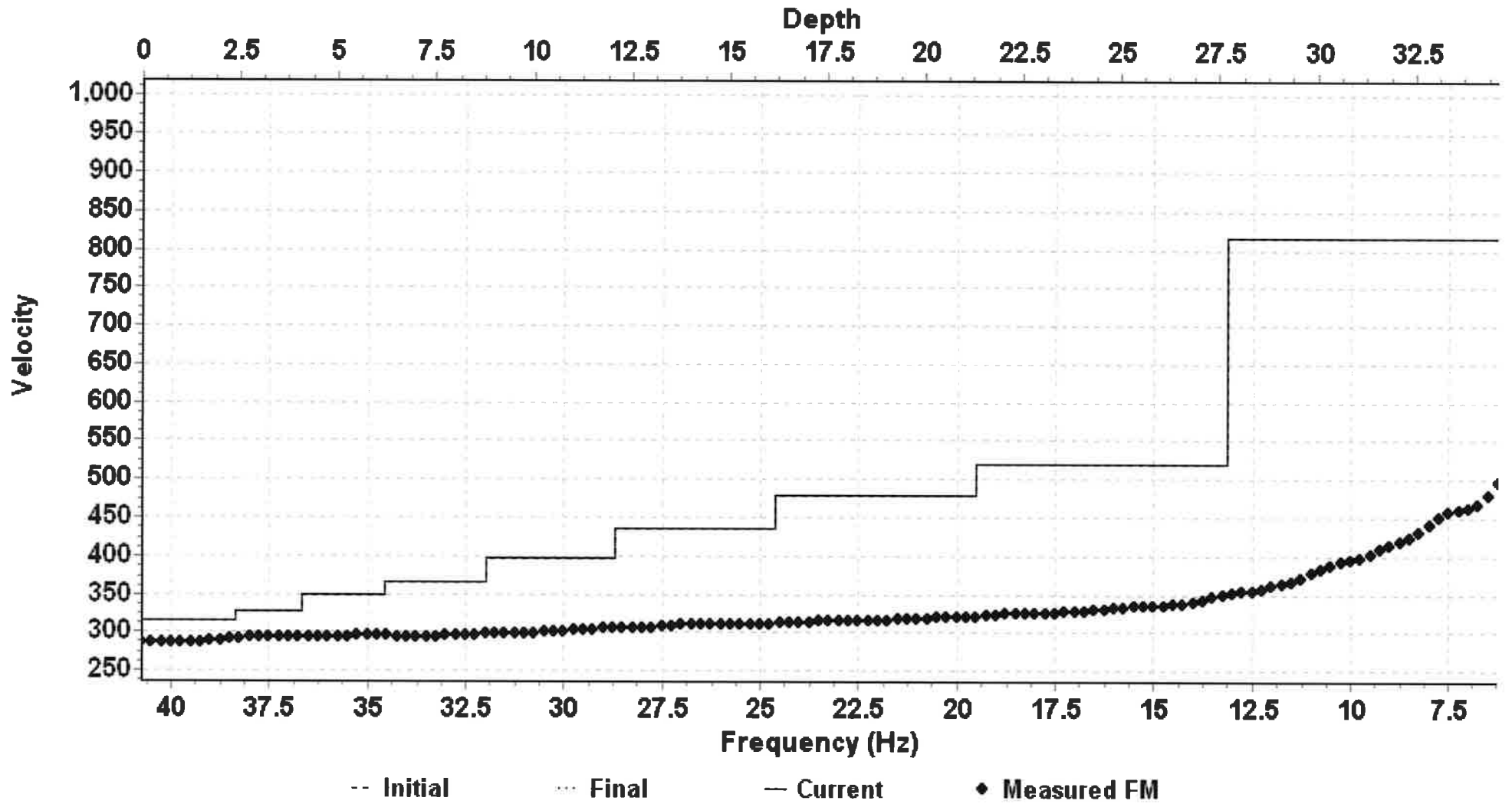
Velocity Model

Figure 12c

10-LAYER VELOCITY MODEL (Record = 62)
(Mid-Station = 12.5)

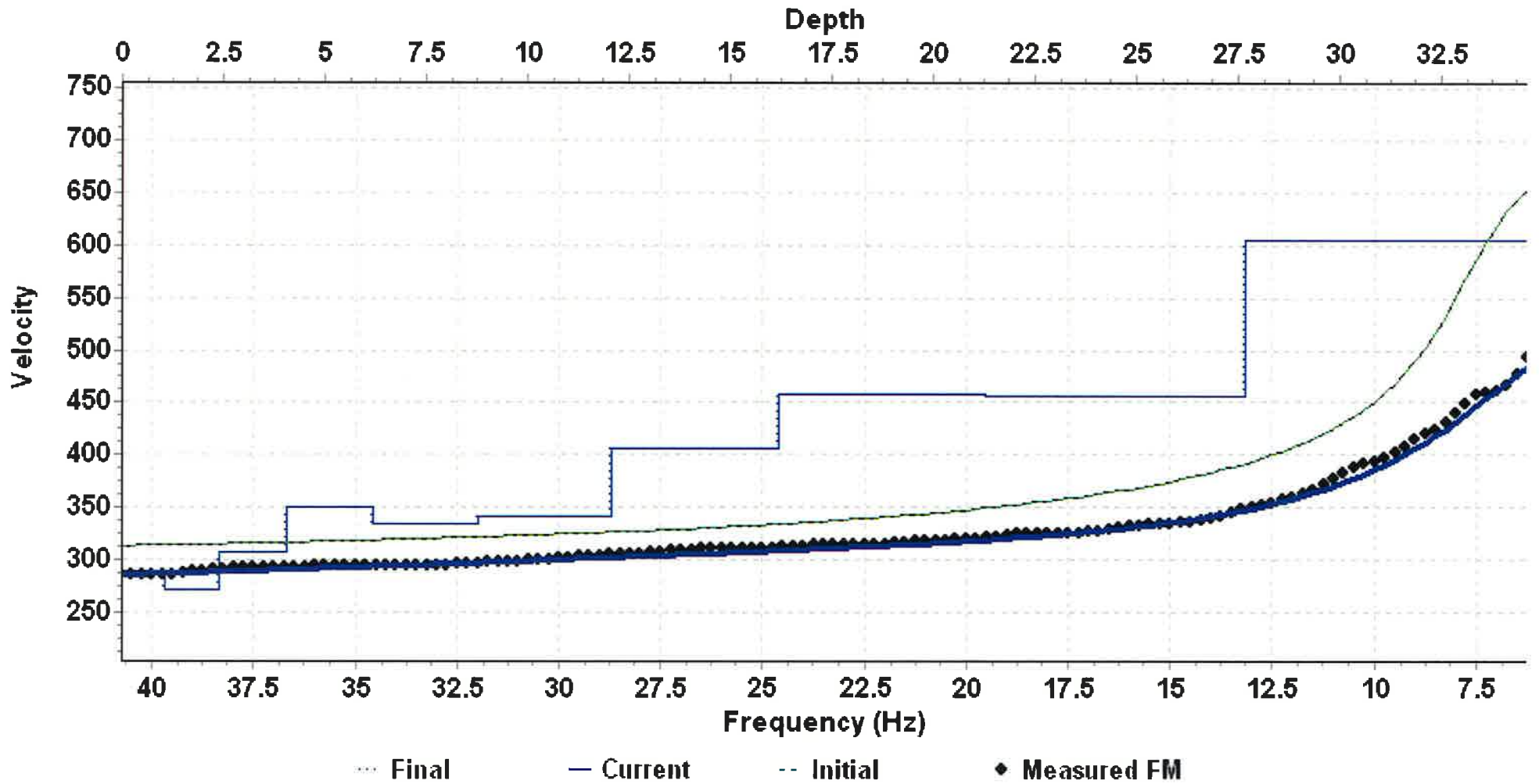


Figure 12d

MASW Line 62

| Layer | Depth (ft) | Vs Velocity (ft/s) |
|--------------|-------------------|---------------------------|
| 1 | -1.074 | 289.585 |
| 2 | -2.416 | 271.404 |
| 3 | -4.094 | 307.027 |
| 4 | -6.191 | 349.836 |
| 5 | -8.812 | 335.054 |
| 6 | -12.089 | 342.044 |
| 7 | -16.185 | 406.6 |
| 8 | -21.305 | 457.61 |
| 9 | -27.705 | 455.837 |
| 10 | -34.631 | 604.429 |

Figure 13

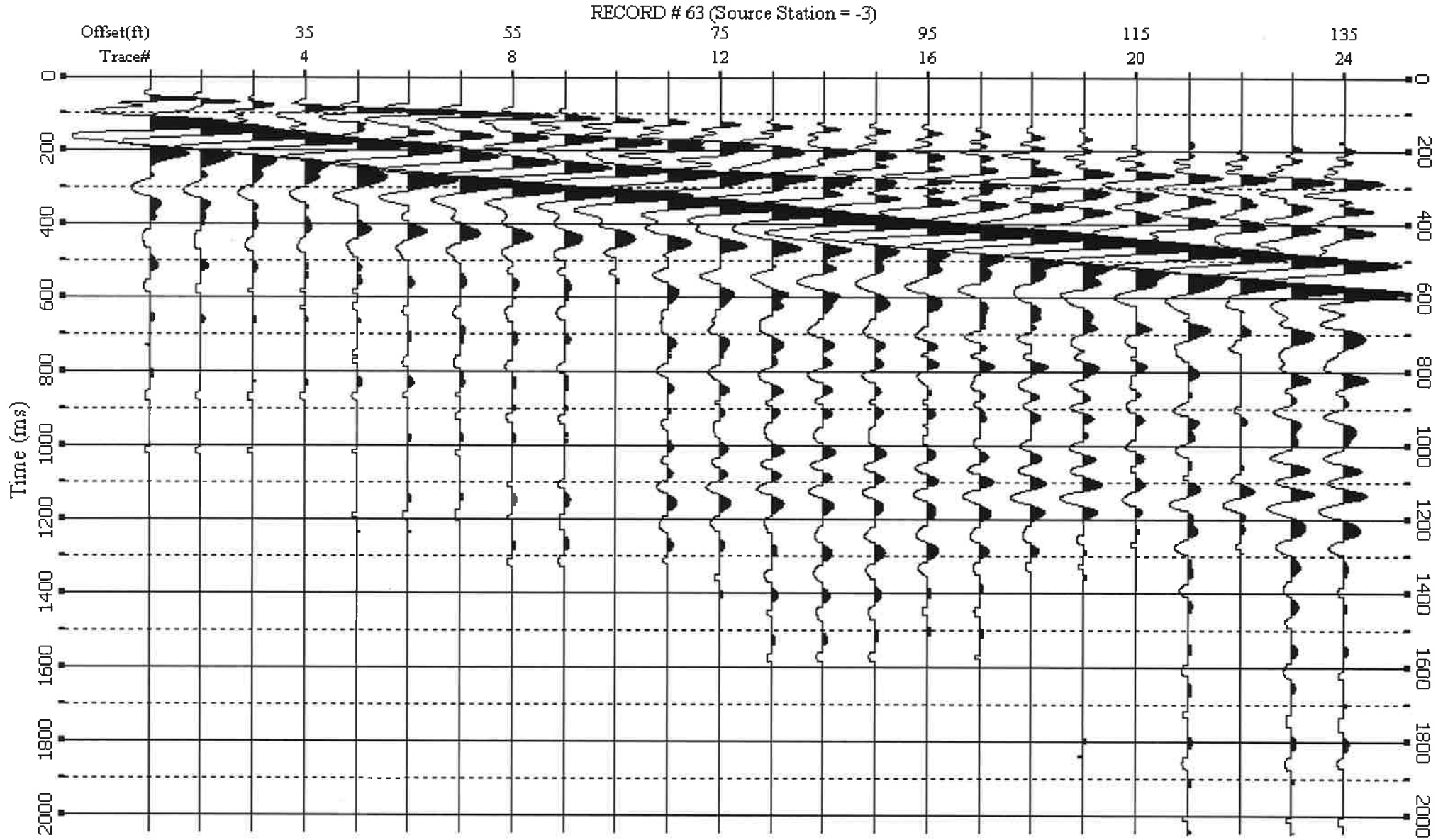


Figure 13a

Dispersion Curve (Record # = 63)
(Mid-Station # = 12.5)

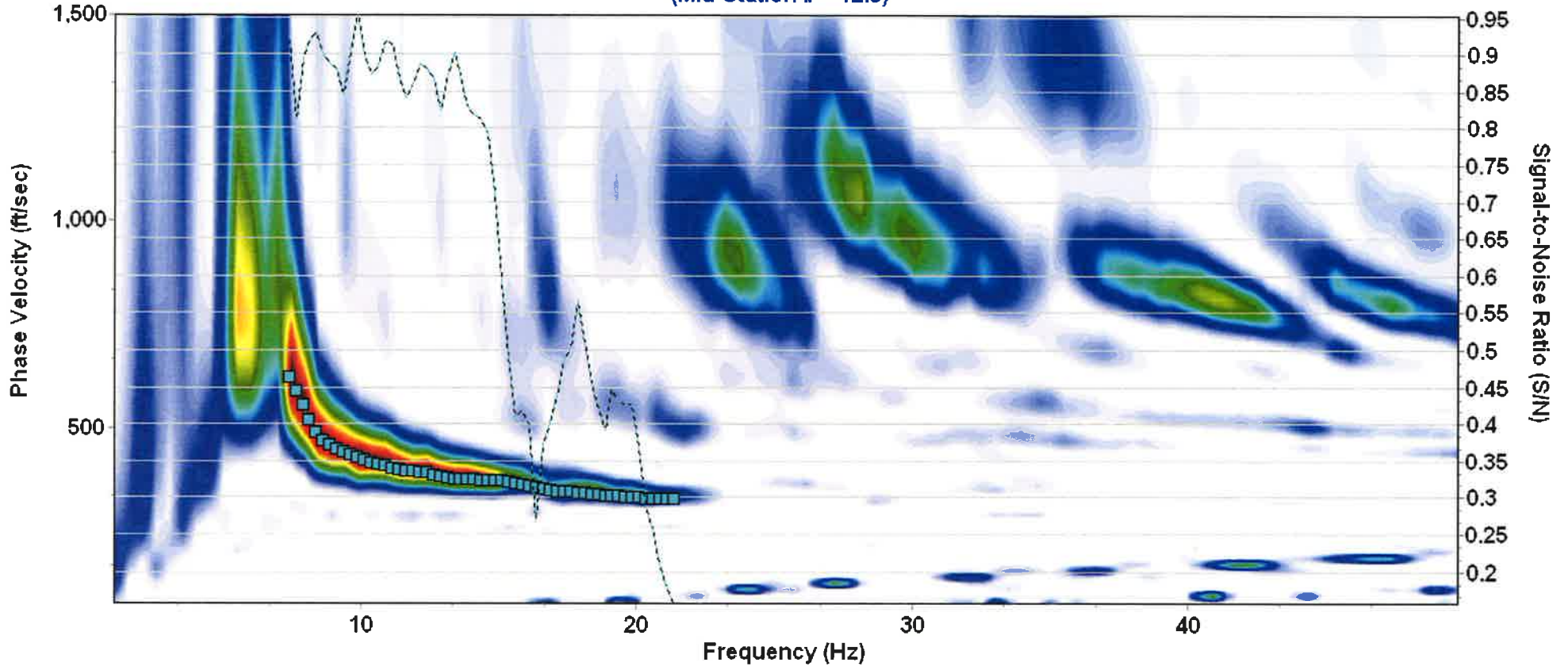
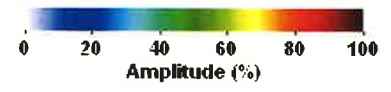


Figure 13b

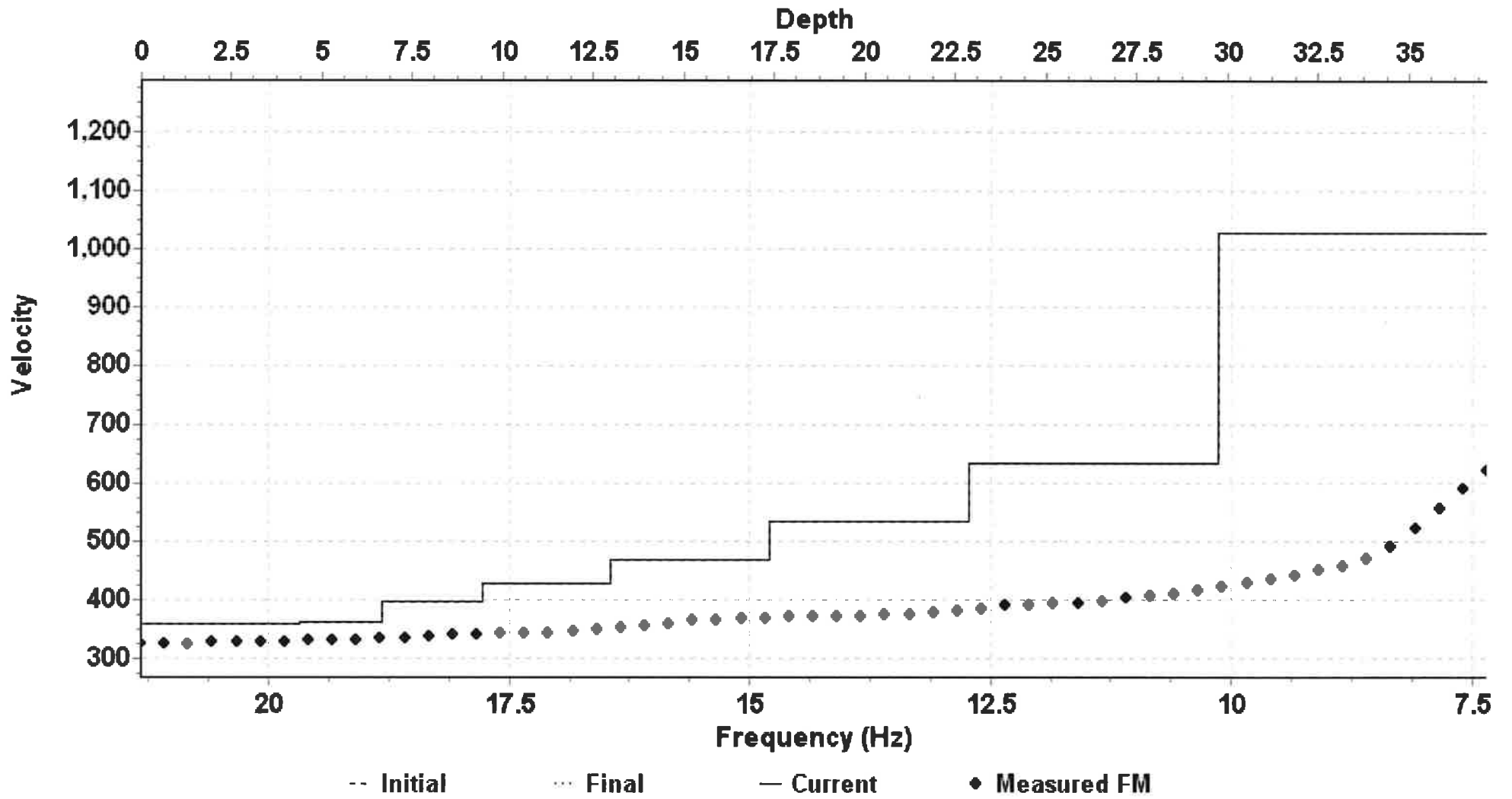
Velocity Model

Figure 13c

10-LAYER VELOCITY MODEL (Record = 63)
 (Mid-Station = 12.5)

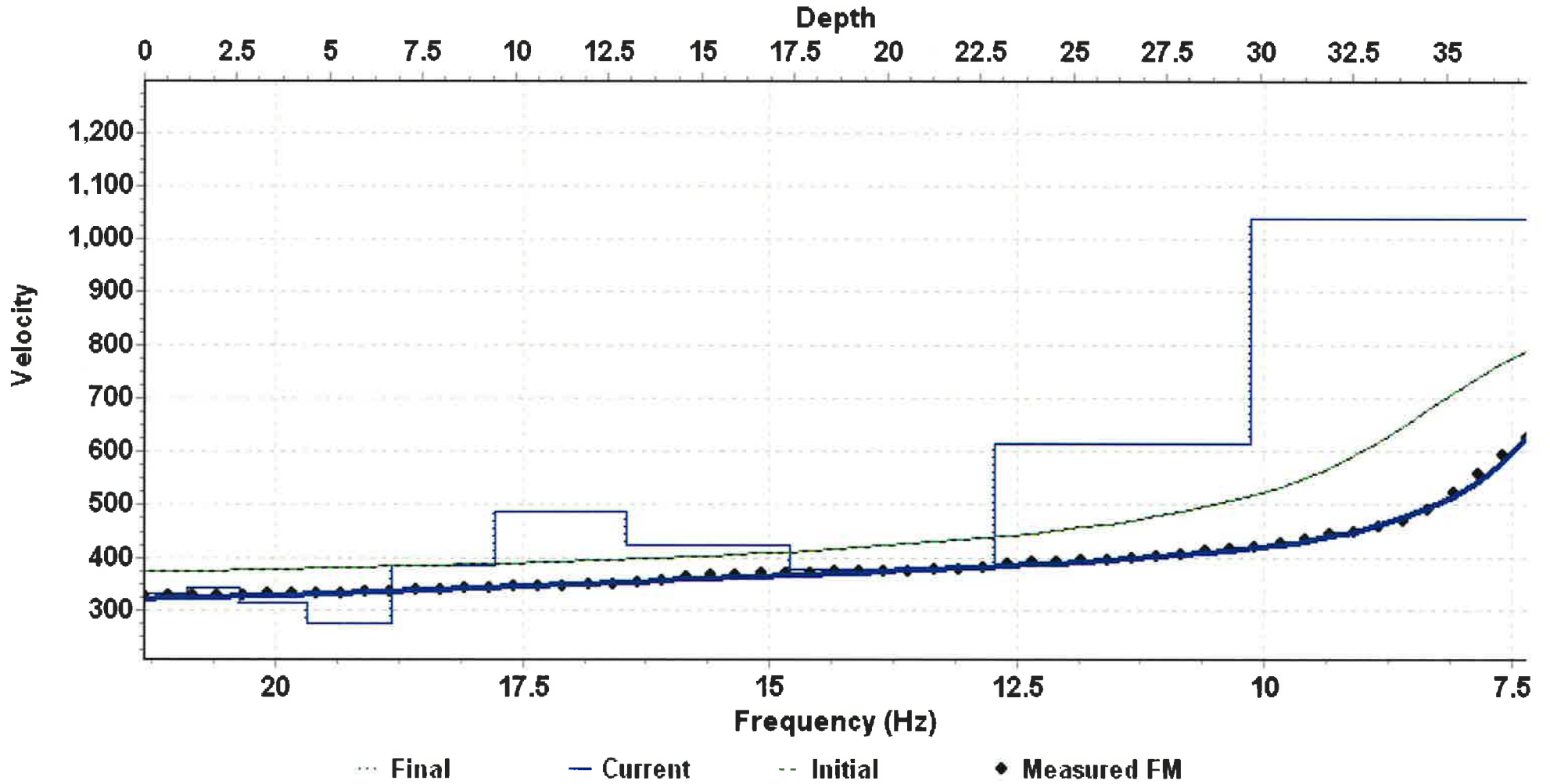


Figure 13d

MASW Line 63

| Layer | Depth (ft) | Vs Velocity (ft/s) |
|--------------|-------------------|---------------------------|
| 1 | -1.153 | 331.654 |
| 2 | -2.594 | 340.882 |
| 3 | -4.395 | 312.447 |
| 4 | -6.646 | 276.246 |
| 5 | -9.46 | 384.992 |
| 6 | -12.978 | 488.124 |
| 7 | -17.375 | 422.918 |
| 8 | -22.871 | 375.656 |
| 9 | -29.741 | 615.712 |
| 10 | -37.176 | 1038.432 |

Figure 14

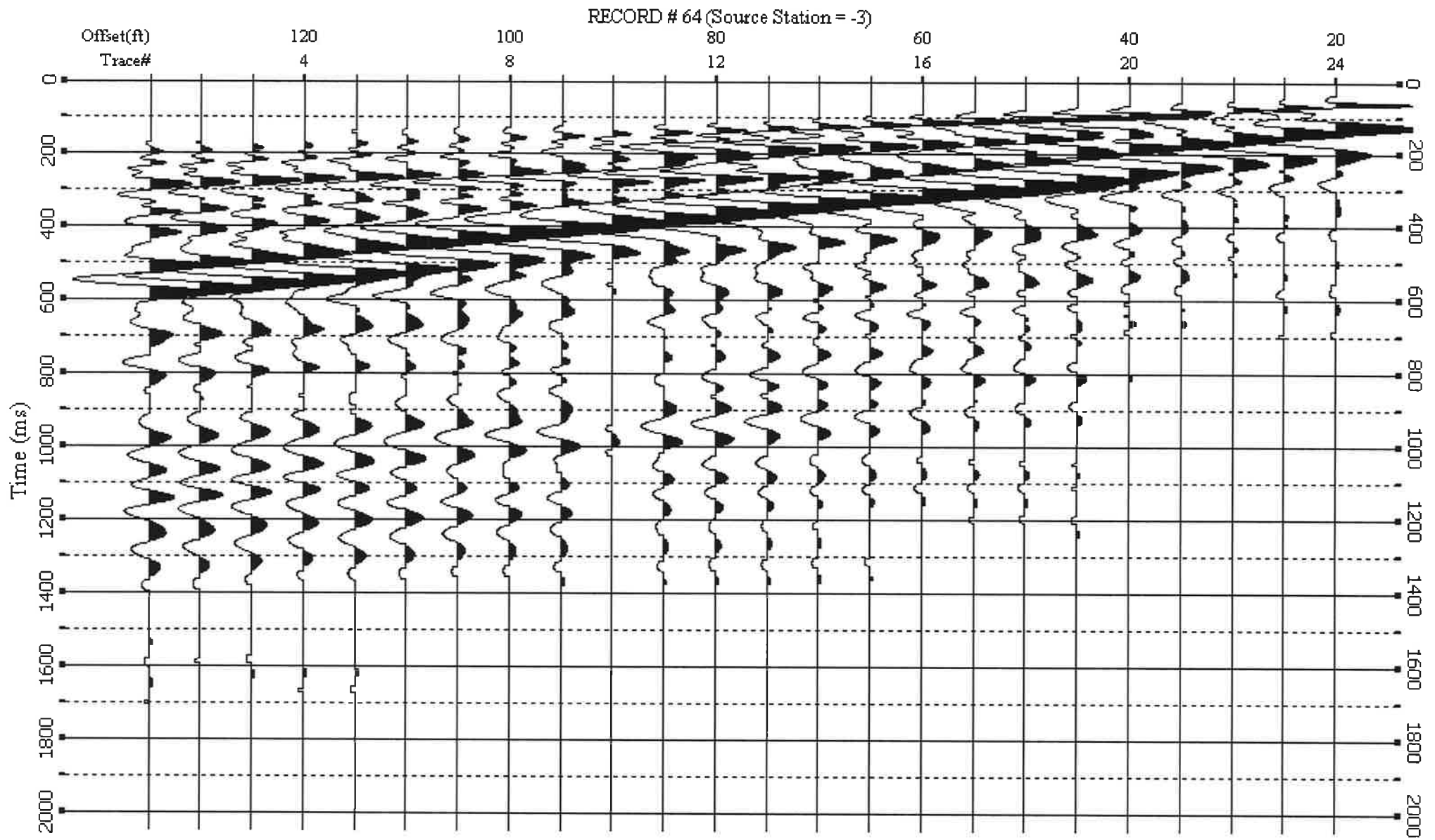


Figure 14a

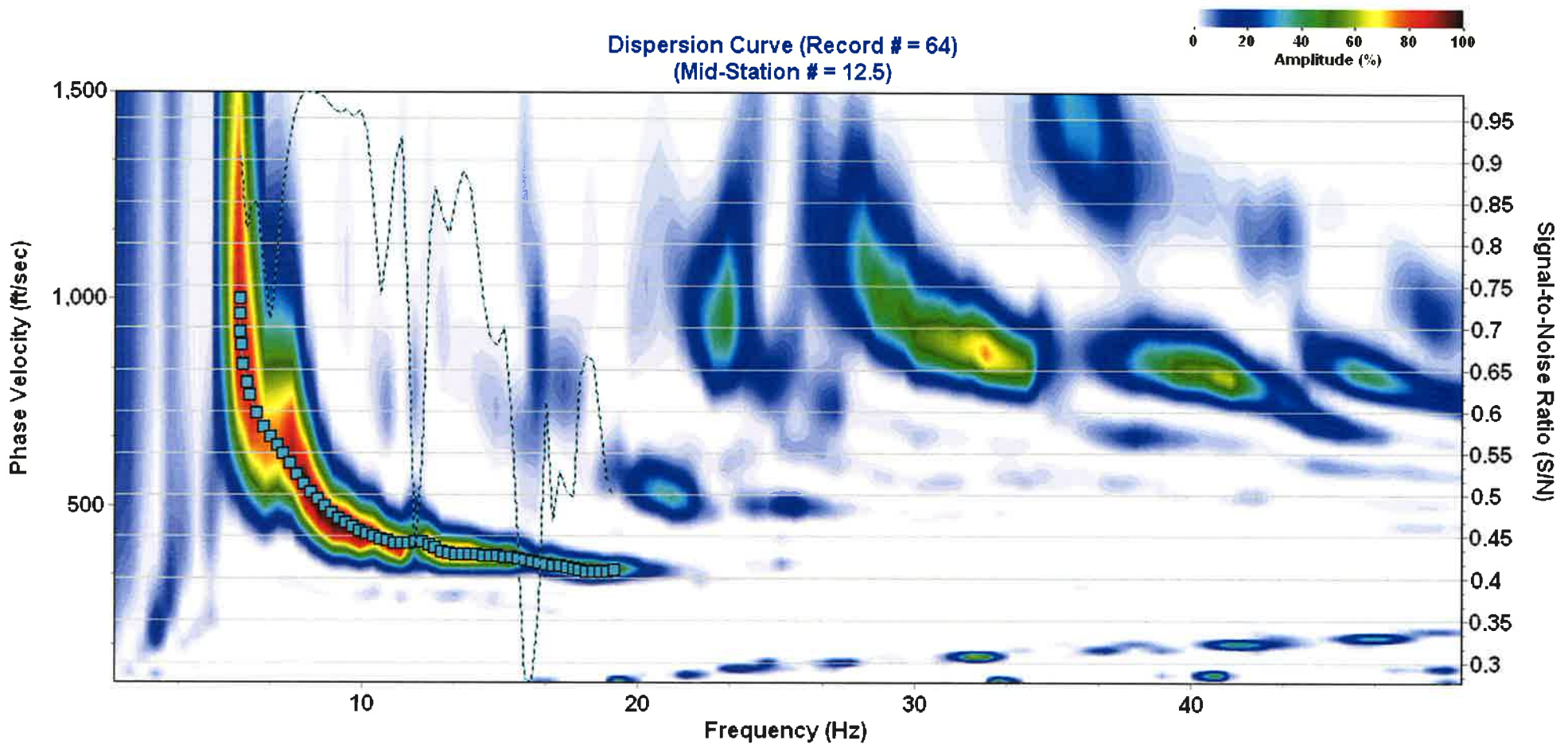


Figure 14b

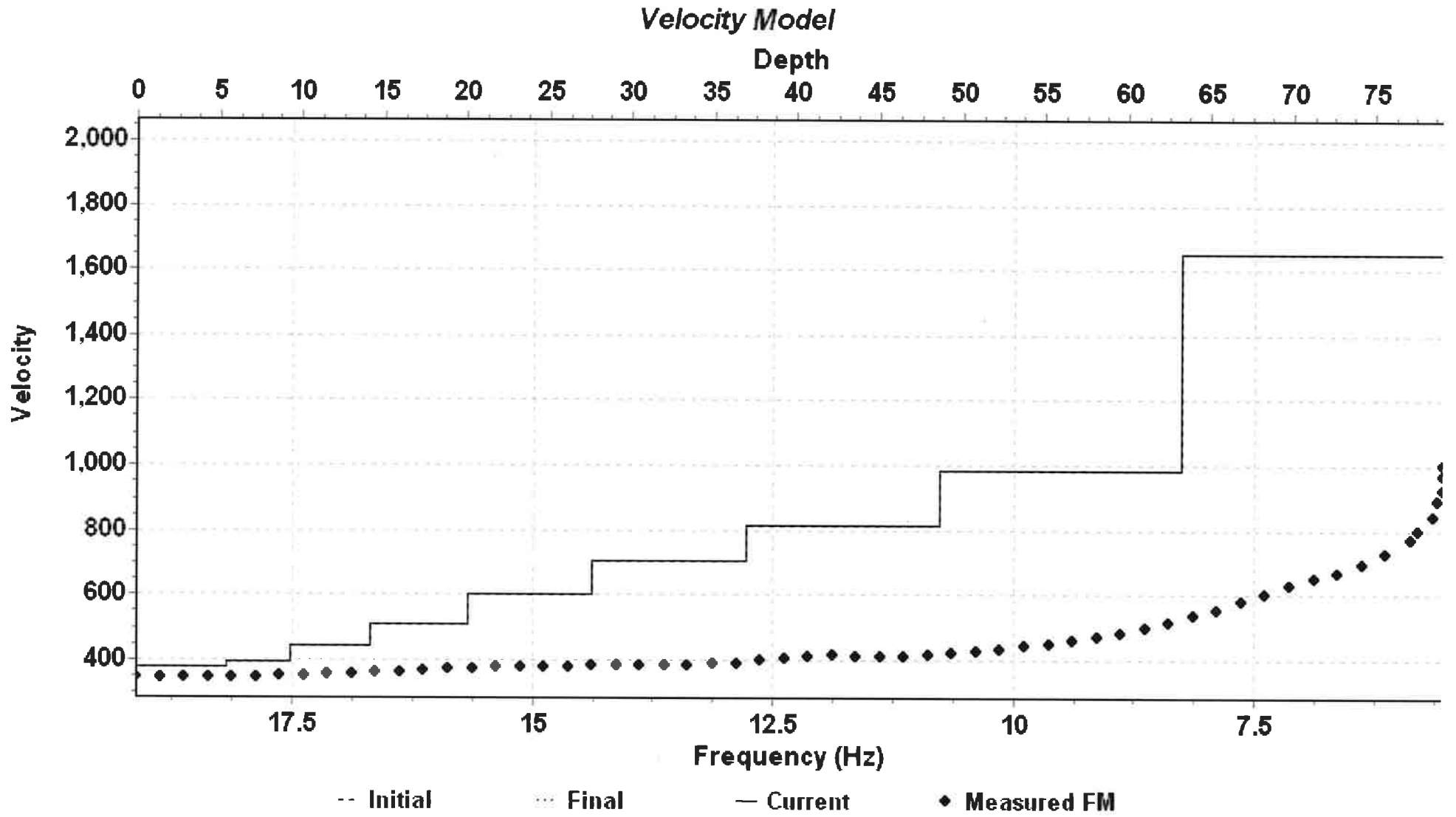


Figure 14c

10-LAYER VELOCITY MODEL (Record = 64)
(Mid-Station = 12.5)

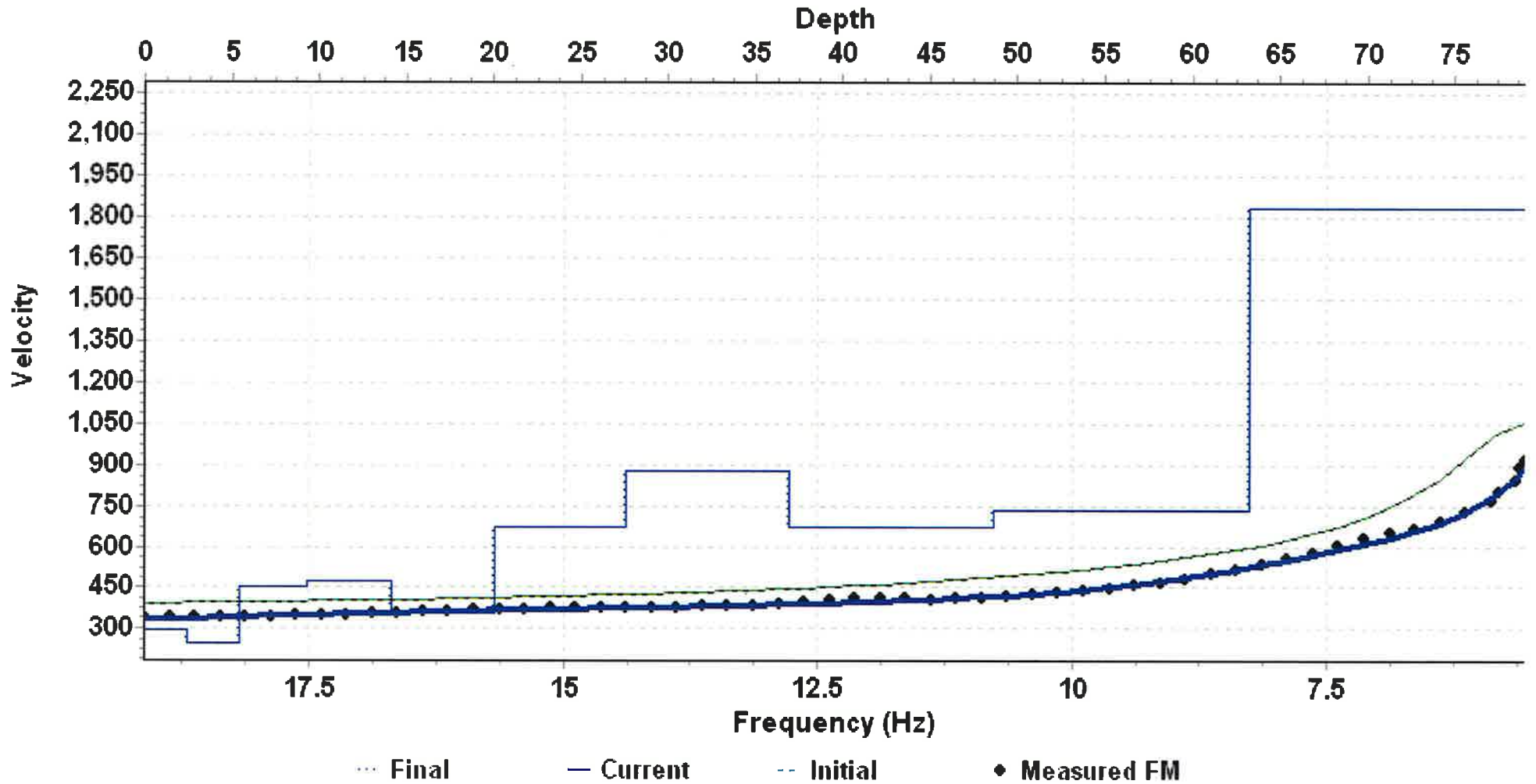


Figure 14d

MASW Line 64

| Layer | Depth | Vs Velocity |
|--------------|--------------|--------------------|
| 1 | -2.451 | 297.358 |
| 2 | -5.515 | 248.657 |
| 3 | -9.345 | 450.282 |
| 4 | -14.132 | 472.219 |
| 5 | -20.116 | 354.651 |
| 6 | -27.596 | 673.719 |
| 7 | -36.946 | 875.471 |
| 8 | -48.634 | 669.089 |
| 9 | -63.244 | 736.409 |
| 10 | -79.055 | 1834.998 |

Figure 15

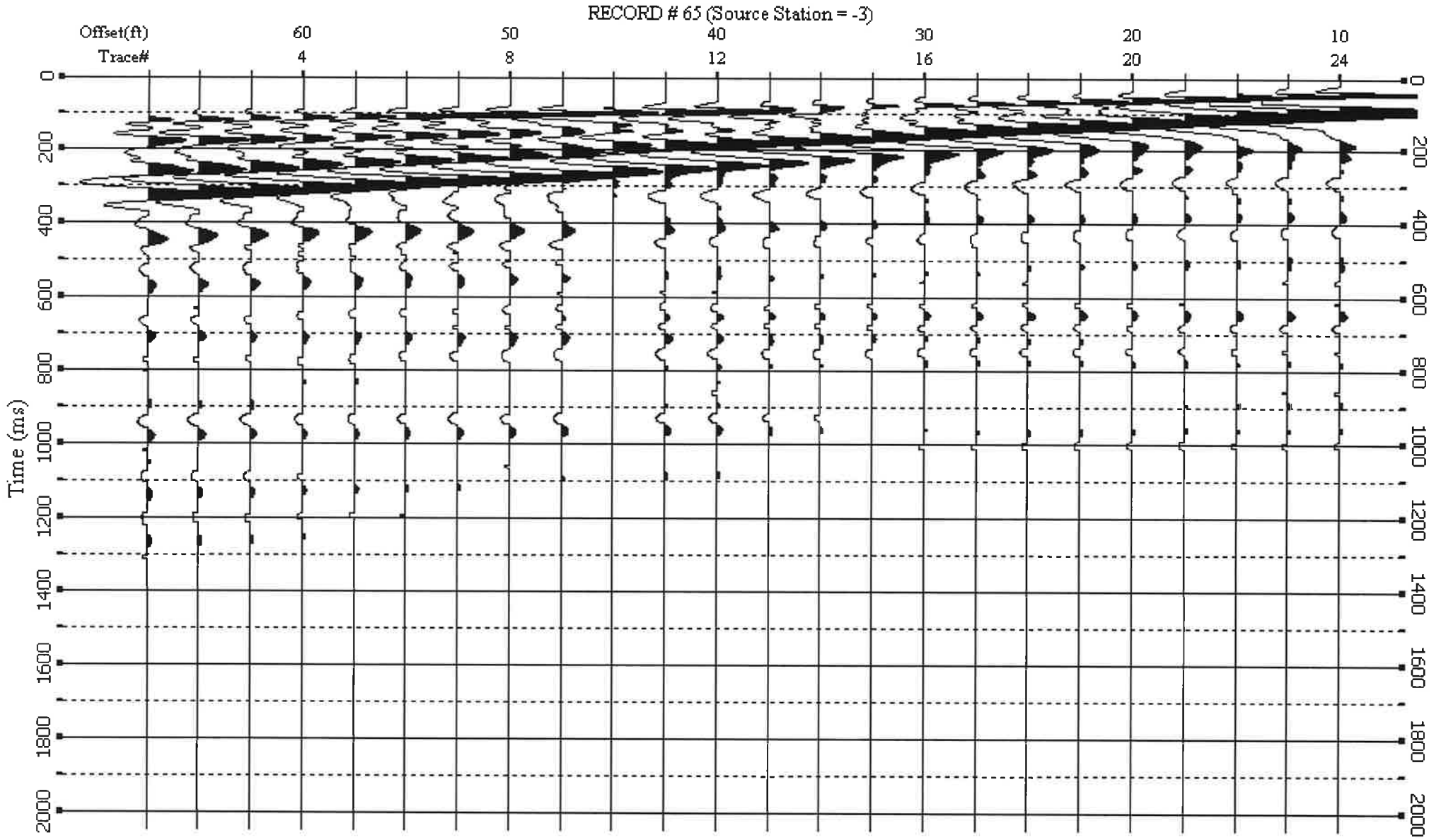


Figure 15a

Dispersion Curve (Record # = 65)
(Mid-Station # = 12.5)

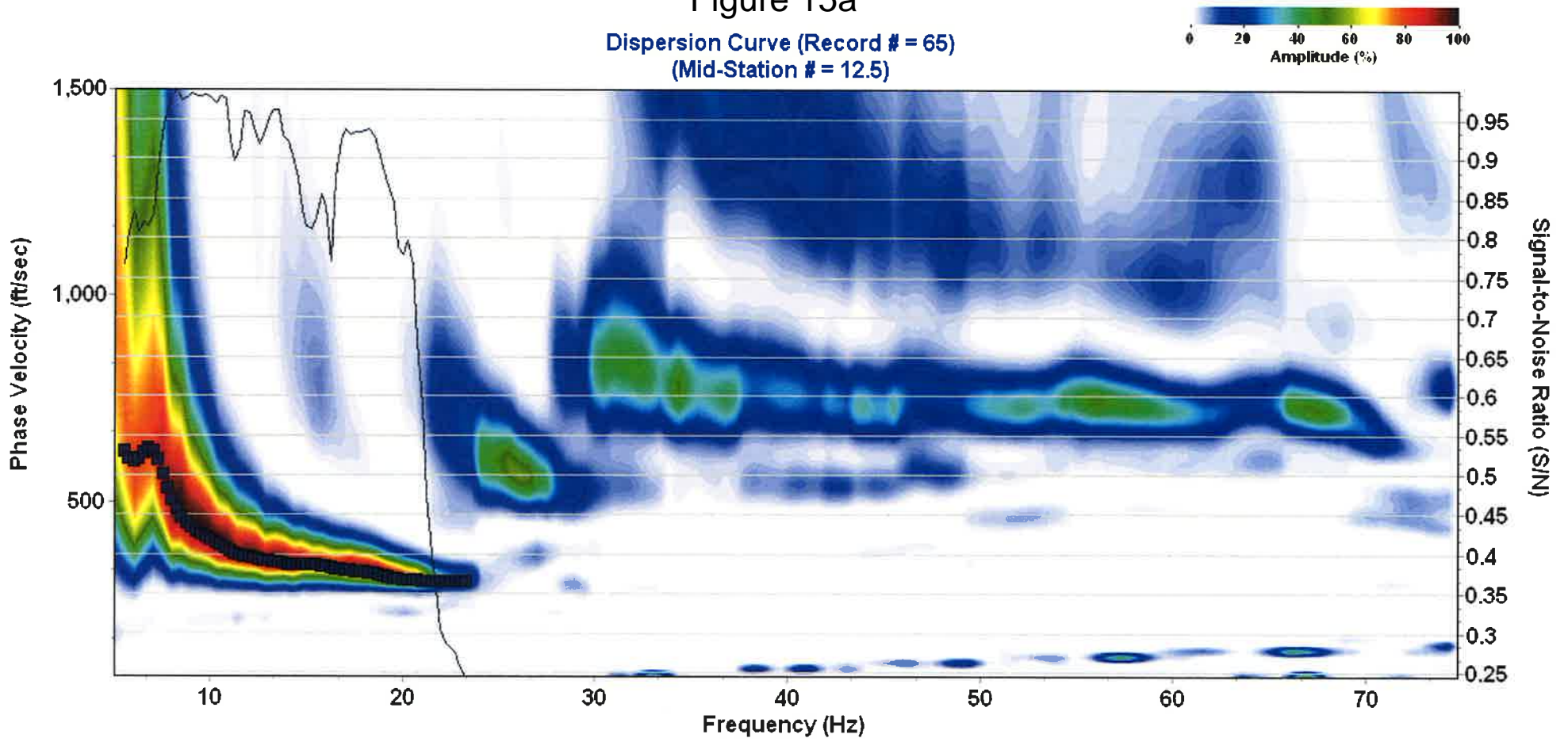


Figure 15b

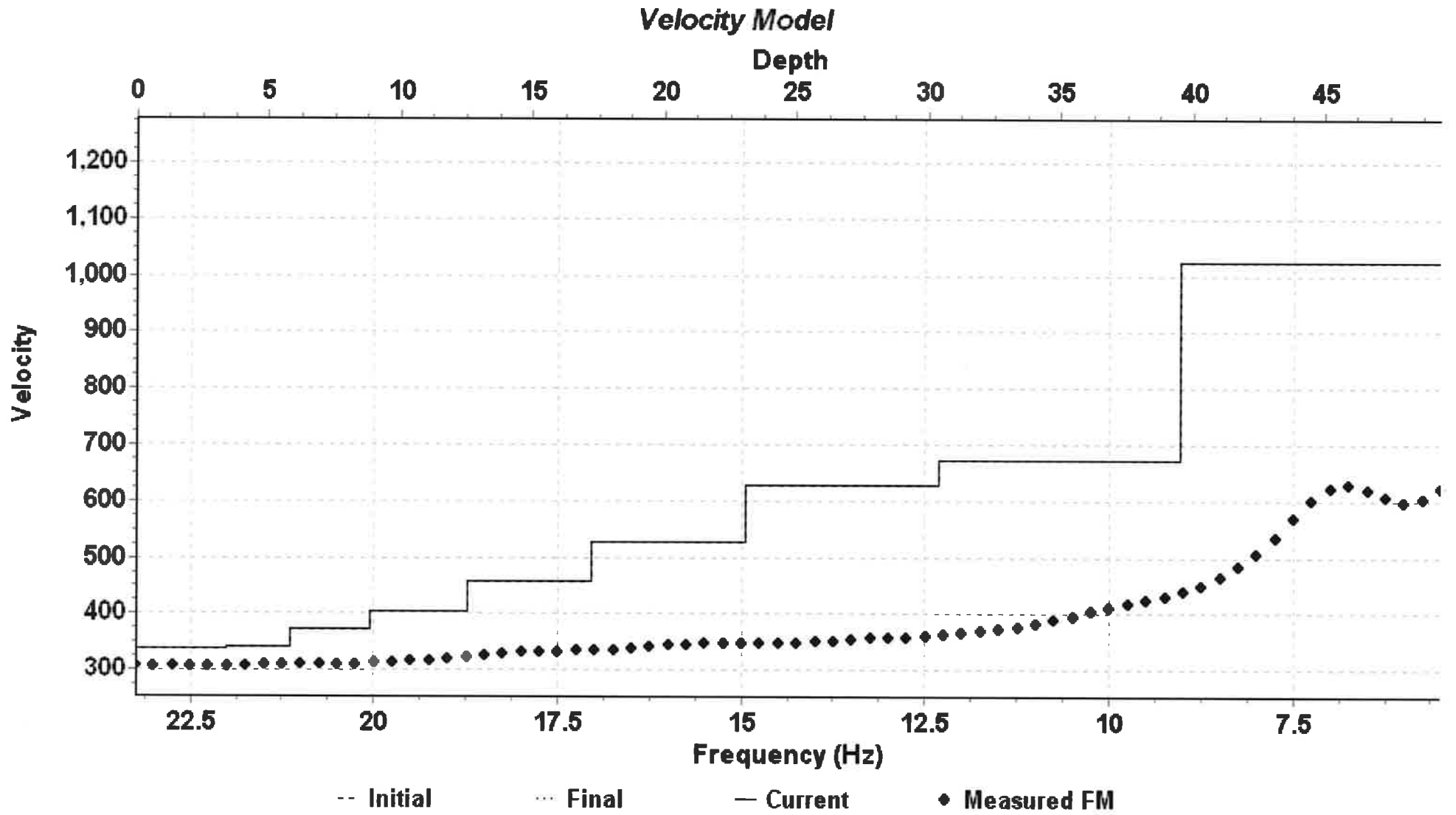


Figure 15c

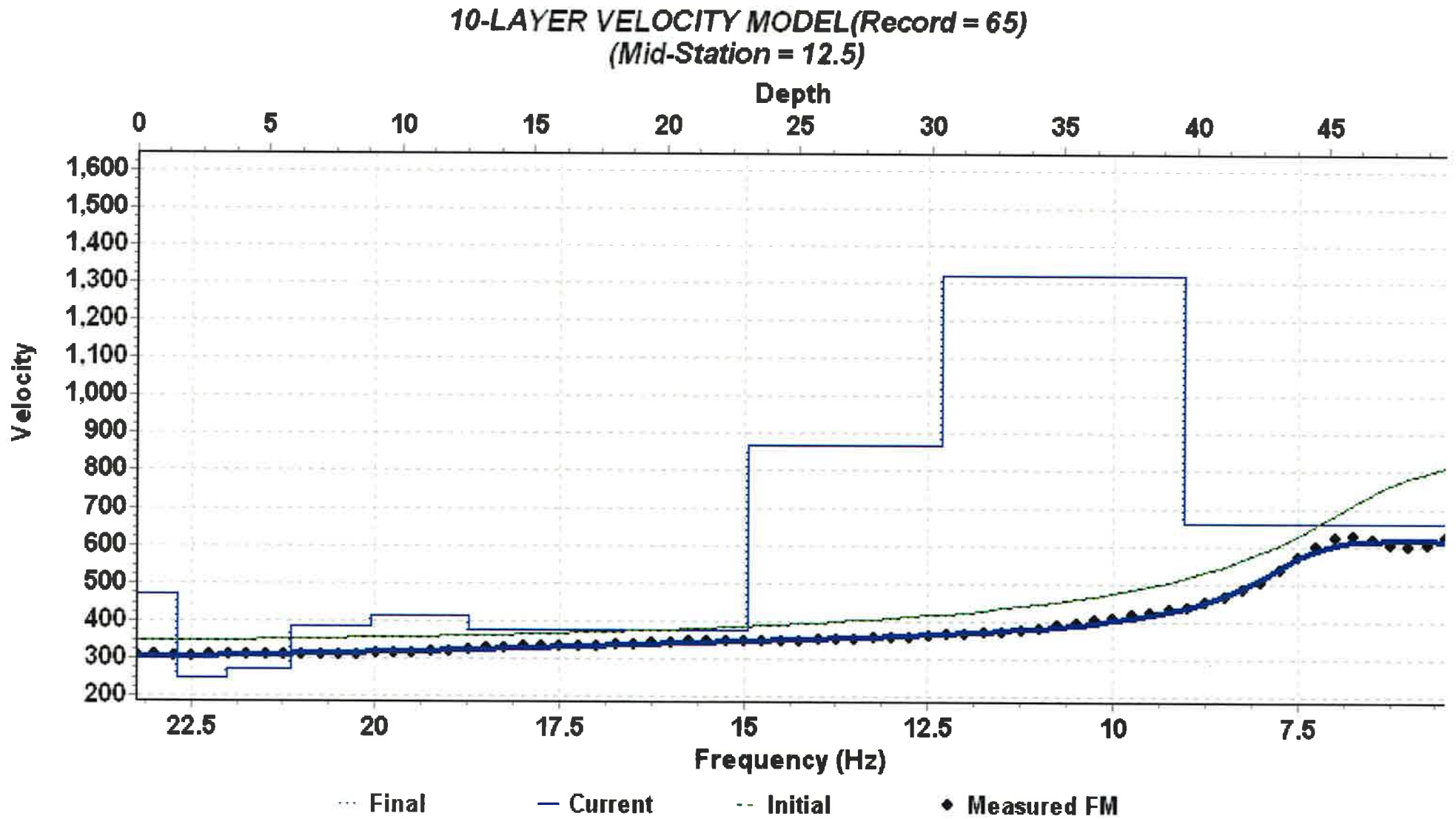


Figure 15d

MASW Line 65

| Layer | Depth (ft) | Vs Velocity (ft/s) |
|--------------|-------------------|---------------------------|
| 1 | -1.533 | 471.847 |
| 2 | -3.449 | 247.162 |
| 3 | -5.844 | 270.313 |
| 4 | -8.838 | 385.298 |
| 5 | -12.58 | 412.498 |
| 6 | -17.257 | 376.895 |
| 7 | -23.104 | 375.864 |
| 8 | -30.412 | 868.044 |
| 9 | -39.547 | 1317.329 |
| 10 | -49.434 | 658.959 |

Figure 16

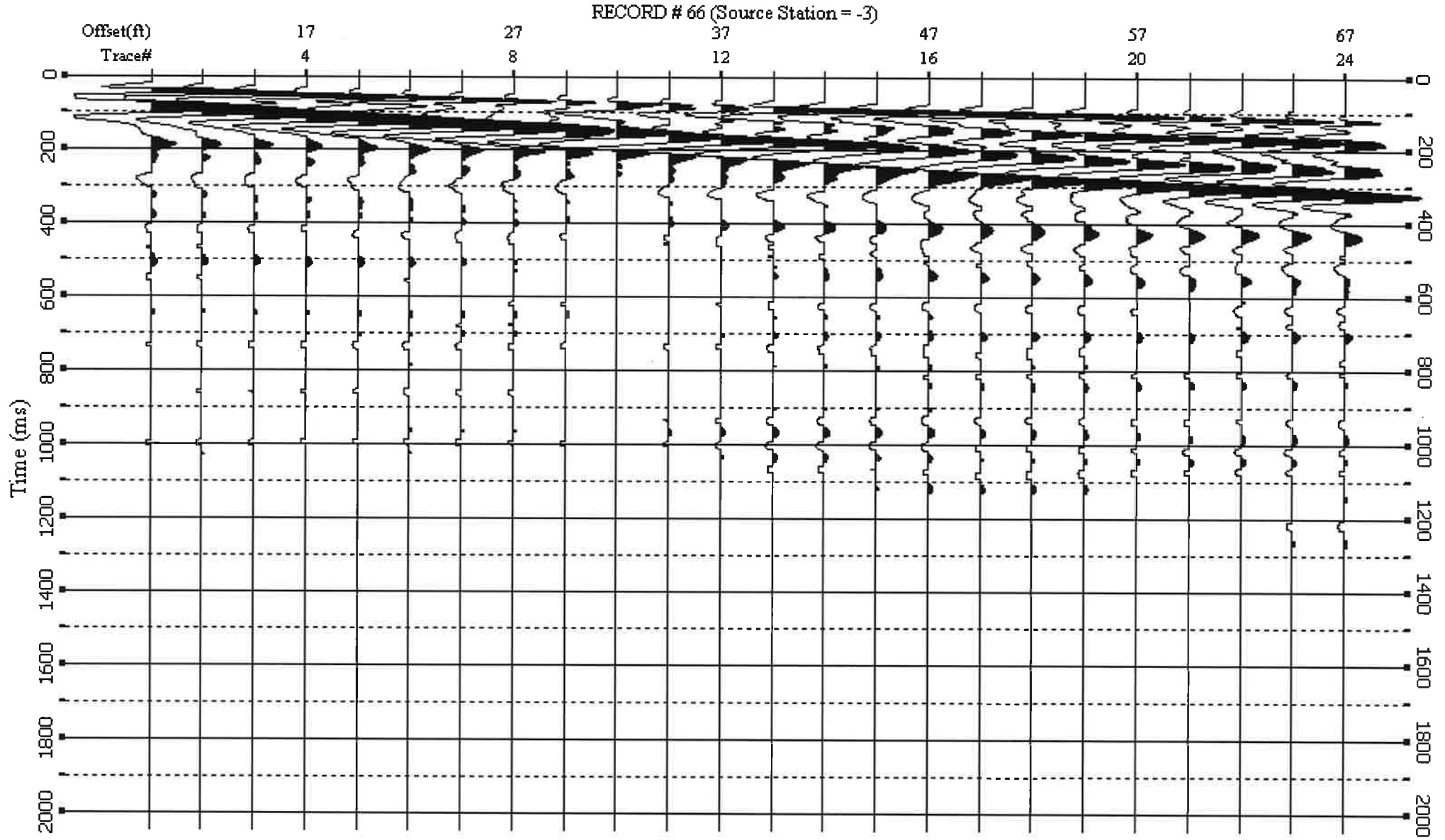


Figure 16a

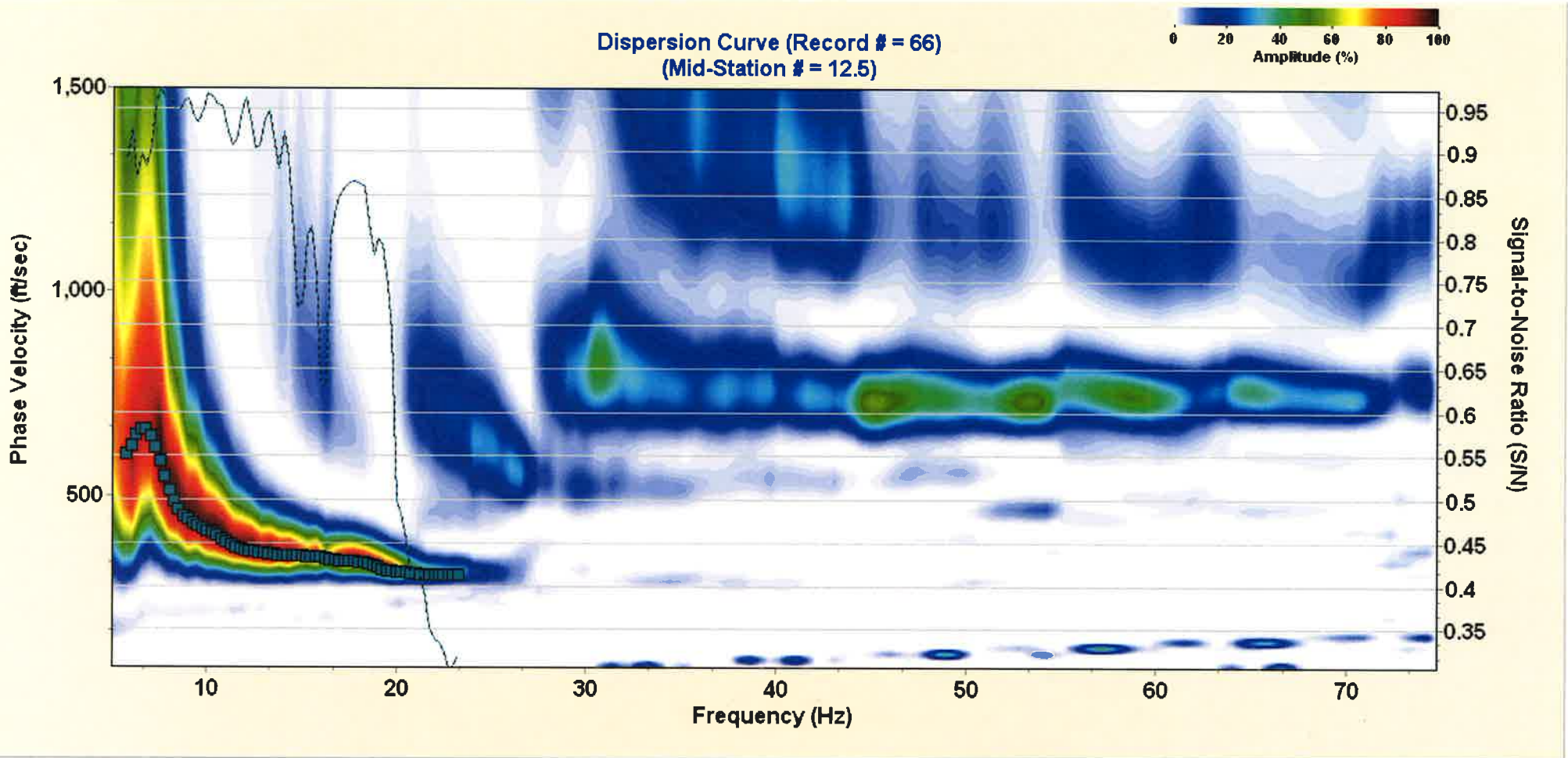


Figure 16b
Velocity Model

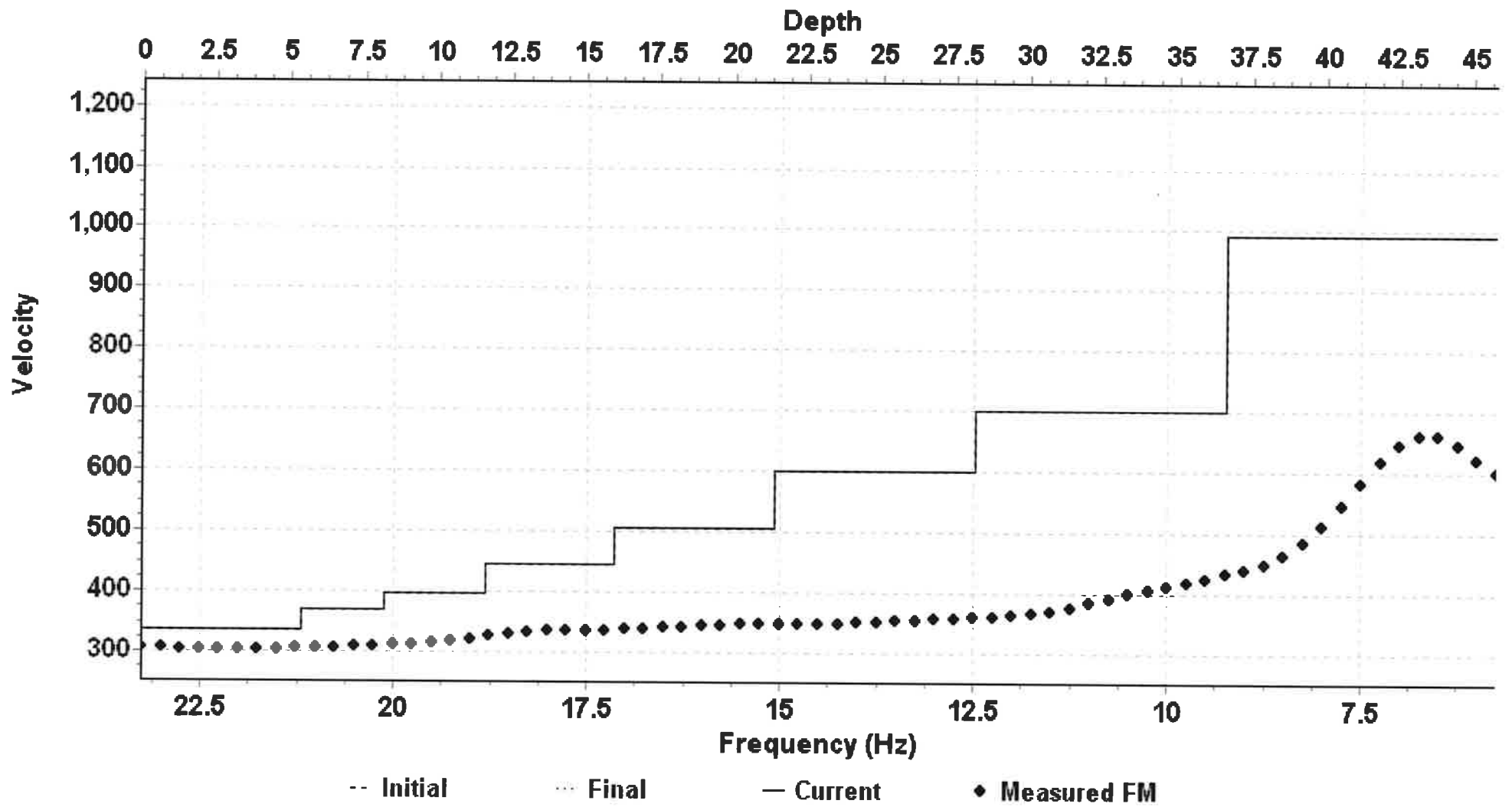


Figure 16c

10-LAYER VELOCITY MODEL (Record = 66)
(Mid-Station = 12.5)

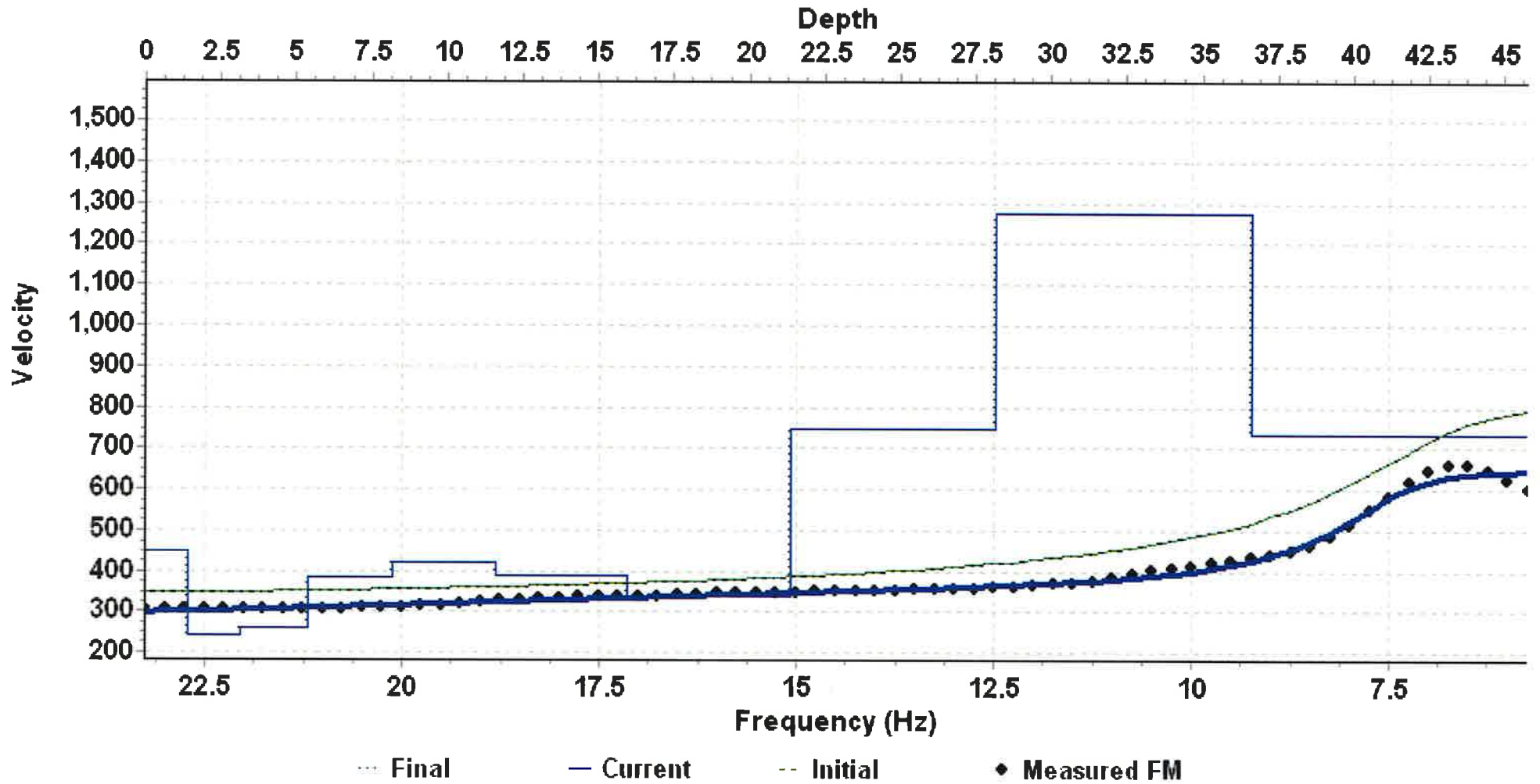


Figure 16d

MASW Line 66

| Layer | Depth (ft) | Vs Velocity (ft/s) |
|--------------|-------------------|---------------------------|
| 1 | -1.42 | 446.942 |
| 2 | -3.194 | 242.623 |
| 3 | -5.412 | 261.391 |
| 4 | -8.185 | 382.211 |
| 5 | -11.651 | 421.329 |
| 6 | -15.983 | 387.591 |
| 7 | -21.398 | 337.953 |
| 8 | -28.167 | 746.623 |
| 9 | -36.628 | 1277.978 |
| 10 | -45.785 | 734.302 |

Appendix C

SPREAD3 shots: 1 2 3 4 5 6 7

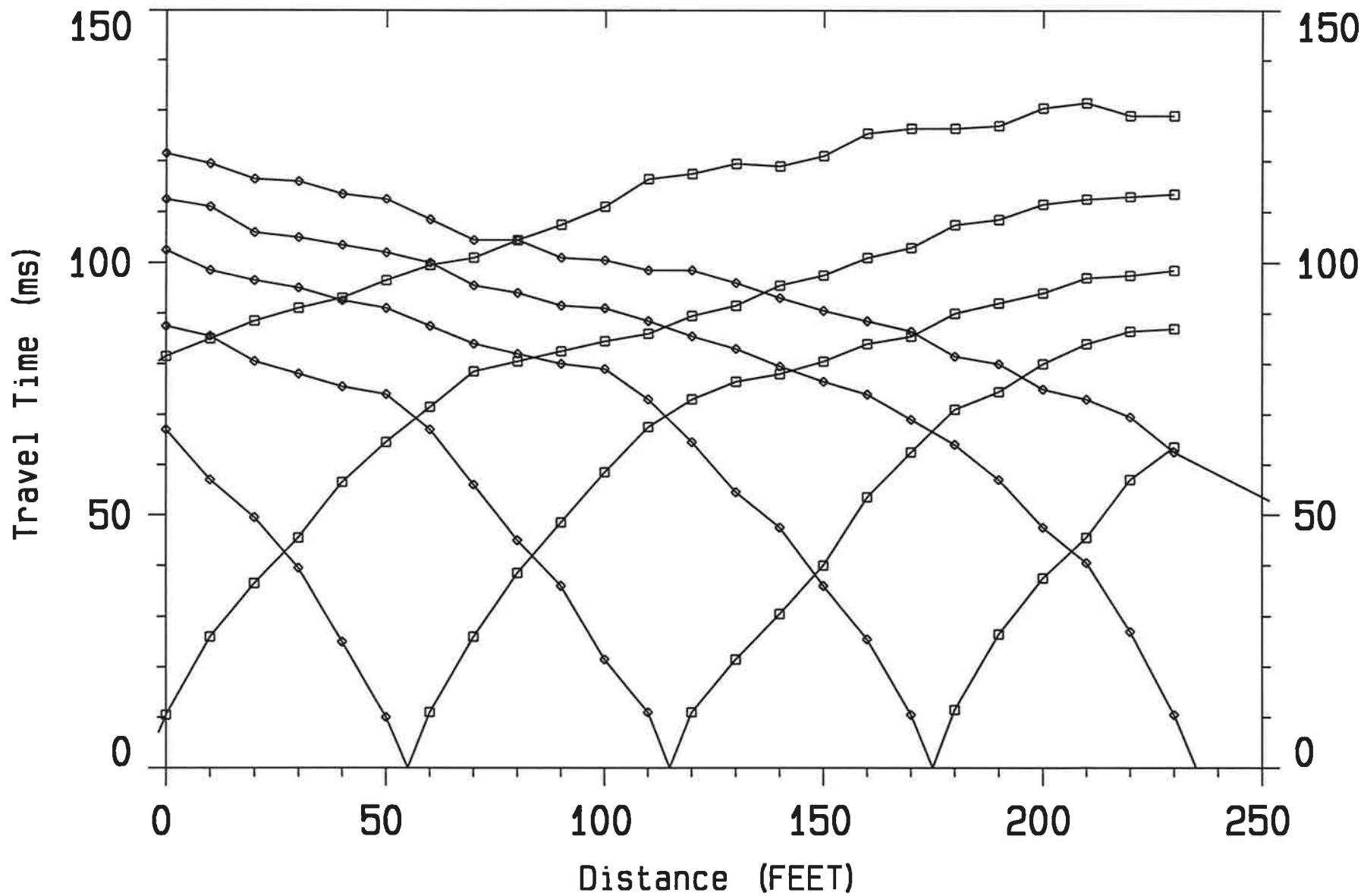


Figure 17a

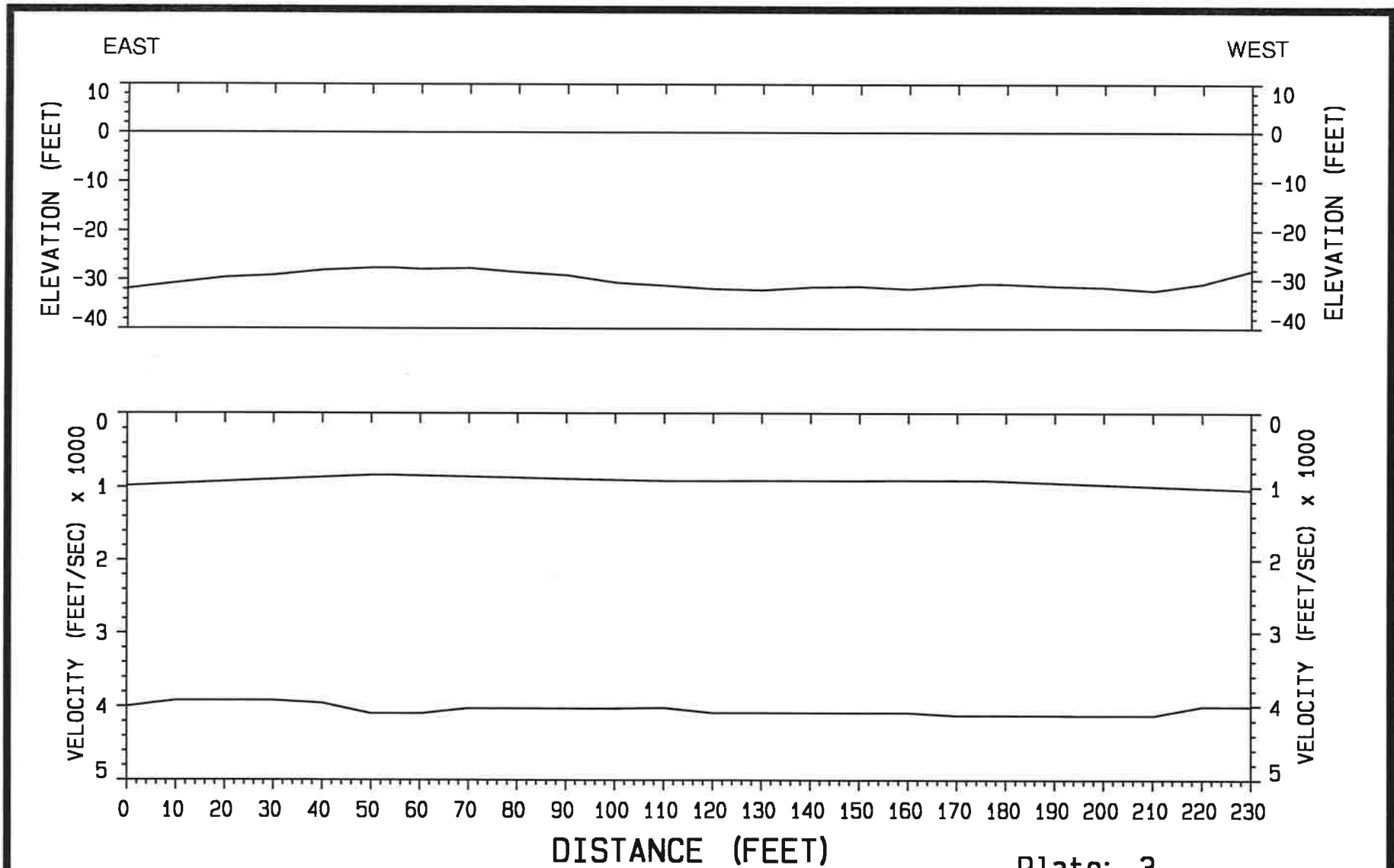


Plate: 3

| | | | |
|-------------------------------|------------------|-----------------------------|--|
| for: Penn State | | Penn State Research Project | |
| by: VIBRA-TECH ENGINEERS INC. | | Jeddo 8 | |
| Data Set: SPREAD3 | Date: 07/31/2017 | | |
| Equipment: GEOMETRICO SLR | Spread: 00001 | Azimuth: | |

SUMMARY OF GRM CURVE ANALYSIS:

| SEGMENT | SHOT1 | SHOT2 | R1 | R2 | RA | X-Y | No. Pts |
|---------|-------|-------|----|----|----|-------|---------|
| 1 | 5 | 1 | 1 | 1 | 1 | 10.00 | 12 |
| 2 | 6 | 1 | 1 | 1 | 1 | 0.00 | 17 |
| 3 | 6 | 2 | 1 | 1 | 1 | 60.00 | 16 |
| 4 | 7 | 1 | 1 | 1 | 1 | 0.00 | 24 |
| 5 | 7 | 2 | 1 | 1 | 1 | 40.00 | 17 |
| 6 | 7 | 3 | 1 | 1 | 1 | 0.00 | 13 |

Reciprocal time estimates from refractors R1 and R2
 Refractor RA is refractor analyzed

Optimum X-Y value estimates:

| LAYER | MINIMUM X-Y | AVERAGE X-Y | MAXIMUM X-Y |
|-------|-------------|-------------|-------------|
| 1 | 11.25 | 13.69 | 15.66 |

GRM DEPTH SECTION RESULTS:

S-N: STATION NUMBER, V: VELOCITY (FEET/sec), Z: DEPTH (FEET)

| S-N | V1 | V2 | V3 | V4 | Z1 | Z2 | Z3 |
|-------|--------|---------|----|----|--------|----|----|
| | 982.29 | 3999.48 | | | 31.882 | | |
| 1.00 | 952.83 | 3918.04 | | | 30.704 | | |
| 2.00 | 923.38 | 3918.04 | | | 29.580 | | |
| 3.00 | 893.92 | 3918.04 | | | 29.100 | | |
| 4.00 | 864.46 | 3956.31 | | | 28.078 | | |
| 5.00 | 835.01 | 4096.40 | | | 27.595 | | |
| 5.50 | 835.01 | 4096.40 | | | 27.595 | | |
| 6.00 | 842.21 | 4096.40 | | | 27.843 | | |
| 7.00 | 856.61 | 4025.95 | | | 27.675 | | |
| 8.00 | 871.01 | 4025.95 | | | 28.497 | | |
| 9.00 | 885.41 | 4025.95 | | | 29.105 | | |
| 10.00 | 899.81 | 4025.95 | | | 30.604 | | |
| 11.00 | 914.21 | 4018.81 | | | 31.218 | | |
| 11.50 | 914.21 | 4053.32 | | | 31.566 | | |
| 12.00 | 913.44 | 4087.83 | | | 31.886 | | |
| 13.00 | 911.90 | 4087.83 | | | 32.110 | | |
| 14.00 | 910.35 | 4087.83 | | | 31.493 | | |
| 15.00 | 908.81 | 4087.83 | | | 31.390 | | |
| 16.00 | 907.26 | 4087.83 | | | 31.892 | | |
| 17.00 | 905.72 | 4124.29 | | | 31.188 | | |
| 17.50 | 905.72 | 4124.29 | | | 30.811 | | |
| 18.00 | 917.97 | 4124.29 | | | 30.867 | | |
| 19.00 | 942.46 | 4124.29 | | | 31.312 | | |

GRM DEPTH SECTION RESULTS:

S-N: STATION NUMBER, V: VELOCITY (FEET/sec), Z: DEPTH (FEET)

| S-N | V1 | V2 | V3 | V4 | Z1 | Z2 | Z3 |
|-------|---------|---------|----|----|--------|----|----|
| 20.00 | 966.96 | 4129.26 | | | 31.555 | | |
| 21.00 | 991.46 | 4129.26 | | | 32.233 | | |
| 22.00 | 1015.96 | 4006.82 | | | 30.852 | | |
| 23.00 | 1040.46 | 4006.82 | | | 28.147 | | |

Figure 17c

SPREAD3

197
PAGE 1

DATA SET: SPREAD3

| | |
|--------------------------------------|---------------------------|
| CLIENT: Penn State | DATE: 07/31/2017 |
| LOCATION: Jeddo 8 | LINE NO.: 00001 |
| COUNTY: | AZIMUTH: |
| PROJECT: Penn State Research Project | G-SPACING: 10.00 FEET |
| SOURCE: Kinepak | EQUIPMENT: GEOMETRICS Str |

-----RECIPROCAL TIME ESTIMATES -----

| SHOT | SHOT | RT1 (msec) | RT2 (msec) | DIFF | LAYERS |
|------|------|------------|------------|-------|--------|
| 3 | 1 | 98.00 | N/A | N/A | 2 ? |
| 3 | 2 | 68.00 | 67.00 | 1.00 | 1 1 |
| 4 | 1 | 117.00 | N/A | N/A | 2 ? |
| 4 | 2 | 87.75 | 87.50 | 0.25 | 2 2 |
| 4 | 3 | 70.25 | 70.50 | -0.25 | 1 1 |
| 5 | 1 | 126.50 | N/A | N/A | 2 ? |
| 5 | 2 | 105.25 | 102.50 | 2.75 | 2 2 |
| 5 | 3 | 87.75 | 89.25 | -1.50 | 2 2 |
| 5 | 4 | 66.75 | 68.75 | -2.00 | 1 1 |
| 6 | 1 | 129.00 | N/A | N/A | 2 ? |
| 6 | 2 | 113.50 | 112.50 | 1.00 | 2 2 |
| 6 | 3 | 98.50 | 101.00 | -2.50 | 2 2 |
| 6 | 4 | 87.00 | 87.00 | 0.00 | 2 2 |
| 6 | 5 | 63.50 | 66.50 | -3.00 | 1 1 |
| 7 | 2 | N/A | 121.50 | N/A | ? 2 |
| 7 | 3 | N/A | 110.50 | N/A | ? 2 |
| 7 | 4 | N/A | 98.50 | N/A | ? 2 |
| 7 | 5 | N/A | 84.00 | N/A | ? 2 |

-----ESTIMATES BETWEEN FAR SHOTS-----

| SHOT | SHOT | RT (ms) | RT (I-A) | RT (J-B) | RTAB | LAYERS |
|------|------|---------|----------|----------|--------|--------|
| 7 | 1 | 137.50 | 121.50 | 129.00 | 113.00 | 2 2 |

Figure 18

SPREAD2 shots: 1 2 3 4 5 6 7

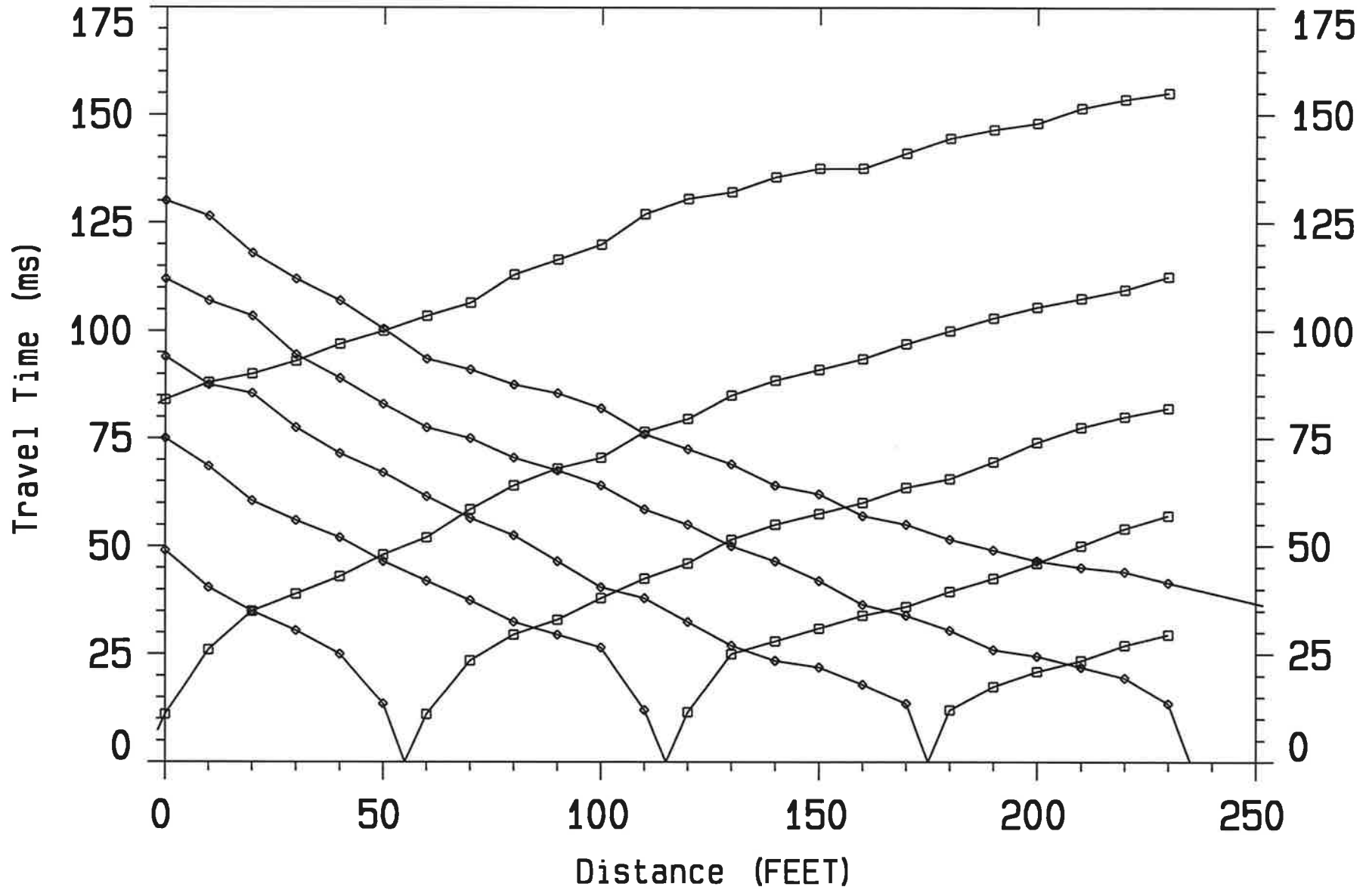


Figure 18a

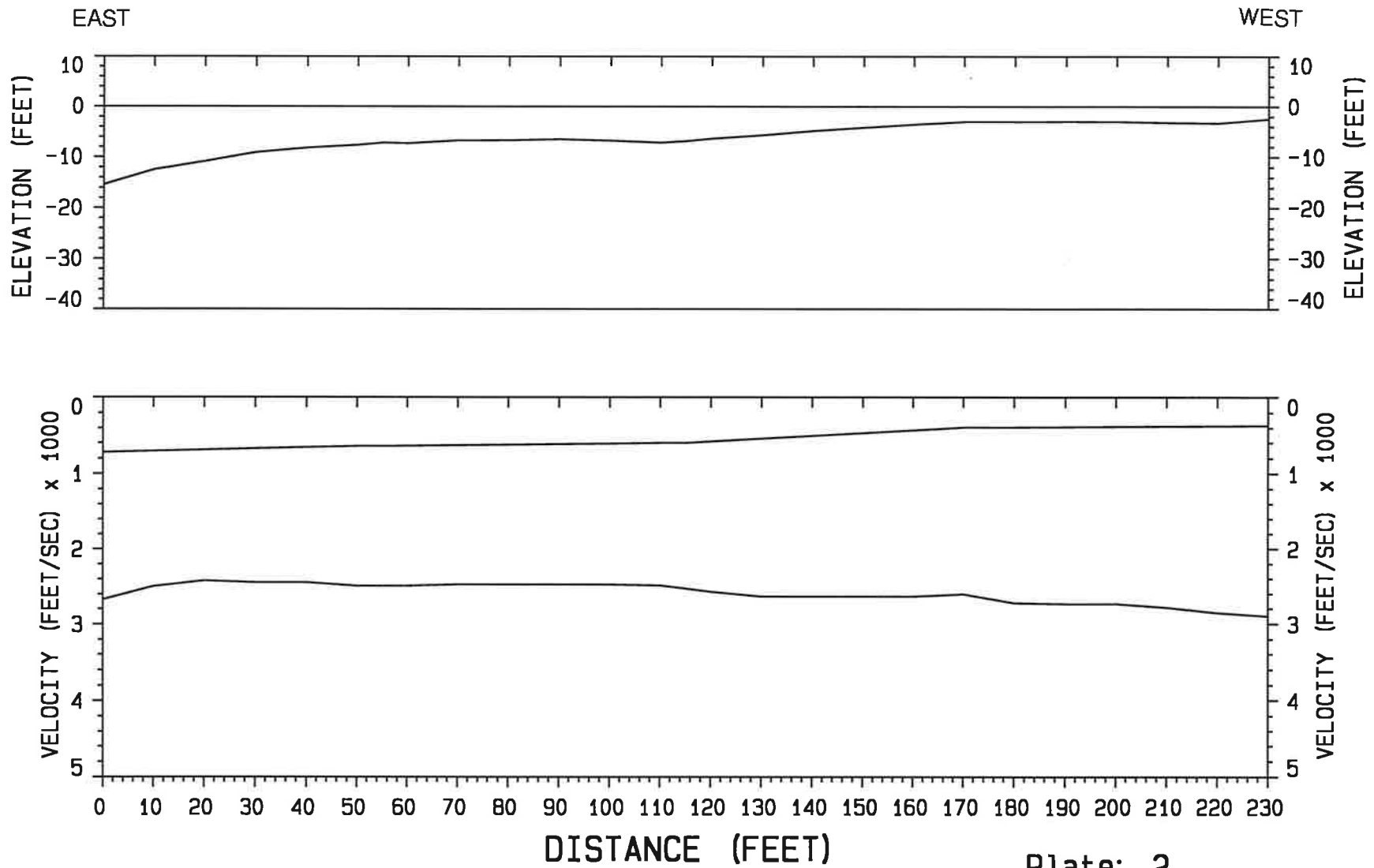


Plate: 2

| | | | |
|-------------------------------|------------------|-----------------------------|--|
| for: Penn State | | Penn State Research Project | |
| by: VIBRA-TECH ENGINEERS INC. | | Jeddo 14 | |
| Data Set: SPREAD2 | Date: 07/31/2017 | | |
| Equipment: GEOMETRICAL SUR | Spread: 00001 | Azimuth: | |

SUMMARY OF GRM CURVE ANALYSIS:

| SEGMENT | SHOT1 | SHOT2 | R1 | R2 | RA | X-Y | No. Pts |
|---------|-------|-------|----|----|----|------|---------|
| 1 | 4 | 2 | 1 | 1 | 1 | 0.00 | 10 |
| 2 | 5 | 2 | 1 | 1 | 1 | 0.00 | 16 |
| 3 | 5 | 3 | 1 | 1 | 1 | 0.00 | 11 |
| 4 | 6 | 1 | 1 | 1 | 1 | 0.00 | 24 |
| 5 | 6 | 2 | 1 | 1 | 1 | 0.00 | 18 |
| 6 | 6 | 3 | 1 | 1 | 1 | 0.00 | 17 |
| 7 | 6 | 4 | 1 | 1 | 1 | 0.00 | 11 |
| 8 | 6 | 5 | 1 | 1 | 1 | 0.00 | 6 |
| 9 | 7 | 1 | 1 | 1 | 1 | 0.00 | 21 |
| 10 | 7 | 2 | 1 | 1 | 1 | 0.00 | 18 |
| 11 | 7 | 3 | 1 | 1 | 1 | 0.00 | 17 |
| 12 | 7 | 4 | 1 | 1 | 1 | 0.00 | 11 |

Reciprocal time estimates from refractors R1 and R2
 Refractor RA is refractor analyzed

Optimum X-Y value estimates:

| LAYER | MINIMUM X-Y | AVERAGE X-Y | MAXIMUM X-Y |
|-------|-------------|-------------|-------------|
| 1 | 0.62 | 2.92 | 8.32 |

GRM DEPTH SECTION RESULTS:

S-N: STATION NUMBER, V: VELOCITY (FEET/sec), Z: DEPTH (FEET)

| S-N | V1 | V2 | V3 | V4 | Z1 | Z2 | Z3 |
|-------|--------|---------|----|----|--------|----|----|
| | 723.04 | 2676.63 | | | 15.394 | | |
| 1.00 | 706.94 | 2499.53 | | | 12.460 | | |
| 2.00 | 690.84 | 2422.70 | | | 10.871 | | |
| 3.00 | 674.74 | 2446.23 | | | 9.106 | | |
| 4.00 | 658.64 | 2446.23 | | | 8.209 | | |
| 5.00 | 642.54 | 2493.57 | | | 7.636 | | |
| 5.50 | 642.54 | 2493.57 | | | 7.220 | | |
| 6.00 | 638.57 | 2493.57 | | | 7.317 | | |
| 7.00 | 630.62 | 2472.86 | | | 6.749 | | |
| 8.00 | 622.67 | 2472.86 | | | 6.716 | | |
| 9.00 | 614.72 | 2472.86 | | | 6.510 | | |
| 10.00 | 606.77 | 2472.86 | | | 6.776 | | |
| 11.00 | 598.83 | 2486.61 | | | 7.171 | | |
| 11.50 | 598.83 | 2528.70 | | | 6.865 | | |
| 12.00 | 580.16 | 2570.73 | | | 6.344 | | |
| 13.00 | 542.83 | 2635.63 | | | 5.671 | | |
| 14.00 | 505.50 | 2635.63 | | | 4.826 | | |

GRM DEPTH SECTION RESULTS:

S-N: STATION NUMBER, V: VELOCITY (FEET/sec), Z: DEPTH (FEET)

| S-N | V1 | V2 | V3 | V4 | Z1 | Z2 | Z3 |
|-------|--------|---------|----|----|-------|----|----|
| 15.00 | 468.18 | 2635.63 | | | 4.180 | | |
| 16.00 | 430.85 | 2635.63 | | | 3.546 | | |
| 17.00 | 393.52 | 2604.85 | | | 3.013 | | |
| 17.50 | 393.52 | 2663.86 | | | 3.030 | | |
| 18.00 | 391.41 | 2722.90 | | | 3.030 | | |
| 19.00 | 387.21 | 2735.01 | | | 2.967 | | |
| 20.00 | 383.00 | 2735.01 | | | 2.978 | | |
| 21.00 | 378.79 | 2783.49 | | | 3.160 | | |
| 22.00 | 374.58 | 2854.36 | | | 3.277 | | |
| 23.00 | 370.37 | 2897.59 | | | 2.443 | | |

Figure 18c

DATA SET: SPREAD2

| | |
|--------------------------------------|---------------------------|
| CLIENT: Penn State | DATE: 07/31/2017 |
| LOCATION: Jeddo 14 | LINE NO.: 00001 |
| COUNTY: | AZIMUTH: |
| PROJECT: Penn State Research Project | G-SPACING: 10.00 FEET |
| SOURCE: Kinepak | EQUIPMENT: GEOMETRICS Str |

-----RECIPROCAL TIME ESTIMATES -----

| SHOT | SHOT | RT1 (msec) | RT2 (msec) | DIFF | LAYERS |
|------|------|------------|------------|-------|--------|
| 3 | 1 | 98.00 | N/A | N/A | 2 ? |
| 3 | 2 | 48.25 | 49.00 | -0.75 | 2 2 |
| 4 | 1 | 128.75 | N/A | N/A | 2 ? |
| 4 | 2 | 78.00 | 75.00 | 3.00 | 2 2 |
| 4 | 3 | 41.75 | 43.50 | -1.75 | 2 2 |
| 5 | 1 | 142.75 | N/A | N/A | 2 ? |
| 5 | 2 | 96.75 | 94.00 | 2.75 | 2 2 |
| 5 | 3 | 63.75 | 64.25 | -0.50 | 2 2 |
| 5 | 4 | 35.75 | 35.25 | 0.50 | 2 2 |
| 6 | 1 | 155.00 | N/A | N/A | 2 ? |
| 6 | 2 | 112.50 | 112.00 | 0.50 | 2 2 |
| 6 | 3 | 82.00 | 80.25 | 1.75 | 2 2 |
| 6 | 4 | 57.00 | 56.75 | 0.25 | 2 2 |
| 6 | 5 | 29.50 | 32.25 | -2.75 | 2 2 |
| 7 | 2 | N/A | 130.00 | N/A | ? 2 |
| 7 | 3 | N/A | 97.00 | N/A | ? 2 |
| 7 | 4 | N/A | 74.25 | N/A | ? 2 |
| 7 | 5 | N/A | 52.50 | N/A | ? 2 |

-----ESTIMATES BETWEEN FAR SHOTS-----

| SHOT | SHOT | RT (ms) | RT (I-A) | RT (J-B) | RTAB | LAYERS |
|------|------|---------|----------|----------|--------|--------|
| 7 | 1 | 172.75 | 130.00 | 155.00 | 112.25 | 2 2 |

RECIPROCAL TIME INFORMATION:

SHOT TYPE ----- RECIPROCAL TIMES (msec) -----

| | | | | | | | |
|---|---|--------|--------|-------|-------|-------|--|
| 2 | A | | | | | | |
| 3 | E | 98.00 | 48.63 | | | | |
| 4 | E | 128.75 | 76.50 | 42.63 | | | |
| 5 | E | 142.75 | 95.38 | 64.00 | 35.50 | | |
| 6 | B | 155.00 | 112.25 | 81.13 | 56.88 | 30.88 | |
| 7 | D | 172.75 | 130.00 | 97.00 | 74.25 | 52.50 | |

| | | | | | | |
|-------|---|---|---|---|---|---|
| TYPE: | C | A | E | E | E | B |
| SHOT: | 1 | 2 | 3 | 4 | 5 | 6 |

*

VIBRA-TECH ENGINEERS INC.

*

Figure 19

SPREAD1 shots: 2 1 3 4 5 6 7

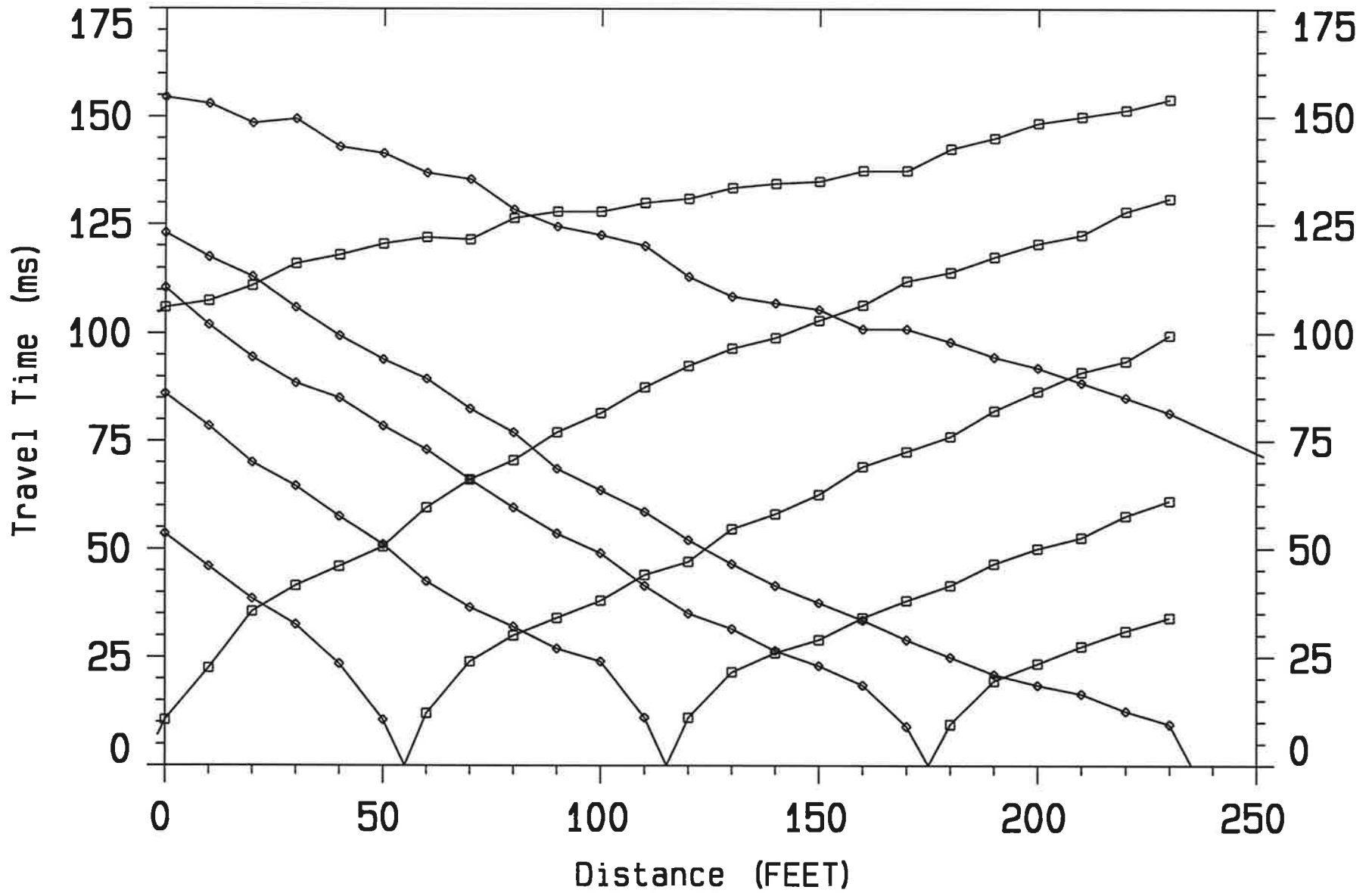
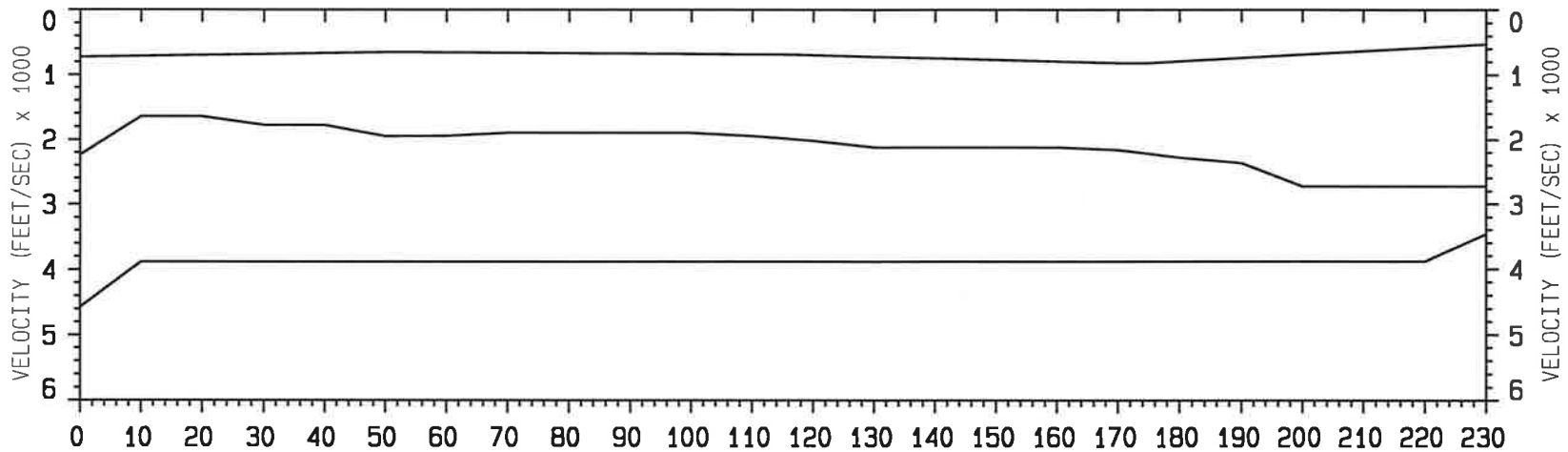
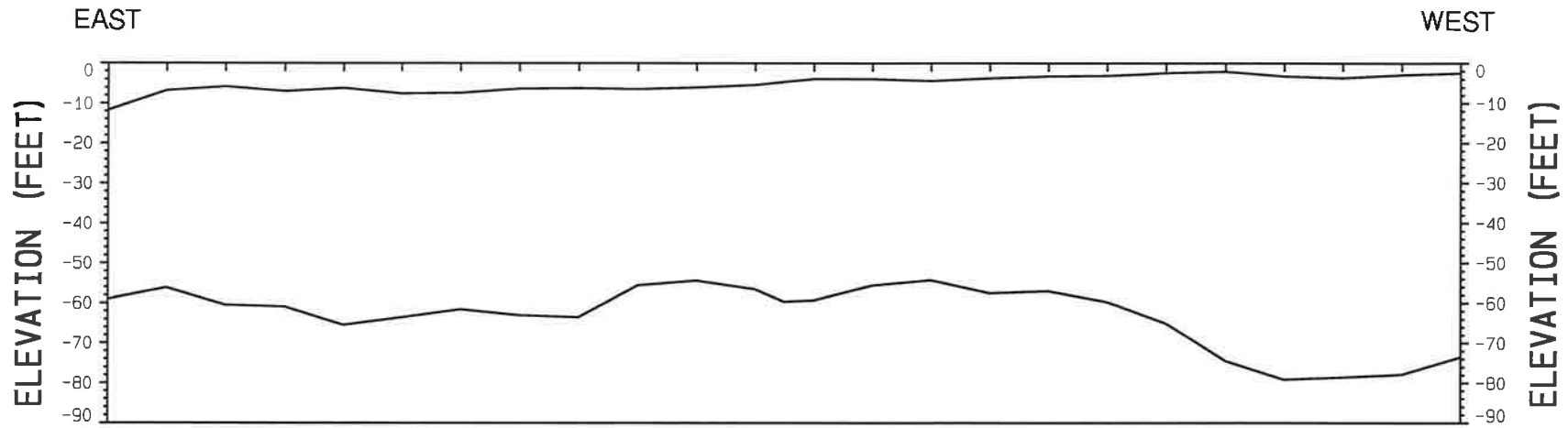


Figure 19a



DISTANCE (FEET)

Plate: 1

| | | | |
|-------------------------------|------------------|------------------------------|--|
| for: Penn State | | Penn State Research Project | |
| by: VIBRA-TECH ENGINEERS INC. | | Jeddo 14 SOUTH END | |
| Data Set: SPREAD1 | Date: 07/31/2017 | | |
| Equipment: GEOMETRICS DTR | Spread: 00001 | Azimuth: | |

SUMMARY OF GRM CURVE ANALYSIS:

| SEGMENT | SHOT1 | SHOT2 | R1 | R2 | RA | X-Y | No. Pts |
|---------|-------|-------|----|----|----|-------|---------|
| 1 | 4 | 1 | 1 | 1 | 1 | 10.00 | 10 |
| 2 | 5 | 1 | 1 | 1 | 1 | 60.00 | 16 |
| 3 | 5 | 3 | 1 | 1 | 1 | 30.00 | 13 |
| 4 | 6 | 1 | 2 | 2 | 1 | 60.00 | 14 |
| 5 | 6 | 3 | 1 | 1 | 1 | 60.00 | 16 |
| 6 | 6 | 4 | 1 | 1 | 1 | 0.00 | 11 |
| 7 | 7 | 2 | 2 | 2 | 2 | 20.00 | 22 |

Reciprocal time estimates from refractors R1 and R2
 Refractor RA is refractor analyzed

Optimum X-Y value estimates:

| LAYER | MINIMUM X-Y | AVERAGE X-Y | MAXIMUM X-Y |
|-------|-------------|-------------|-------------|
| 1 | 0.96 | 3.50 | 7.62 |
| 2 | 43.48 | 65.96 | 127.90 |

GRM DEPTH SECTION RESULTS:

S-N: STATION NUMBER, V: VELOCITY (FEET/sec), Z: DEPTH (FEET)

| S-N | V1 | V2 | V3 | V4 | Z1 | Z2 | Z3 |
|-------|--------|---------|---------|----|--------|--------|----|
| | 727.50 | 2235.48 | 5258.34 | | 11.712 | 59.033 | |
| 1.00 | 712.23 | 1646.28 | 3885.44 | | 6.784 | 56.197 | |
| 2.00 | 696.97 | 1646.28 | 3885.44 | | 5.837 | 60.474 | |
| 3.00 | 681.70 | 1777.64 | 3885.44 | | 6.959 | 60.937 | |
| 4.00 | 666.44 | 1777.64 | 3885.44 | | 6.179 | 65.488 | |
| 5.00 | 651.18 | 1949.17 | 3885.44 | | 7.564 | 63.555 | |
| 5.50 | 651.18 | 1946.03 | 3885.44 | | 7.460 | 62.559 | |
| 6.00 | 654.14 | 1942.89 | 3885.44 | | 7.395 | 61.594 | |
| 7.00 | 660.07 | 1896.93 | 3885.44 | | 6.335 | 63.049 | |
| 8.00 | 666.00 | 1896.93 | 3885.44 | | 6.197 | 63.544 | |
| 9.00 | 671.93 | 1896.93 | 3885.44 | | 6.414 | 55.644 | |
| 10.00 | 677.86 | 1896.93 | 3885.44 | | 6.038 | 54.465 | |
| 11.00 | 683.80 | 1942.89 | 3885.44 | | 5.365 | 56.579 | |
| 11.50 | 683.80 | 1979.97 | 3885.44 | | 4.601 | 59.663 | |
| 12.00 | 695.89 | 2017.04 | 3885.44 | | 3.917 | 59.334 | |
| 13.00 | 720.09 | 2118.40 | 3885.44 | | 3.916 | 55.611 | |
| 14.00 | 744.29 | 2118.40 | 3885.44 | | 4.397 | 54.313 | |
| 15.00 | 768.49 | 2118.40 | 3885.44 | | 3.737 | 57.524 | |
| 16.00 | 792.69 | 2118.40 | 3885.44 | | 3.268 | 57.006 | |
| 17.00 | 816.89 | 2158.52 | 3885.44 | | 3.135 | 59.726 | |
| 17.50 | 816.89 | 2218.34 | 3885.44 | | 2.837 | 62.363 | |

GRM DEPTH SECTION RESULTS:

S-N: STATION NUMBER, V: VELOCITY (FEET/sec), Z: DEPTH (FEET)

| S-N | V1 | V2 | V3 | V4 | Z1 | Z2 | Z3 |
|-------|--------|---------|---------|----|-------|--------|----|
| 18.00 | 790.47 | 2278.16 | 3885.44 | | 2.450 | 65.069 | |
| 19.00 | 737.64 | 2363.40 | 3885.44 | | 2.069 | 74.415 | |
| 20.00 | 684.81 | 2724.45 | 3885.44 | | 3.272 | 79.115 | |
| 21.00 | 631.98 | 2724.45 | 3885.44 | | 3.655 | 78.534 | |
| 22.00 | 579.15 | 2724.45 | 3885.44 | | 2.889 | 77.854 | |
| 23.00 | 526.32 | 2724.45 | 3046.76 | | 2.481 | 73.504 | |

*

VIBRA-TECH ENGINEERS INC.

*

DATA SET: SPREAD1

| | |
|--------------------------------------|---------------------------|
| CLIENT: Penn State | DATE: 07/31/2017 |
| LOCATION: Jeddo 14 | LINE NO.: 00001 |
| COUNTY: | AZIMUTH: |
| PROJECT: Penn State Research Project | G-SPACING: 10.00 FEET |
| SOURCE: Kinepak | EQUIPMENT: GEOMETRICS Str |

-----RECIPROCAL TIME ESTIMATES-----

| SHOT | SHOT | RT1 (msec) | RT2 (msec) | DIFF | LAYERS |
|------|------|------------|------------|-------|--------|
| 3 | 1 | 55.00 | 53.50 | 1.50 | 2 2 |
| 3 | 2 | 121.25 | N/A | N/A | 3 ? |
| 4 | 1 | 91.00 | 90.50 | 0.50 | 2 2 |
| 4 | 2 | 130.50 | N/A | N/A | 3 ? |
| 4 | 3 | 45.50 | 46.00 | -0.50 | 2 2 |
| 5 | 1 | 112.25 | 111.50 | 0.75 | 2 2 |
| 5 | 2 | 140.00 | N/A | N/A | 3 ? |
| 5 | 3 | 74.25 | 75.75 | -1.50 | 2 2 |
| 5 | 4 | 35.75 | 37.00 | -1.25 | 2 2 |
| 6 | 1 | 122.00 | 120.50 | 1.50 | 3 3 |
| 6 | 2 | 154.00 | N/A | N/A | 3 ? |
| 6 | 3 | 89.50 | 91.75 | -2.25 | 2 2 |
| 6 | 4 | 55.50 | 56.00 | -0.50 | 2 2 |
| 6 | 5 | 27.50 | 27.00 | 0.50 | 2 2 |
| 7 | 1 | N/A | 154.50 | N/A | ? 3 |
| 7 | 3 | N/A | 139.25 | N/A | ? 3 |
| 7 | 4 | N/A | 116.50 | N/A | ? 3 |
| 7 | 5 | N/A | 99.50 | N/A | ? 3 |

-----ESTIMATES BETWEEN FAR SHOTS-----

| SHOT | SHOT | RT (ms) | RT (I-A) | RT (J-B) | RTAB | LAYERS |
|------|------|---------|----------|----------|--------|--------|
| 7 | 2 | 187.25 | 154.50 | 154.00 | 121.25 | 3 3 |

RECIPROCAL TIME INFORMATION:

SHOT TYPE ----- RECIPROCAL TIMES (msec) -----

| | | | | | | | |
|---|---|--------|--------|--------|--------|-------|--|
| 2 | C | | | | | | |
| 3 | E | 54.25 | 121.25 | | | | |
| 4 | E | 90.75 | 130.50 | 45.75 | | | |
| 5 | E | 111.88 | 140.00 | 75.00 | 36.38 | | |
| 6 | B | 121.25 | 154.00 | 90.63 | 55.75 | 27.25 | |
| 7 | D | 154.50 | 187.25 | 139.25 | 116.50 | 99.50 | |

| | | | | | | |
|-------|---|---|---|---|---|---|
| TYPE: | A | C | E | E | E | B |
| SHOT: | 1 | 2 | 3 | 4 | 5 | 6 |

Appendix D

Concepts of Seismic Refraction Prospecting

The purpose of this discussion and the attached figure is to describe the basic principles of the seismic refraction technique. This discussion is intended primarily for those who have heard of the seismic refraction technique but do not know how it works. We will examine the simplest case for a seismic refraction model - the single, horizontal layer.

Seismic refraction surveying is one of the most powerful tools an architect, engineer, or construction contractor can employ for detecting subsurface structure. The seismic refraction method had its beginnings in 1910, when the German geophysicist L. Mintrop pointed out the practical use of the transmission of seismic waves through the earth. By 1925 the refraction method was a well-established tool for detecting hidden salt domes in oil exploration. In 1941 the first seismic depth-to-bedrock investigation was carried out in Sweden for a planned hydroelectric power plant, initiating the use of the method on civil and geotechnical engineering projects. During the past ten years, the revolution in computers and electronics has enabled the development of new seismographs for data acquisition and processing, permitting cost savings in field and office time.

The seismic method utilizes the propagation of elastic waves (sound waves) in the subsurface in order to model structure. The elastic wave can be generated by means of a weight drop, hammer, explosives, or projectile impact. Once generated, the elastic wave moves away from the source in an ever-expanding circle. The circle at the outer edge of an advancing wave marks the wave front. A pebble tossed into a quiet pond is an example of this process at work.

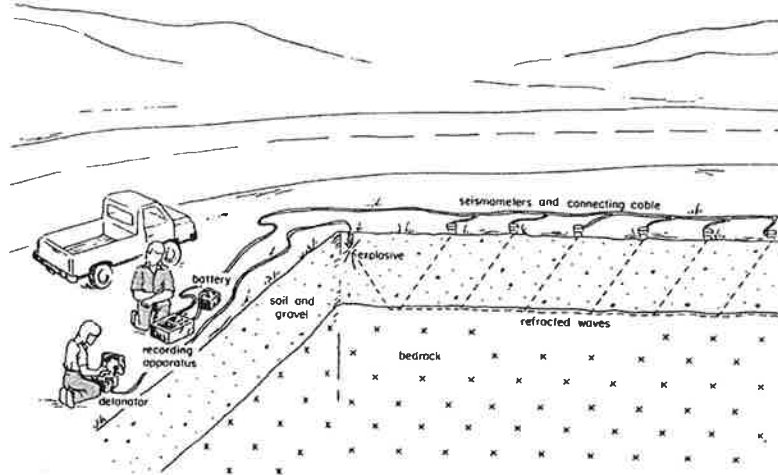


Figure 1

Graphic representation of a standard field setup for a seismic refraction survey. The geophones spaced at varying distances are used to measure the arrival time of the refracted wave. The arrival times are analyzed to find the compressional wave velocity of the material and the depth to the refractor.

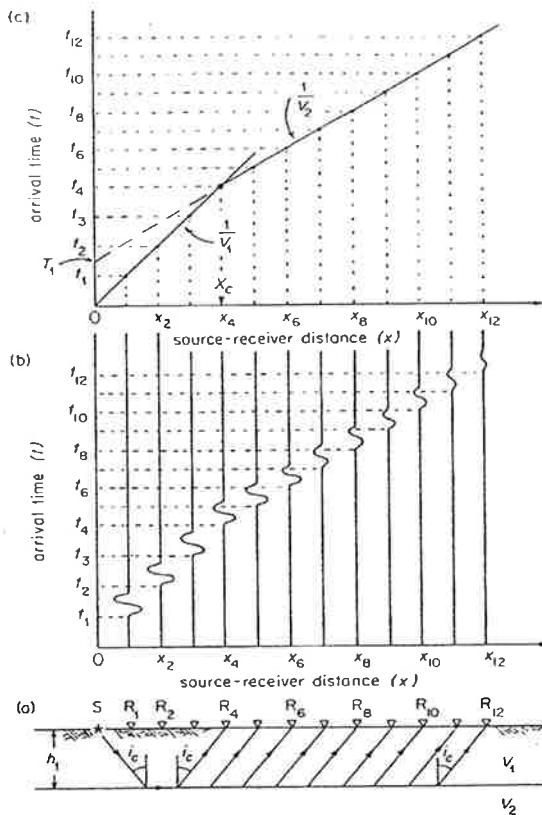


Figure 2
Simple analysis for standard seismic refraction survey.

direct wave is the wave that travels directly from the source to the receiver without being refracted. For the remaining geophones the fastest wave will be the refracted wave. The refracted wave is the wave that travels through the first layer to the boundary of the second layer, is refracted, and travels at the speed of the second layer to the receiver. You may ask, how does the wave make its way to the surface? The complete answer would be very complicated, but in short, this process can be explained from *Huygen's principle*, which states every point on a wave front is a source of new waves that travel away from it in all directions. Figure 1 on the previous page shows a graphic representation of a typical setup for a seismic refraction survey.

Figure 2 above shows a recording of direct and refracted waves for this typical setup. Figure (a) shows our single, horizontal layer model of thickness h . The critical ray from the source (S) is refracted along the interface and back to the surface from geophones G_3 to G_{12} . Geophones G_1 to G_3 observe the arrival of the direct wave. Figure (b) shows the resultant seismogram. The seismogram consists of twelve traces observed at each geophone position. Each trace represents ground vibration as a function of time. The onset of the first arriving waves is marked on the vertical time axis, and the distance from the source to the geophones is marked on the horizontal axis. Figure (c) is a travel - time curve constructed from the information provided in Figure (b). The slopes of the best-fit lines through the points indicate the seismic velocity of the layer. By

As the wave front travels through the subsurface, it will encounter boundaries between two substances in which the wave speeds are different. At this boundary it divides into waves that bounce (reflect) from the boundary and other waves that pass (refract) across the boundary. An example of the refraction process at work, occurs ever time you poke a stick into a pond. Recall how the stick appears to bend (refract) at the water surface. This also happens to seismic waves in the subsurface. Because of this process we are able to map structure in the subsurface by the seismic method.

Suppose we now lay down a line of geophones along the surface and place an explosive charge at the end of the line. We detonate the explosive charge in order to create our wave front. Imagine these geophones as stopwatches that start at the time of detonation and stop when the wave

front reaches each one. The recorded time is the arrival time of the fastest wave. For some geophones close to the source the fastest wave will be the direct wave. The

knowing the velocities V_1 and V_2 , and the intercept time T_i , we can calculate the depth to V_2 below the shotpoint by the simple formula given below.

$$h_1 = \frac{T_i V_1 V_2}{2\sqrt{(V_2^2 - V_1^2)}}$$

There are many more complex routines for analyzing seismic refraction than the simple example given above. Many of the more advanced procedures calculate depths beneath every geophone as opposed to the depth below the shotpoint as given in the above equation. One method which is particularly useful is the Generalized Reciprocal Method (GRM) developed by Derricke Palmer in the late 1970's. This method has the advantage of estimating both the refractor depth and seismic velocity for up to 4 different layers of materials having a different seismic velocity under each geophone, and also allows the delineation of dipping refractor surfaces at depth. Figure 3 below shows the source-receiver configuration used in this method.

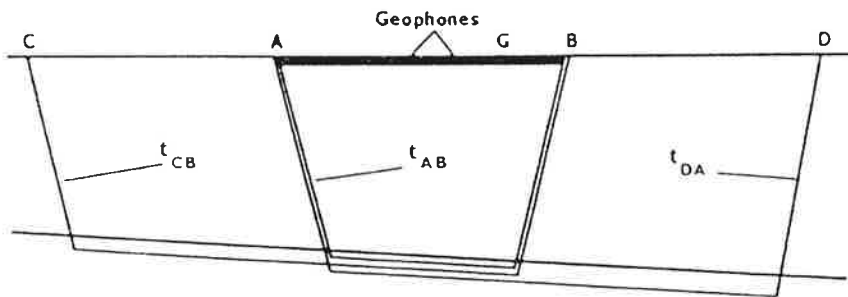


Figure 3 Raypaths used in calculation of a reciprocal time from an intermediate value.

Suppose we fire and record shots at locations A, B, C, and D. By the physical laws of seismic refraction, the time it takes a seismic wave to travel from location A to location D (forward) is the same as the (reciprocal) time it takes to travel from location D to location A (reverse). By averaging the recorded times, we can then obtain a very accurate estimate of this travel time. Suppose we record forward and reverse shots at locations B and D from points A and C. If we then add the averaged travel times from B to C to those from A to D and subtract the time from C to D, we obtain a function called the time-depth which depends **only** on the refractor depth and velocity under the receiver positions A and B. If we then subtract the time from C to B from the time from A to D and add it to the time from C to D, we then obtain a function called the

velocity analysis function whose slope is approximately the same (usually within 5%) as the inverse of the refractor velocity for different positions of the geophone position G, when G is located mid-way between A and B.

Suppose we wish to determine the depth to the refractor under the geophones at point G. We need to accurately determine which geophones detected the arrival of the refracted wave coming off of a point directly beneath point G. Consider the curves shown in Figure 4 below.

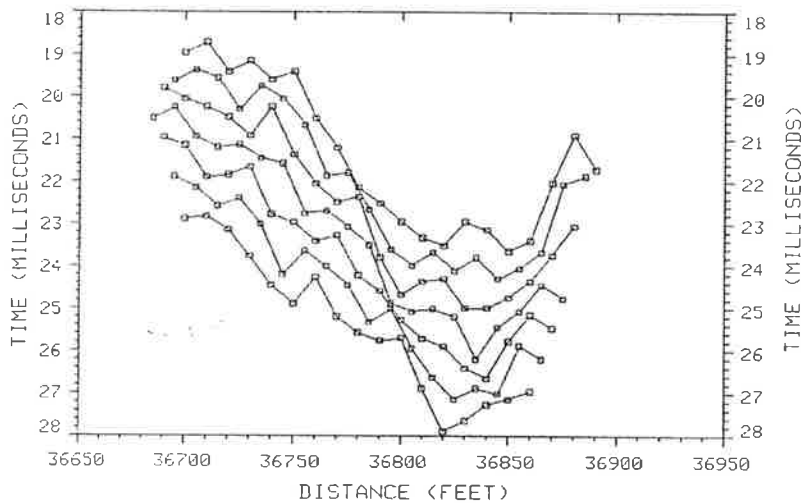


Figure 4 Plot of time-depth functions for A-B of 0 through 60 for a refractor.

Curves 1 through 7 are the time-depths, plotted for values of distance between A and B from 0 to 60 feet for refraction's off Layer 2 recorded from shots C and D at all geophone locations. We examine these curves and try to choose the one which best locates the refractor under G for all geophone locations. The best curve gives the sharpest definition of the refractor, in this case the fourth curve, corresponding to an A-B spacing of 30 feet. We then obtain an estimate of the refractor depth by computing the time to this point and dividing it by the distance through the known velocities and depths of the above refractors.

We then seek to determine the refractor velocity by examining the graph in Figure 5 on the next page. This graph is a plot of the velocity analysis functions for the corresponding time-depths functions shown in Figure C-4. We seek to determine the velocity of the refractor for the correct spacing of A and B. We choose the A-B value to be the one

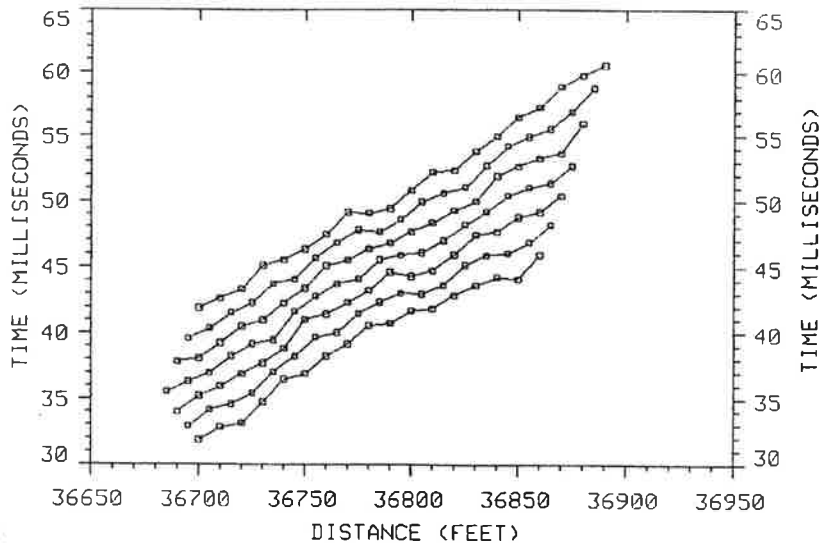


Figure 5 Plot of velocity analysis functions for A-B of 0 through 60 for a refractor.

which minimizes the error in this function, in this case 20 feet. Overall, however the 30-foot value gives the best resolution of both the refractor depth and velocity, so we choose an A-B spacing of 30 and compute the estimated depth to the refractor and its corresponding velocity.

In theory, the method could resolve any number of refractors from arrival times recorded at crossing geophones A and B, provided that the arrival times can be accurately be determined. In practice, the method is limited to usually no more than four layers. However, the accuracy with which this method delineates refractor depth and velocity even in irregular terrain with dipping refractors has brought it into widespread use in the analysis of engineering seismic refraction data, and is the method employed in the analysis of the data collected in this study.

In review, the seismic refraction method measures the speed or velocity at which the seismic wave is traveling in the subsurface. This velocity is directly related to the material properties of the medium the wave is traveling through.

The seismic refraction method relies on the propagation of elastic waves (sound waves) in the subsurface and is based on three fundamental principles:

- The seismic velocity changes as the seismic wave moves from one type of geologic material into another, depending on the physical properties of these materials.
- The contrast between the velocities desired to be mapped must be large.
- The layer velocities **must** increase with depth.

If these fundamental principles do not exist, it will make it difficult, if not impossible to map the subsurface structure. It is fortunate that these velocity conditions are the norm rather than the exception.

APPENDIX II

Blast Data for Site 1

12:08

N 40° 58.864 W 075° 56.831 - Hole Location

Jeddo 14 Impoundment Looking North 175' x 100'

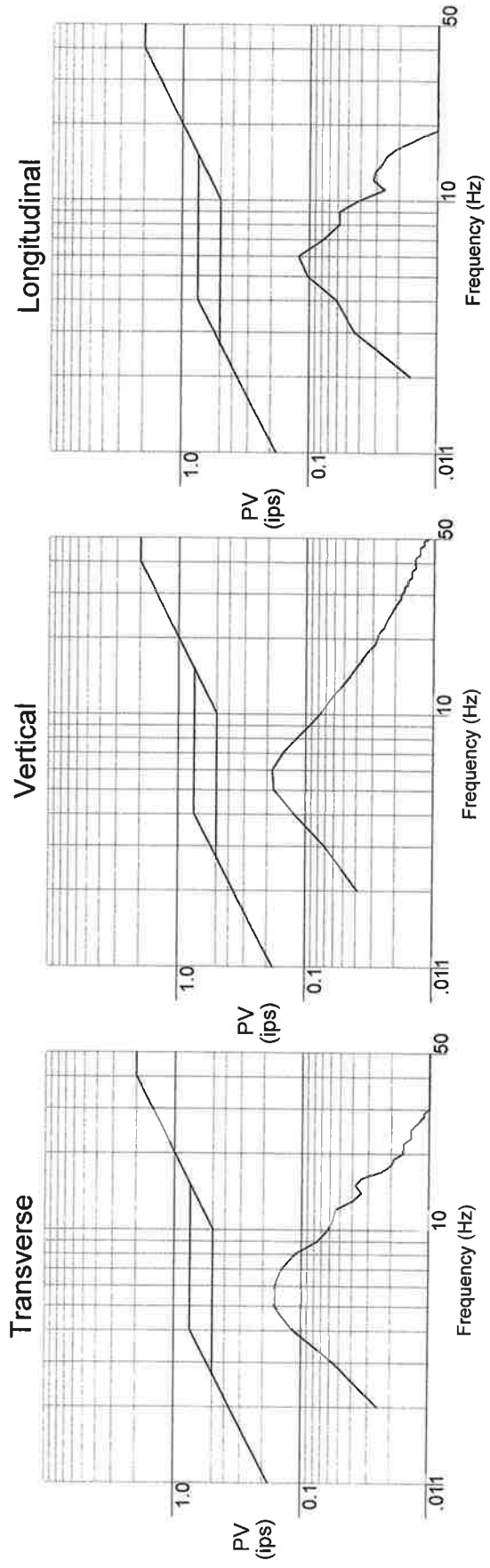
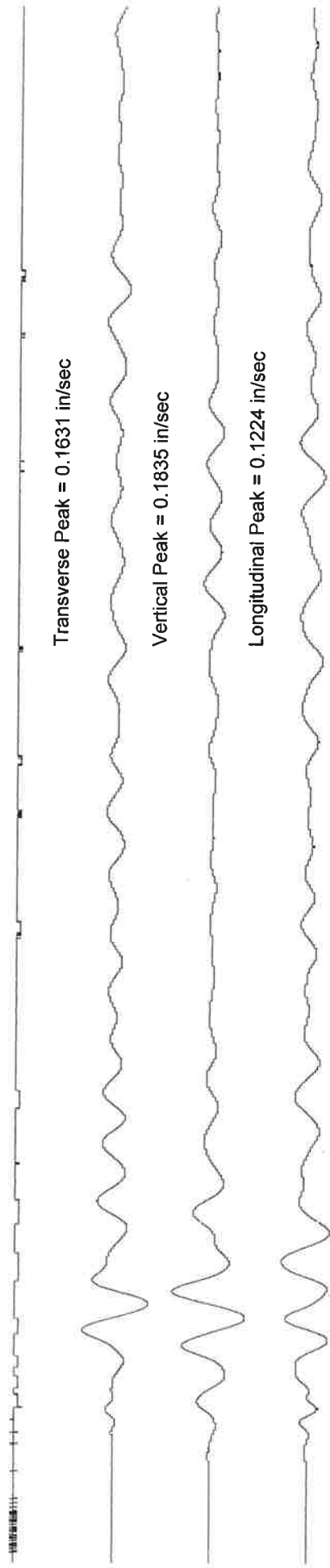
| | | | | |
|---|--|--|--|--|
| Serial # - SN: 4611 Location - N 40° 59.030 W 075° 56.805 PPV - 0.0918 Distance to blast - 1,015' | SN: 4644 N 40° 59.031 W 075° 56.784 0.1937 <u>1,037'</u> | SN: 4325 N 40° 59.028 W 075° 56.763 0.1631 <u>1,044'</u> | SN: 4779 4779 N 40° 59.026 W 075° 56.740 0.1427 <u>1,069'</u> | SN: 4165 N 40° 59.026 W 075° 56.718 0.0816 <u>1,113'</u> |
| SN: 4493 N 40° 59.001 W 075° 56.808 0.2111 <u>839'</u> | SN: 4786 N 40° 59.000 W 075° 56.786 0.1427 <u>851'</u> | SN: 4785 N 40° 58.999 W 075° 56.765 0.1122 <u>874'</u> | SN: 4789 N 40° 58.999 W 075° 56.743 0.1733 <u>914'</u> | SN: 4674 N 40° 58.999 W 075° 56.723 0.1122 <u>959'</u> |
| SN: 4619 N 40° 58.972 W 075° 56.811 0.3263 <u>662'</u> | SN: 4085 N 40° 58.971 W 075° 56.790 0.1835 <u>677'</u> | SN: 4403 N 40° 58.970 W 075° 56.768 0.1835 <u>700'</u> | SN: 4673 N 40° 58.969 W 075° 56.746 0.1835 <u>748'</u> | SN: 4491 N 40° 58.968 W 075° 56.724 0.1427 <u>801'</u> |

PENN STATE UNIVERSITY - JEDDO COAL FIELD TESTING

Date and Time: 07/06/2017 12:08:28

Geosonics Instrument: 4403 Location: 0:stn04 : 700'

Peak Air Overpressure = 0.00056 psi = 105.7158 dB

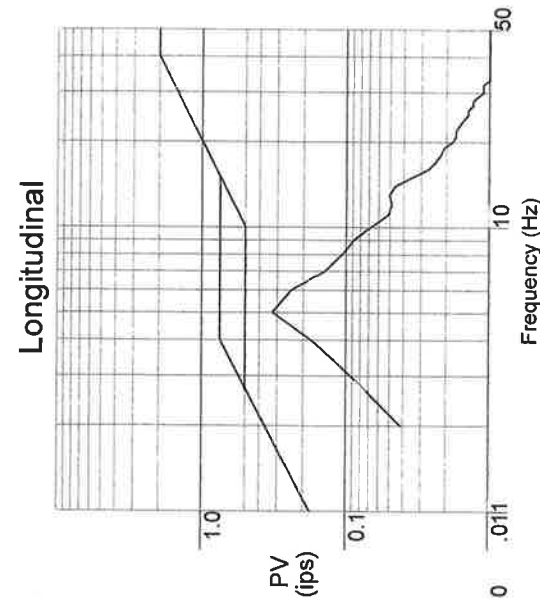
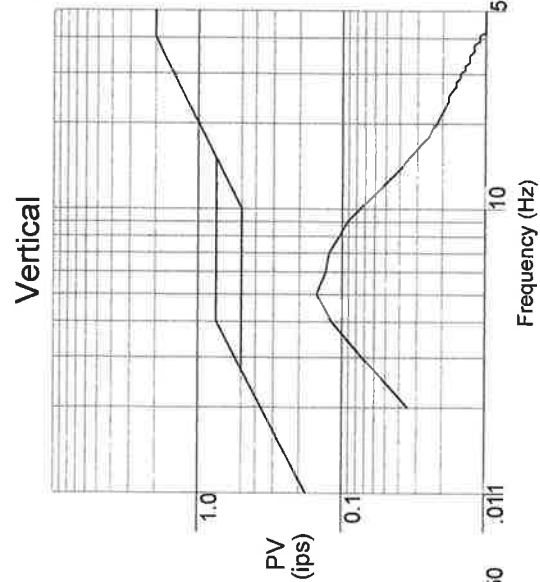
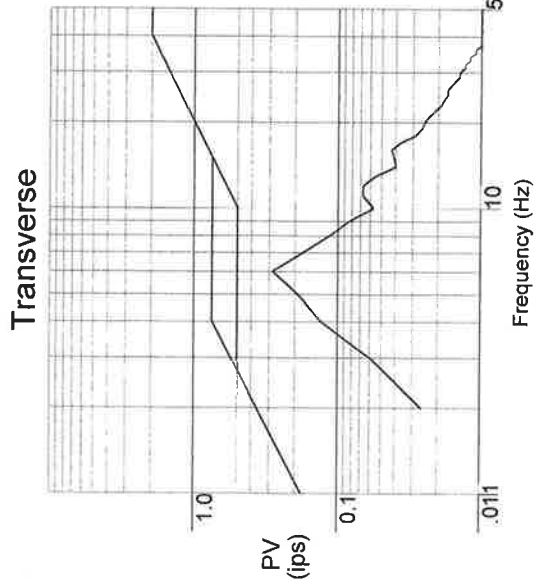
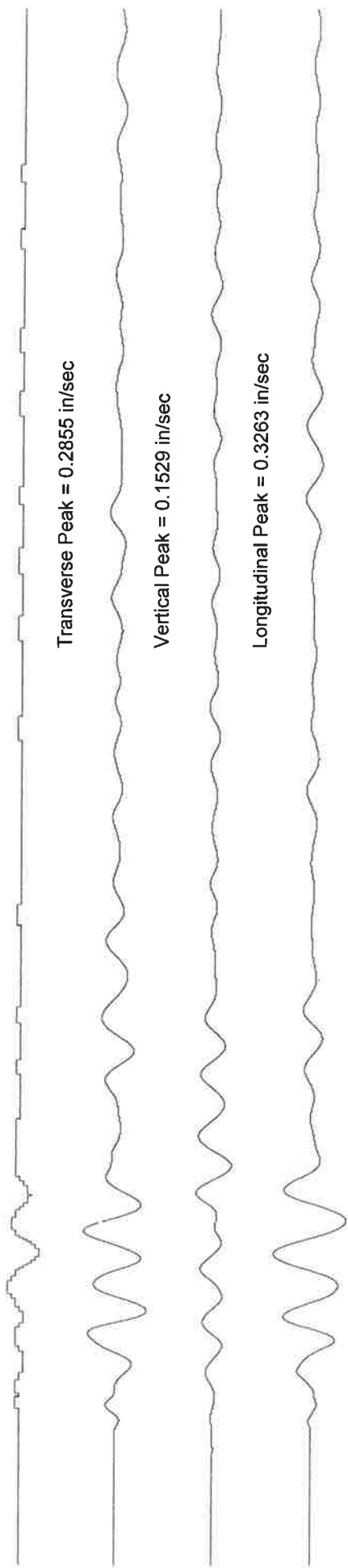


PENN STATE UNIVERSITY - JEDDO COAL FIELD TESTING

Date and Time: 07/06/2017 12:08:26

Geonics Instrument: 4619 Distance = 662 ft Location:

Peak Air Overpressure = 0.00141 psi = 113.7086 dB

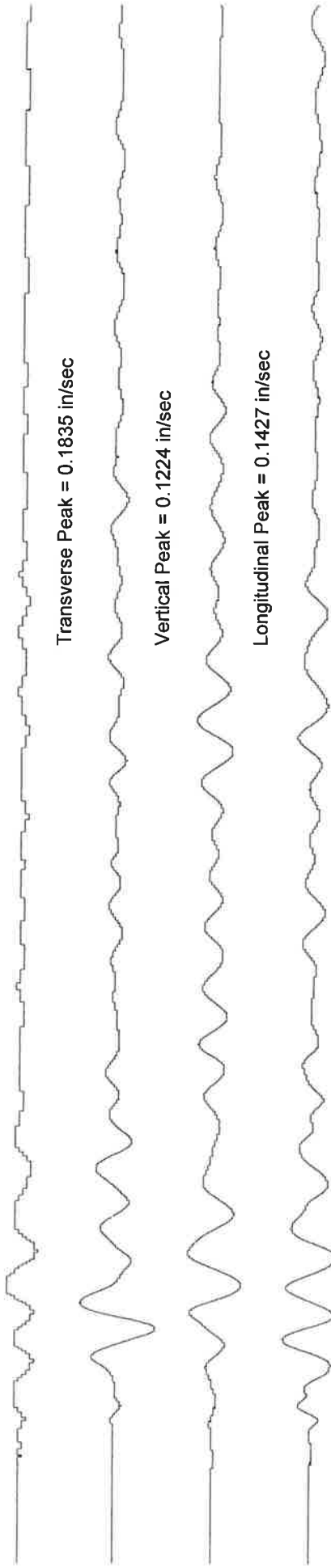


PENN STATE UNIVERSITY - JEDDO COAL FIELD TESTING

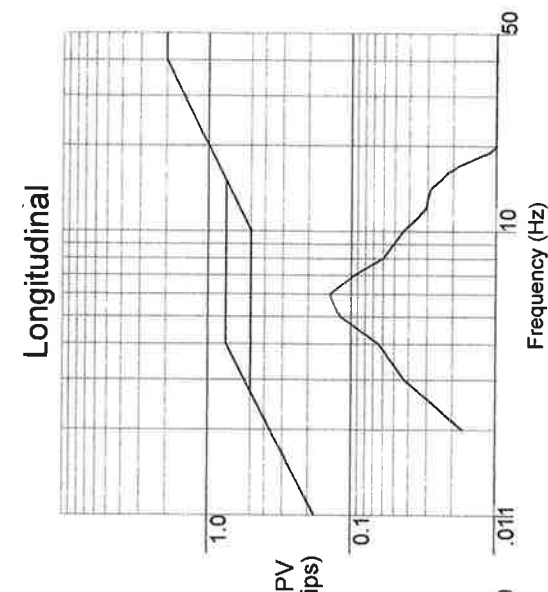
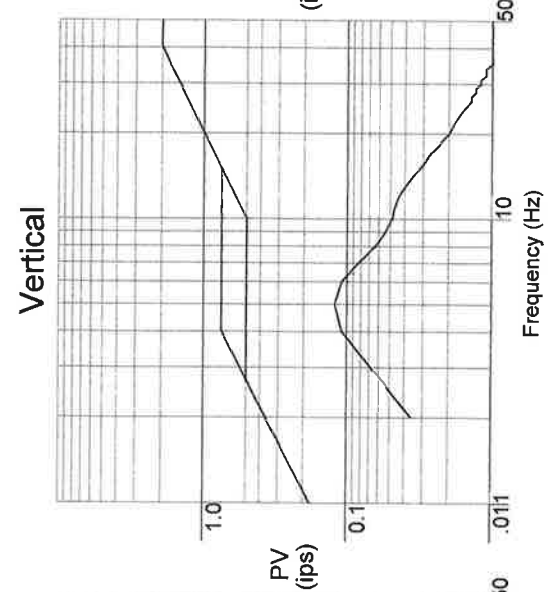
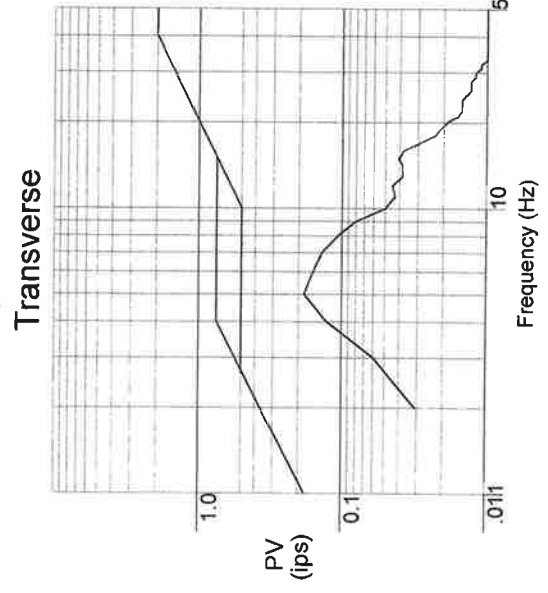
Date and Time: 07/06/2017 12:08:26

Geosonics Instrument: 4085 Distance = 677 ft Location:

Peak Air Overpressure = 0.00141 psi = 113.7086 dB



Ground Scale 1" = 0.73 IPS Air Scale 1" = 0.14336 PSI

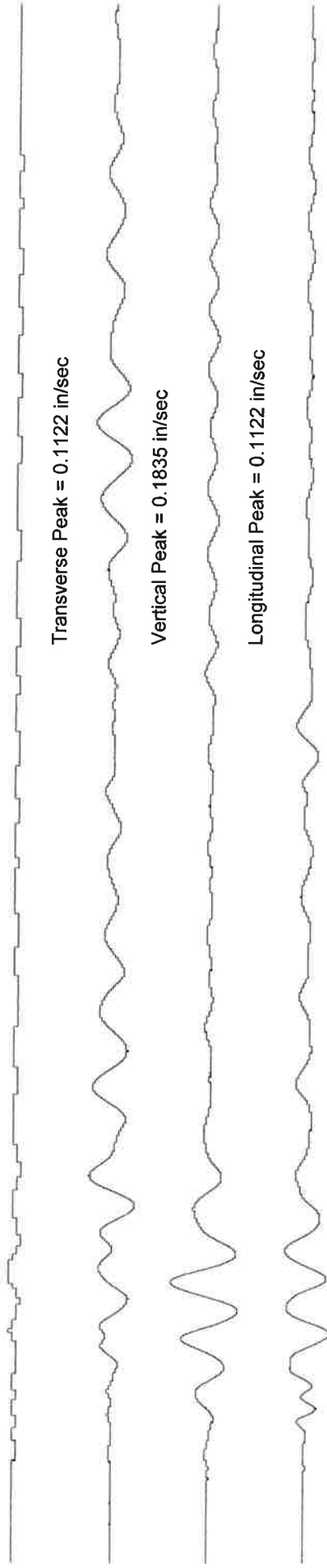


PENN STATE UNIVERSITY - JEDDO COAL FIELD TESTING

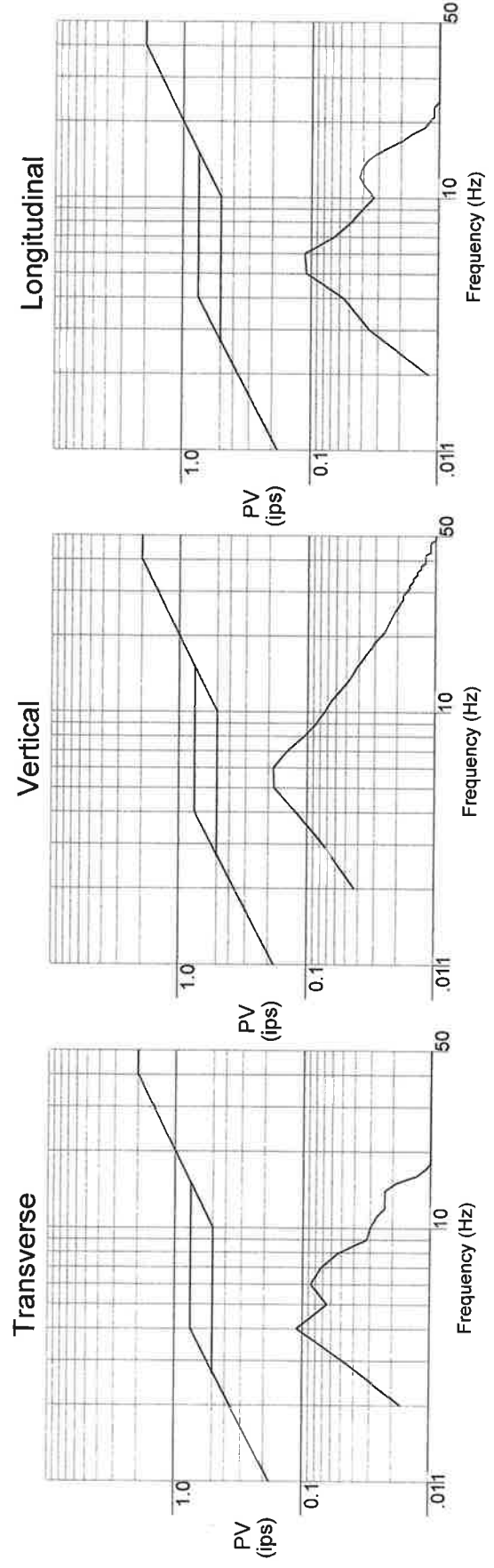
Date and Time: 07/06/2017 12:08:26

Geosonics Instrument: 4673 Distance = 748 ft Location:

Peak Air Overpressure = 0.00056 psi = 105.7158 dB



Ground Scale 1" = 0.73 IPS Air Scale 1" = 0.05712 PSI

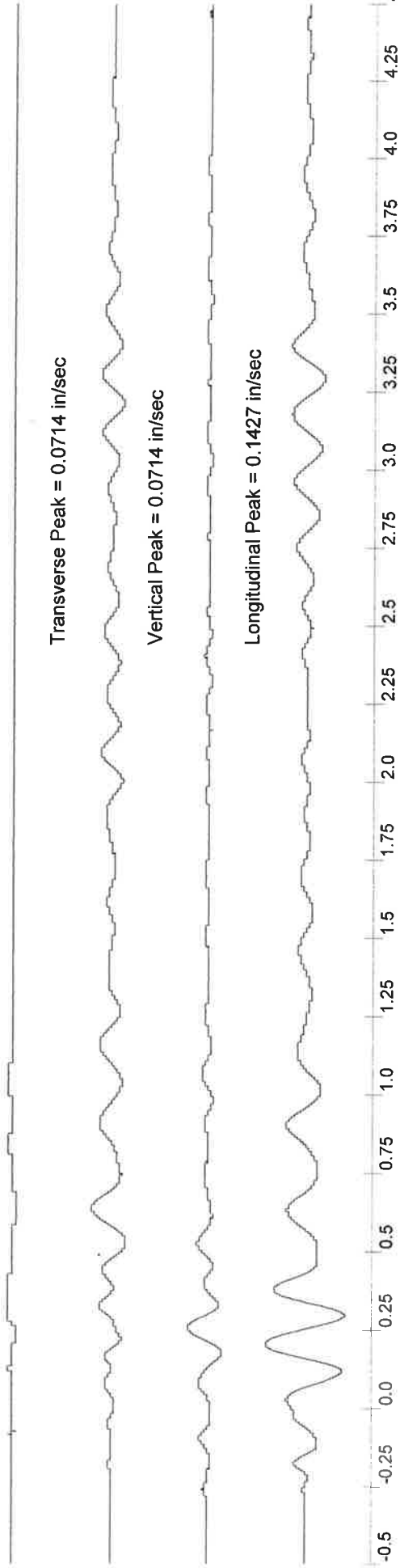


PENN STATE UNIVERSITY - JEDDO COAL FIELD TESTING

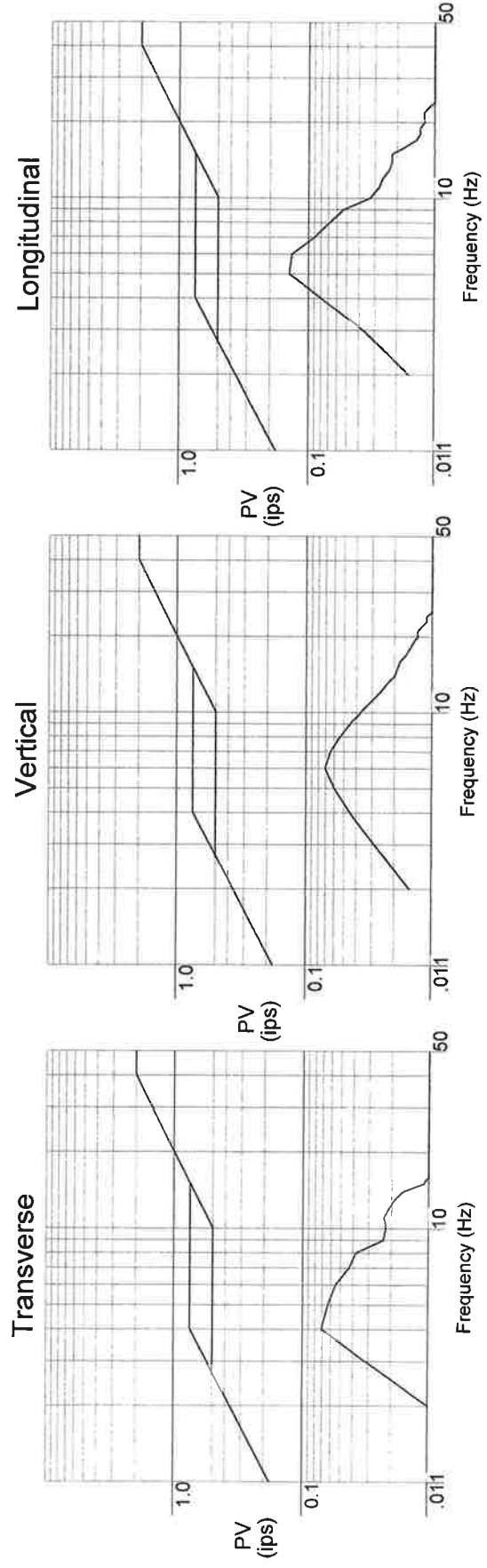
Date and Time: 07/06/2017 12:08:27

Geosonics Instrument: 4491 Distance = 801 ft Location:

Peak Air Overpressure = 0.00029 psi = 99.8639 dB



Ground Scale 1" = 0.57 IPS Air Scale 1" = 0.02912 PSI



0416000 00400400403.9303064761 00600400601.8102184977 00600400504.4302304960 069500.149 100100100

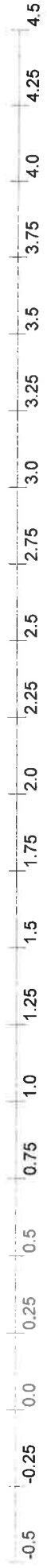
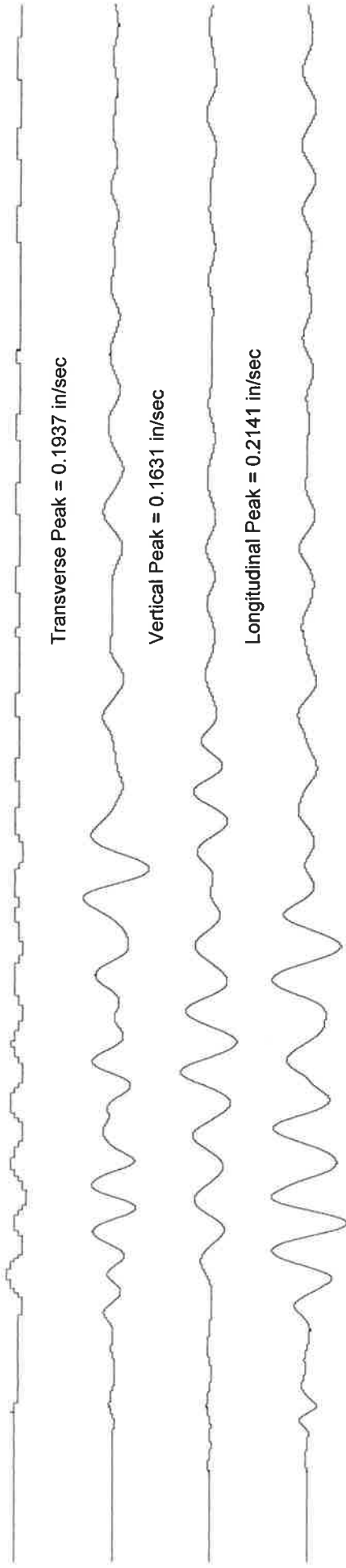
RSVP

PENN STATE UNIVERSITY - JEDDO COAL FIELD TESTING

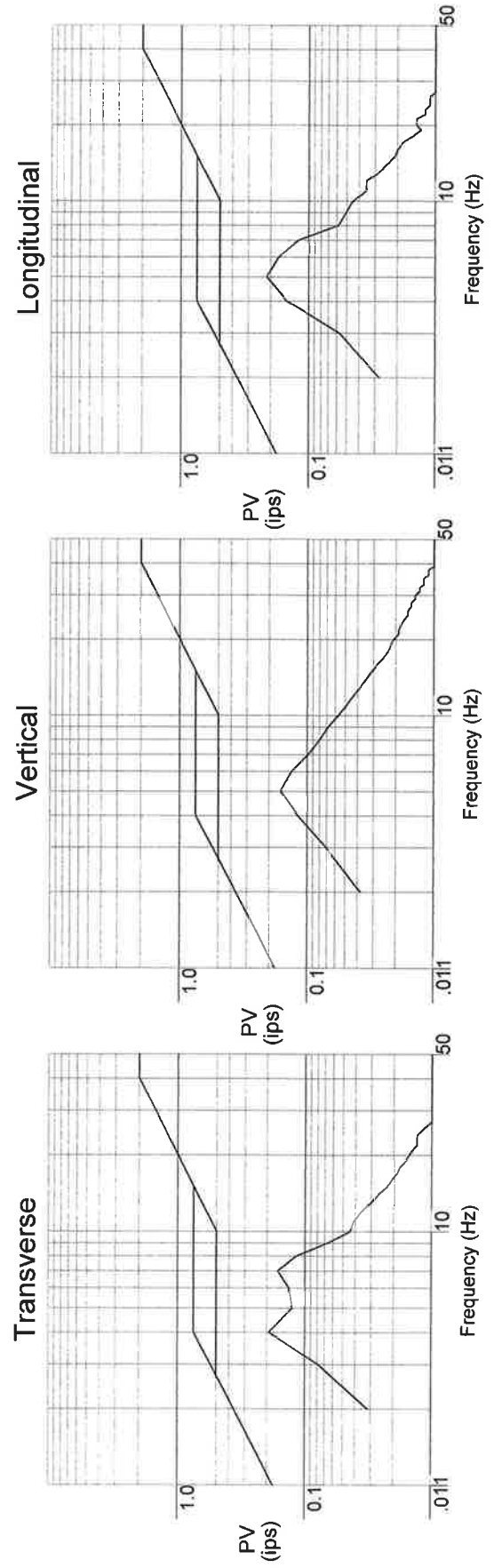
Date and Time: 07/06/2017 12:08:26

Geosonics Instrument: 4493 Distance = 839 ft Location:

Peak Air Overpressure = 0.00083 psi = 109.1807 dB



Ground Scale 1" = 0.86 IPS Air Scale 1" = 0.08512 PSI



1144000 00500500403.6804294999 00500500502.0802934989 00600500505.1202934999 108000.237 100100100

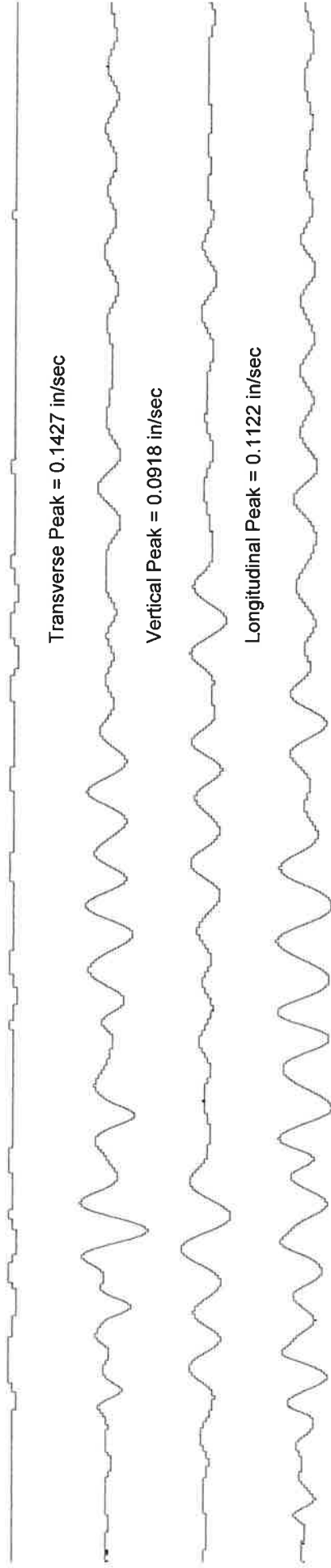
RSVP

PENN STATE UNIVERSITY - JEDDO COAL FIELD TESTING

Date and Time: 07/06/2017 12:08:28

Geosonics Instrument: 4786 Distance = 851 ft Location:

Peak Air Overpressure = 0.00029 psi = 99.8639 dB

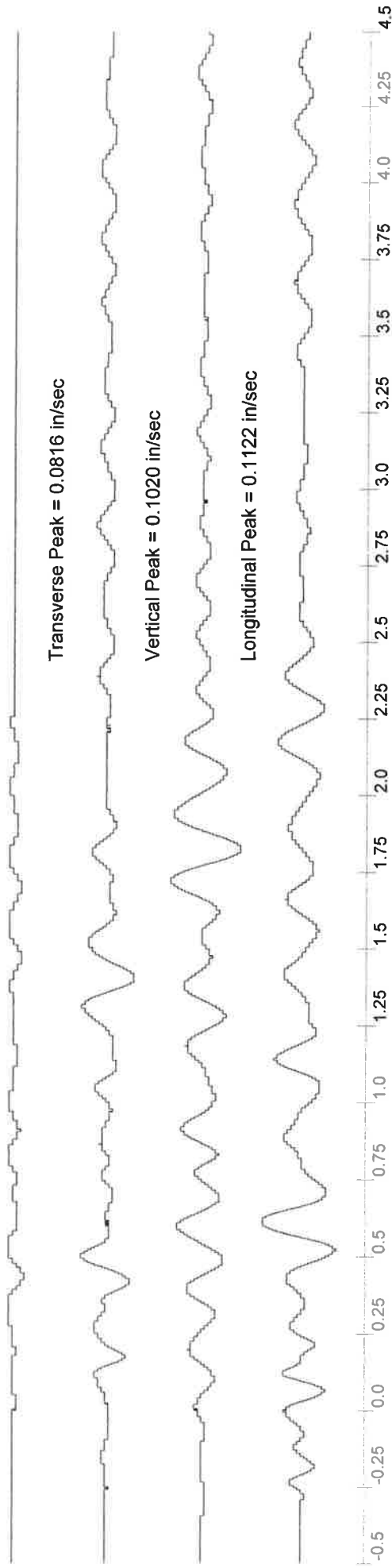


PENN STATE UNIVERSITY - JEDDO COAL FIELD TESTING

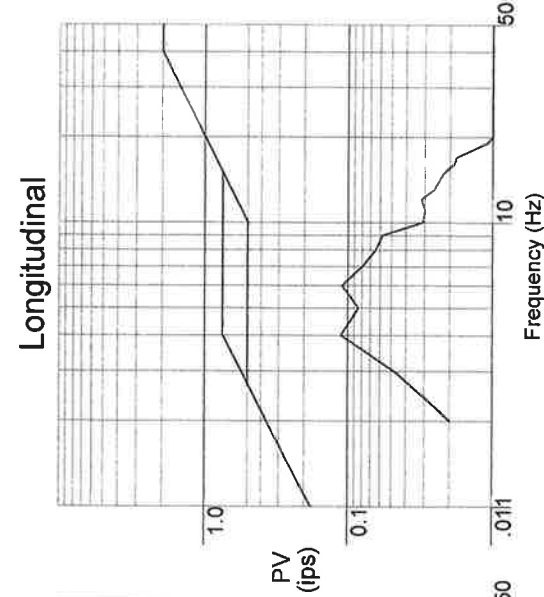
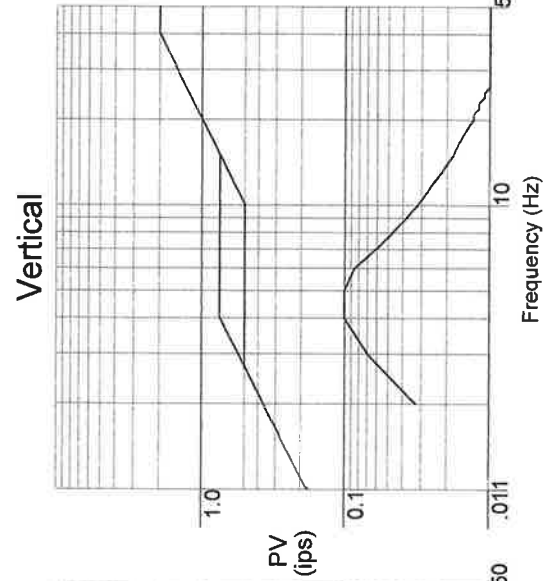
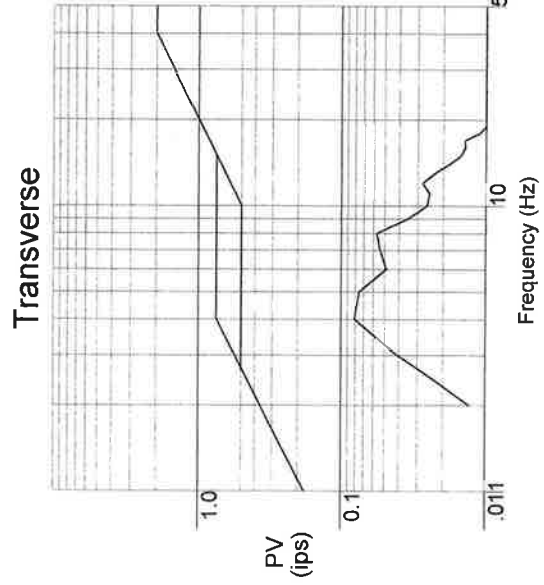
Date and Time: 07/06/2017 12:08:27

Geosonics Instrument: 4785 Distance = 874 ft Location:

Peak Air Overpressure = 0.00083 psi = 109.1807 dB



Ground Scale 1" = 0.45 IPS Air Scale 1" = 0.08512 PSI

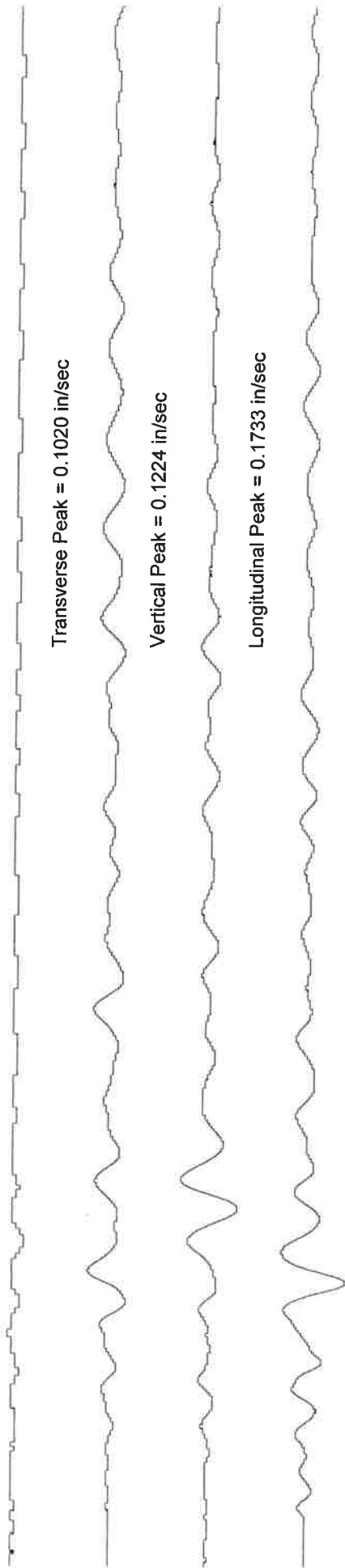


PENN STATE UNIVERSITY - JEDDO COAL FIELD TESTING

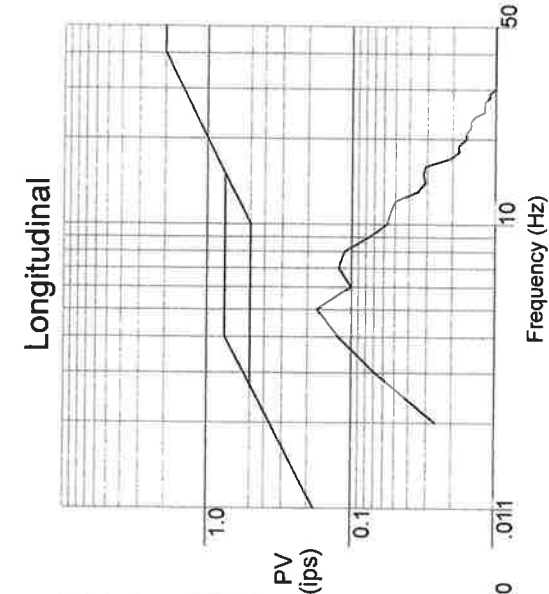
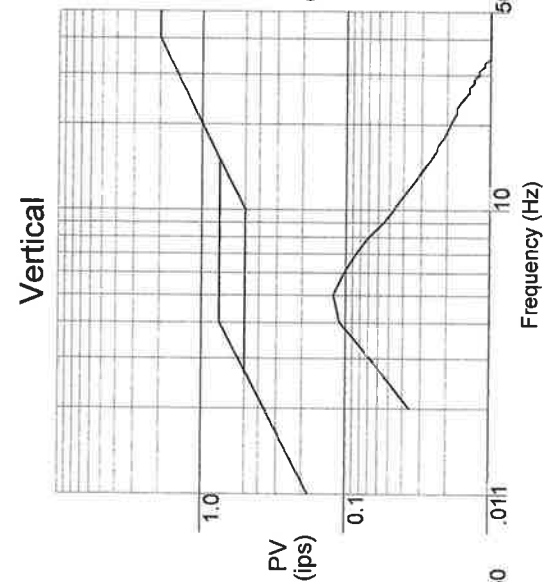
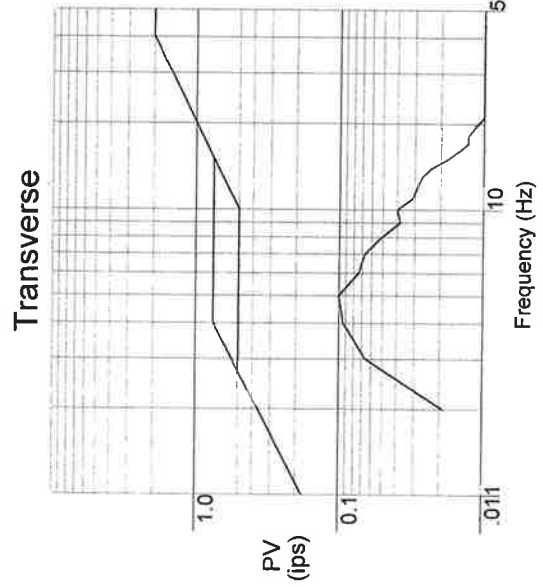
Date and Time: 07/06/2017 12:08:27

Geosonics Instrument: 4789 Distance = 914 ft Location:

Peak Air Overpressure = 0.00083 psi = 109.1807 dB



Ground Scale 1" = 0.69 IPS Air Scale 1" = 0.08512 PSI

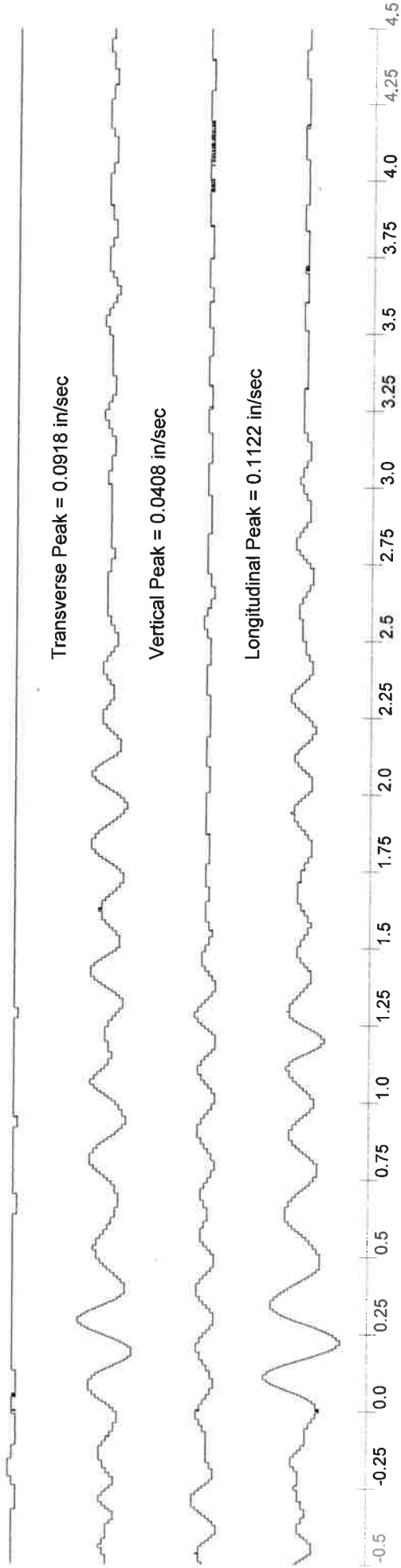


PENN STATE UNIVERSITY - JEDDO COAL FIELD TESTING

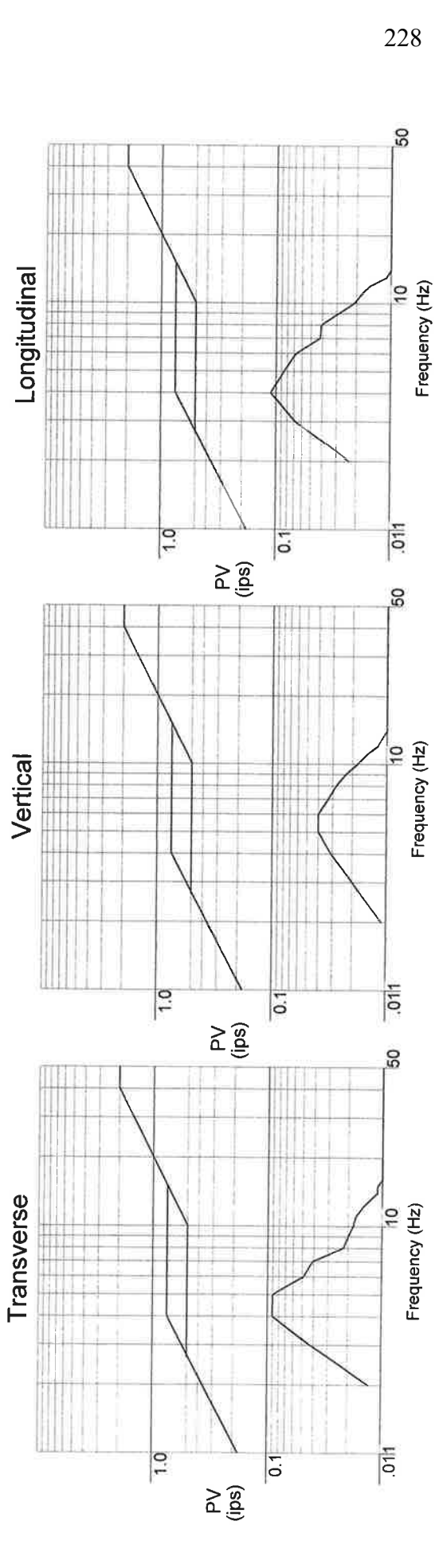
Date and Time: 07/06/2017 12:08:26

Geosonics Instrument: 4674 Distance = 959 ft Location:

Peak Air Overpressure = 0.00029 psi = 99.8639 dB



Ground Scale 1" = 0.45 IPS Air Scale 1" = 0.02912 PSI

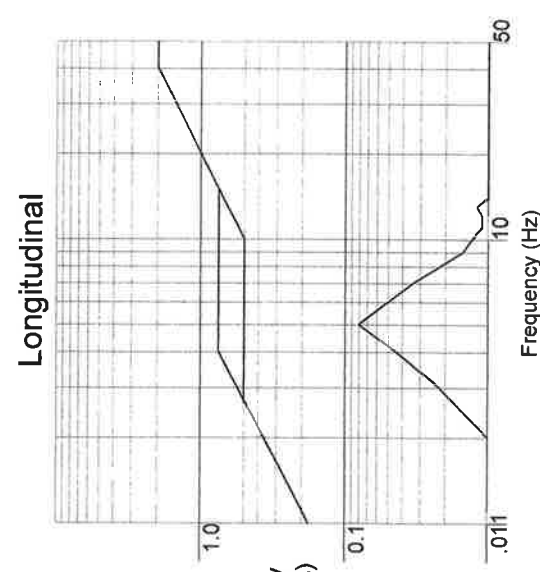
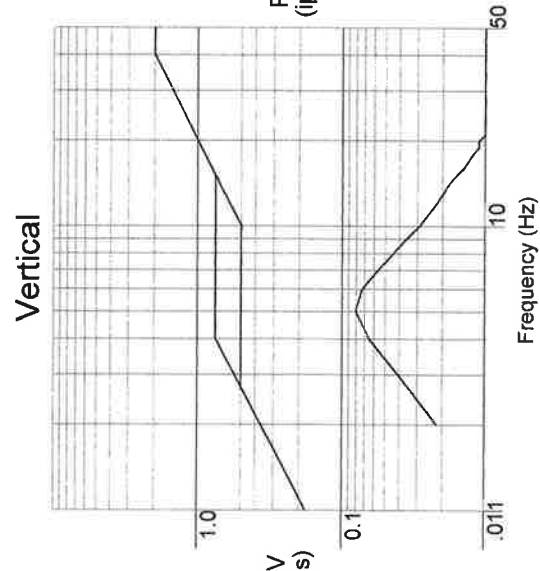
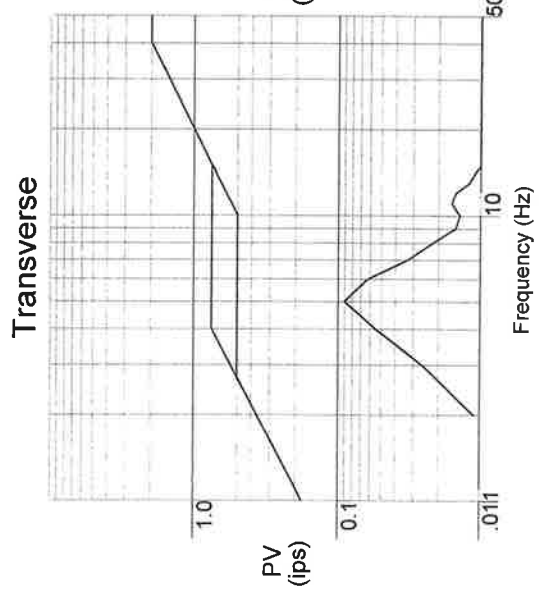
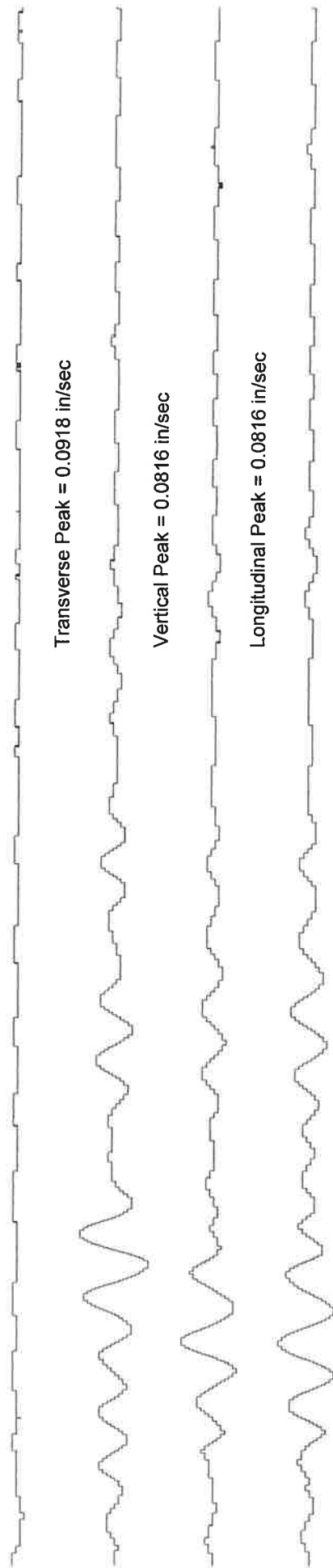


PENN STATE UNIVERSITY - JEDDO COAL FIELD TESTING

Date and Time: 07/06/2017 12:08:27

Geosonics Instrument: 4611 Distance = 1015 ft Location:

Peak Air Overpressure = 0.00056 psi = 105.7158 dB

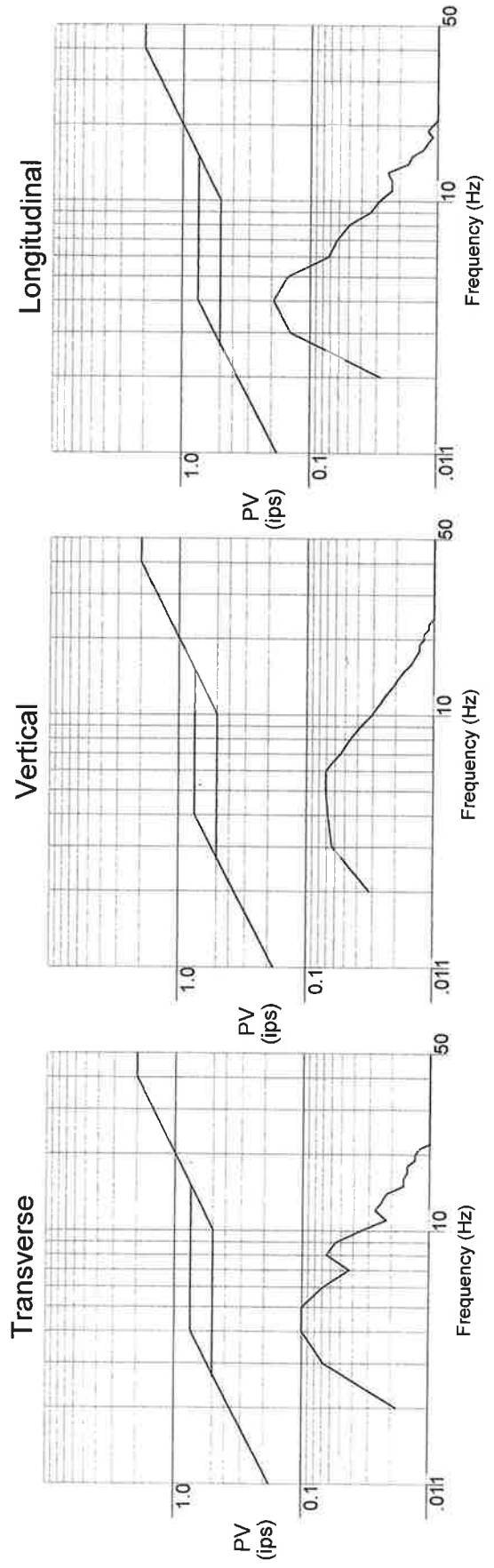
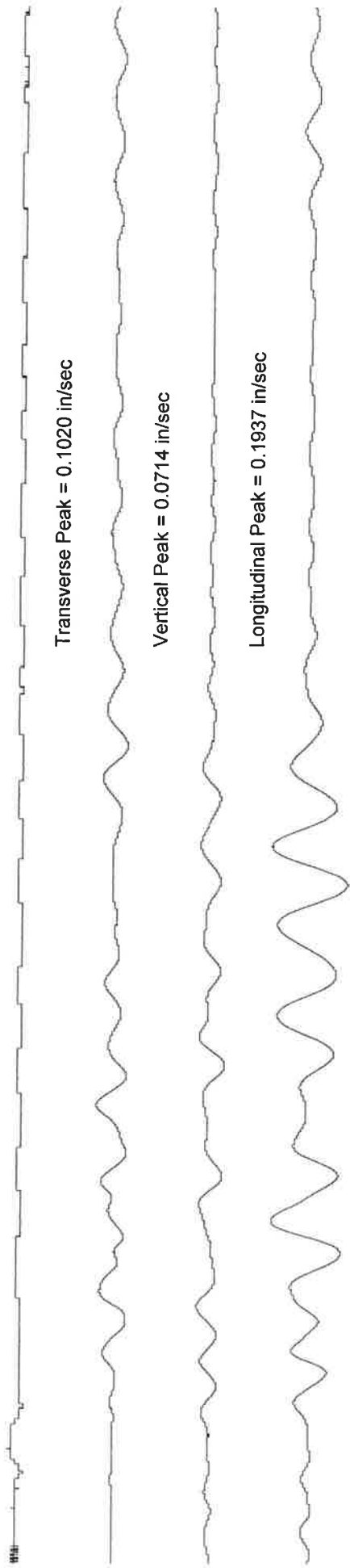


PENN STATE UNIVERSITY - JEDDO COAL FIELD TESTING

Date and Time: 07/06/2017 12:08:28

Geosonics Instrument: 4644 Distance = 1037 ft Location:

Peak Air Overpressure = 0.00056 psi = 105.7158 dB

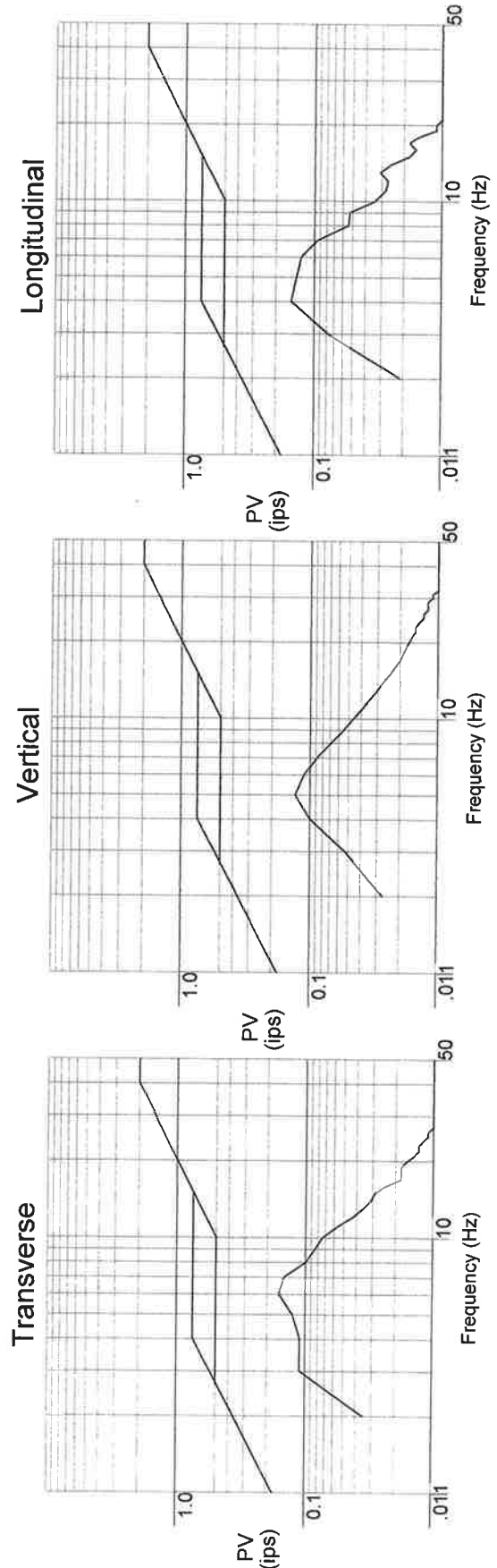
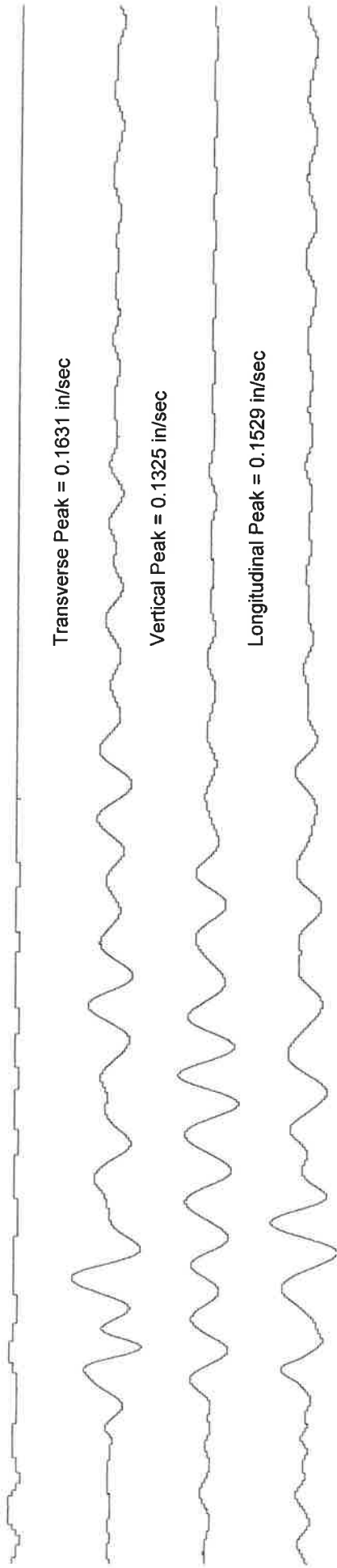


PENN STATE UNIVERSITY - JEDDO COAL FIELD TESTING

Date and Time: 07/06/2017 12:08:26

Geosonics Instrument: 4325 Distance = 1044 ft Location:

Peak Air Overpressure = 0.00056 psi = 105.7158 dB



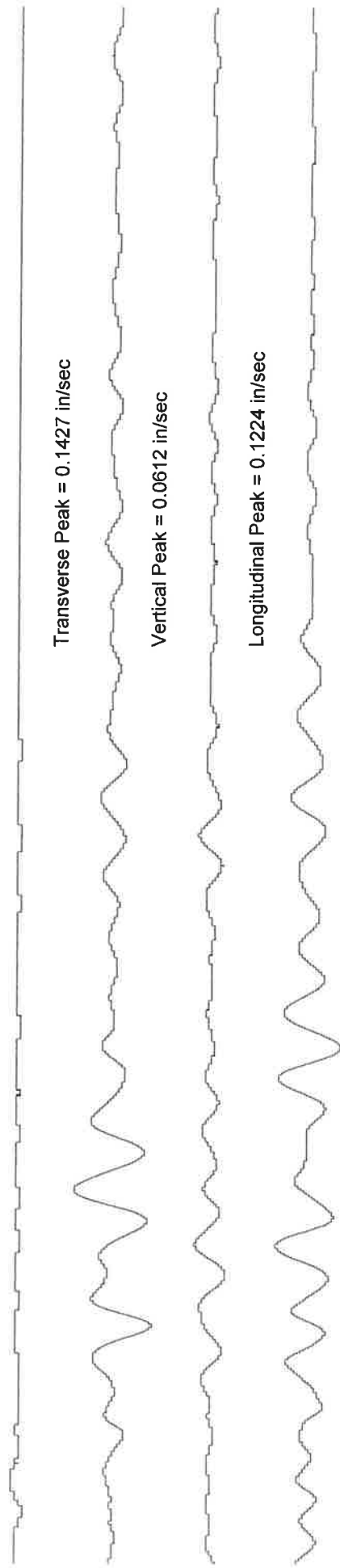
0061000 00500300603.4500164986 00500500502.1500004999 00500500403.4300004999 090500.187 100100100

PENN STATE UNIVERSITY - JEDDO COAL FIELD TESTING

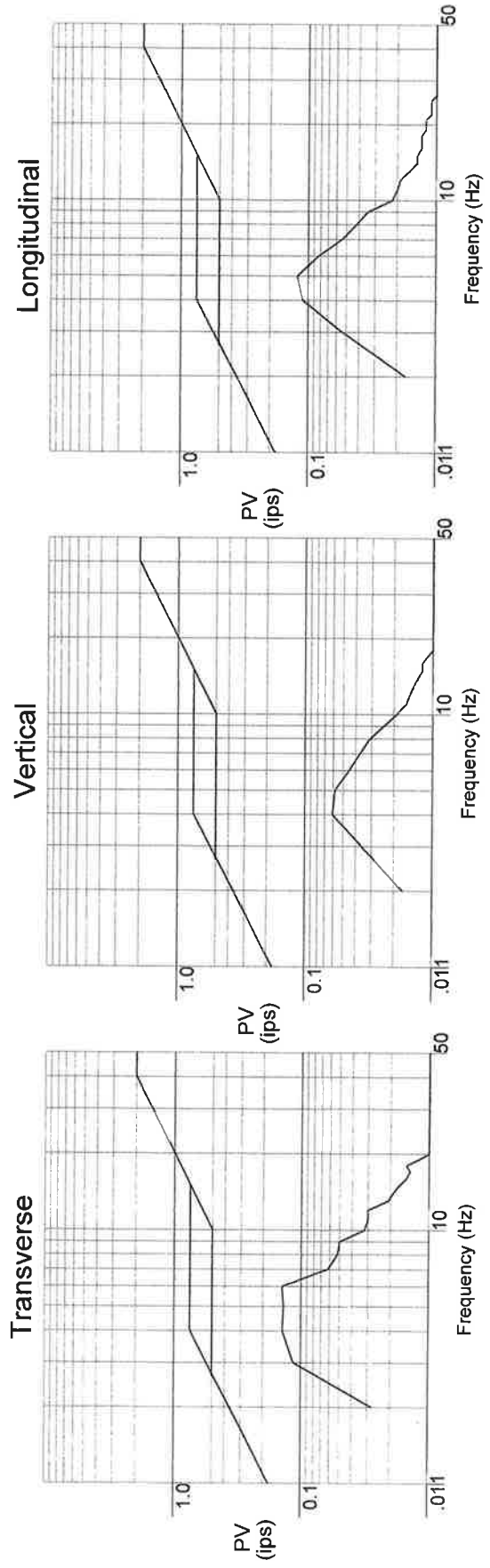
Date and Time: 07/06/2017 12:08:27

Geosonics Instrument: 4779 Distance = 1069 ft Location:

Peak Air Overpressure = 0.00056 psi = 105.7158 dB



Ground Scale 1" = 0.57 IPS Air Scale 1" = 0.05712 PSI



0150000 00400400603.5300004999 00400400401.8200004977 00500400504.1300004999 120400.152 100100100

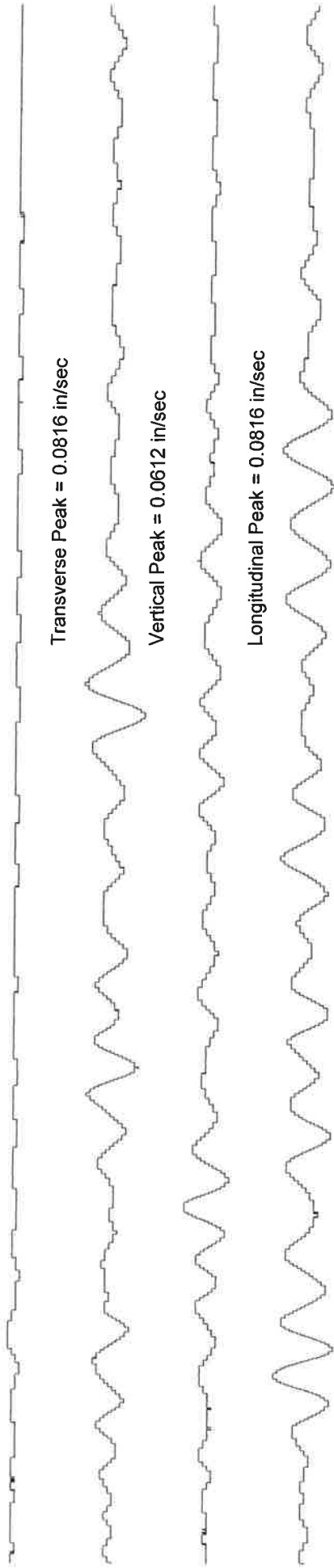
RSVP

PENN STATE UNIVERSITY - JEDDO COAL FIELD TESTING

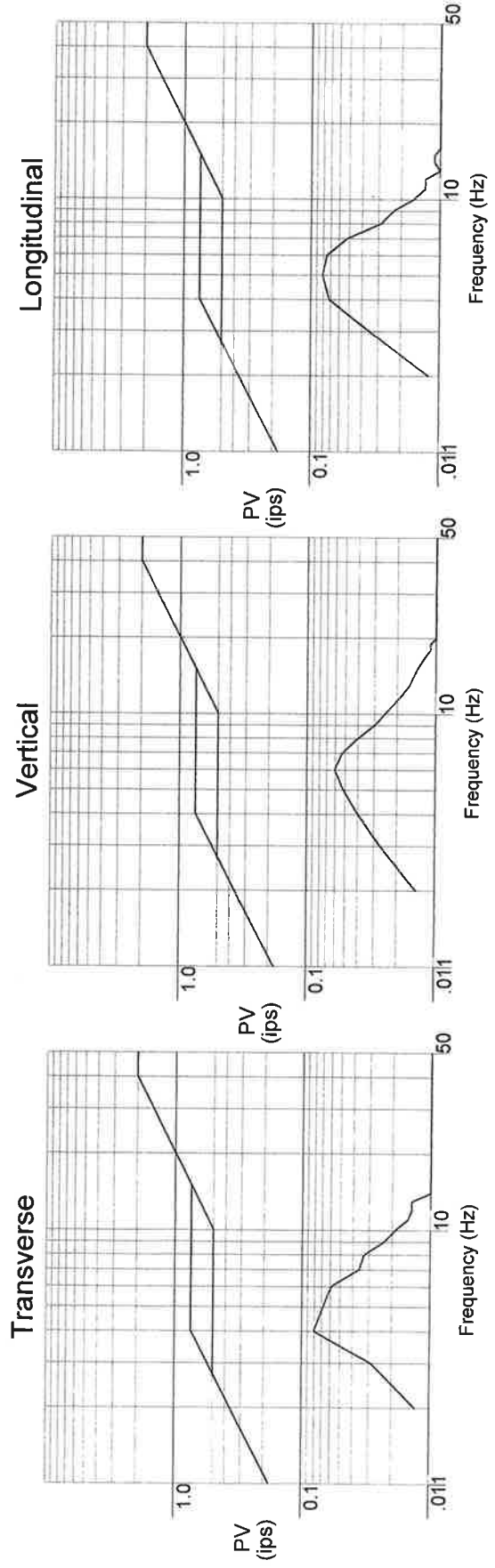
Date and Time: 07/06/2017 12:08:27

Geosonics Instrument: 4165 Distance = 1113 ft Location:

Peak Air Overpressure = 0.00056 psi = 105.7158 dB



Ground Scale 1" = 0.4 IPS Air Scale 1" = 0.05712 PSI

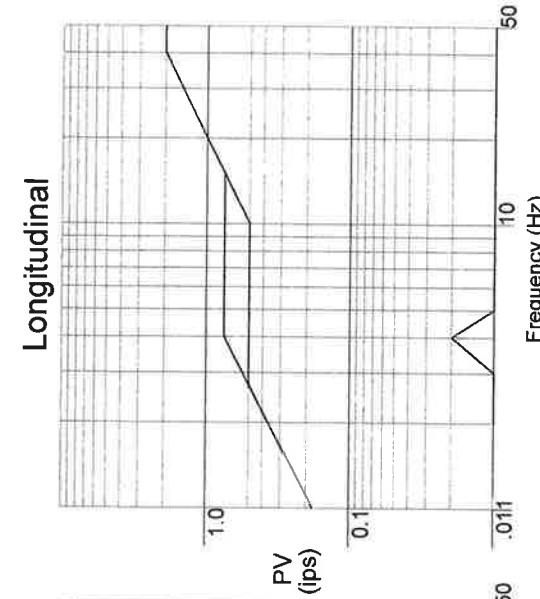
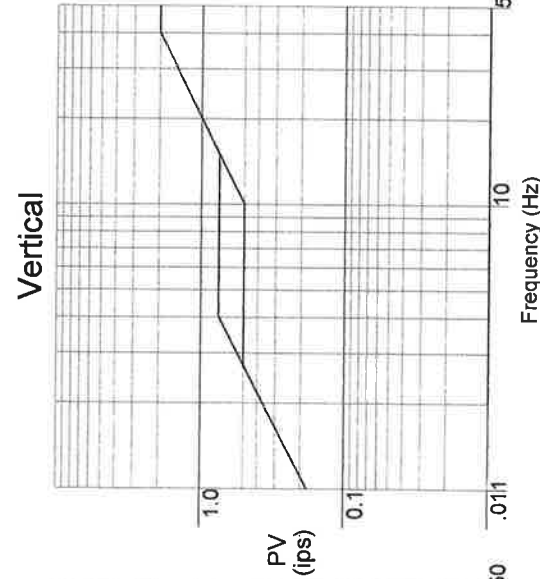
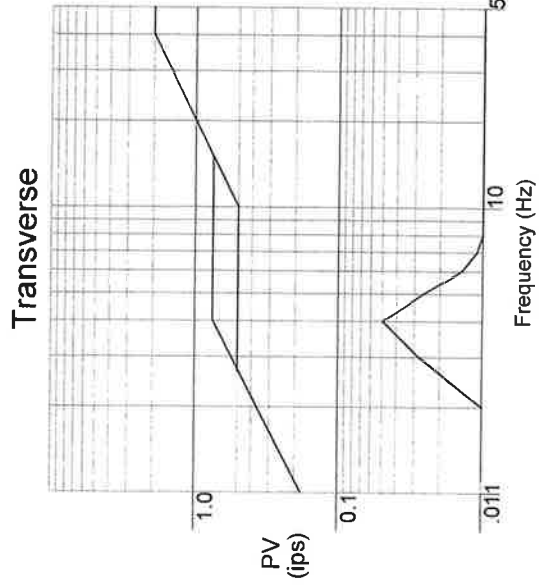
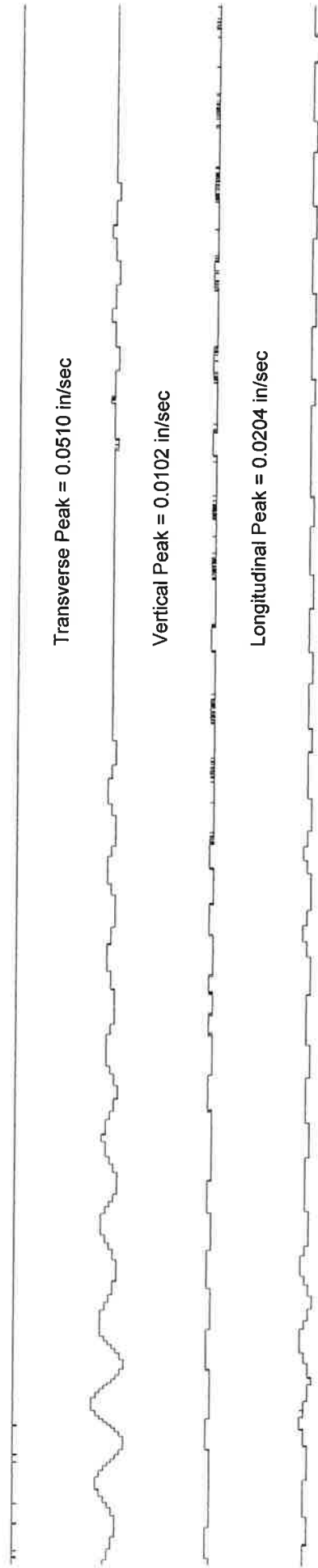


PENN STATE UNIVERSITY - JEDDO COAL FIELD TESTING

Date and Time: 07/06/2017 12:08:29

Geonics Instrument: 4814 Distance = 2180 ft Location:

Peak Air Overpressure = 0.00029 psi = 99.8639 dB



APPENDIX III

Blast Data for Site 2

13:02
 $\frac{N40^\circ 58.937}{W075^\circ 56.092}$ - Hole Location

Jeddo 8 Impoundment Looking North 60' x 130'

| Serial # | SN: | x | x | x | x | x |
|-------------------|------------------------|---|---|---|---|---|
| | 4059 | | | | | |
| Location - | N40° 58.932 | | | | | |
| PPV - | W075° 56.364 | | | | | |
| Distance to Blast | $\frac{0.0510}{1,252}$ | | | | | |
| | SN: 4814 | | | | | |
| | N40° 58.924 | | | | | |
| | W075° 56.364 | | | | | |
| | $\frac{0.0510}{2,180}$ | | | | | |
| | - 12:08 | | | | | |
| | $\frac{0.0918}{1,251}$ | | | | | |
| | - 13:02 | | | | | |
| | SN: 4163 | | | | | |
| | N40° 58.912 | | | | | |
| | W075° 56.366 | | | | | |
| | $\frac{0.0714}{1,270}$ | | | | | |
| | SN: 4116 | | | | | |
| | N40° 58.933 | | | | | |
| | W075° 56.334 | | | | | |
| | - Malfunction | | | | | |
| | SN: 4168 | | | | | |
| | N40° 58.933 | | | | | |
| | W075° 56.305 | | | | | |
| | $\frac{0.0918}{980}$ | | | | | |
| | SN: 4763 | | | | | |
| | N40° 58.923 | | | | | |
| | W075° 56.337 | | | | | |
| | $\frac{0.0510}{1,131}$ | | | | | |
| | SN: 4810 | | | | | |
| | N40° 58.923 | | | | | |
| | W075° 56.307 | | | | | |
| | $\frac{0.1325}{993}$ | | | | | |
| | SN: 4158 | | | | | |
| | N40° 58.913 | | | | | |
| | W075° 56.309 | | | | | |
| | $\frac{0.1122}{1,009}$ | | | | | |
| | SN: 4154 | | | | | |
| | N40° 58.914 | | | | | |
| | W075° 56.282 | | | | | |
| | $\frac{0.1427}{885}$ | | | | | |
| | SN: 4149 | | | | | |
| | N40° 58.915 | | | | | |
| | W075° 56.252 | | | | | |
| | $\frac{0.1529}{748}$ | | | | | |
| | SN: 4237 | | | | | |
| | N40° 58.925 | | | | | |
| | W075° 56.251 | | | | | |
| | $\frac{0.3365}{735}$ | | | | | |
| | SN: 4826 | | | | | |
| | N40° 58.934 | | | | | |
| | W075° 56.248 | | | | | |
| | $\frac{0.2651}{718}$ | | | | | |
| | SN: 4154 | | | | | |
| | N40° 58.924 | | | | | |
| | W075° 56.279 | | | | | |
| | $\frac{0.1325}{863}$ | | | | | |
| | SN: 4158 | | | | | |
| | N40° 58.913 | | | | | |
| | W075° 56.309 | | | | | |
| | $\frac{0.1122}{1,009}$ | | | | | |
| | SN: 4354 | | | | | |
| | N40° 58.913 | | | | | |
| | W075° 56.337 | | | | | |
| | - Malfunction | | | | | |

PENN STATE UNIVERSITY - JEDDO COAL FIELD TESTING

Date and Time: 07/06/2017 13:02:51

Geosonics Instrument: 4826 Distance = 718 ft Location:

Peak Air Overpressure = 0.00112 psi = 111.7364 dB

Transverse Peak = 0.2651 in/sec

Vertical Peak = 0.0816 in/sec

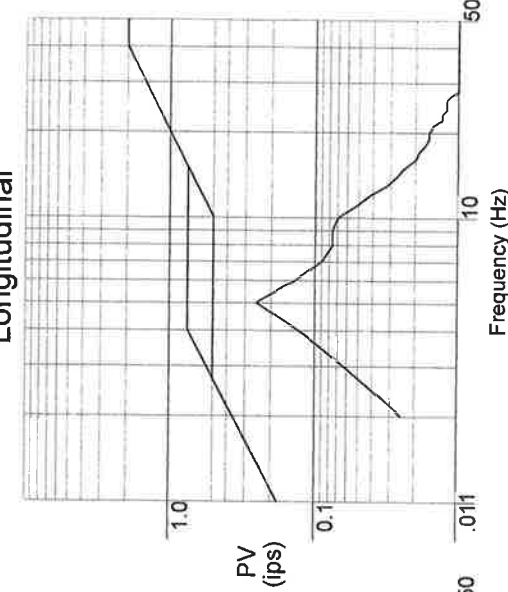
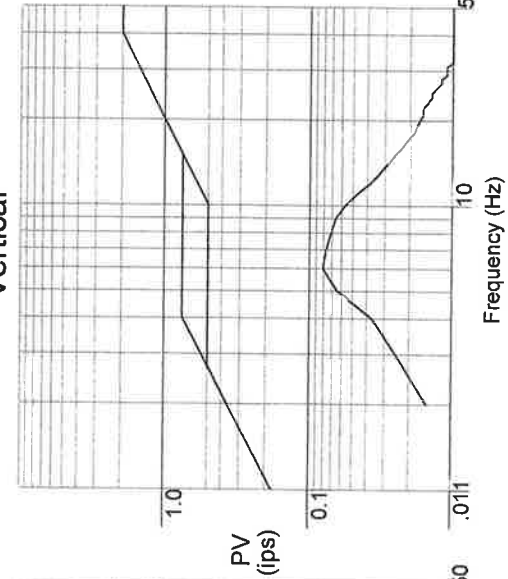
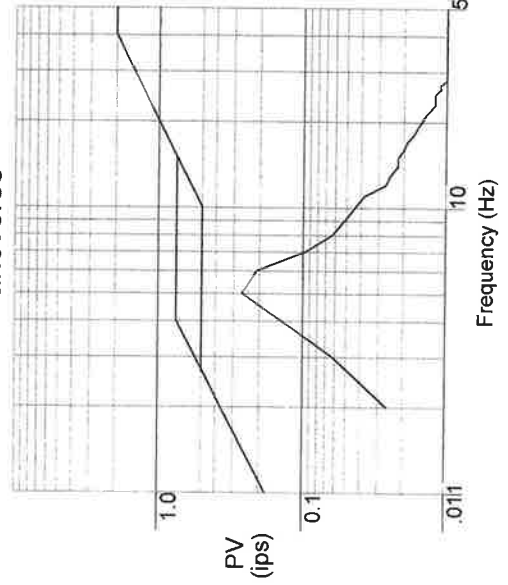
Longitudinal Peak = 0.2549 in/sec



Transverse

Vertical

Longitudinal



PENN STATE UNIVERSITY - JEDDO COAL FIELD TESTING

Date and Time: 07/06/2017 13:02:50

Geosonics Instrument: 4237 Distance = 735 ft Location:

Peak Air Overpressure = 0.00280 psi = 119.6952 dB

Transverse Peak = 0.3365 in/sec

Vertical Peak = 0.0816 in/sec

Longitudinal Peak = 0.2345 in/sec

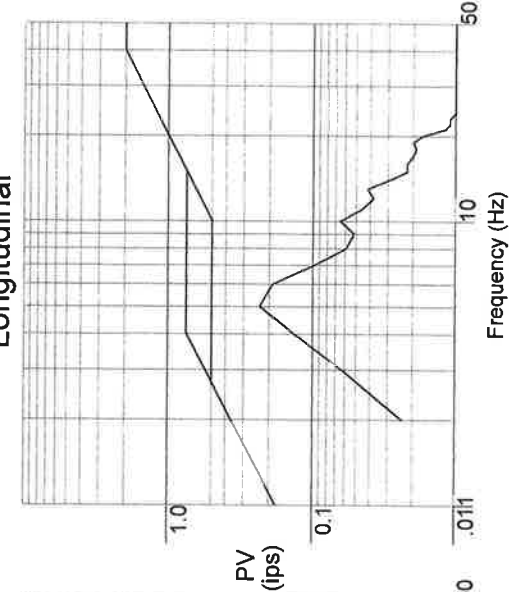
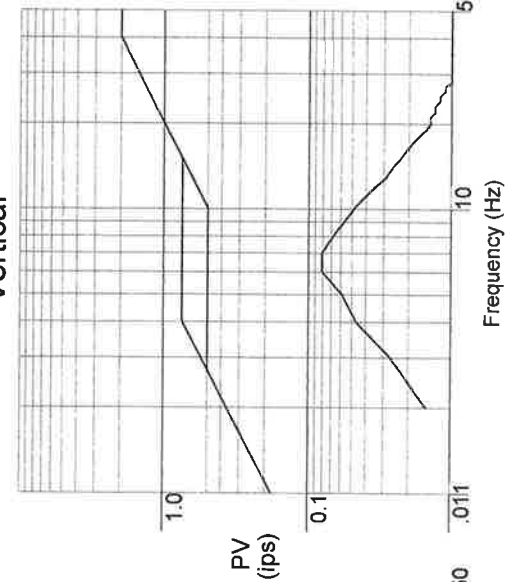
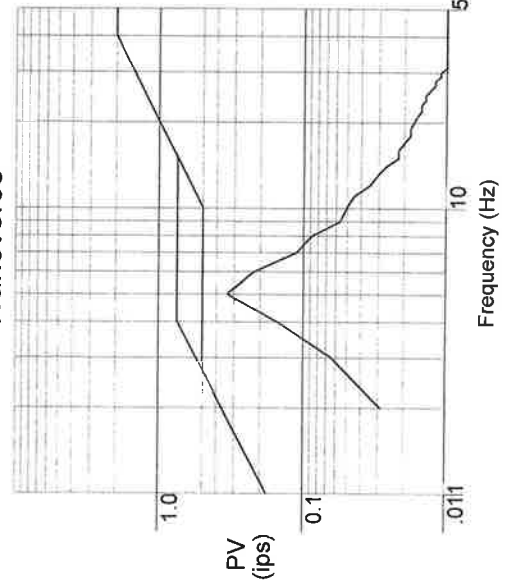


Ground Scale 1" = 1.35 IPS Air Scale 1" = 0.2856 PSI

Transverse

Vertical

Longitudinal

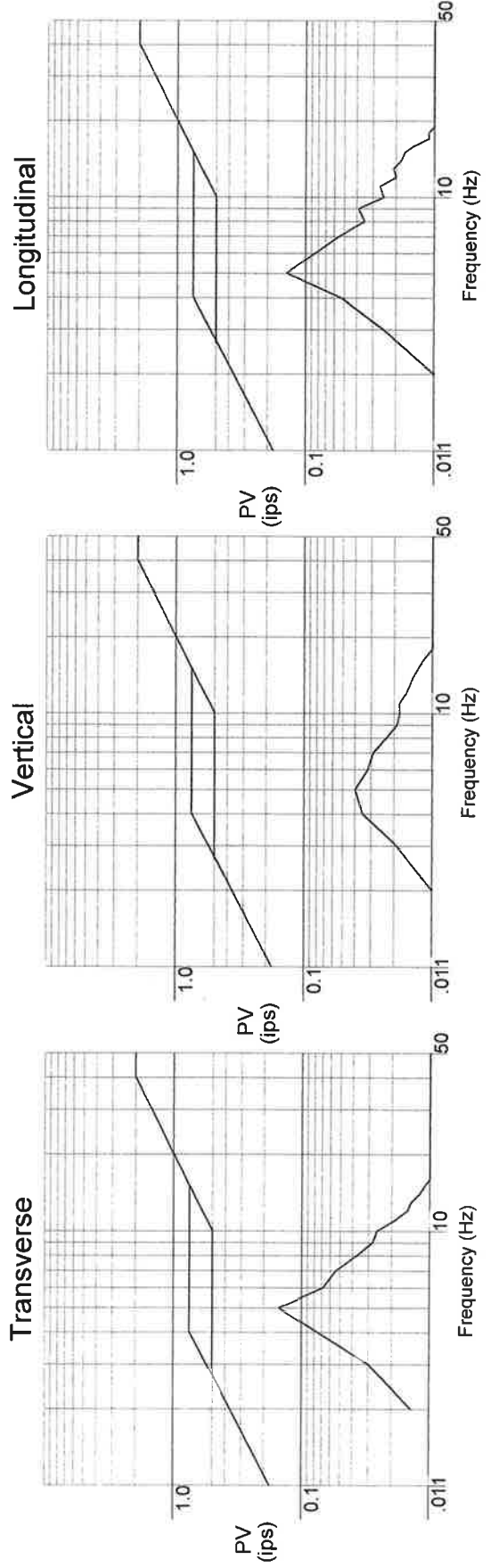
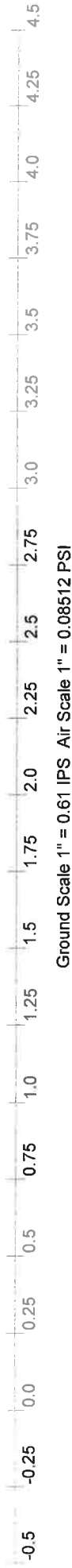
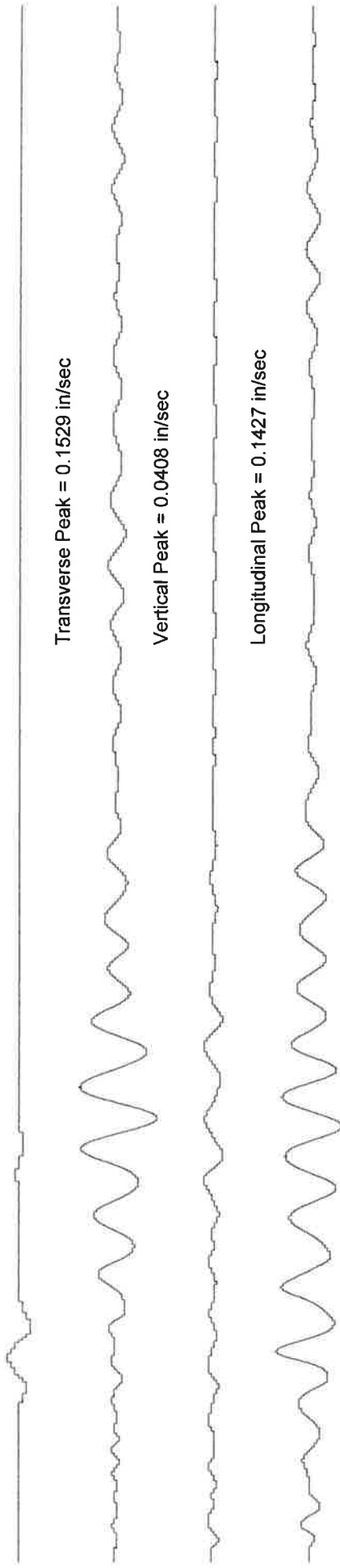


PENN STATE UNIVERSITY - JEDDO COAL FIELD TESTING

Date and Time: 07/06/2017 13:02:51

Geosonics Instrument: 4149 Distance = 748 ft Location:

Peak Air Overpressure = 0.00083 psi = 109.1807 dB

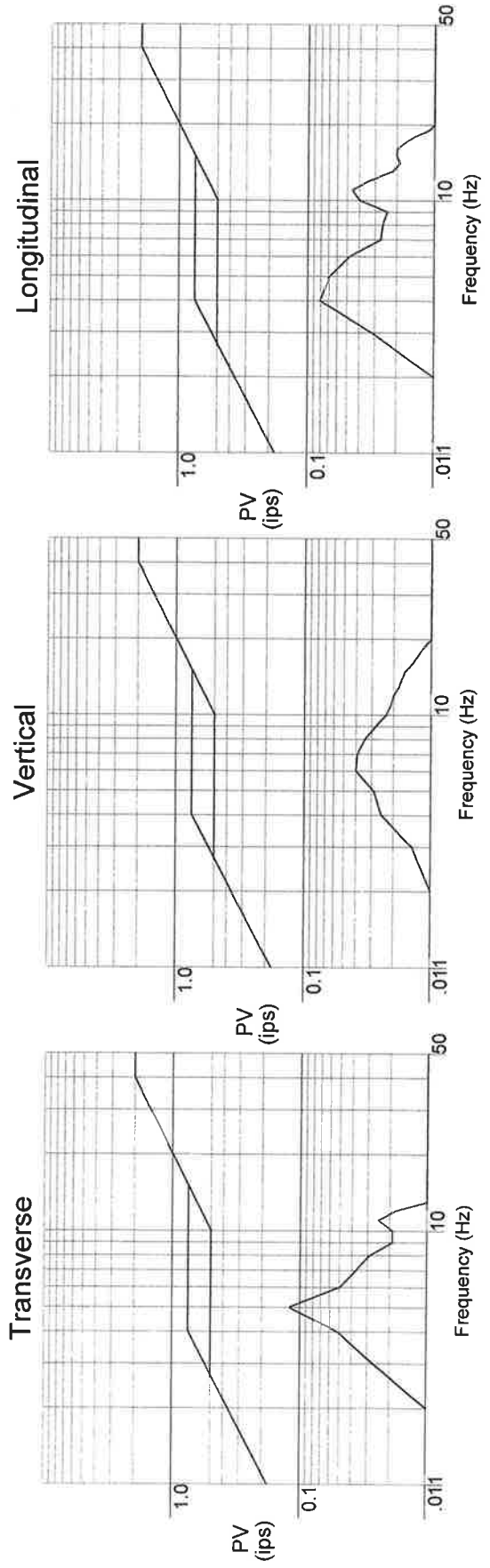
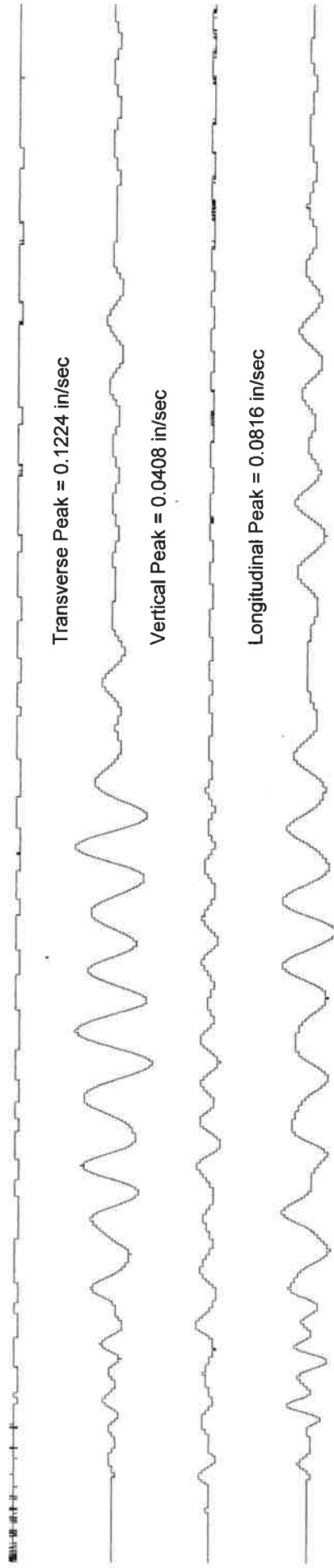


PENN STATE UNIVERSITY - JEDDO COAL FIELD TESTING

Date and Time: 07/06/2017 13:02:50

Geosonics Instrument: 4634 Distance = 856 ft Location:

Peak Air Overpressure = 0.00029 psi = 99.8639 dB

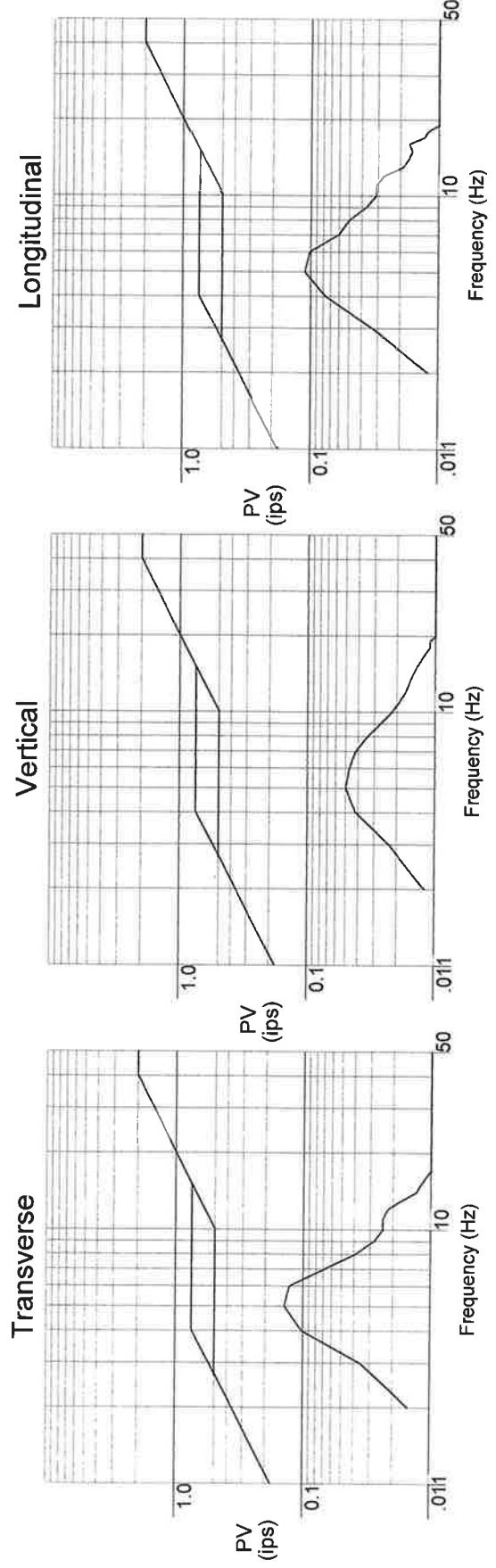
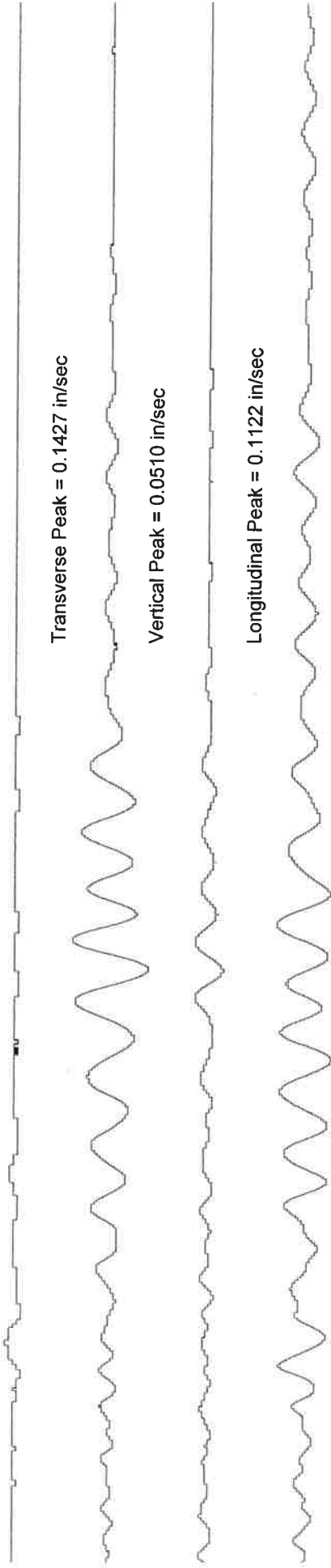


PENN STATE UNIVERSITY - JEDDO COAL FIELD TESTING

Date and Time: 07/06/2017 13:02:50

Geosonics Instrument: 4154 Distance = 885 ft Location:

Peak Air Overpressure = 0.00056 psi = 105.7158 dB

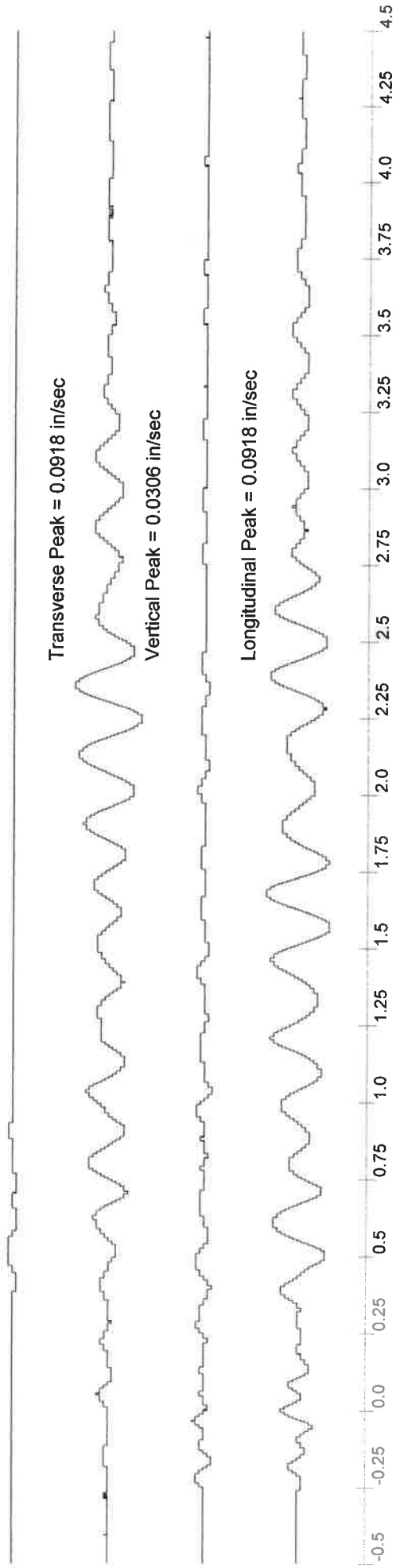


PENN STATE UNIVERSITY - JEDDO COAL FIELD TESTING

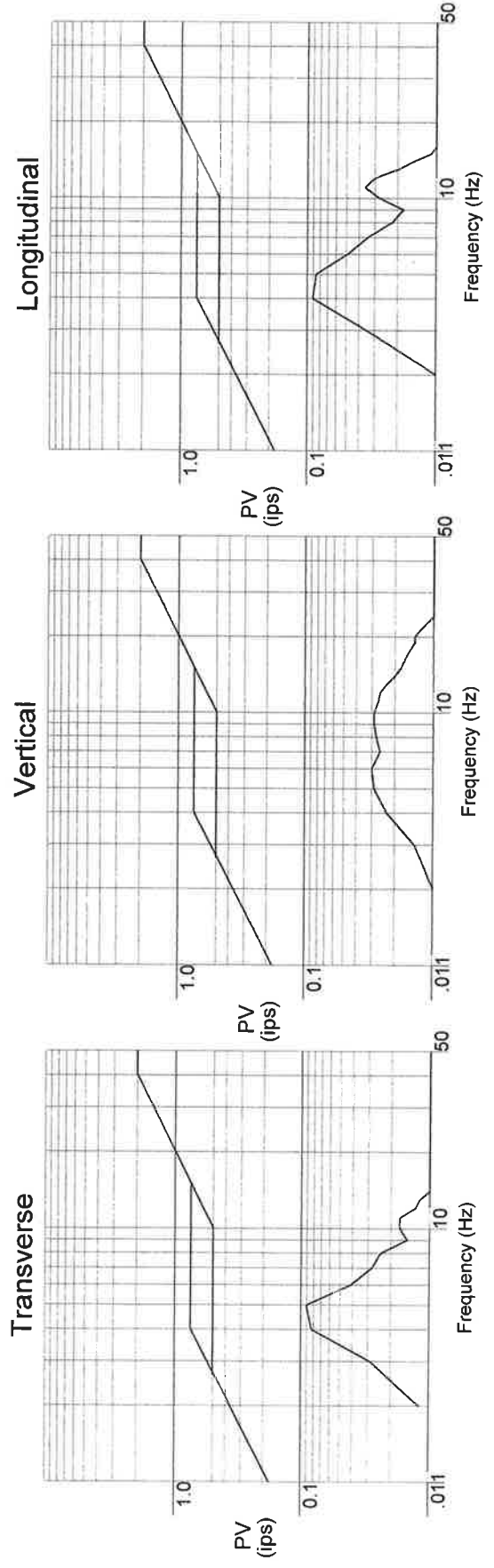
Date and Time: 07/06/2017 13:02:49

Geosonics Instrument: 4168 Distance = 980 ft Location:

Peak Air Overpressure = 0.00029 psi = 99.8639 dB



Ground Scale 1" = 0.4 IPS Air Scale 1" = 0.02912 PSI

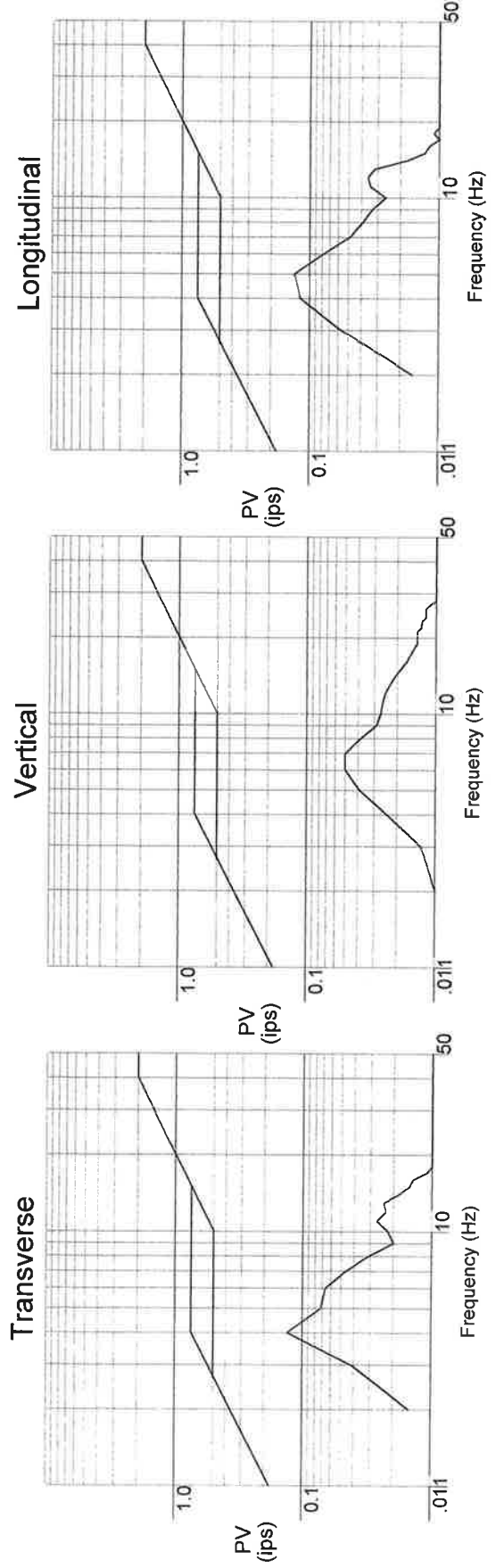
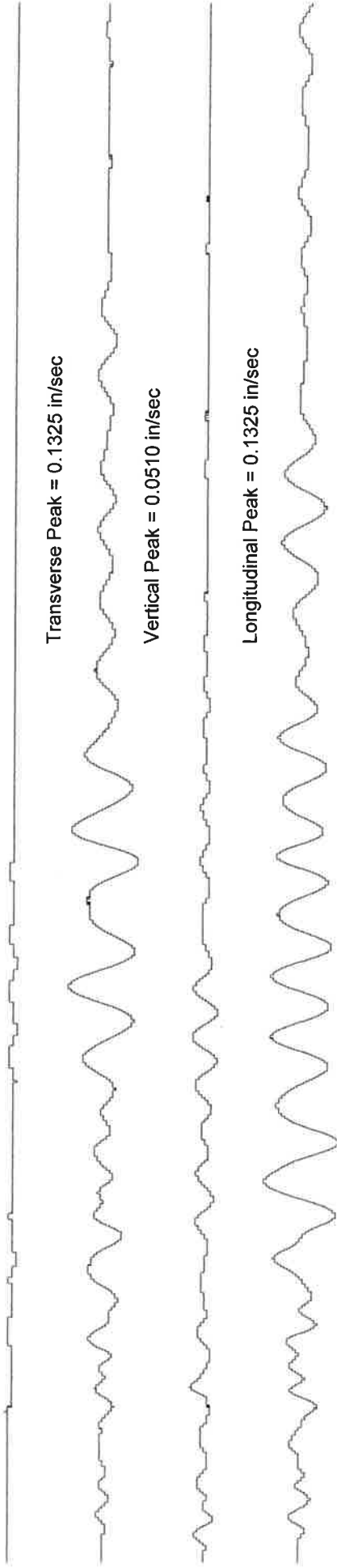


PENN STATE UNIVERSITY - JEDDO COAL FIELD TESTING

Date and Time: 07/06/2017 13:02:51

Geosonics Instrument: 4812 Distance = 863 ft Location:

Peak Air Overpressure = 0.00056 psi = 105.7158 dB

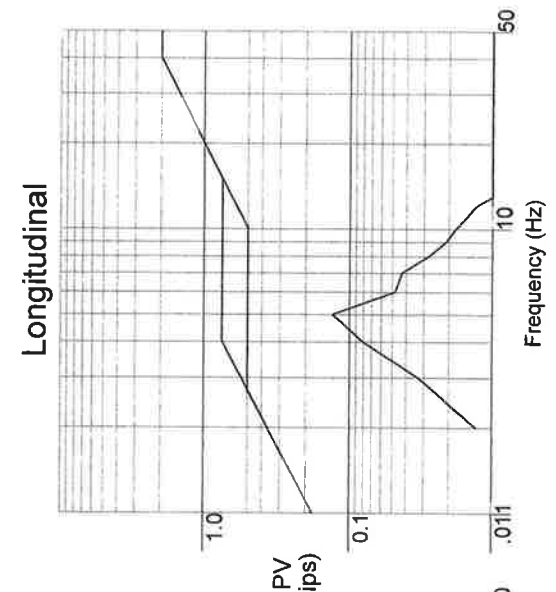
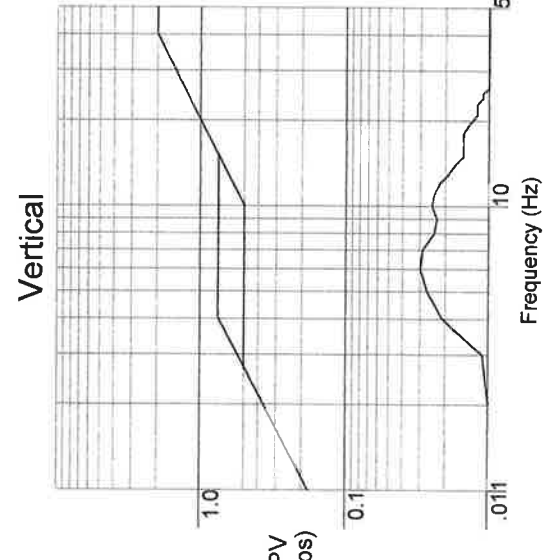
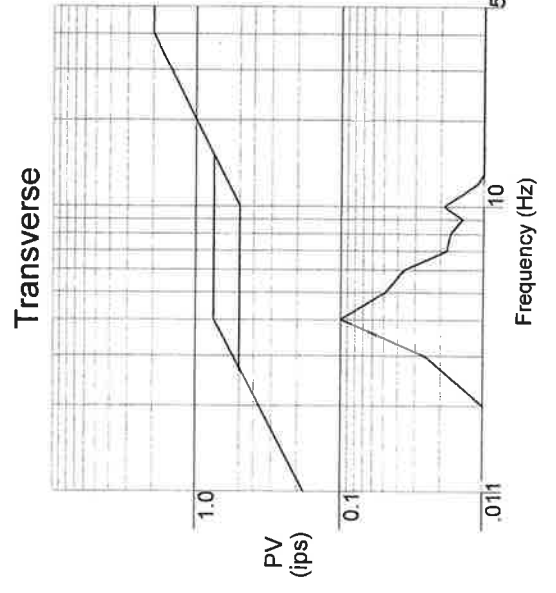
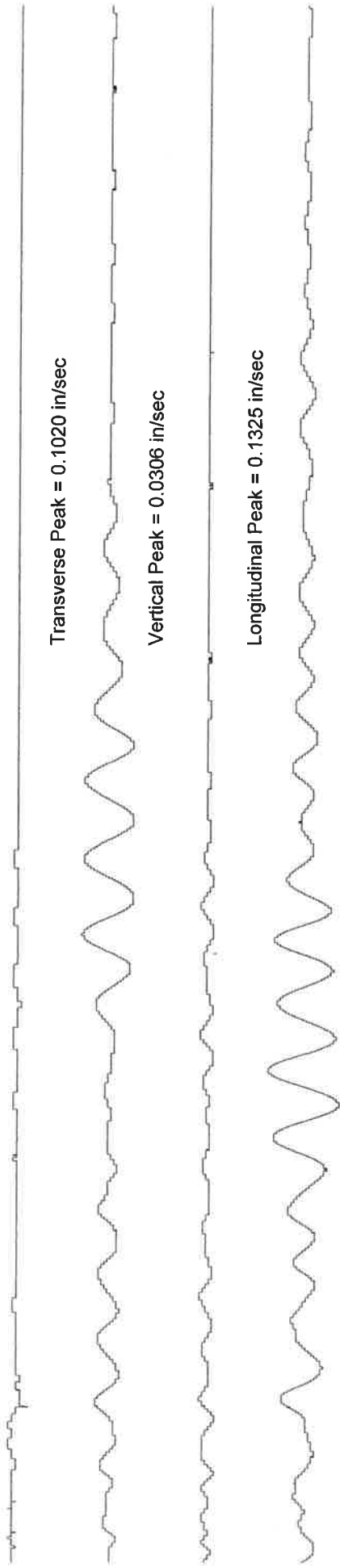


PENN STATE UNIVERSITY - JEDDO COAL FIELD TESTING

Date and Time: 07/06/2017 13:02:51

Geosonics Instrument: 4763 Distance = 993 ft Location:

Peak Air Overpressure = 0.00112 psi = 111.7364 dB

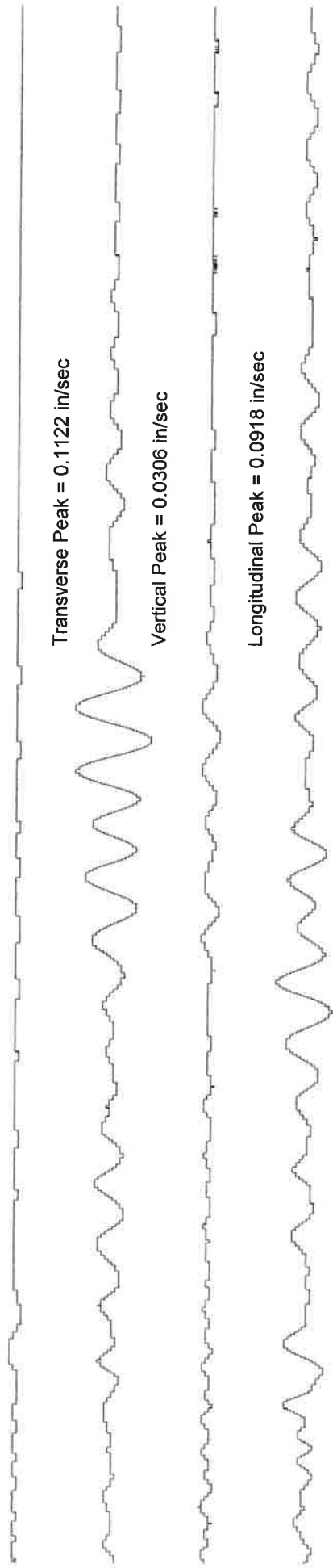


PENN STATE UNIVERSITY - JEDDO COAL FIELD TESTING

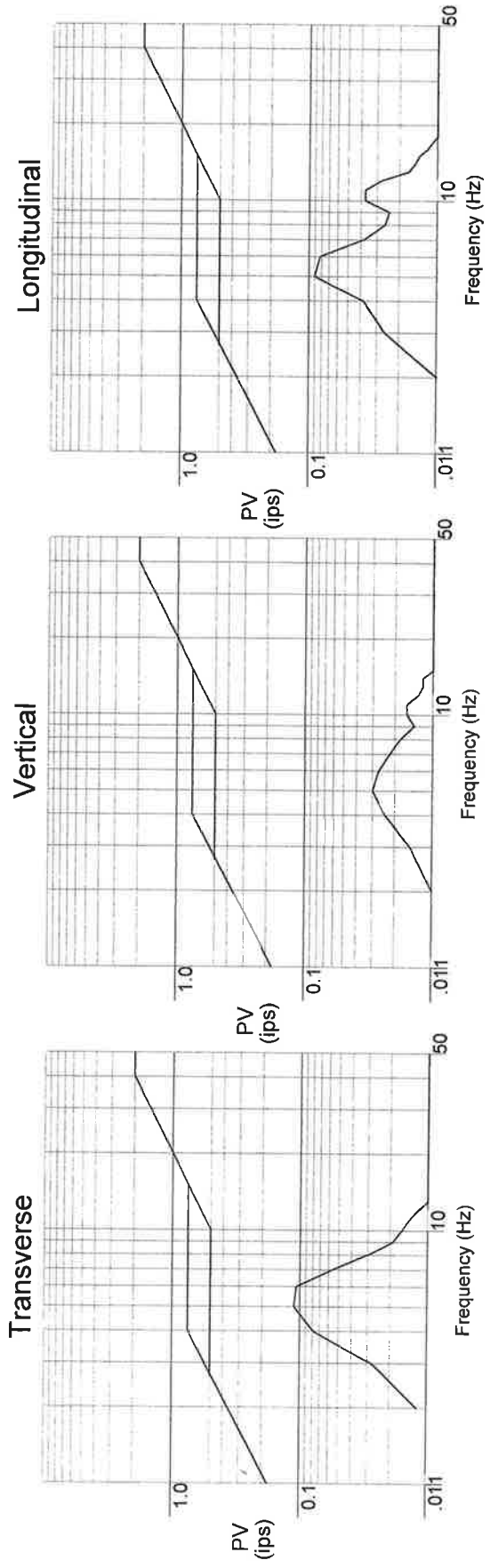
Date and Time: 07/06/2017 13:02:52

Geosonics Instrument: 4158 Distance = 1009 ft Location:

Peak Air Overpressure = 0.00056 psi = 105.7158 dB



Ground Scale 1" = 0.45 IPS Air Scale 1" = 0.05712 PSI

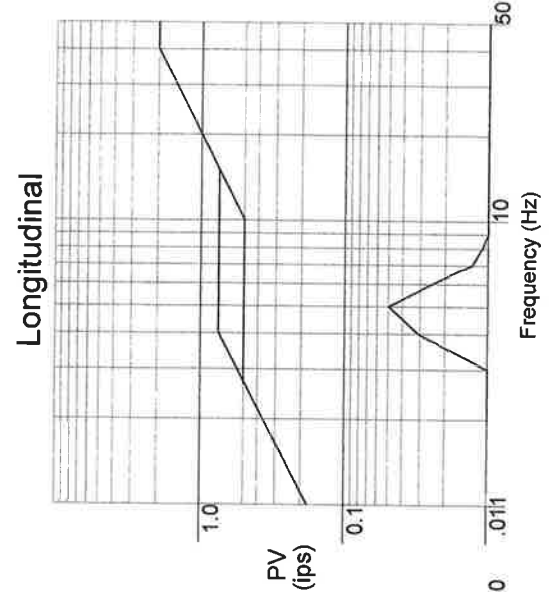
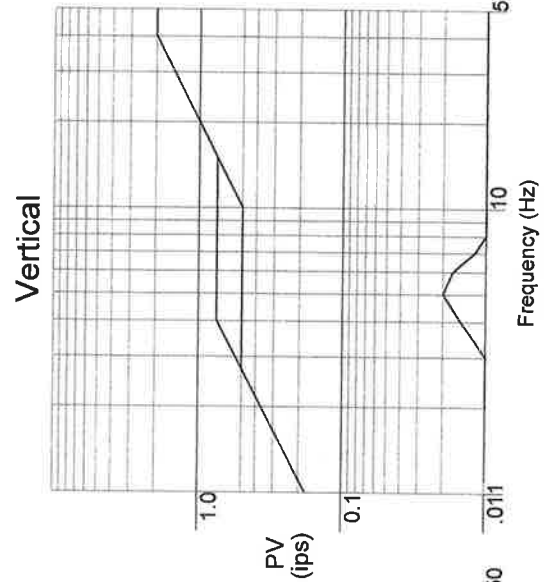
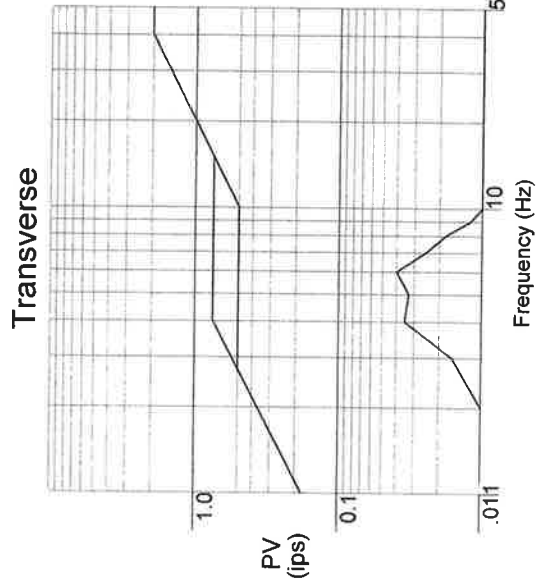
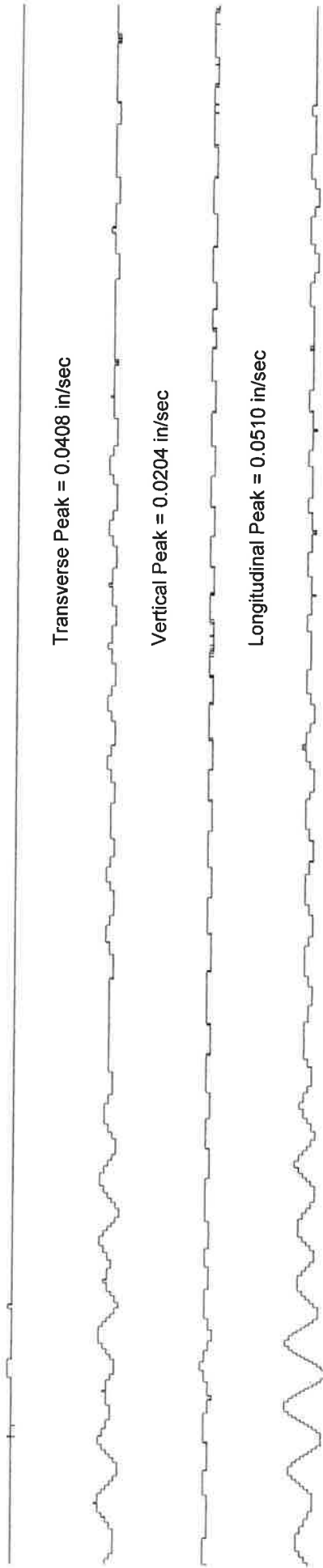


PENN STATE UNIVERSITY - JEDDO COAL FIELD TESTING

Date and Time: 07/06/2017 13:02:51

Geosonics Instrument: 4810 Distance = 1131 ft Location:

Peak Air Overpressure = 0.00029 psi = 99.8639 dB

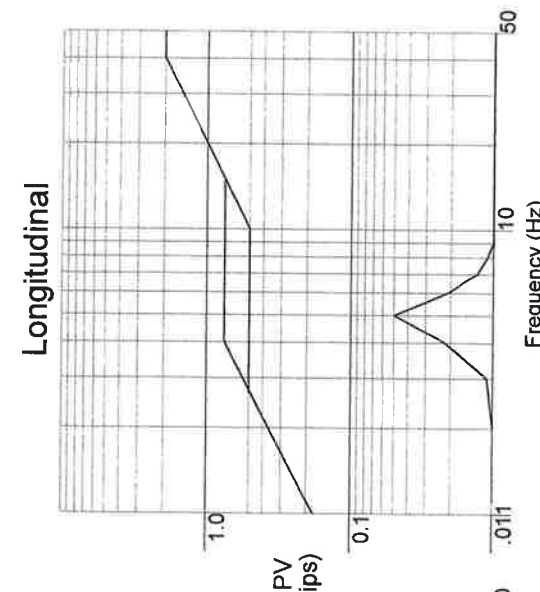
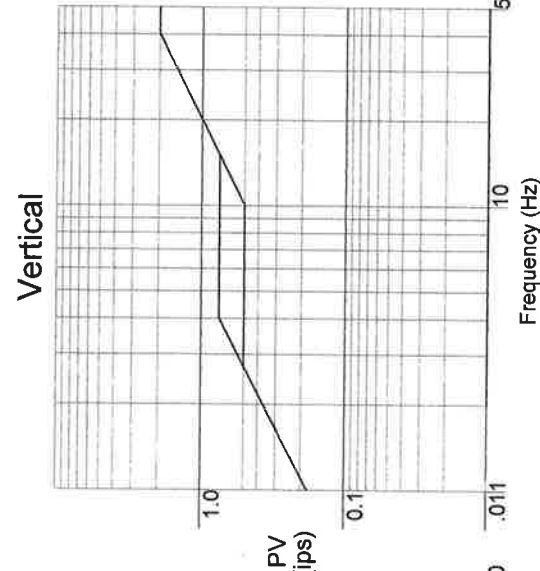
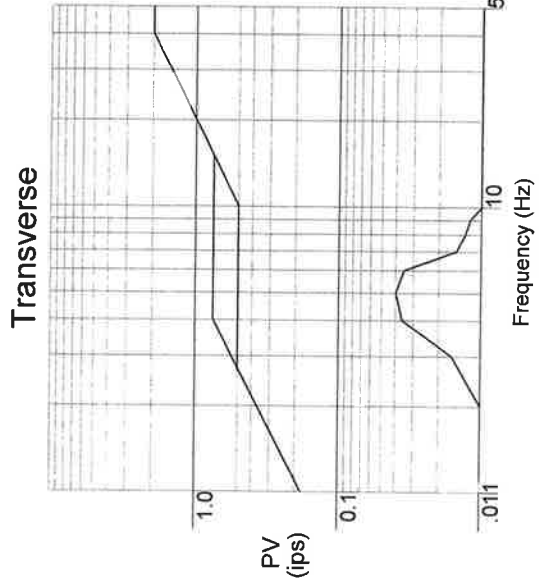
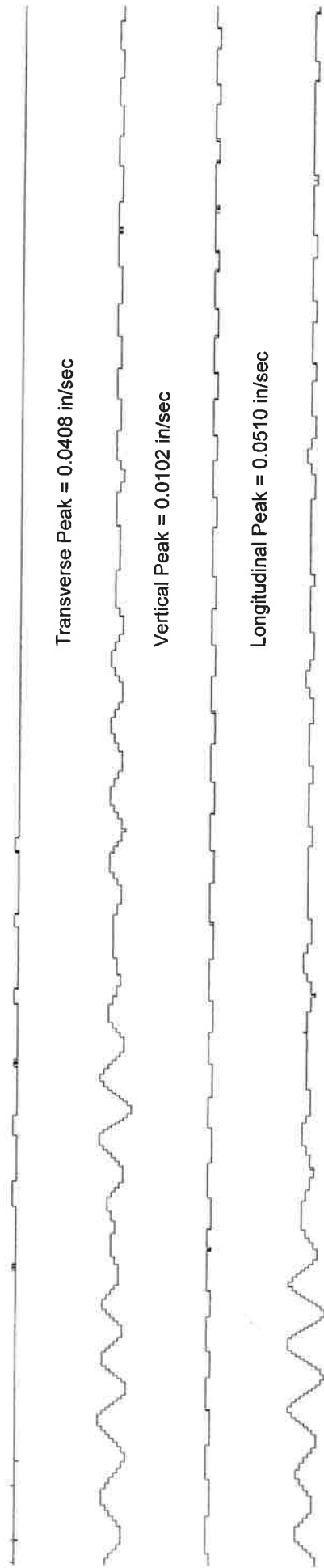


PENN STATE UNIVERSITY - JEDDO COAL FIELD TESTING

Date and Time: 07/06/2017 13:02:54

Geosonics Instrument: 4059 Distance = 1252 ft Location:

Peak Air Overpressure = 0.00029 psi = 99.8639 dB



PENN STATE UNIVERSITY - JEDDO COAL FIELD TESTING

Date and Time: 07/06/2017 13:02:51

Geosonics Instrument: 4814 Distance = 1254 ft Location:

Peak Air Overpressure = 0.00000 psi = 0.0000 dB

Transverse Peak = 0.0918 in/sec

Vertical Peak = 0.0204 in/sec

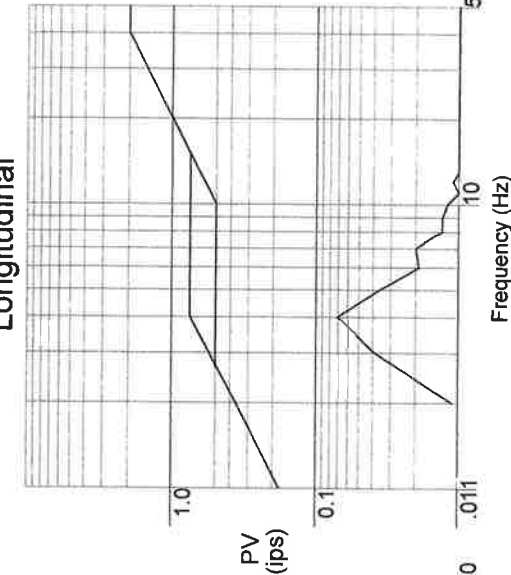
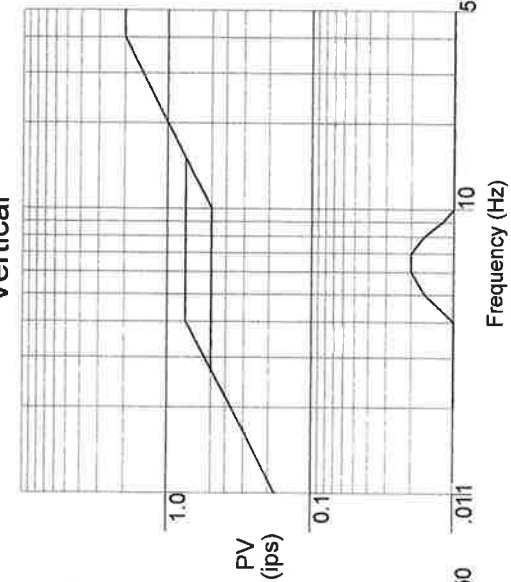
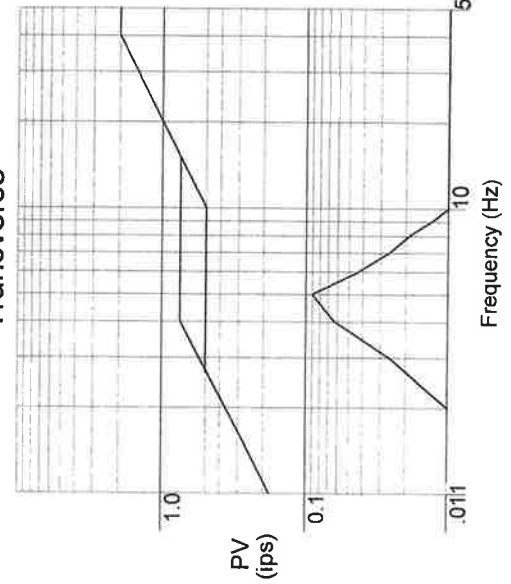
Longitudinal Peak = 0.0714 in/sec



Transverse

Vertical

Longitudinal



PENN STATE UNIVERSITY - JEDDO COAL FIELD TESTING

Date and Time: 07/06/2017 13:02:51

Geosonics Instrument: 4463 Distance = 1270 ft Location:

Peak Air Overpressure = 0.00029 psi = 99.8639 dB

